

**DEVELOPMENT OF NANOMATERIALS BASED ON
BACTERIOPHAGE-CHROMOPHORE BIOCONJUGATES**

MATTHEW TRIDGETT

**A thesis submitted to the University of Birmingham for the degree of
DOCTOR OF PHILOSOPHY**

**School of Biosciences
College of Life and Environmental Sciences
University of Birmingham
September 2018**

UNIVERSITY OF
BIRMINGHAM

University of Birmingham Research Archive

e-theses repository

This unpublished thesis/dissertation is copyright of the author and/or third parties. The intellectual property rights of the author or third parties in respect of this work are as defined by The Copyright Designs and Patents Act 1988 or as modified by any successor legislation.

Any use made of information contained in this thesis/dissertation must be in accordance with that legislation and must be properly acknowledged. Further distribution or reproduction in any format is prohibited without the permission of the copyright holder.

Abstract

A continuing trend in nanotechnology is the use of materials of biological origin to develop novel nanomaterials. Accordingly, it is important to consider alteration of biomaterials to achieve optimal performance. One such entity that has garnered significant research attention is the filamentous M13 bacteriophage. This has been deployed in a broad range of nanotechnology applications, from the production of individually functional nanoparticles, to self-assembled materials with advanced properties reliant on their nano-scale structural characteristics.

The present work had three principal aims: First to optimise the M13 bacteriophage major coat protein for labelling with exogenous compounds; second to investigate the use of dye-labelled M13 in a pathogen sensor; and third, the generation of a self-assembled nanomaterial based on dye-labelled M13.

The results of this work demonstrate: 1) the generation of a mutant strain of M13 bacteriophage optimised to bind amine-directed exogenous compounds. A maximum increase in conjugation efficiency of 520 additional exogenous groups compared to the wild type was observed using absorbance spectroscopy; 2) the extension of the linear dichroism (LD) signal of M13 bacteriophage into the visible range by labelling with cyanine-based dyes; and 3) the generation of an aster-like self-assembled structure based on dye-labelled M13 bacteriophage, characterised by transmission electron microscopy, atomic force microscopy and dynamic light scattering.

The results of this work will aid the further development of a pathogen sensor based on the LD signal of M13 bacteriophage. The extension of the M13 LD signal into the visible region, and the maximisation of that signal by the mutagenic optimisations made here, will enable improved portability and sensitivity of the sensor. Finally, the development of a self-assembled, dye-labelled M13-based structure will have implications in the branch of research that aims to understand how alterations to nanomaterials lead to changes in the way they self-assemble.

Acknowledgments

This work was supported by the Midlands Integrative Biosciences Training Partnership, funded by the Biotechnology and Biosciences Research Council (BB/M01116X/1).

I first thank Professor Timothy R. Dafforn for hosting this project, and for his supervision throughout. In addition, I am highly grateful to Dr Pola Goldberg Oppenheimer and Professor Alison Rodger, and thank them for their collaboration on the projects within this thesis.

Furthermore, I would like to say a huge thank you all members of the seventh floor of Biosciences for their friendship and support over the past few years. In particular I thank Charles for all the conversations about politics, science and the future; I thank Ian for all the hot gastro-chat; I thank Aysha for keeping everyone smiling; I thank Haydn and Rich L for showing me the ropes; I thank Rich M for providing a wonderful soundtrack to the lab; and Gareth, I don't care what everyone else says, I think you're an OK guy.

The manuscripts contained within this thesis contain some work undertaken by various other researchers (not graded for any other qualification). I am highly grateful for their enthusiasm and efforts. Their specific contributions are stated on the respective manuscript title pages.

Finally, I thank Dr Klaus Fütterer and Professor Louise Serpell for their examination of this work, and their constructive recommendations for its improvement.

Table of contents

1. INTRODUCTION.....	1
1.1. Introduction.....	2
1.2. Nanotechnology.....	3
1.2.1. Definition.....	3
1.2.2. Why operate on the nano-scale?.....	5
1.2.3. Biological materials in nanotechnology.....	8
1.2.4. Biological systems contain inherently nano-scale components.....	8
1.2.5. Bionanoparticles are often homogenous.....	9
1.2.6. Biomaterials are easily modified.....	10
1.2.7. Limitations of bionanotechnology.....	11
1.2.8. Bionanotechnology case study.....	13
1.3. M13 bacteriophage.....	14
1.3.1. Structure.....	14
1.3.2. Life cycle.....	17
1.3.3. Uses of M13 bacteriophage in nanotechnology.....	20
1.3.4. Uses of M13 bacteriophage in incremental nanotechnology.....	20
1.3.5. Uses of M13 bacteriophage in evolutionary nanotechnology.....	24
1.3.6. Limitations of M13 bacteriophage in nanotechnology.....	28
1.4. M13 bacteriophage-based bioassay by Pacheco-Gómez <i>et al.</i> (2012).....	29
1.5. Thesis aims.....	31
2. EXPERIMENTAL.....	33
2.1. Materials.....	34
2.2. Strains.....	35
2.2.1. Bacterial host.....	35
2.2.2. M13 bacteriophage.....	35
2.3. Media and buffers.....	35
2.3.1. Luria Bertani (LB) broth.....	35
2.3.2. 2x TY broth.....	36
2.3.3. NB2 broth.....	36
2.3.4. Bottom agar.....	36
2.3.5. Top agar.....	36
2.3.6. Super optimal broth with catabolite repression (SOC media).....	36
2.3.7. 50 mM potassium phosphate buffer pH 8.0.....	37
2.3.8. Poly(ethylene glycol) solution.....	37

2.3.9. Tris buffer	37
2.3.10. Iodide buffer	37
2.3.11. Bicine buffers	37
2.3.12. Thioflavin T buffer	38
2.4. General	38
2.4.1. Bacteriophage host glycerol stock preparation	38
2.4.2. M13 bacteriophage propagation and purification	39
2.5. Linear dichroism of visible-region chromophores using M13 bacteriophage as an alignment scaffold	40
2.5.1. Triton X-100 disaggregation of dyes from bacteriophage conjugates	40
2.6. Mutation of M13 bacteriophage major coat protein for increased conjugation to exogenous compounds	40
2.6.1. Site-directed mutagenesis	40
2.6.2. Plaque assay	41
2.6.3. Bacteriophage amplification from plaques	42
2.6.4. Preparation of single-stranded bacteriophage DNA for sequencing	43
2.6.5. Sequencing	43
2.6.6. Preparation of double-stranded bacteriophage DNA	44
2.6.7. Agarose gel electrophoresis	44
2.6.8. Determination of molar extinction coefficient of 4-chloro-7-nitrobenzofurazan bound to an amine group	44
2.6.9. Nonlinear regression analysis	45
2.6.10. UV-visible absorbance spectroscopy	46
2.6.11. Conjugation efficiency calculation	47
2.7. Bacteriophage thermal stability	47
2.7.1. Circular dichroism	47
2.7.2. Deconvolution of circular dichroism data	48
2.7.3. Thioflavin T assay	49
2.8. Assembly of multi-virion structures mediated by xanthene dye H-aggregation	50
2.8.1. Conjugation of Cyanine3 NHS ester to M13 bacteriophage	50
2.8.2. Ammonium sulphate precipitation of M13Cy3	50
2.8.3. Screen for alternative salts to induce dye H-aggregation	51
3. LINEAR DICHROISM OF DYES USING M13 BACTERIOPHAGE AS AN ALIGNMENT SCAFFOLD	52

3.1. Introduction	53
3.2. Linear dichroism spectroscopy	54
3.3. Linear dichroism spectroscopy methods	56
3.3.1. Small molecule orientation methods	56
3.3.2. Macromolecular orientation methods	60
3.3.3. Förster resonance energy transfer (FRET)	62
3.4. Project aims	64
3.5. Manuscript number 1 (M1).....	65
M1.1. Abstract.....	66
M1.2. Introduction	66
M1.3. Experimental	70
M1.3.1. Materials.....	70
M1.3.2. Mass Spectrometry	70
M1.3.3. Stretched-film linear dichroism measurements	70
M1.3.4. Production of M13 bacteriophage	71
M1.3.5. Bacteriophage-dye conjugation.....	71
M1.3.6. Bacteriophage-dye conjugate linear dichroism measurements	73
M1.3.7. Bacteriophage mutagenesis.....	73
M1.3.8. Bacteriophage-dye conjugate fluorescence measurements	73
M1.4. Results and Discussion	74
M1.4.1. Cyanine3 NHS ester	76
M1.4.2. Cyanine5 NHS ester	79
M1.4.3. Alexa Fluor 555 C ₂ -maleimide	82
M1.4.4. Alexa Fluor 647 C ₂ -maleimide	84
M1.4.5. LD to inform FRET optimisation	88
M1.5. Conclusions	93
M1.6. Supporting information.....	93
3.6. Additional results	94
3.7. Discussion	95
3.8. Conclusions	100
4. MUTATION OF M13 BACTERIOPHAGE MAJOR COAT PROTEIN FOR	
INCREASED CONJUGATION TO EXOGENOUS COMPOUNDS	101
4.1. Introduction	102
4.2. Project aims	102
4.3. Manuscript number 2 (M2).....	103
M2.1. Abstract.....	104
M2.2. Introduction	104
M2.3. Results	107
M2.4. Discussion	113

M2.5. Conclusion	114
M2.6. Supporting information.....	114
M2.6.1. Experimental procedures	114
M2.6.2. Effect of N12D mutation on conjugation efficiency.....	117
M2.6.3. Determination of ϵ_{475} of 4-chloro-7-nitrobenzofurazan following reaction with amine group.....	119
M2.6.4. Optimisation of conjugation to wild type M13 bacteriophage	122
M2.6.5. Gel analysis of dye conjugation	123
M2.6.6. Plaque-forming ability of bacteriophage mutants	125
4.4. Additional results	127
4.5. Discussion	128
4.6. Conclusions	130
5. BACTERIOPHAGE THERMAL STABILITY	131
5.1. Introduction	132
5.1.1. Circular dichroism spectroscopy	133
5.1.2. Derivation of protein structural information from circular dichroism spectroscopy	135
5.1.3. Thioflavin T.....	137
5.1.4. Thioflavin T assay limitations	138
5.2. Project aims	139
5.3. Results.....	140
5.3.1. Bacteriophage melting temperature	140
5.3.2. Bacteriophage secondary structure during thermal denaturation	142
5.3.3. Bacteriophage unfolding and re-folding	147
5.4. Discussion	150
5.5. Conclusions	156
6. ASSEMBLY OF MULTI-VIRION STRUCTURES VIA DYE H-AGGREGATION .	157
6.1. Introduction	158
6.2. Ordered assembly of organic dyes	158
6.3. Why are J-aggregates sought-after?	161
6.4. Production of dye aggregates.....	163
6.5. Tetramethylrhodamine isothiocyanate (TRITC).....	165
6.6. Project aims	167
6.7. Manuscript number 3 (M3).....	168
M3.1. Abstract.....	169
M3.2. Introduction	170
M3.3. Experimental section	172
M3.3.1. Growth of M13 bacteriophage.....	172

M3.3.2. Conjugation of tetramethylrhodamine isothiocyanate to M13 bacteriophage	172
M3.3.3. Mass spectrometry	173
M3.3.4. Conjugation of TRITC to L-Alanine	173
M3.3.5. Conjugation of M13 to N-succinimidyl S-acetylthioacetate	174
M3.3.6. Ammonium sulphate precipitation	174
M3.3.7. Absorbance measurements	174
M3.3.8. Linear dichroism measurements	175
M3.3.9. Fluorescence anisotropy measurements	175
M3.3.10. Transmission electron microscopy	176
M3.3.11. Scanning transmission electron microscopy	176
M3.3.12. Atomic force microscopy	176
M3.3.13. Dynamic light scattering	177
M3.4. Results and discussion	177
M3.4.1. Conjugation of TRITC to M13 bacteriophage.....	177
M3.4.2. Formation of TRITC H-aggregates.....	179
M3.4.3. Induction of H-aggregate formation using ammonium sulphate.....	180
M3.4.4. Assembly of M13 bacteriophage using TRITC.....	181
M3.4.5. Induction of H-aggregate formation using ammonium sulphate.....	184
M3.4.6. Linear dichroism studies of M13TRITC association.....	186
M3.4.7. Fluorescence anisotropy studies of M13TRITC assembly.....	190
M3.4.8. Mechanism of H-aggregation	192
M3.4.9. Structure of the M13TRITC assembly.....	193
M3.4.10. Dynamic light scattering analysis of M13TRITC assembly	197
M3.5. Conclusion	198
M3.6. Supporting information.....	200
M3.6.1. Mechanism of H-aggregation	200
M3.6.2. Transmission electron micrographs of bacteriophage structures.....	201
6.8. Additional results	202
6.8.1. Cyanine3 NHS ester	202
6.8.2. Screen for alternative salts to induce dye H-aggregation	209
6.9. Discussion	213
6.9.1. Dye assembly.....	213
6.9.2. Bacteriophage assembly.....	214

6.10. Conclusions	216
7. DISCUSSION AND FUTURE WORK.....	218
7.1. Discussion	219
7.1.1. Linear dichroism of organic dyes using M13 bacteriophage as an alignment scaffold	219
7.1.2. Mutation of M13 bacteriophage major coat protein for increased conjugation to exogenous compounds.....	220
7.1.3. Thermal stability of bacteriophage mutants	221
7.1.4. Assembly of multi-virion structures via dye H-aggregation	222
7.1.5. General discussion.....	223
7.2. Conclusions.....	226

List of figures

Figure 1.1. Examples of Evolutionary and Incremental nanotechnologies.....	5
Figure 1.2. Creation of a tumour-labelling particle using bacteriophage display.	11
Figure 1.3. M13 bacteriophage structure.....	16
Figure 1.4. Schematic of M13 bacteriophage replication cycle, showing initial host infection, bacteriophage DNA replication, and bacteriophage assembly and exit.....	19
Figure 1.5. Methods for directing the assembly of M13 bacteriophage-based structures.....	21
Figure 1.6. Schematic of the Pacheco-Gómez <i>et al.</i> (2012) assay.	31
Figure 2.1. Linear map of M13KE genome.....	35
Figure 3.1. Schematic of angle (α) between transition dipole moment of tryptophan and orientation axis.	56
Figure 3.2. Experimental setup for stretched-film linear dichroism spectroscopy. ...	60
Figure 3.3. Couette flow alignment of rod-like macromolecules.....	61
Figure M1.1. Dye structures. Molecular long axes denoted by blue arrow.....	75
Figure M1.2. Linear dichroism spectra of Cyanine3 NHS ester and M13 bacteriophage Cy3 conjugate (M13Cy3).....	78
Figure M1.3. Linear dichroism spectra of Cyanine5 NHS ester and M13 bacteriophage Cy5 conjugate (M13Cy5).....	80
Figure M1.4. Linear dichroism spectra of Alexa Fluor 555 C ₂ -maleimide and M13 bacteriophage AF555 conjugate (M13AF555)..	83
Figure M1.5. Linear dichroism spectra of Alexa Fluor 647 C ₂ -maleimide and M13 bacteriophage AF647 conjugate (M13AF647)..	86
Figure M1.6. Proposed dimer geometry of Alexa Fluor 647. Z = orientation axis; z = cyanine chromophore long axis.....	86
Figure M1.7. Relationship between dye relative alignment and FRET efficiency.....	92
Figure 3.4. Disaggregation of Cy5 bound to M13 bacteriophage using Triton X-100	94
Figure 3.5. AF647 in the presence of Triton X-100.	95
Figure M2.1. Scheme for the generation of M13 mutants displaying additional lysine residues.....	107
Figure M2.2. Conjugation of exogenous chromophores to M13 variants.....	112

Figure M2.S1. Effect of various bacteriophage mutations on conjugation efficiency.	118
Figure M2.S2. Determination of the molar extinction coefficient at 475 nm of NBD-Cl when conjugated to an amine moiety.....	121
Figure M2.S3. Screen for optimised conjugation reaction conditions.....	123
Figure M2.S4. Analysis of dye conjugation by gel electrophoresis in denaturing conditions.....	125
Figure M2.S5. Titre of M13 bacteriophage mutants and wild type.....	126
Figure 4.1. Linear dichroism of bacteriophage-dye conjugates.....	127
Figure 5.1. Light polarisation.....	134
Figure 5.2. Typical circular dichroism spectra of protein secondary structure elements.....	136
Figure 5.3. Chemical structure of thioflavin T. Drawn using ChemDraw Professional software.....	137
Figure 5.4. Denaturation curves of bacteriophage variants.....	141
Figure 5.5. Circular dichroism (ellipticity; θ) of bacteriophage variants, and high tension (HT) voltage of wild type bacteriophage before and after thermal denaturation.....	143
Figure 5.6. Protein secondary structure composition of bacteriophage variants during thermal denaturation.....	144
Figure 5.7. Thioflavin T assay on heat-denatured bacteriophage variants.....	146
Figure 5.8. Circular dichroism at 222 nm (ellipticity; θ_{222}) of bacteriophage variants during heating and cooling.....	147
Figure 5.9. Alpha helical content of bacteriophage variants during heating and cooling.....	148
Figure 5.10. Circular dichroism spectra (ellipticity; θ) of bacteriophage variants before (15 °C i), during (60 °C) and after (15 °C f) heating.....	149
Figure 5.11. Intersubunit contact between pVIII N-terminal residues and region where aromatic residues are most abundant (determined by nuclear magnetic resonance spectroscopy).....	153
Figure 6.1. Schematic of H- and J-aggregates.....	159
Figure 6.2. H- and J-aggregation of dyes.....	161

Figure 6.3. Protein labelling with tetramethylrhodamine isothiocyanate.....	166
Figure M3.1. (a) UV-Vis spectrum of M13 bacteriophage before and after conjugation to tetramethylrhodamine isothiocyanate (TRITC). (b) Mass spectrum of M13 before and after conjugation to TRITC.	179
Figure M3.2. (a) Changes in the absorbance spectrum of TRITC with respect to TRITC concentration in 50 mM potassium phosphate buffer at pH 8.0.	180
Figure M3.3. (a) Molar absorbance spectrum of M13TRITC at varying dilutions in 50 mM potassium phosphate buffer at pH 8..	183
Figure M3.4. (a) Molar absorption of 1.2 μ M TRITC covalently bound to M13 in varying concentrations of ammonium sulphate in 50 mM potassium phosphate buffer at pH 8.0.....	185
Figure M3.5. Relationship between linear dichroism signal of M13 alone (a) and in M13TRITC conjugate (b), and concentration of ammonium sulphate up to 2.25 M in 50 mM potassium phosphate buffer at pH 8.0.	188
Figure M3.6. Fluorescence anisotropy of TRITC and M13TRITC during ammonium sulphate precipitation	192
Figure M3.7. Electron micrographs of M13 and M13TRITC conjugate in 50 mM potassium phosphate buffer at pH 8.0, in varying concentrations of ammonium sulphate (AS) up to 2.00 M.....	195
Figure M3.8. Characterisation of M13TRITC structure in varying contexts.....	197
Figure M3.S1. Removal of free dye by filtration..	200
Figure M3.S2. Transmission Electron Micrographs of M13TRITC conjugate in 1.00 M ammonium sulphate.	201
Figure 6.4. Chemical structure of Cyanine 3 NHS ester.....	202
Figure 6.5. Spectral properties of Cy3 alone and when bound to M13 bacteriophage.	203
Figure 6.6. Addition of ammonium sulphate to Cy3 and M13Cy3	206
Figure 6.7. Linear dichroism of M13 bacteriophage-Cy3 conjugate in the presence of precipitant.....	208
Figure 6.8. Screen for salts to induce H-aggregation of TRITC alone and bound to M13 bacteriophage.....	210

Figure 6.9. Comparison of H-aggregation of TRITC and M13TRITC in various 1.00 M salt solutions.....	211
Figure 6.10. (a) Linear dichroism of M13 and M13TRITC in 0.00-2.25 M NaH ₂ PO ₄	213

List of tables

Table 2.1. Materials	34
Table 2.2. UV-visible absorbance spectroscopy parameters.....	46
Table 2.3. Parameters used in thermal denaturation experiments	48
Table 3.1. Molecular orientation methods.....	57
Table 3.2. Macromolecular orientation methods.....	62
Table M1.S1. Linear dichroism parameters	93
Table M2.1. Effect of mutation on major coat protein charge and bacteriophage viability.....	108
Table M2.S1. Mutagenic and sequencing primers.....	115

Abbreviations

AF555	Alexa Fluor 555 C ₂ -maleimide
AF647	Alexa Fluor 647 C ₂ -maleimide
AFM	Atomic force microscopy
Ala	Alanine
AlaTRITC	Alanine-tetramethylrhodamine conjugate
A _n	Absorbance of light of n nanometre wavelength
AS	Ammonium sulphate
CD	Circular dichroism
CD _n	Circular dichroism at n nanometres
Cy	Cyanine
Cy3	Cyanine3 NHS ester
Cy5	Cyanine5 NHS ester
ΔI _n	Change in fluorescence intensity at n nanometres
D _n	Hydrodynamic radius
D.I.T.	Digital integration time
DLS	Dynamic light scattering
DMSO	Dimethyl sulfoxide
DNA	Deoxyribonucleic acid
dNTP	Deoxyribonucleoside triphosphate
DSSC	Dye-sensitised solar cell
<i>E. coli</i>	<i>Escherichia coli</i>
EDTA	Ethylenediaminetetraacetic acid
ε _n	Molar extinction coefficient at n nanometres
FITC	Fluorescein isothiocyanate
FRET	Förster resonance energy transfer
HT	High tension
I _n	Fluorescence intensity at n nanometres
IPTG	Isopropyl-β-D-1-galactopyranoside
LB	Luria Bertani broth
LD	Linear dichroism
LD _n	Linear dichroism at n nanometres
LD ^r	Reduced linear dichroism
LHC	Light-harvesting complex
LUMO	Lowest unoccupied molecular orbital
Lys	Lysine
λA _{max}	Wavelength of maximal absorbance
λLD _{max}	Wavelength of maximal linear dichroism
λ _{em}	Wavelength of maximal emission
λ _{ex}	Wavelength of maximal excitation
m/v	Mass/volume
M13AF555	M13 bacteriophage-Alexa Fluor 555 bioconjugate
M13AF647	M13 bacteriophage-Alexa Fluor 647 bioconjugate
M13Cy3	M13 bacteriophage-Cyanine3 bioconjugate
M13Cy3 ₃₅₀	M13 bacteriophage with ~350 Cy3 groups per virion
M13Cy5	M13 bacteriophage-Cyanine5 bioconjugate

M13SATA	M13 bacteriophage-N-succinimidyl-S-acetylthioacetate bioconjugate
M13TRITC	M13 bacteriophage-tetramethylrhodamine bioconjugate
MES	2-(N-morpholino)ethanesulfonic acid
MW	Molecular weight
NB2	Nutrient broth 2
NBD-Cl	4-chloro-7-nitrobenzofurazan
NMR	Nuclear magnetic resonance
NHS	N-hydroxysuccinimide
OD _n	Optical density at n nanometre wavelength
PCR	Polymerase chain reaction
PE	Polyethylene
PEG	Poly(ethylene glycol)
PE ^{ox}	Oxidised polyethylene
pfu	plaque-forming units
PVA	Polyvinyl alcohol
PVC	Polyvinyl chloride
RNA	Ribonucleic acid
rpm	Revolutions per minute
SATA	N-succinimidyl-S-acetylthioacetate
S/N	Serial number
STEM	Scanning transmission electron microscopy
TAE	Tris-acetic acid-ethylenediaminetetraacetic acid
TEM	Transmission electron microscopy
ThT	Thioflavin T
TMR	Tetramethylrhodamine
TMV	Tobacco Mosaic Virus
TOF MS ES+	Positive electrospray ionisation time of flight mass spectrometry
TRITC	Tetramethylrhodamine isothiocyanate
TX100	Triton X-100
UAA	Unnatural amino acid
UV	Ultraviolet
UV-Vis	Ultraviolet-visible
v/v	Volume/volume
wt	Wild type
X-gal	5-bromo-4-chloro-3-indolyl-β-D-galacto-pyranoside

1. INTRODUCTION

1.1. Introduction

The main body of this thesis deals with the use of M13 bacteriophage to generate nanomaterials. This chapter aims to give the reader an understanding of the motives behind the development of nanomaterials.

The results chapters contained within this thesis are distinct in their aims and approaches. Consequently, this introductory chapter will be broad in what it covers and each results chapter will have an introduction that is shorter and more focused than this one. First in this introductory chapter, nanotechnology will be defined and subcategorised. In addition, the motives that underpin development in this field will be explained. Following this, the rationale behind the use of biologically derived – rather than inorganic – materials in the development of nanomaterials will be discussed with relevant examples. In addition, the benefits and drawbacks of such an approach will be discussed. To bring the introduction closer to the subject matter of this work, the use of M13 bacteriophage in the development of advanced materials and nanomaterials will be covered. Its advantages and weaknesses in such applications will also be reviewed, preceded by an introduction to its structure and life cycle. Furthermore, to highlight the knowledge gap that motivated the majority of the sub-projects in this thesis, the limitations of a study in which an M13-based pathogen detection assay was developed will be discussed. Finally, the overall aims of this work and the aims of the individual results chapters will be stated.

It is intended that in reading this introductory chapter, the reader should gain an understanding of the broad aims of nanomaterial development. It is also intended

that the rationale behind the use of biologically derived materials in nanotechnology, and the advantages and disadvantages associated with this, are understood. Furthermore this introductory chapter aims to provide the reader a familiarity with the previous biotechnological deployments of M13 bacteriophage. Particular emphasis is given to the technology that the majority of the thesis aimed to improve.

1.2. Nanotechnology

1.2.1. Definition

There are a number of varying definitions of nanotechnology. However, a common theme amongst them is the assertion that nanotechnology deals with materials with at least one dimension between approximately one and one hundred nanometres in size (British Standards Institution, 2007; Royal Society and Royal Academy of Engineering, 2004; Scientific Committee on Emerging and Newly Identified Health Risks, 2006). Some definitions also include the aims of nanotechnology. They state that it is for the development of useful materials with novel or advanced properties over their bulk equivalent (Binns, 2010; Roco, 2011). These definitions do indeed encapsulate nanotechnology, however they are limited, as they do not reflect the different branches of the field. This point was raised by Richard Jones, who in his book *Soft Machines Nanotechnology and Life* (2004), made the distinction between two branches of nanotechnology: *Incremental* and *Evolutionary* nanotechnology. Incremental nanotechnology aims to generate materials with novel properties by controlling the arrangement of the constituent atoms. Evolutionary nanotechnology, however, aims to generate nano-scale particles that discretely execute a useful task.

Illustrative examples are provided below and further examples are displayed in Figure 1.1.

An example of incremental nanotechnology is the control of the grain structure of metals. The mechanical properties of metals are dictated by the interactions between the grains (randomly-orientated crystalline regions) that comprise their macroscopic structure. Thus, producing nano-grained metals (<100 nm diameter) – with greater inter-grain interaction than typical micro-grained metals – can lead to the production of metals with superior macroscopic mechanical properties (Wang *et al.*, 2002; Weertman *et al.*, 1999; Yu *et al.*, 2012; Yu *et al.*, 2016).

In contrast, an example of evolutionary nanotechnology is the development of DNA-containing liposomes by Kim *et al.* (2009). These enhance transdermal delivery of DNA *in vivo*. They thereby allow enhanced expression of the gene coded by the delivered sequence compared to the application of DNA alone. This was developed for non-invasive gene therapy.

While both of these examples fall under the umbrella of nanotechnology, their aims and approaches are distinct: the incremental example aims to harness effects that arise due to the size of particles, whereas the evolutionary example aims to create particles that individually perform a task. This illustrates the usefulness of the sub-categorisation of the field into the incremental and evolutionary branches. The main body of this thesis deals with projects that fall into the evolutionary branch. However, the final results chapter would be better categorised as incremental nanotechnology.

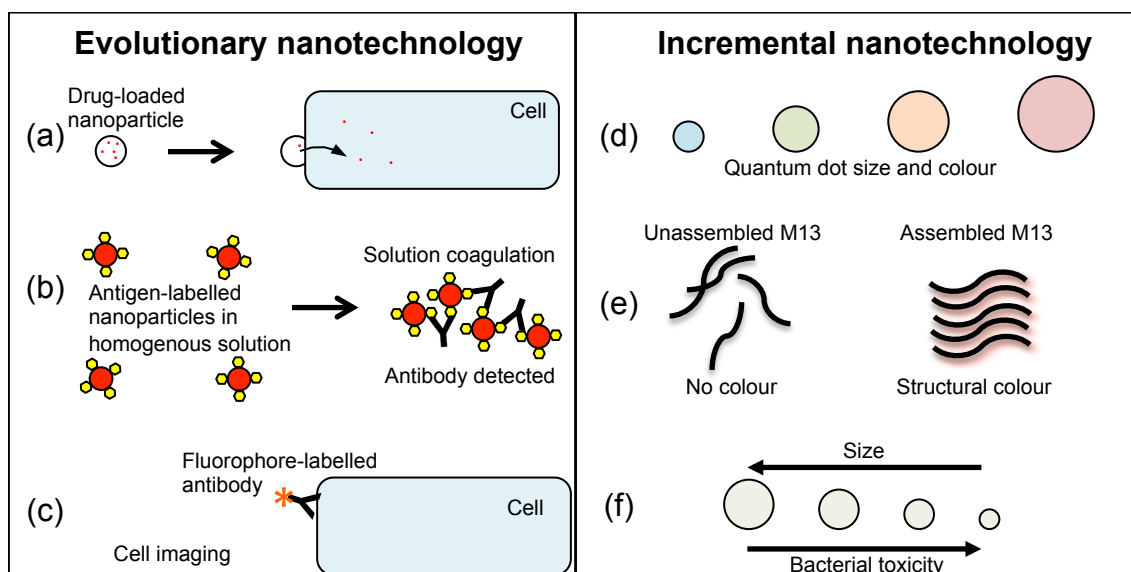


Figure 1.1. Examples of Evolutionary and Incremental nanotechnologies. (a) Cell-specific drug delivery by a nanovector. (b) Antibody detection assay based on the coagulation of antigen-labelled nanoparticles. Antibody presence (indicative of immune response to – and thus infection by – pathogen from which the antigen on the nanoparticle was derived) is indicated by the visible heterogeneity of the solution upon sample addition (Riggin *et al.*, 1987). (c) Cell-specific imaging using a modified antibody. (d) Size effect on quantum dot colour. (e) M13 bacteriophage assembly leading structural colour (an emergent property). (f) Size effect on the bacterial toxicity of silver nanoparticles.

1.2.2. Why operate on the nano-scale?

The definitions of nanotechnology provided above cover what the subject is and what it aims to achieve. They do not, however, provide any indication of the rationale behind operating at this scale. When explaining this, it is again useful to make the distinction between the two branches, because their reasons for operating at the nano-scale are very different.

From the perspective of those working in incremental nanotechnology it is interesting to work at the nano-scale because of the properties that materials exhibit when the characteristics of surface atoms become dominant over the bulk. Atoms at the

surface of particles behave differently to those contained within the bulk as their electrons are in a different environment. Thus when the size of a particle is greatly decreased and the proportion of atoms at its surface becomes very high, the macroscopic properties of the material begin to resemble those of the surface atoms rather than the bulk, which is what would be observed in materials comprising large particles. This also allows for the tuning of a material's properties by controlling precisely the size of the constituent particles to achieve a blend of the surface and bulk properties. This notion is well illustrated by the example of silver nanoparticles. Silver nanoparticles are antimicrobial, and it has been shown that their toxicity towards various microbes inversely correlates with their size (Khurana *et al.*, 2013; Lu *et al.*, 2013; Ivask *et al.*, 2014). From the perspective of incremental nanotechnologists, therefore, operating at the nano-scale presents the opportunity to uncover novel or enhanced material properties.

In addition, one of the aims of incremental nanotechnology is to discover and harness the macro-scale properties of materials that emerge following self-assembly on the nano-scale. These properties are termed *emergent properties*. An example of this is the non-Newtonian behaviour of a liquid sample of polymeric capsules (polycaps), triggered by the chemical induction of polycap self-assembly (i.e. the solution becomes more viscous as a result of polycap self-assembly) (Castellano *et al.*, 2000). Others have investigated the mechanical induction of nanoparticle self-assembly to trigger non-Newtonian fluid behaviour. This technology has been proposed for use within flexible body armour that becomes rigid and therefore protective when subjected to blunt force (Hasanzadeh and Mottaghitalab, 2014).

Incremental nanotechnologists, therefore, are interested in operating at the nano-scale as it may allow for the generation of materials with interesting macro-scale properties by tuning the nano-scale arrangement of the constituent particles.

In contrast to incremental nanotechnologists, evolutionary nanotechnologists generally do not operate at the nano-scale to harness the characteristics of surface atoms when they become dominant over the bulk. They are instead aimed towards miniaturisation of current technologies or delivery of individually functional particles to their location of action. For example, the many instances where carbon nanotubes have been used as wires in nano-scale electronics e.g. nano-scale transistors (Laocharoensuk *et al.*, 2008; Li *et al.*, 1999; Shulaker *et al.*, 2013; Cao *et al.*, 2013; Jeon and Ha, 2016; Peng *et al.*, 2014 and references therein), or the creation of nanovectors. These are nanoparticles that are functionalised to deliver drugs to specific cell types (e.g. cancer cells or bacterial cells), reducing off-target effects and ameliorating the issue of host sensitivity to the administered drug (Ferrari, 2005; Sercombe *et al.*, 2015; Kersharwani and Iyer, 2015; Klumpp *et al.*, 2006; Accardo *et al.*, 2013; Liechty *et al.*, 2010).

The majority of the work in this thesis would be better categorised as evolutionary rather than incremental nanotechnology. As the starting materials used here were of biological origins, the use of biomaterials in nanotechnology is introduced in the following sections.

1.2.3. Biological materials in nanotechnology

The use of biological materials in nanotechnology has given rise to the adoption of the term *Bionanotechnology*. The main aims of bionanotechnology are the same as those of nanotechnology. The starting materials used, however, are biologically derived, for example, DNA, RNA, proteins (enzymatic and structural), polysaccharides and lipids. Bionanotechnologists aim to reassemble these biomaterials into arrangements that yield useful functionalities. This resembles the aim of nanotechnologists to rearrange atoms and harness the resultant properties. The commonality is the control of matter at the nano-scale. For bionanotechnologists the exploitation of biomaterials has a number of advantages, which include:

- that biological systems already comprise nano-scale components, such as proteins and nucleic acids,
- that biological systems can be harnessed to produce homogenous samples of nanoparticles, and
- biological systems provide defined, technically accessible routes for site-specific modification.

1.2.4. Biological systems contain inherently nano-scale components

There are a number of motivations behind the use of biomaterials in nanotechnology. Firstly, biological systems are essentially macro-scale assemblies of components that are nano-scale. This may seem a trivial point, however, much time and effort is spent during the synthesis of inorganic nanomaterials generating particles of the desired size, using techniques such as size-exclusion chromatography and filtration (Robertson *et al.*, 2016). In contrast, subcellular components are naturally nano-

scale, so optimisation of size can be avoided. Thus, biomaterials hold an advantage in this regard (Binns, 2010).

1.2.5. Bionanoparticles are often homogenous

The second reason to use biomaterials in nanotechnology is the structural homogeneity with which they are produced. It is a challenge in nanoparticle production to produce homogenous batches of particles to isolate the optimised performance that is expressed at the desired size. For example, the function of quantum dots (brightly coloured nanoparticles composed of a semiconducting material (Bera *et al.*, 2010)) relies on their colour, which in turn relies on tight control of their size. This becomes particularly important if multiple species of quantum dots with discrete, distinguishable signals are required, for example in medical imaging applications (Jin *et al.*, 2011). In this case, control of size homogeneity within the separate quantum dot populations is essential. Methods to reduce the size distribution of a nanoparticle sample include mass filtration, size-exclusion chromatography and centrifugation. Initial optimisations of the techniques used to prepare the nanoparticles may also be carried out in the first place. Optimisations could include screening solvent conditions, temperature and pressure (Robertson *et al.*, 2016; Hou *et al.*, 2008). In the case of biomaterials, however, evolutionary optimisation of particle uniformity is an implicit part of maintaining life. Thus, again, biomaterials hold an advantage over inorganic materials in this regard.

1.2.6. Biomaterials are easily modified

The two reasons to use biomaterials in nanotechnology introduced so far have emerged due to biological evolution. This process can be harnessed further through artificial selection methods or mutagenesis. This approach is used to alter the structure of biomaterials, make adjustments to their natural function, or endow them with entirely non-biological functions. For example, the technique of bacteriophage display involves randomisation of parts of the sequence of the coat proteins of M13 bacteriophage. A screen for binding of the bacteriophage to the ligand of choice is then performed, yielding a bacteriophage stock that binds more strongly to the desired ligand than the wild type. This technique has been used to generate a vast number of bacteriophage variants expressing proteins that bind to biological ligands e.g. tumour cells (Rasmussen *et al.*, 2002; Ghosh *et al.*, 2012; Figure 1.2), pathogenic bacteria (Huang *et al.*, 2012) and mammalian membrane proteins (Molek *et al.*, 2011). Non-biological ligands may also be targeted e.g. metal borides (Ploss *et al.*, 2014), fullerene (Morita *et al.*, 2004) and graphene (Cui *et al.*, 2010). This possibility makes biomaterials particularly useful in evolutionary nanotechnology applications where it may be desired that a functional nanoparticle be delivered to a given location to perform its task.

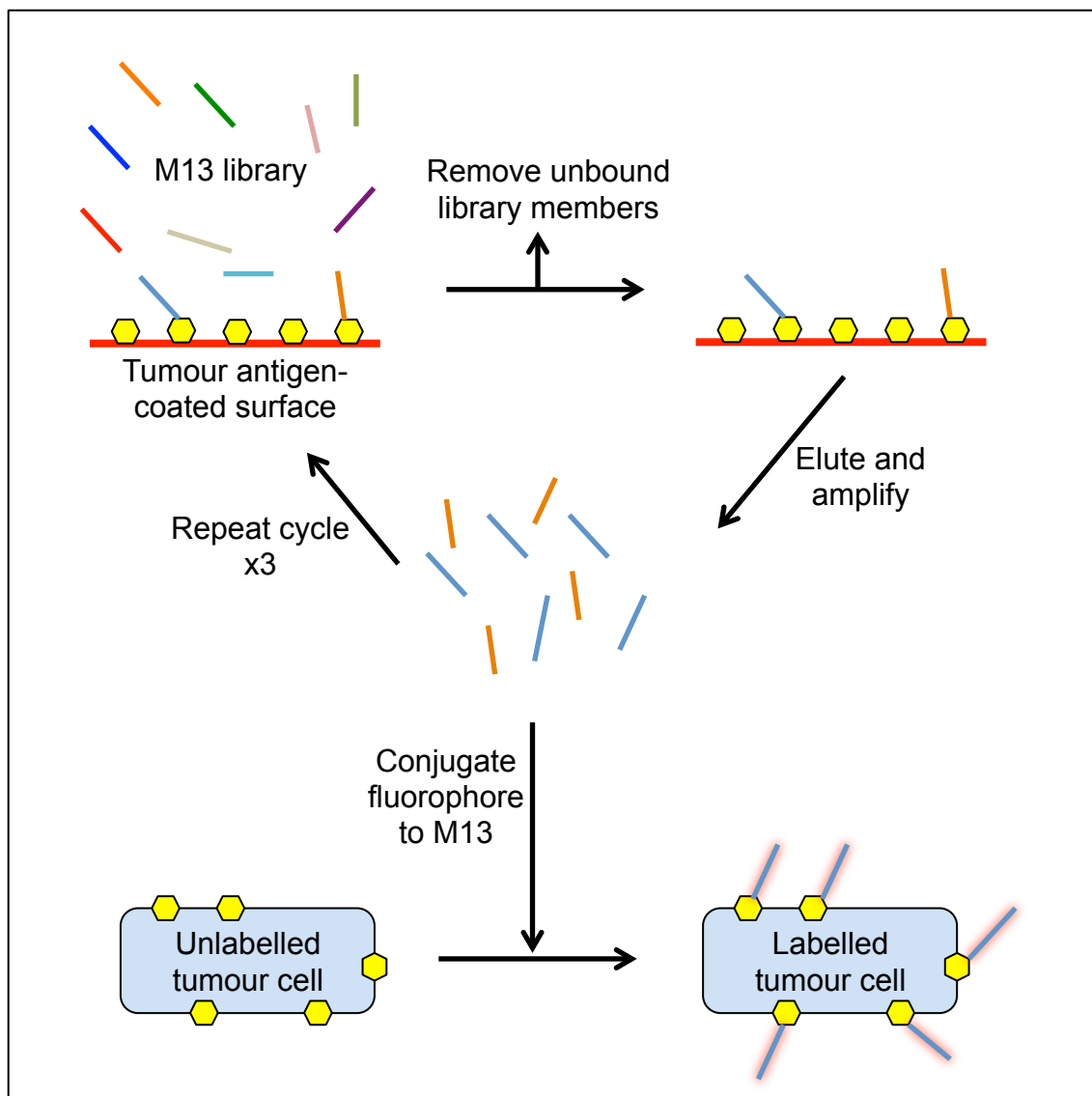


Figure 1.2. Creation of a tumour-labelling particle using bacteriophage display. Multiple rounds of bacteriophage display are carried out against the target, producing a stock of M13 that binds to tumour cells. Labelling of the resulting bacteriophage yields a tumour-labelling particle.

1.2.7. Limitations of bionanotechnology

The use of biomaterials in nanotechnology is limited by a narrow set of conditions in which they are stable. For example enzymes are limited to a narrow range of temperatures in which they are fully efficient due to their altered conformation in non-optimal temperatures (e.g. the thermostable lactate dehydrogenase from

Thermoanaerobacter ethanolicus is optimally efficient at 60 °C and loses around 10 % activity in temperatures ± 5 °C of the optimum; Zhou and Shao, 2010). In addition, enzymes and structural proteins can be destabilised by alterations in pH and salt concentration. Environmental sensitivity depends on the protein so it is difficult to generalise about their stability, however this is a well-documented limitation to the use of proteins in technology (Reetz, 2016; Talley and Alexov, 2010). In addition, DNA-based biomaterials are sensitive to nucleases, which are abundant *in vivo* and may be present in the environment due to bacterial contamination (Tørring and Gothelf, 2013). Furthermore, the rapid metabolism or excretion of medical bionanomaterials can limit the extent to which they are effective *in vivo*. For example, protein- and lipid-based bionanomaterials may be rapidly metabolised as the body is well equipped to decompose and/or excrete exogenous proteins. This would prevent sustained action of medical biomaterials. In addition, the metabolic products must be identified and tested for toxicity (Honek, 2013).

These sensitivities limit the locations to which biomaterials may be deployed for nanotechnological applications. This can be partially ameliorated by directed evolution, site-directed mutagenesis or chemical modification of biomaterials (Matsuura *et al.*, 2005; Zhu *et al.*, 2015). The requirement for such optimisations, however, presents a challenge during the use of biomaterials for nanotechnology.

1.2.8. Bionanotechnology case study

A description of a fully commercialised biomaterial-based medicine is provided here as a clear example of the utility of bionanotechnology. The example chosen is trastuzumab, an antibody-based anti-cancer drug, commonly known as Herceptin.

Herceptin is a monoclonal antibody that binds to human epidermal growth factor 2 (HER2), which is a cell-surface receptor overexpressed in 15-25 % of breast cancers (Garnock-Jones *et al.*, 2010). In doing this, Herceptin triggers the partial reversal of the cancer phenotype by a number of potential mechanisms, as reviewed by Garnock-Jones *et al.* (2010).

The Herceptin antibody was initially raised in mice, meaning that it would be incompatible with the human immune system (i.e. an immune response would be raised against it) and thus ineffective as a human anti-cancer drug. However, exploiting the genetic flexibility of the biomaterial (the antibody), Carter *et al.* (1992) converted the antibody into a form that is human compatible, using a commonly used process called *humanisation*.

Herceptin is now a Food and Drug Administration (FDA) –approved drug (FDA, 1998) and is regarded by the World Health Organisation (WHO) as an essential medicine (WHO, 2015).

The utility of bionanotechnology is well illustrated by this example, as it highlights the advantages of using biomaterials as starting materials in the development of

nanomaterials, specifically, the ease with which they may be modified for the desired purpose.

1.3. M13 bacteriophage

It is the aim of this section to provide the reader with some background information about M13 bacteriophage, the biomaterial used throughout this thesis in nanomaterial development. All of the applications of M13 bacteriophage developed in this thesis rely on harnessing its structure, and there is only one occasion where its life cycle is of importance. Accordingly, this section is focused more on the structure of M13 bacteriophage than its life cycle.

1.3.1. Structure

M13 bacteriophage is a filamentous virus that solely infects *Escherichia coli* (*E. coli*) that expresses the F-pilus (F^+ *E. coli*). It is cylindrical with a diameter of 6 nm and length of $\sim 916 \pm 2$ nm (Beck and Duenki, 1990) (Figure 1.3 a). It is thus a nanomaterial according to the British Standards Institution (2007) definition. The structure of M13 bacteriophage comprises only DNA and protein: ~ 6400 nucleotides of circular, single-stranded (apart from the packaging signal) DNA sheathed by a protein coat comprising five different proteins (Russel and Model, 1989; van Wezenbeek *et al.*, 1980). The entire genome of M13 encodes just eleven gene products, five of which are the coat proteins pIII, pVI, pVII, pVIII and pIX (Figure 1.3 a).

The major coat protein, pVIII, is the best characterised of the M13 coat proteins. It comprises 50 amino acid residues and is almost entirely alpha-helical, as determined by nuclear magnetic resonance spectroscopy (Morag *et al.*, 2015). Within the bacteriophage structure it is arranged with its carboxyl-terminal (C-terminal) positively charged lysine (Lys) residues associated with the negatively charged oxygen atoms within the phosphodiester bonds of the DNA core (Armstrong *et al.*, 1983; Hunter *et al.*, 1987). Its five unstructured amino-terminal (N-terminal) residues are on the outer face, exposed to the solvent (Stopar *et al.*, 2003) (Figure 1.3 b). Together, the 2700 copies of pVIII form a cylindrical coat around the DNA core, and comprise around 85 % of the bacteriophage mass (Morag *et al.*, 2015).

The 50 amino acid residues of pVIII form three sections: residues 1-20 comprise the negatively charged N-terminal region; 21-39 the hydrophobic region; and 40-50 the positively charged C-terminal region (Spruijt *et al.*, 1996) (Figure 1.3 c). Spanning residues 6-48 is a single slightly curved alpha helix (Morag *et al.*, 2015).

Neighbouring pVIII subunits associate with each other in an arrangement that resembles roof tiles (Morag *et al.*, 2015). The pVIII subunits overlap with one another, with the alpha helix long axes tilted approximately 16° to the bacteriophage long axis (Wang *et al.*, 2006; Overman *et al.*, 1996) (Figure 1.3 b). The tight packing of the pVIII coat means that the bacteriophage is highly stable and shows no significant loss of infectivity following desiccation, exposure to temperatures up to 80 °C, or pH values between 3 and 11 (Branston *et al.*, 2013), and no change in structure following exposure to nonpolar solvents (Moghimian *et al.*, 2016).

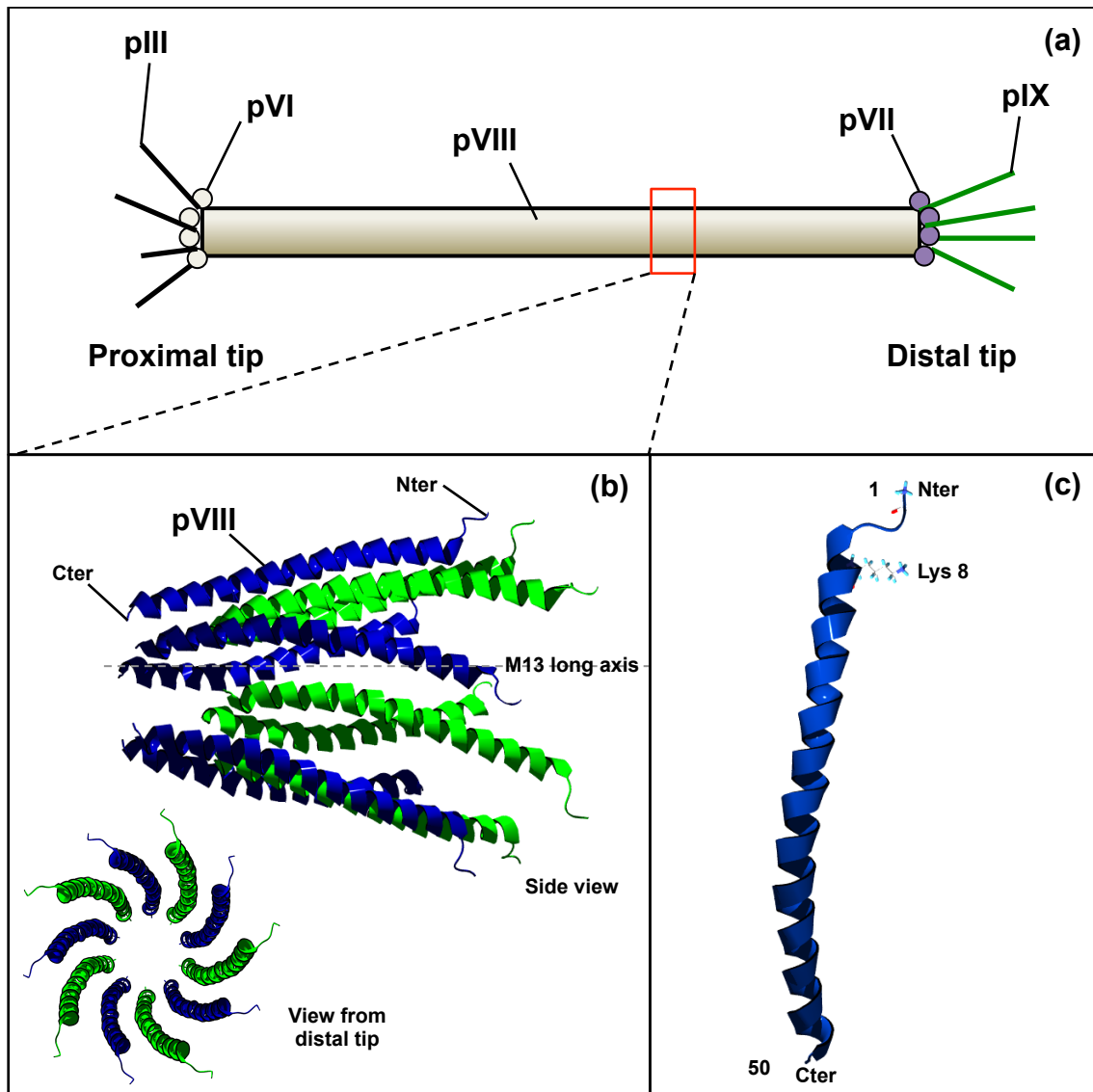


Figure 1.3. M13 bacteriophage structure. (a) Schematic of overall virion structure. (b) Orientation of pVIII subunits within bacteriophage coat. Side view (same orientation as in box a) and view from distal tip (c) pVIII coat protein structure with groups targeted by amine-directed conjugation displayed as ball-and-stick model (N-terminus and Lysine at position eight). Figure produced using PDB entry 2MJZ (Morag *et al.*, 2015).

The minor coat proteins of M13 bacteriophage are less well characterised than pVIII and are not of particular relevance to this thesis. Accordingly, they are not covered in depth here. At the distal end of M13 bacteriophage there are five copies each of

minor coat proteins pVII and pIX, and at the proximal end there are five copies each of pIII and pVI (Figure 1.3 a). Together, the minor coat proteins comprise only around 3 % of the total bacteriophage mass (Morag *et al.*, 2015). The minor coat proteins are involved in host infection and virion extrusion from the host, as will be discussed in the section on M13 bacteriophage life cycle.

Despite the limited characterisation of the minor coat proteins they have been used a number of times to express protein fragments to endow the bacteriophage with non-biological functions. The minor coat proteins can tolerate the insertion of sequences up to ~25 kDa. The major coat protein, pVIII, however, has only been shown to tolerate eight-residue insertions (Henry *et al.*, 2015). This discrepancy in tolerance is due to the density of packing of the different coat proteins: pVIII is very closely packed, whereas the minor coat proteins are sparse by comparison.

The simple and robust structure, and the genetic simplicity and flexibility of M13 bacteriophage have made it an attractive starting material in nanomaterial development, as will be discussed in following sections.

1.3.2. Life cycle

M13 bacteriophage replication is episomal and non-lytic. This means that the bacteriophage genome does not incorporate into the host genome, and the virions are released in a way that does not lyse the host cells. The life cycle occurs in three distinct stages (Figure 1.4): 1) Host attachment and DNA insertion; 2) DNA replication and gene expression; 3) Progeny assembly and exit. First, virions attach

via pIII to the exterior of the host, F⁺ *E. coli*, by the F-pilus (Riechmann and Holliger, 1997) then by the C-terminal domain of the TolA receptor (Lubkowski *et al.*, 1999). Following this, bacteriophage DNA (positive (sense) strand) is injected into the host cytoplasm in a process that involves contraction of the pVIII coat (Griffith *et al.*, 1981). Using host enzymes, the complementary negative (antisense) strand is then synthesised. From this, bacteriophage proteins are expressed (Brutlag *et al.*, 1971; Jacob and Hofschneider, 1969). The double-stranded bacteriophage genome is termed the “replicative form” and is nicked by bacteriophage protein pII. This enables the production of multiple copies of the positive strand (Tseng and Marvin, 1972; Lin and Pratt, 1972). Initially, while the concentration of bacteriophage protein pV is low, the multiple positive strand copies serve as templates for the production of negative (antisense) strands (Staudenbauer and Hofschneider, 1973; Salstrom and Pratt, 1971). However, above an unknown critical concentration, pV sequesters positive strands for packaging into progeny virions (Oey and Knippers, 1972). At the same time, pVIII in its immature form (displaying a signal sequence of 23 amino acid residues at its N-terminus) is expressed. Via the membrane protein insertase YidC, immature pVIII is inserted into the host inner membrane (Samuelson *et al.*, 2000). In the periplasm, the signal sequence is cleaved by a host peptidase, yielding mature pVIII (Wickner *et al.*, 1987). Bacteriophage proteins pI, pIV and pXI form a complex that spans both host membranes (Haigh and Webster, 1999; Feng *et al.*, 1999; Rapoza and Webster, 1995). This complex assembles and extrudes progeny bacteriophage by first binding a complex between minor coat proteins pVII and pIX (bacteriophage distal tip) and the hairpin packaging signal of pV-coated DNA (Russel and Model, 1989). Bacteriophage progeny are then assembled by the displacement

of pV from the DNA by pVIII. Minor coat proteins pIII and pVI bind last, forming the proximal tip of the progeny bacteriophage. No mechanism for the prevention of re-infection of an already infected cell by M13 progeny has been observed (Berngruber *et al.*, 2010). The M13 bacteriophage life cycle is shown in Figure 1.4.

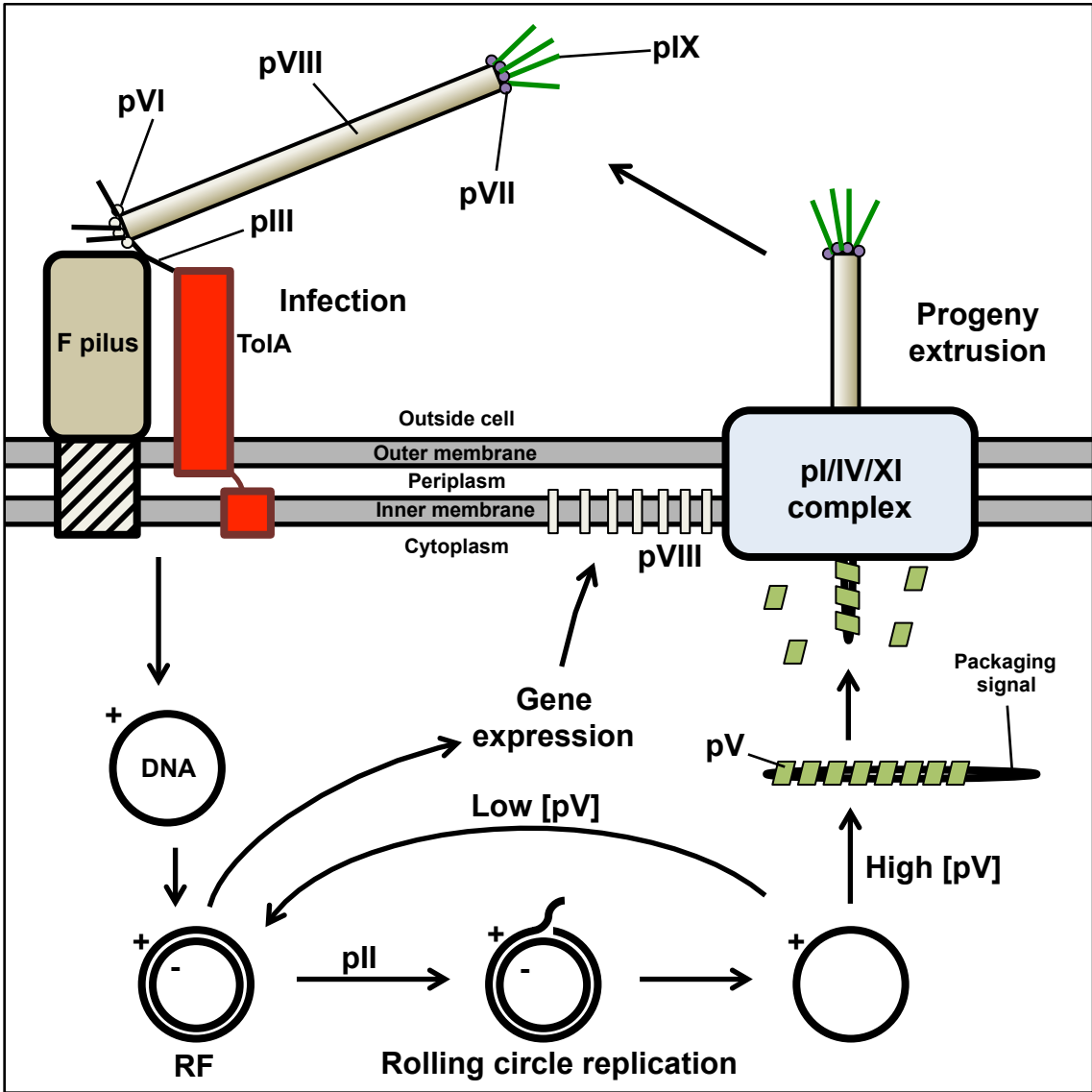


Figure 1.4. Schematic of M13 bacteriophage replication cycle, showing initial host infection, bacteriophage DNA replication, and bacteriophage assembly and exit.

1.3.3. Uses of M13 bacteriophage in nanotechnology

The aim of this section is to give the reader an overview of the use of M13 bacteriophage in nanotechnology. It should be noted that the number of studies in this field is vast (searching *M13 bacteriophage* on Web of Science produces 3,402 results, with only 28 results also containing *life cycle*). It is therefore not the aim of this section to provide a comprehensive review of the topic but rather to give the reader an understanding of the approaches taken to use M13 bacteriophage as a starting material in the development of nanomaterials. This section is subcategorised into incremental and evolutionary nanotechnology.

1.3.4. Uses of M13 bacteriophage in incremental nanotechnology

The approach most commonly used in the development of nanomaterials based on self-assembled arrays of M13 bacteriophage involves exploiting its tendency to form liquid crystals (an ordered array of molecules or particles, which can flow (Andrienko, 2018)) when highly concentrated. This has been exploited for a variety of reasons, from the study of rod self-assembly (Lee *et al.*, 2003) to the development of substrates for directed neural progenitor cell growth for regenerative therapies (Merzlyak *et al.*, 2009). In both cases, a method for deposition of ordered M13 arrays on surfaces was used. The method involves the slow retraction of a silicon substrate from a highly concentrated solution of M13 bacteriophage. Virions are deposited on the surface in an ordered manner as they dry at the meniscus formed between the silicon substrate and the bacteriophage solution surface (Chung *et al.*, 2011; Figure 1.5 a). This technique has recently been employed to develop a volatile organic compound (VOC) sensor. This device detects the change in structural colour of

bacteriophage self-assemblies due to their specific structural rearrangement upon exposure to different VOCs (Lee *et al.*, 2017).

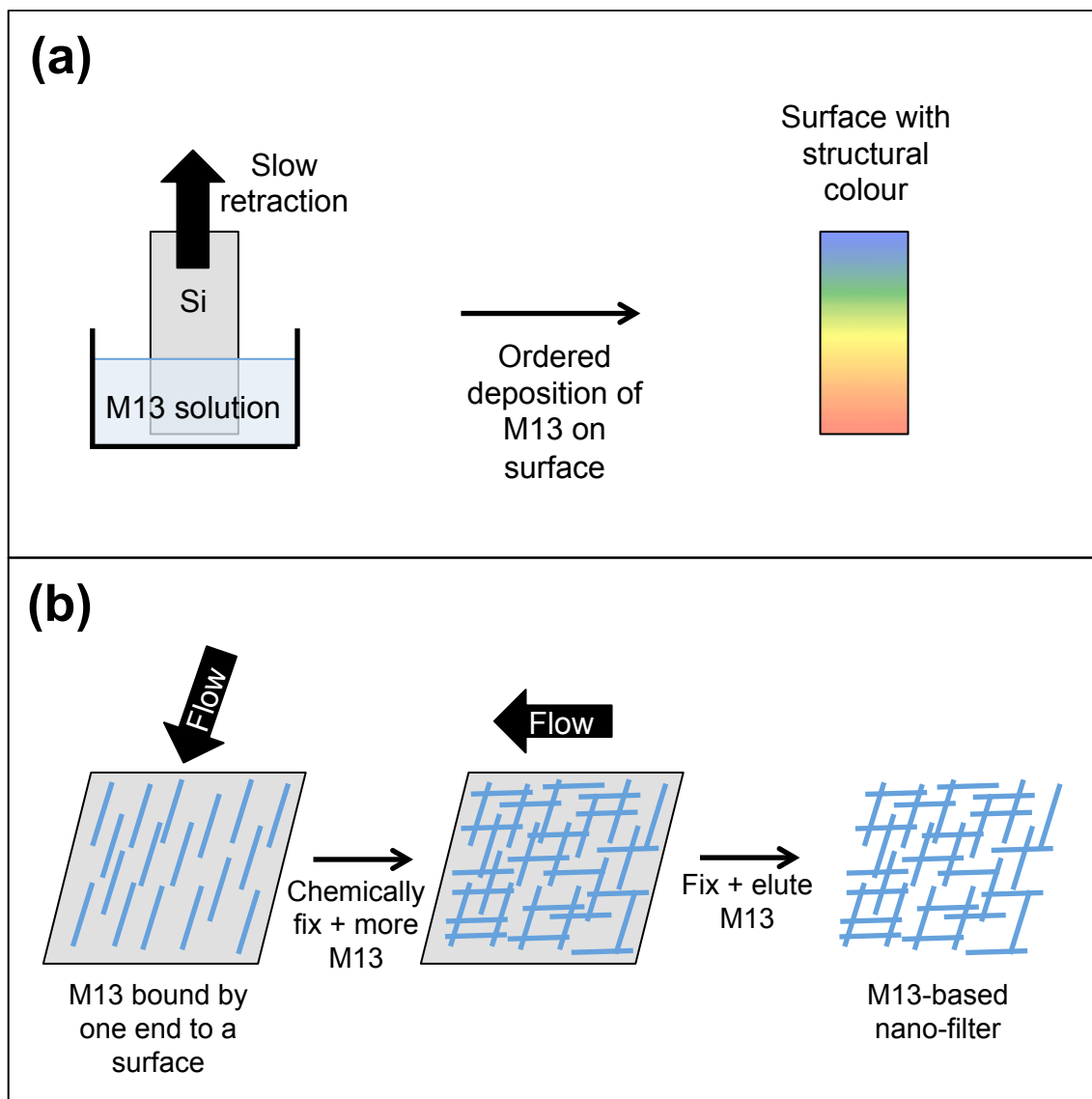


Figure 1.5. Methods for directing the assembly of M13 bacteriophage-based structures. (a) Method developed by Lee *et al.* (2003). Slow retraction of a silicon substrate from an M13 solution yields a surface coated with an ordered array of M13, yielding structural colour. (b) Method used by Lee *et al.* (2014). Directional deposition of M13 combined with a chemical fixative was used to generate a filter based on an M13 bacteriophage assembly.

As stated earlier, one of the advantages of using protein- or DNA-based biomaterials in nanotechnology is the ease with which they may be altered through mutation. This allows the creation of a whole library based around one starting biomaterial. This approach has been taken with M13 bacteriophage and closely related filamentous bacteriophages to generate an array of self-assemblies with altered properties compared to those comprising wild type bacteriophage. For example, Barry *et al.* (2009) investigated the effect of a mutation that alters the persistence length (rigidity) of fd bacteriophage (closely related to M13). They demonstrated that the topological characteristics of the resulting liquid crystals were altered as a result of this mutation. Furthermore, they demonstrated that mixtures of the two variants have liquid crystalline properties intermediate to the two clonal samples. They highlighted that their observations may inform the study of self-assemblies based on rigid rods. This would be of fundamental interest in the field of soft condensed matter physics. In addition, Abramov *et al.* (2017) observed that charge-altering mutations to the M13 coat significantly alter the topological characteristics of the resultant liquid crystal. They suggested that their observations might inform the rational tuning of bacteriophage-based incremental nanomaterials.

Additionally, the bacteriophage may be altered chemically. The dense display of functional groups on the bacteriophage surface enables the alteration of its overall chemistry by bioconjugation. For example, the amine groups of the amino-terminus and the lysine residue at position eight in the pVIII protein can be targeted to covalently link exogenous compounds to the bacteriophage surface (Bernard and Francis, 2014) (Figure 1.3 c), an approach used throughout this thesis. Accordingly,

in a recent review (Gibaud, 2017), a number of possible routes towards the creation of filamentous bacteriophage liquid crystal libraries were discussed, including bioconjugation. A number of examples were covered, including modifying bacteriophage with poly(ethylene glycol), titanium dioxide, DNA, temperature-responsive polymers and charged groups to reverse the viral coat charge. In all cases the resulting bacteriophage assemblies were altered compared to those comprising native bacteriophage. The collective aim of the studies reviewed was to investigate how to alter bacteriophage to obtain predictable changes to its macroscopic organisation and therefore its macroscopic properties. This would theoretically enable bottom-up design of incremental nanomaterials based on self-assembled nano-rods (Gibaud, 2017).

Other approaches taken to induce bacteriophage liquid crystal formation and to alter the structure of the crystals include: coupling the ends of the bacteriophage to nanoparticles (Lee *et al.*, 2002); using alternative viruses (Dogic and Fraden, 1997); and altering solution ionic strength and temperature (Dogic and Fraden, 2000).

Bacteriophage-based incremental nanomaterials have also been generated using directional deposition. In this approach, shear force is applied to bacteriophages that are non-covalently bound by one end to a surface. This is achieved via a peptide expressed in a minor coat protein, chosen to bind to the desired surface. For example Lee *et al.* (2014) used graphene oxide-binding peptide, identified by phage display, to adhere M13 to a graphene oxide surface for directional deposition. A fixative is then applied. This yields a single-virion layer of bacteriophage with their

long axes approximately parallel to each other. The process is repeated with the shear flow applied perpendicular to the long axes of the first layer, yielding a two-virion-thick mesh (Figure 1.5 b). Lee *et al.* (2014) used this approach to generate a water filter with high permeability whilst retaining good separation efficiency.

A further technique used to generate bacteriophage-based incremental nanomaterials is layer-by-layer (LbL) deposition. This technique simply involves the repeated non-directional adsorption of bacteriophage onto a surface followed by chemical crosslinking. This was used by Courchesne *et al.* (2014) to create a porous network of M13 bacteriophage that was used to order the assembly of gold nanoparticles (AuNPs). The authors suggested that this approach might be used to create a biosensor based on the surface plasmon resonance of the embedded nanoparticles. However, this was not demonstrated until 2016, when Kim *et al.* used the deposition technique developed by the Seung-Wuk Lee group to order M13 bacteriophage coated with a short streptavidin-binding peptide, generating a surface plasmon resonance-based streptavidin sensor. This example illustrates the use of the deposition technique to develop hybrid materials that rely on the properties of components other than the bacteriophage. The bacteriophage in this setting is thus being used as a scaffold.

1.3.5. Uses of M13 bacteriophage in evolutionary nanotechnology

Bacteriophage display is the most frequently used approach in the use of M13 bacteriophage in evolutionary nanotechnology. This method is covered briefly first, however, more focus will be applied here to examples where bioconjugation and

rationally designed mutations were used, as they are more pertinent to the content of this thesis.

Bacteriophage display is a technique in which short sections of the genes encoding either pIII or pVIII of M13 bacteriophage are genetically randomised. This is achieved by the addition of a mixture of bases rather than pure bases during DNA synthesis (Creative Biolabs, 2019; Mena and Daugherty, 2005). This generates a library of bacteriophages that display random peptides. The library is washed over the binding partner of choice. The non-binding library members are washed away, leaving the variants that bind to the target, which are then amplified by host infection. This process is repeated around four times to generate a sample of bacteriophage displaying a peptide that binds to the target (Smith, 1985). As explained earlier, this approach has been taken a number of times to generate bacteriophage-based nanovectors for drug delivery or cell imaging. In addition, this approach has been taken to generate bacteriophage variants that bind to metals to generate nanowires (Huang *et al.*, 2005) and single-walled carbon nanotubes to improve the electron collection efficiency of dye-sensitised solar cells (Dang *et al.*, 2011).

The approach towards modifying M13 bacteriophage for evolutionary nanotechnology that is most pertinent to this thesis is bioconjugation. This is the modification of biomolecules through chemical means. As the outer coat of M13 bacteriophage is a regular lattice of a large number of functional groups that can be functionalised in mild conditions it is an ideal target for bioconjugation. An advantage of this approach over genetic modification is that the modification is not limited by

genetic non-viability, as modifications can be made after bacteriophage assembly. In addition, it is also possible to endow the bacteriophage with non-biological moieties, thus extending its functionality beyond what is achievable genetically. For example, Carrico *et al.* (2012) produced fluorophore-modified bacteriophage expressing anti-cancer biomarker antibody fragments in its pIII sequence. They demonstrated how this might be used to image cells for cancer diagnosis. In addition Hilderbrand *et al.* (2008) developed a method to measure intracellular pH. This was achieved by using M13 bacteriophage modified with a pH-sensitive fluorophore and a pH-insensitive reference fluorophore. The authors noted that this might be used in the diagnosis of diseases associated with tissue hypoxia. Li *et al.* (2010) also created a cancer-targeted fluorescent M13 bacteriophage. In contrast to the other, they achieved this by covalently modifying with a fluorophore and folic acid. This is the ligand of the folic acid receptor, which is overexpressed in a number of cancers. The approach taken by Li *et al.* (2010) demonstrates that bacteriophage may be modified to bind to biological targets without the screening process used in bacteriophage display. If the ligand-receptor interaction is known, this approach may be simpler than bacteriophage display. However, it is not possible if the interaction is unknown. The authors noted that this approach might be used to deliver anti-cancer drugs to cancer cells. However, this was not achieved until the following year. In 2011, the same research group published an article detailing the delivery of doxorubicin-loaded nanoparticles to cancer cells using the folate-modified bacteriophage (Suthiwangcharoen *et al.*, 2011).

Bioconjugation is not limited to medical evolutionary nanotechnology applications, however. This was demonstrated by Niu *et al.* (2008), who to generate nanowires without relying on bacteriophage display conjugated the conductive polymer, polyaniline, to M13 bacteriophage. This produced nanowires, which they anticipate will have applications in nanoelectronics and sensing.

One must be aware that the disadvantage of using bioconjugation rather than mutagenic approaches to modify bacteriophage is the limited conjugation efficiency. None of the references above achieved 100 % labelling (i.e. one exogenous group per pVIII subunit). Bacteriophage display-derived or rationally designed mutations, however, are displayed with 100 % efficiency.

A further approach to the modification of M13 bacteriophage for evolutionary nanotechnology purposes is the introduction of rationally designed mutations. This approach has been used to create nanowires (Chen *et al.*, 2013; Park *et al.*, 2014; Zirpel *et al.*, 2015), a nuclear magnetic resonance imaging contrast agent (Palaniappan *et al.*, 2013), and an anti-cancer drug delivery vector (Sreeram *et al.*, 2010). In 2012, Pacheco-Gómez *et al.*, published a further example of the use of rationally designed mutations. This will be discussed later within a dedicated section as it is of central importance to this thesis and formed the basis of the majority of this work's aims.

Finally, it should also be noted that the approaches outlined above are not always used in isolation. Kelly *et al.* (2006) used bacteriophage display in conjunction with

bioconjugation to generate an *in vivo* disease biomarker-imaging agent. Similarly, Yacoby *et al.* (2006) combined rationally designed mutation with bioconjugation to generate a targeted antibacterial drug delivery nanovector.

1.3.6. Limitations of M13 bacteriophage in nanotechnology

M13 bacteriophage has the same weaknesses, as explained earlier, as all biomaterials (i.e. instability in non-native environments/conditions). These generic weaknesses will not be explained here. Instead only those weaknesses unique to M13 bacteriophage or often cited as being problematic to its use in nanomaterial development will be explained here.

First is the issue of the size limit of peptides displayed on the coat proteins of M13. The minor coat proteins can display proteins up to ~25 kDa, and the major coat protein can only accommodate insertions of around eight to nine amino acid residues (Henry *et al.*, 2015 and references within). While the utility of bacteriophage display has been demonstrated a vast number of times, this weakness limits the scope of the technique.

It is interesting to note that there is often very little in the way of follow-up to the studies outlined above. The authors of said studies often only mention the *potential* applications of their developments. Why this is the case is unclear. However, it could be due to the lack of progress in producing large enough quantities of bacteriophage to realise the creation of a commercially viable product. This has been addressed to an extent (Grieco *et al.*, 2009; Grieco *et al.*, 2012; Warner *et al.*, 2014), with

researchers claiming significant improvements in yield. However, these studies report yields of the order of tens of milligrams per litre of media. This is far smaller than the achieved yields of other biotechnologically relevant biomolecules, for example monoclonal antibodies (mAbs). Yields of mAbs up to 5 g.L^{-1} have been reported (Shukla and Thömmes, 2010). This could, therefore, be a limiting factor in bacteriophage product development.

1.4. M13 bacteriophage-based bioassay by Pacheco-Gómez *et al.* (2012)

Of specific interest to this thesis is the work of Pacheco-Gómez *et al.* In 2012, they published details of a novel immunoassay platform, which uses the linear dichroism (LD) signal of M13 bacteriophage as a read-out. M13 was modified for purpose via the genetic insertion of an antibody-binding domain into pIII. To this, antibodies were bound non-covalently. In this assay, a solution of modified M13 is aligned about an axis using shear flow in a Couette cell. In the absence of the antibody target, in this case *Escherichia coli* O157, the functionalised bacteriophage particles remain aligned about a common axis. This yields a strong LD signal (Figure 1.6 a). When the target is added, the antibody-functionalised bacteriophage binds to the target. This restricts the impact of shear flow on the bacteriophage. Thus causing its alignment, and therefore its LD signal, to decrease proportionally with the amount of target added (Figure 1.6 b).

Work has been ongoing in this laboratory to covalently bind antibodies along the length of the bacteriophage, along with visible-region dyes. The reasons for this are as follows: the assay could not be developed into a multiplex version as the

antibodies were bound non-covalently to the bacteriophage. They were thus in equilibrium between being bound and free in solution. This means that if there were two populations of bacteriophage, each with different antibodies bound, the antibodies would equilibrate between the two populations and both would detect both targets. Additionally, the bacteriophages conjugated to different antibodies would have the same LD spectrum as each other. This means it would not be possible to tell which signal had decreased as a result of the addition of which target. To overcome this flaw, it is necessary to covalently bind the antibodies to the bacteriophage. It is also necessary to covalently label each bacteriophage population with a unique dye that adds a distinguishing peak to the phage LD spectrum. In addition, to enable miniaturisation and thereby portability of the assay, the dyes bound must be visible-region. At present the assay detects the UV-region signal of M13. This requires that the optical instrumentation be flushed with nitrogen. This is to prevent the formation of ozone from oxygen photolysis by UV light, which causes corrosion of optical elements within spectrophotometers. The removal of oxygen from the system is also required to minimise loss of incident irradiation due to oxygen absorbance (Dohan and Masschelein, 1987). Were the signal in the visible region, the nitrogen, and the large nitrogen tanks or gas lines required to supply it, would not be needed. Labelling the bacteriophage with visible-region dyes would thus reduce the equipment requirements and enable significant miniaturisation of the technology.

Also, in order to maximise the sensitivity and dynamic range of the assay, it is necessary to maximise the number of antibodies and dye molecules bound to the bacteriophage surface.

The first three of the four results chapters of this thesis attempt to address the weaknesses of this assay, as is stated in more detail in their individual introductory sections.

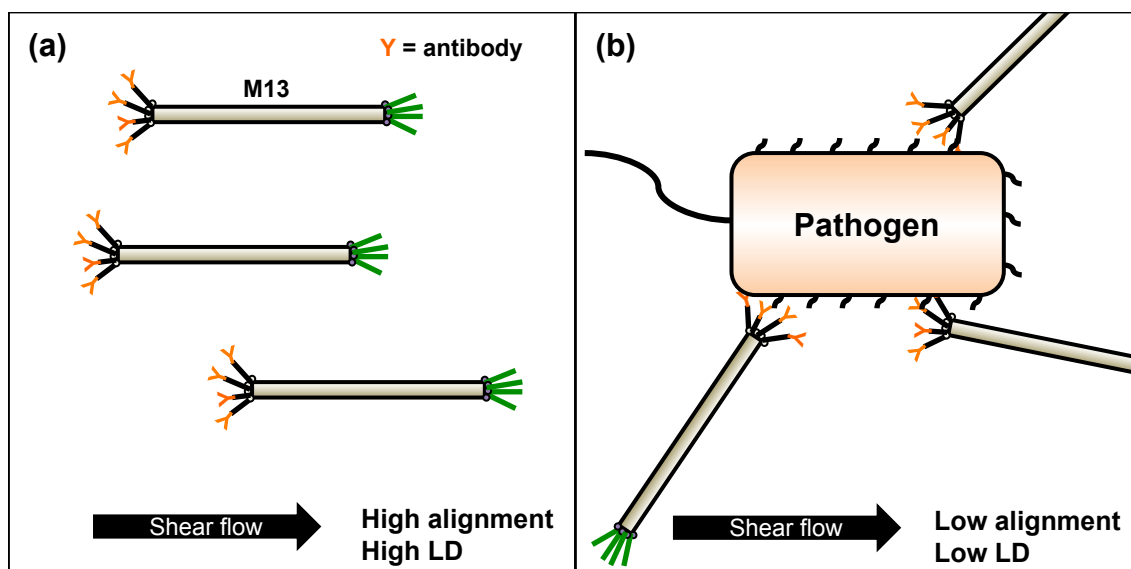


Figure 1.6. Schematic of the Pacheco-Gómez *et al.* (2012) assay. (a) Antibody-labelled M13 bacteriophage in the absence of pathogen target. Bacteriophage is free to align under the influence of shear flow and has a high linear dichroism (LD) signal. (b) Following addition of sample that contains the antibody target (pathogen), the antibody binds the pathogen, disrupting the alignment of the bacteriophage to which it is attached. The concurrent drop in LD signal indicates pathogen presence.

1.5. Thesis aims

The overall aim of this research was to investigate the use of M13 bacteriophage as a starting material in the development of nanomaterials through modification of its surface chemistry. The approaches taken to achieve this were mutation and chemical modification with amine-targeted organic dyes.

The aim of the first results chapter was to investigate the use of M13 as an alignment scaffold to allow the measurement of the linear dichroism signal of organic dyes in

aqueous solution. This was to advance development of the Pacheco-Gómez *et al.* (2012) assay and other references highlighted in the introduction of Manuscript 1.

The aim of the second results chapter was to genetically modify M13 bacteriophage to increase the number of dye-targeted amine groups displayed on its surface. This was again to advance the development of the Pacheco-Gómez *et al.* (2012) assay and other references highlighted in the introduction of Manuscript 2.

The aim of the third results chapter was to ascertain whether or not the mutations introduced to the bacteriophage in the previous chapter had an impact on the thermal stability of the bacteriophage. This is pertinent in product development as the Pacheco-Gómez *et al.* (2012) assay is intended to be portable (therefore not refrigerated) and relies on the structural integrity of the bacteriophage for its continued function.

The aim of the fourth results chapter was to determine whether or not M13 bacteriophage could be induced into assembling multi-virion structures by modifying its coat with a dye that has a propensity to aggregate. It was also the aim of this chapter to investigate whether the formation of the multi-virion structures would result in the emergence of properties that the individual virions do not possess. This chapter is thus distinct from the previous three, as it does not set out to address the shortcomings of the Pacheco-Gómez *et al.* (2012) assay. It also falls into the category of incremental nanotechnology rather than evolutionary nanotechnology.

2. EXPERIMENTAL

As this thesis contains some projects in manuscript format, this chapter aims to provide where needed more experimental details than would normally be expected in a research article, and details of experiments not included in the manuscripts.

2.1. Materials

Table 2.1. Materials

Reagent	Supplier
Alexa Fluor 555 C ₂ -maleimide	Molecular Probes
Alexa Fluor 647 C ₂ -maleimide	Molecular Probes
4-chloro-7-nitrobenzofurazan	Sigma Aldrich
Cyanine3-NHS ester	Lumiprobe
Cyanine5-NHS ester	Lumiprobe
dNTP mix	Thermo Fisher Scientific
FastDigest® DpnI	Thermo Fisher Scientific
GenElute™ kit	Sigma Aldrich
6x loading dye	Thermo Scientific
Nuclease-free water	Promega
Nutrient broth 2	Oxoid
PD midiTrap G-25 column	GE Healthcare
pfu buffer	Thermo Fisher Scientific
pfu polymerase	Thermo Fisher Scientific
Poly(ethylene glycol) 6000	Sigma Aldrich
Primers	Sigma Aldrich
QIAquick® PCR purification kit	Qiagen
10x TAE buffer	Sigma Aldrich
Template DNA (M13KE gIII cloning vector)	New England Biolabs
Tetramethylrhodamine-(5) and 6-isothiocyanate	Molecular Probes
Thioflavin T	Sigma Aldrich

2.2. Strains

2.2.1. Bacterial host

The bacterial host used to propagate M13 bacteriophage was OneShot™ TOP10F' Chemically competent *Escherichia coli* supplied by Invitrogen (catalogue number C303003) ($F'[\text{lacI}^q \text{ Tn10}(\text{tet}^R)]$).

2.2.2. M13 bacteriophage

The strain of M13 bacteriophage used was derived from M13KE gIII cloning vector supplied by New England Biolabs (catalogue number E8101S). The genome of the M13 bacteriophage strain is displayed in Figure 2.1.

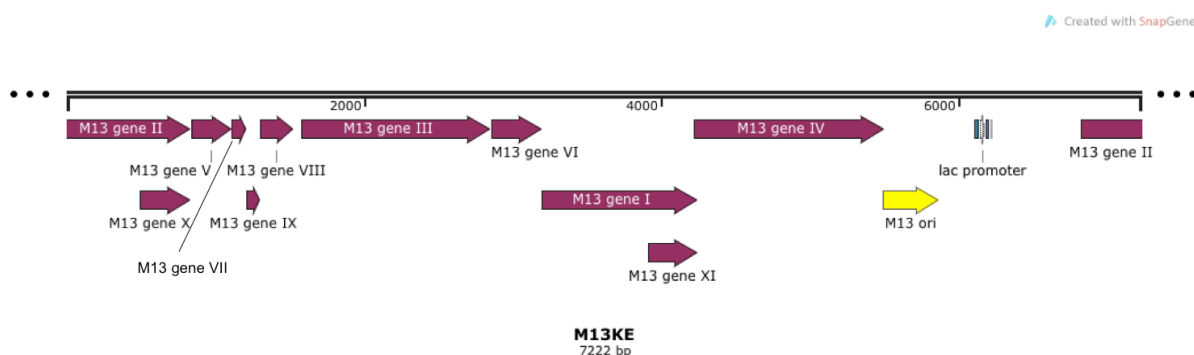


Figure 2.1. Linear map of M13KE genome. DNA was supplied in double-stranded (displayed) form. Within virions, DNA is single-stranded (positive strand).

2.3. Media and buffers

2.3.1. Luria Bertani (LB) broth

In distilled water the following ingredients were combined to the following concentrations: Enzymatic digest of casein, 10 g.L^{-1} ; Yeast extract, 5 g.L^{-1} ; Sodium chloride, 10 g.L^{-1} . The resulting solution was sterilised by autoclave at $121 \text{ }^\circ\text{C}$ for 20 minutes.

2.3.2. 2x TY broth

In distilled water the following ingredients were combined to the following concentrations: Enzymatic digest of casein, 16 g.L⁻¹; Yeast extract, 10 g.L⁻¹; Sodium chloride, 5 g.L⁻¹. The resulting solution was sterilised by autoclave at 121 °C for 20 minutes.

2.3.3. NB2 broth

Nutrient Broth 2 powder (Oxoid) was added to distilled water at a concentration of 25 g.L⁻¹. The resulting solution was sterilised by autoclave at 121 °C for 20 minutes.

2.3.4. Bottom agar

LB broth (above) was supplemented with 15 g.L⁻¹ agar, sterilised by autoclave at 121 °C for 20 minutes, then supplemented with 50 µg.mL⁻¹ isopropyl-β-D-1-galactopyranoside (IPTG) (Bioline) and 40 µg.mL⁻¹ 5-bromo-4-chloro-3-indolyl-β-D-galacto-pyranoside (X-gal) (VWR).

2.3.5. Top agar

2x TY media (above) supplemented with 10 g.L⁻¹ agar and sterilised by autoclave at 121 °C for 20 minutes.

2.3.6. Super optimal broth with catabolite repression (SOC media)

Used as supplied with ThermoScientific One Shot® TOP10F' chemically competent *Escherichia coli* cells.

2.3.7. 50 mM potassium phosphate buffer pH 8.0

Dipotassium phosphate (K_2HPO_4) and potassium dihydrogen phosphate (KH_2PO_4) were prepared in 1 M stocks and combined at a volumetric ratio of 47:3 protic:diprotic, with a combined concentration of 50 mM, and an approximate pH of 8.0. The pH of the resulting buffer solutions was checked using a pH meter and where necessary adjusted to pH 8.0 using the 1 M solutions of K_2HPO_4 or KH_2PO_4 (Fisher Bioreagents, 2018).

2.3.8. Poly(ethylene glycol) solution

Poly(ethylene glycol) (PEG; MW 6000; Sigma) and NaCl were combined in distilled water at concentrations of 25 % (m/v) and 2.5 M, respectively. The resulting solution was sterilised by autoclave at 121 °C for 20 minutes.

2.3.9. Tris buffer

Tris-HCl was dissolved to 50 mM in distilled water and pH was adjusted to 8.0 using hydrochloric acid (HCl).

2.3.10. Iodide buffer

Iodide buffer was prepared by combining the following: 10 mM Tris-HCl (pH 8.0), 1 mM ethylenediaminetetraacetic acid (EDTA), and 4 M sodium iodide (NaI).

2.3.11. Bicine buffers

In distilled water a 10 mM solution of bicine was prepared. Using 1 M sodium hydroxide (NaOH) solution, pH was adjusted to 8.0, 8.5 and 9.0.

2.3.12. Thioflavin T buffer

K_2HPO_4 and KH_2PO_4 were prepared in 1 M stocks and combined at a volumetric ratio of 61.5:38.5 protic:diprotic, with a combined final concentration of 10 mM, and an approximate pH of 7.0 (Fisher Bioreagents, 2018). To this mixture sodium chloride (NaCl) was added to a final concentration of 150 mM and the pH was adjusted to 7.0 before addition of 20 μ M thioflavin T. Finally, volume was adjusted using distilled water.

2.4. General

The following section details protocols that were employed in multiple chapters.

2.4.1. Bacteriophage host glycerol stock preparation

To 50 mL of LB broth supplemented with 5 μ g.mL⁻¹ tetracycline, 50 μ L of ThermoScientific One Shot® TOP10F' chemically competent *E. coli* cells were added and shaken at 200 rpm at 37 °C until the OD₆₀₀ reached 0.4-0.45, at which point the flask was transferred immediately to ice for 20 minutes to halt further growth. To the chilled culture 50 mL of chilled, 0.2 μ m filtered, 50 % (v/v) glycerol was added and mixed thoroughly. This mixture was left at room temperature for 20 minutes to allow thorough surrounding of cells by glycerol before 1 mL aliquots of the mixture in 1.5 mL microcentrifuge tubes were snap-frozen using liquid nitrogen and stored at -80 °C.

2.4.2. M13 bacteriophage propagation and purification

To six 2 L conical flasks each containing 400 mL of autoclaved NB2 broth supplemented with $5 \mu\text{g.mL}^{-1}$ tetracycline, 500 μL of *E. coli* glycerol stock inoculated with 0.1 mg.mL^{-1} M13 bacteriophage was added. Following incubation at 37°C at 200 rpm for 16 hours, the cultures were centrifuged at 8500 rpm (JLA 10.5 rotor) for 30 minutes at 4°C . The resulting supernatant was centrifuged again in the same conditions and the pellets from both centrifugations were discarded. To the supernatant of the second centrifugation poly(ethylene glycol) (PEG) solution was added at a volumetric ratio of 1:5 (PEG:supernatant). The resulting mixture was kept stirring on ice for 90 minutes before further centrifugation at 10000 rpm (JLA 10.5 rotor) for 25 minutes at 4°C . The supernatant was discarded and the pellet was suspended in $\sim 6 \text{ mL}$ of 50 mM potassium phosphate buffer (depending on yield). The resulting solution was then centrifuged in an MSE Micro Centaur microcentrifuge (MSB010.CX2.5) at 13000 rpm (rotor radius 65 mm) for five minutes to sediment any remaining host cells. The pellet was discarded and PEG precipitation was again performed on the supernatant to sediment bacteriophage. Following a 15-minute, 13000 rpm centrifugation in an MSE Micro Centaur microcentrifuge (rotor radius 65 mm), the supernatants were discarded and each pellet was suspended in $\sim 200 \mu\text{L}$ of 50 mM potassium phosphate buffer, pH 8.0. Purified bacteriophage was stored at 4°C .

2.5. Linear dichroism of visible-region chromophores using M13 bacteriophage as an alignment scaffold

The majority of experimental procedures employed in this chapter are detailed in Manuscript number 1.

2.5.1. Triton X-100 disaggregation of dyes from bacteriophage conjugates

M13Cy5 and M13AF647 bioconjugates were diluted to $0.12 \text{ mg}\cdot\text{mL}^{-1}$ bacteriophage concentration in 50 mM potassium phosphate buffer, pH 8.0. Following measurement of their absorbance and LD spectra (parameters in supporting information of Manuscript 1), Triton X-100 was added to a 1/1000 (v/v) concentration and the spectral measurements were repeated. The spectral measurements of M13AF647 were again repeated in the presence of Triton X-100 at a 2/1000 (v/v) concentration. All spectra were baseline subtracted against 50 mM potassium phosphate, pH 8.0 in the same cuvette in which sample spectra were measured.

2.6. Mutation of M13 bacteriophage major coat protein for increased conjugation to exogenous compounds

2.6.1. Site-directed mutagenesis

Polymerase chain reactions (PCR) were performed in 50 μL reaction volumes comprising: 1x pfu buffer; 200 μM dNTP mix; 100 ng of template DNA; 0.5 μM forward primer; 0.5 μM reverse primer; nuclease-free water to adjust the volume to 49.5 μL ; and 1.0 unit (0.5 μL) of pfu polymerase added last (primer sequences in Table M2.S1). Flat-capped, 0.2 mL PCR tubes containing the reaction mix were loaded into a Biometra® T3000 thermocycler, preheated to 95 °C, and the following

programme was run: [95 °C for 60 seconds; 50 °C for 60 seconds; 68 °C for 14 minutes and 24 seconds] x 12, hold at 4 °C. Template DNA was digested with 2 µL of FastDigest® DpnI, added directly to the PCR tube after the PCR reaction was complete. Following a two-hour incubation at 37 °C, the PCR product was purified using a QIAquick® PCR purification kit. DNA content was assessed by Nanodrop™ analysis.

Sixteen microliters of ThermoScientific One Shot® TOP10F' chemically competent *E. coli* cells were thawed on ice for 30 minutes. To the thawed bacteria, 10 pg-100 ng of DNA was added and the mixture was left on ice for 20-30 minutes. The mixture was heat-shocked in a 42 °C water bath for 60 seconds then returned to the ice for two minutes. Two hundred microliters of 37 °C SOC outgrowth media was added to the bacteria, which was then incubated at 37 °C, shaking at 200 rpm, for 45 minutes. The recovered bacterial stock was then plated onto selection agar or added into the plaque assay protocol, below.

2.6.2. Plaque assay

Bottom agar was prepared as above and poured into petri dishes under sterile conditions. The resulting plates were stored at 4 °C until required. Top agar was prepared as above and stored in a glass reagent bottle at ambient temperature until required. Top agar was melted in a microwave then, using aseptic technique, separated into 3 mL aliquots in 15 mL conical tubes and maintained at 45 °C in a water bath until required.

When plaque assays were performed to assess the titre of M13 bacteriophage in a stock, TOP10F' *E. coli* was grown at 37 °C in LB with 5 µg.mL⁻¹ tetracycline for 5-6 hours until lightly turbid. One hundred microliters of this culture was added to one 3 mL aliquot of top agar, shortly followed by 100 µL of phage stock. Following brief mixture by hand, the mixture was poured onto a plate of bottom agar.

When plaque assays were performed to amplify bacteriophage following heat shock of bacteriophage DNA into *E. coli*, 100 µL of recovered culture was added to each 3 mL aliquot of 45 °C top agar, briefly mixed, then poured onto a plate of bottom agar.

Plates were allowed to cool at room temperature for five minutes then were incubated at 37 °C overnight and plaques were counted the following morning.

2.6.3. Bacteriophage amplification from plaques

A sterile toothpick was used to lift a fresh, well-separated (> 1 cm separation from nearest neighbour) plaque into 1 mL of *E. coli* TOP10F' that had been incubated in LB with 5 µg.mL⁻¹ tetracycline for four hours at 37 °C with vigorous shaking. The culture was then incubated at 37 °C with vigorous shaking for a further four hours. The culture was then transferred to a sterile microcentrifuge tube and centrifuged for five minutes at 13000 rpm in a Micro Centaur microcentrifuge (MSB010.CX2.5, rotor radius 65 mm). The pellet was discarded and the supernatant was transferred to a fresh microcentrifuge tube and centrifuged again as before. The upper 80 % of the supernatant was transferred to a fresh microcentrifuge tube and stored at 4 °C, and the remaining supernatant was discarded with the pellet. The stored fraction of the

supernatant was used as inoculum in bacteriophage propagation and purification, and as the starting material in the preparation of single-stranded bacteriophage DNA for sequencing.

2.6.4. Preparation of single-stranded bacteriophage DNA for sequencing

Five hundred microliters of the product of the bacteriophage amplification from plaques procedure was combined with 200 μL of PEG solution, gently mixed and left to stand at room temperature for 20 minutes. The solution was then centrifuged at 13000 rpm at 4 $^{\circ}\text{C}$ for 10 minutes and the supernatant was discarded. The microcentrifuge tube was then briefly re-centrifuged and the supernatant was carefully removed with a pipette. The pellet was then re-suspended in 100 μL of iodide buffer. Two hundred and fifty microliters of ethanol was then added and the solution was incubated for 15 minutes at room temperature. The solution was then centrifuged at 13000 rpm at 4 $^{\circ}\text{C}$ for 10 minutes and the supernatant was discarded. Following the addition of 500 μL of 70 % ethanol (stored at -20 $^{\circ}\text{C}$), the solution was centrifuged again as before. The supernatant was discarded and the pellet was briefly dried. The pellet was then re-suspended in 30 μL of nuclease-free water and the DNA content was assessed by NanoDrop™ analysis.

2.6.5. Sequencing

DNA sequencing was performed at the University of Birmingham Functional Genomics Facility using pVIII_seq_r primer (Table M2.S1).

2.6.6. Preparation of double-stranded bacteriophage DNA

An entire 1 mL glycerol stock of *Escherichia coli* TOP10F' (protocol for preparation above) was used to inoculate 5 mL of 2xTY media supplemented with 5 $\mu\text{g}\cdot\text{mL}^{-1}$ tetracycline. This was grown overnight at 37 °C, shaking at 200 rpm. Twenty millilitres of fresh 2xTY supplemented with 5 $\mu\text{g}\cdot\text{mL}^{-1}$ tetracycline and 1 % (w/v) glucose was inoculated with 2 mL of the overnight culture and incubated at 37 °C, shaking at 200 rpm. When the OD_{600} reached 0.8-1.0, M13 bacteriophage was added at a concentration of 1.4 $\mu\text{g}\cdot\text{mL}^{-1}$. Fifteen minutes following M13 infection, chloramphenicol was added to a concentration of 15 $\mu\text{g}\cdot\text{mL}^{-1}$ to promote the accumulation of double-stranded DNA (Ray, 1970). Following a further two-hour incubation at 37 °C, double-stranded bacteriophage DNA was extracted using a Sigma-Aldrich GenElute™ kit. DNA concentration and size were measured by Nanodrop™ analysis and gel electrophoresis, respectively.

2.6.7. Agarose gel electrophoresis

Ten microliters of DNA and 2 μL of 6x loading dye were mixed then pipetted into each well of a horizontal 1% (m/v) agarose gel prepared with 1X Tris-Acetic acid-Ethylenediaminetetraacetic acid (TAE) buffer. Gels were electrophoresed at 80-100 V for 30-40 minutes in TAE buffer.

2.6.8. Determination of molar extinction coefficient of 4-chloro-7-nitrobenzofurazan bound to an amine group

Reaction details are provided in the Supporting information of Manuscript 2.

2.6.9. Nonlinear regression analysis

To calculate the value of A_{475} at infinite time, nonlinear regression was performed on the data obtained from the above protocol against the reverse of an equation describing single-phase exponential decay. The rationale behind reversing the sign of such an equation is described in this section.

The concentrations of the reactant and product in a first order reaction change at opposite rates, as shown below:

$$\frac{d[\text{reactant}]}{dt} = -\frac{d[\text{product}]}{dt} \quad \text{Equation 2.1}$$

where t is time. In the pseudo first order reaction here therefore,

$$\frac{d[\text{NBD} - \text{Cl}]}{dt} = -\frac{d[\text{NBD} - \text{Ala}]}{dt} \quad \text{Equation 2.2}$$

The model for single-phase exponential decay describes the loss of reactant in a chemical reaction:

$$Y = s e^{-kt} + p \quad \text{Equation 2.3}$$

where Y is the reactant concentration (mol.L^{-1}), s is the difference between Y at zero time and infinity (mol.L^{-1}), k is the rate constant (s^{-1}), t is time (s) and p is the y-axis value at infinite t (mol.L^{-1}). Based on Equations 2.1 and 2.2, gain of the product, NBD-Ala, would be expressed as

$$Y' = -s e^{-kt} + p \quad \text{Equation 2.4}$$

Where Y' is A_{475} , proportional to the concentration of product, NBD-Ala. Based on this formula, the value of A_{475} at infinite t is equal to p . Using the value of p derived from this nonlinear regression, ϵ_{475} for NBD-amine was derived using the Beer-Lambert law.

2.6.10. UV-visible absorbance spectroscopy

All absorbance readings were taken using a Jasco V-550 UV-Vis spectrometer with the parameters in Table 2.2. Wavelength ranges are indicated in the figures. Samples were baseline subtracted against their corresponding buffer using Spectra Manager software.

Table 2.2. UV-visible absorbance spectroscopy parameters

Parameter	Value
Path length / cm	1
Band width / nm	1.0
Scanning speed / nm.min ⁻¹	200
Data pitch / nm	1.0

2.6.11. Conjugation efficiency calculation

The extent of M13 bacteriophage labelling by the various exogenous groups is expressed as the percentage of pVIII monomers labelled (i.e. one exogenous group per pVIII monomer would equal 100 % conjugation efficiency). Conjugation efficiency is given by

$$\text{Conjugation efficiency} = \frac{[dye]}{27[M13]} \% \quad \text{Equation 2.5}$$

where $[dye]$ is the concentration of the exogenous compound bound to M13 bacteriophage, as determined spectroscopically, and $[M13]$ is the concentration of M13 bacteriophage, determined using ϵ_{269} of $3.84 \text{ mg}^{-1} \cdot \text{cm}^2$ (Berkowitz and Day, 1976) and bacteriophage MW of 16.6 MDa (calculated as sum of molecular weights of coat proteins and DNA).

2.7. Bacteriophage thermal stability

2.7.1. Circular dichroism

All bacteriophage samples were diluted to $0.013 \text{ mg} \cdot \text{mL}^{-1}$ in 50 mM potassium phosphate buffer, pH 8.0. All measurements were taken using a Jasco J-1500 CD spectrometer, a Starna Scientific 6Q quartz cuvette (1 cm path length) and a Jasco PTC-517 Peltier thermostatted single cell holder. Baseline readings were taken against the corresponding buffer of each sample and subtracted from the reading containing the sample. The parameters shown below in Table 2.3 were used.

Table 2.3. Parameters used in thermal denaturation experiments

Parameter	Experiment type		
	222 nm only 15-95 °C	Full spectra 15-95 °C	Full spectra 15-60-15 °C
Start λ / nm	222	270	270
End λ / nm	222	200	200
D.I.T. / sec	2	1	1
Bandwidth / nm	1.00	2.00	2.00
Baseline correction	None	None	None
Shutter control	Auto	Auto	Auto
Accessory	PTC-517	PTC-517	PTC-517
Accessory S/N	A010061646	A010061646	A010061646
Control sensor	Cell 1	Cell 1	Cell 1
Monitor sensor	Cell	Cell	Cell
Start mode	Keep target temp +/- 0.10 °C 5 s	Keep target temp +/-0.10 °C 5 s	Keep target temp +/-0.10 °C 5 s
Scanning speed / nm.min ⁻¹	-	50	50
Data pitch / nm	-	0.2	0.2
Accumulations	-	3	3
Start temp	15	15	15
End temp	95	95	60
Ramp rate / °C.min ⁻¹	0.54	1	1
Temp ramp mode	Continuous	Halt	Halt
Temp interval / °C	0.5	5	5

2.7.2. Deconvolution of circular dichroism data

Throughout this thesis, CD data are shown in raw form with ellipticity as units. For deconvolution, raw circular dichroism spectral data (ellipticity in mdeg), were converted to molar circular dichroism, $\Delta\epsilon$ in M⁻¹.cm⁻¹, using

$$\Delta\varepsilon = \frac{0.1 \left(\frac{M_r}{N}\right)}{l[\textit{protein}]3298}$$
Equation 2.6

where M_r is the molecular weight of the protein in Daltons, N is the number of amino acid residues per protein subunit, l is the path length in cm, and $[\textit{protein}]$ is the protein concentration in $\text{mg}\cdot\text{mL}^{-1}$ (DichroWeb User Guide). All deconvolution was carried out using K2D3 software (Louis-Jeune *et al.*, 2011), yielding alpha helix and beta sheet content of the samples.

2.7.3. Thioflavin T assay

Thioflavin T assays were performed in a Perkin Elmer LS50B fluorimeter with the following settings: Excitation wavelength, 440 nm; emission wavelength, 482 nm; excitation slit width, 10 nm; emission slit width, 10 nm; integration time, 10 s; accumulations, 6. First, a baseline fluorescence intensity reading was taken of 1 mL of thioflavin T buffer in a 1 cm path length cuvette. Next, 40 μL of either native or heat-denatured bacteriophage at $0.013 \text{ mg}\cdot\text{mL}^{-1}$ was added, the sample was mixed for one minute and the fluorescence intensity was measured again. Three 40 μL aliquots were taken and assayed from each sample of bacteriophage, both native and denatured, and there were three repeats of each sample from which the aliquots were taken. The displayed results were calculated as

$$\textit{Change} = \frac{I_{II} - I_I}{I_I} \times 100\%$$
Equation 2.7

where I_{II} is the fluorescence intensity after the addition of bacteriophage sample and I_I is the fluorescence intensity of the blank.

2.8. Assembly of multi-virion structures mediated by xanthene dye H-aggregation

The majority of experimental procedures employed in this chapter are detailed in Manuscript number 3.

2.8.1. Conjugation of Cyanine3 NHS ester to M13 bacteriophage

Cyanine3 NHS ester (Cy3) was dissolved in DMSO to a concentration of 10 mg.mL^{-1} and a 2.5 mg.mL^{-1} solution of M13 was made in 50 mM potassium phosphate buffer, pH 8.0. In a 1.5 mL microcentrifuge tube, 20 μL of the Cy3 solution was added to 980 μL of the M13 solution. The reaction mix was left slowly rotating ($\sim 4 \text{ rpm}$) overnight in the dark at $20 \text{ }^\circ\text{C}$. To remove unbound dye the reaction mix was buffer exchanged, using a PD midiTrap G-25 column, into 1.5 mL of fresh 50 mM potassium phosphate buffer pH 8.0, following manufacturer's instructions.

2.8.2. Ammonium sulphate precipitation of M13Cy3

All experiments were carried out in 50 mM potassium phosphate buffer pH 8.0 with varying concentrations of ammonium sulphate (0.00 – 2.25 M). When UV-Vis absorbance was measured, M13 and Cy3 were combined at concentrations of 0.04 mg.mL^{-1} and $1.5 \text{ } \mu\text{M}$, respectively, whether separate or in the various conjugates. When LD of M13Cy3 was measured, the bacteriophage concentration was 0.04

mg.mL⁻¹ and Cy3 concentration depended on the number of Cy3 groups bound to the bacteriophage (~1400 Cy3 per virion for M13Cy3 and ~350 per virion for M13Cy3₃₅₀).

2.8.3. Screen for alternative salts to induce dye H-aggregation

Solutions of Na₂S₂O₃, NaH₂PO₄, NaCl, NaI and MgCl₂ were prepared at 1.1 M in 50 mM potassium phosphate buffer, pH 8.0. BaCl₂ and CaCl₂ were separately dissolved to 1.1 M in Tris-HCl buffer, pH 8.0 to prevent salt sedimentation. During the screening, salts were combined with bacteriophage and bacteriophage conjugate samples to a final salt concentration of 1 M.

**3. LINEAR DICHROISM OF DYES USING M13
BACTERIOPHAGE AS AN ALIGNMENT SCAFFOLD**

3.1. Introduction

As stated in section 1.4, one of the crucial steps towards the further development of the Pacheco-Gómez assay is endowing the bacteriophage with a visible-region linear dichroism (LD) signal facilitated by the covalent attachment of visible-region dyes to its outer surface. This would enable both multiplex assay development and a significant reduction in the equipment requirements of the assay.

It was hypothesised that labelling M13 bacteriophage with an appropriate chromophore would endow it with a visible-range LD signal as this phenomenon has been studied with other macromolecules. For example, the interaction between DNA and ethidium bromide can be probed by LD spectroscopy using shear flow to drive DNA orientation (Marrington *et al.*, 2004). As ethidium bromide binds to DNA in an ordered fashion (by intercalation) it exhibits an LD signal in shear flow when bound to DNA. In isolation, however, ethidium bromide does not exhibit LD in shear flow. Since the bacteriophage displays a regular array of dye-binding sites (amine groups), it could be used as a scaffold for the alignment of visible-region dyes, thus demonstrating how the Pacheco-Gómez assay may be expanded beyond its current capabilities.

It is the aim of the remainder of this introductory section to provide the reader with a brief introduction to the theory behind LD spectroscopy and the methods used to measure the LD of small molecules and macromolecules.

3.2. Linear dichroism spectroscopy

Linear dichroism (LD) is defined as the differential absorption, by an oriented sample, of light polarised parallel to a laboratory-defined axis and perpendicular to it. LD is most simply expressed by the following equation:

$$LD = A_{\parallel} - A_{\perp} \quad \text{Equation 3.1}$$

where A_{\parallel} is the absorption of light polarised parallel to the laboratory defined axis and A_{\perp} is the absorbance of light polarised perpendicular to the same axis. LD is often reported as *reduced LD* (LD_r), which is defined by the following equation:

$$LD_r = LD/A_{iso} \quad \text{Equation 3.2}$$

where A_{iso} is the isotropic absorbance of the sample. Some molecules have a preferential absorption polarisation because absorption of light involves the transition of their electronic orbitals from the ground state to a higher-energy excited state, and the efficiency of this transition is dependent the polarisation of the incident light. This can be understood by way of analogy: One can imagine that to push a boulder out of a ditch, it would be most effective to push directly towards the bank on either side. Pushing with equivalent energy diagonally or horizontally would result in an incomplete or entirely ineffective transfer from the bottom of the ditch to the top. In this analogy, the direction of pushing corresponds to the polarisation of the incident light. The height of the boulder is its energy level but its position along the ditch does not translate in this analogy. Thus, the boulder when at the bottom of the ditch is the

electron in the ground state. Likewise, the boulder when at the top of the ditch is the electron in the excited state. Finally, the straight line between the initial and final positions of the boulder represents the transition dipole polarisation. The angular dependence of LD is defined by the following equation:

$$LD = \frac{3}{2}SA_{iso}(3\cos^2\alpha - 1) \quad \text{Equation 3.3}$$

where S is the orientation parameter, which can take a value between zero (sample is completely isotropic) and one (all molecules within the sample are perfectly aligned about the same axis); and α is the angle between the transition dipole moment of the molecule and the laboratory-defined axis (Figure 3.1). By measuring the LD of a sample of known orientation, one can therefore determine the value of α and thus the polarisation of the transition dipole moment of a chromophore. This process of mapping transition dipole polarisations was used in Manuscript 1. Furthermore, as the LD of a molecule is thus dependent on α , LD spectroscopy can be used to determine the orientation of a molecule (of known transition dipole polarisation) within an ordered sample, for example, LD spectroscopy can be used to confirm or rule out whether a DNA-binding molecule associates via intercalation (Nordén *et al.*, 2010).

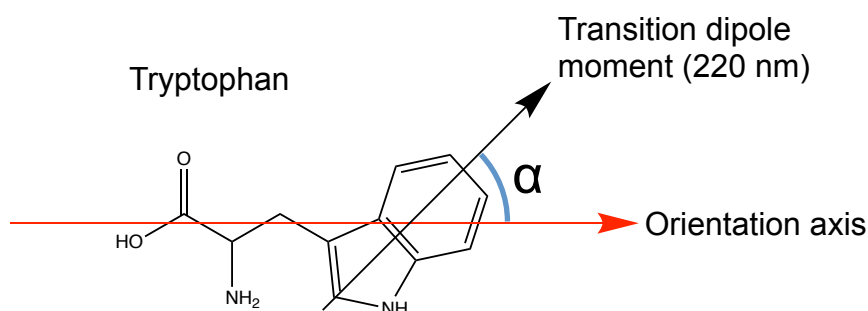


Figure 3.1. Schematic of angle (α) between transition dipole moment of tryptophan and orientation axis (Adapted from Nordén *et al.*, 2010).

3.3. Linear dichroism spectroscopy methods

3.3.1. Small molecule orientation methods

In this work, the LD of cyanine dyes was measured using the stretched-film technique (explained below), using polyethylene (PE) that had been treated to become oxidised (PE^{ox}) (Razmkhah *et al.*, 2014a) as the orientation medium. This section aims to compare this technique to other techniques. The techniques used to orient small molecules may be described as either film-based or non-film-based, as summarised in Table 3.1.

Table 3.1. Molecular orientation methods

Technique	Molecule	Reference
Film-based		
Polyethylene (PE)	Fluoranthene	Thulstrup and Eggers, 1968
	Phenanthrene, pyrene, perylene and benzoperylene	Thulstrup <i>et al.</i> , 1970
	10a,4a,-borazarophenathrene	Michl <i>et al.</i> , 1970
	>100 aromatic molecules	Thulstrup and Michl, 1982
Oxidised polyethylene (PE ^{ox})	Xanthene-based dyes	Razmkhah <i>et al.</i> , 2014a
Polyvinyl alcohol (PVA)	DNA bases	Matsuoka and Nordén, 1982
	Cyanines	Natarajan <i>et al.</i> , 1983
	Colloidal silver	Fornasiero and Grieser, 1987
	Porphyrins	Gryczynski <i>et al.</i> , 1997
	Carbocyanines	Synak and Bojarski, 2005
Polyvinyl chloride (PVC)	Plasticisers	Umemura <i>et al.</i> , 1968
Non-film-based		
Crystallisation	Cobalt	Legut <i>et al.</i> , 2014
	Black phosphorus	Qiao <i>et al.</i> , 2014
Evaporation	Dysprosium	Kappert <i>et al.</i> , 1993
Liquid crystal orientation	Anthracene and beta-carotene	Nordén <i>et al.</i> , 1977

The crystallisation technique (Table 3.1) involves the growth of crystals of the molecule of interest. The LD of very thin sections of said crystal is then measured. The data obtained may be combined with X-ray crystallographic data to ascertain the orientation of the molecules within the crystal and thus map the transition dipole polarisations of the molecule of interest.

The evaporation technique (Table 3.1) involves the drying of a solution of the molecule of interest onto a surface. This can result in oriented deposition, enabling the measurement of the LD of the deposited layer.

The crystallisation and evaporation techniques both rely on the assembly of large numbers of molecules to form some structure with a degree of order within. Crystallisation can result in the perfect orientation of the molecule of interest (Nordén *et al.*, 2010). Because of this the combination of crystallisation data and X-ray structural data is often referred to as 'absolute data'. This is because it does not rely on any assumption about the orientation of the molecule of interest in the laboratory-defined axes. As such it is taken as the highest standard of data for assigning the transition dipole polarisations of a molecule. However this technique, like the evaporation technique relies on the molecule of interest's spontaneous anisotropic assembly. Since this could not be guaranteed for all the dyes used in this project, these techniques were not used.

The liquid crystal technique (Table 3.1) involves the alignment of molecules between lipids arranged in a bilayer. Depending on the shape and charge of the molecule, it will align either between adjacent lipid molecules or between the two layers of lipids. Because of the lipids' amphiphilicity, this technique is appropriate to study both polar and non-polar molecules. However, the complicated sample preparation means that each spectrum takes a few hours to measure, so this technique was not used here.

The film-based techniques (Table 3.1) all involve deposition of molecules onto a polymer-based film, or the soaking of a molecule into a film (Figure 3.2 a), which is then stretched. This aligns the longest axis of the molecule (assuming geometric asymmetry) with the stretch direction (Figure 3.2 b) (Jakobi *et al.*, 1962; Thulstrup *et al.*, 1970; Thulstrup and Michl, 1982). In a typical setup, the stretch direction is parallel to the floor and the parallel (||) light polarisation (Figure 3.2 c; Equation 3.1). This assumption about the orientation of molecules on the films, when tested against crystal-based data, has been found to be true in the vast majority of cases (Thulstrup *et al.*, 1970 and references within). In addition, Thulstrup and Michl, 1982 conducted experiments in which the longest axes of molecules were rotated by 90° by the addition of substituent moieties. This resulted in the inversion of their LD signals, indicating that their orientation on the film had changed in relation to the change in their shape, supporting the assumption that molecules will preferentially align with their longest axis parallel to the stretch direction of the film.

Of the film types used in this approach polyethylene (PE) is the quickest and simplest to use. In this technique molecules dissolved in a volatile solvent e.g. chloroform or methanol, are deposited onto a PE film. This is then dried and stretched, and LD is measured. The total time per spectrum using PE is less than one hour. However PE is best for non-polar molecules due to its own non-polarity. Poly(vinyl acetate) (PVA) and poly(vinyl chloride) (PVC) are better suited to aligning polar molecules (e.g. cyanines) as their structures are more polar than PE. Unfortunately it takes one-to-three days to collect a spectrum using these techniques because the films must be cast and cured prior to stretching. Oxidised polyethylene (PE^{ox}) has the speed and

ease of use of PE, only requiring one additional treatment (film oxidation), which takes around five minutes. Additionally, in contrast to PE, PE^{ox} is suitable for aligning polar molecules, thus was chosen here to study a selection of cyanine dyes.

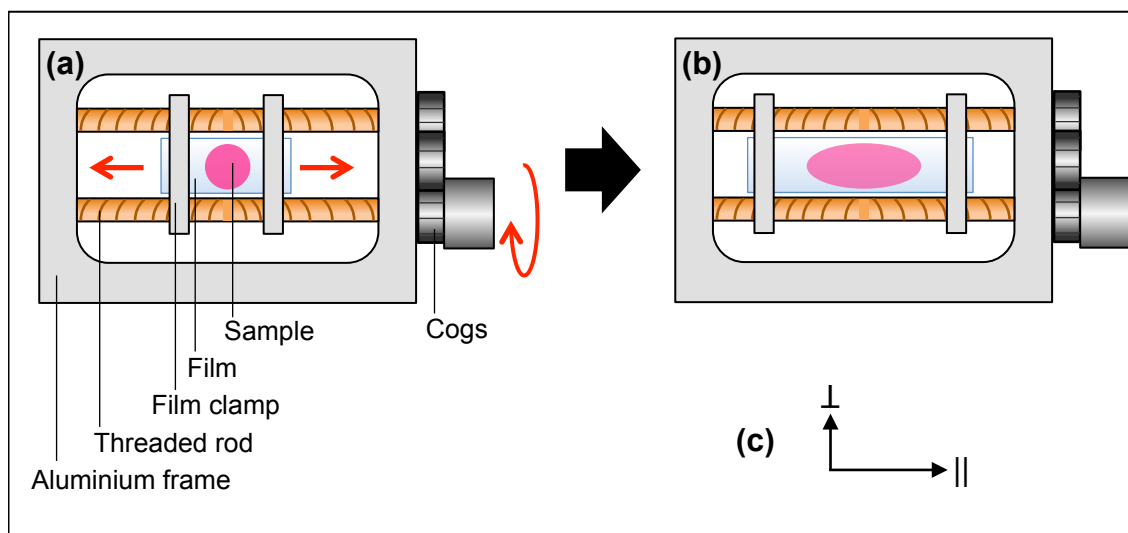


Figure 3.2. Experimental setup for stretched-film linear dichroism spectroscopy. (a) Film stretcher with film and sample prior to stretching. (b) Film stretcher with film and sample after stretching. (c) Experimental orientation axes in relation to light polarisation: horizontal (stretch direction) is parallel (\parallel) and vertical is perpendicular (\perp). Light is incident on the sample through the plane of the diagram.

3.3.2. Macromolecular orientation methods

The technique used by Pacheco-Gómez *et al.* (2012) to orient M13 bacteriophage for their bioassay was Couette flow. As summarised in Table 3.2, this technique is applicable to rod-like macromolecules in solution. A Couette cell comprises a rotating quartz capillary and a stationary central quartz rod. The sample occupies the annulus between these two components and because of the differential motion between them the sample is subjected to shear flow. As the macromolecules probed are rod-like, they preferentially align with their longest axis parallel to the direction of flow. In a

typical laboratory setup, this is parallel to the floor and is also the parallel (||) light polarisation in Equation 3.1 (Figure 3.3).

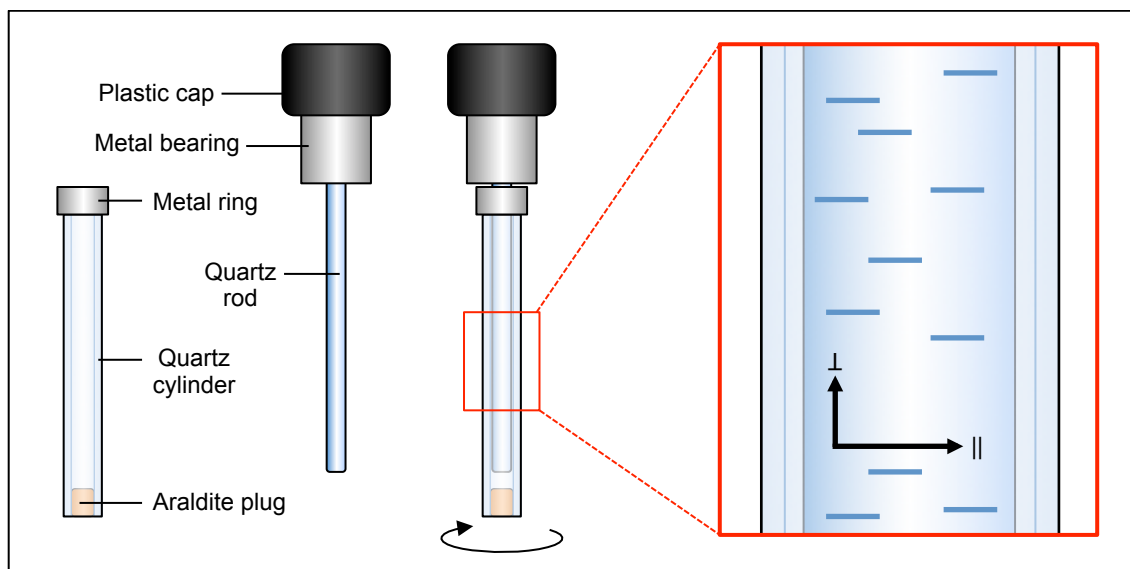


Figure 3.3. Couette flow alignment of rod-like macromolecules. From left to right: Quartz cylinder, which holds the liquid sample; Quartz rod; Quartz rod inside cylinder = a Couette cell. Cylinder is rotated while rod is held stationary; Inset: Rod-like macromolecules (dark blue lines) align with their longest axis parallel to the flow direction, which is equivalent to the parallel light polarisation (||). Light is incident on the sample through the plane of the diagram.

A summary of other techniques used to orient macromolecules for linear dichroism spectroscopy is provided in Table 3.2. As Couette flow was the method used in the Pacheco-Gómez assay, it was also used in this project to orient dye-labelled M13 bacteriophage.

Table 3.2. Macromolecular orientation methods

Technique	Macromolecule	Reference
Couette flow	Fibrous actin	Wada and Kozawa, 1964
	DNA	Wada, 1964; Marrington <i>et al.</i> , 2004
	Amyloid fibrils	Dafforn <i>et al.</i> , 2004
	M13 bacteriophage	Pacheco-Gómez <i>et al.</i> , 2012
Electric field orientation	DNA-histone complex	Houssier and Fredericq, 1966
	Bacteriochlorophyll α -protein	Whitten <i>et al.</i> , 1977
	DNA	Hogan <i>et al.</i> , 1978; Diekmann <i>et al.</i> , 1982
Gel deformation	Photosynthetic pigments	Ganago <i>et al.</i> , 1982
	Bacterial light-harvesting antennae within cyanobacterium whole cells	Bruce and Biggins, 1985
	Bacteriochlorophyll α -protein	Melkozernov <i>et al.</i> , 1998
Gel electrophoresis	DNA	Jonsson <i>et al.</i> , 1988; Borejdo, 1989
	Fibrous actin	Borejdo and Ortega, 1989
Linear flow	DNA	Cavalieri <i>et al.</i> , 1956
	Synthetic polypeptides	Bird <i>et al.</i> , 1958
Magnetic field orientation	Photosynthetic membranes (<i>Halobacterium salinarium</i>)	Borucki <i>et al.</i> , 1998
	Carbon nanotubes	Tumpane <i>et al.</i> , 2008

3.3.3. Förster resonance energy transfer (FRET)

FRET is the transfer of energy from a donor fluorophore in its excited state to an acceptor fluorophore (Lakowicz, 2010). The energy transfer is non-radiative (no photon is emitted and re-absorbed) so the two fluorophores must be in close proximity for FRET to occur. In addition, the emission spectrum of the donor must

overlap with the excitation spectrum of the acceptor. FRET efficiency is dependent on the spatial proximity of the fluorophores, the relative orientation of their transition dipole moments, the quantum yield of the donor, the refractive index of the medium and the extent of spectral overlap (Lakowicz, 2010). Because FRET efficiency is inversely related to donor-acceptor separation, it is used as a “molecular ruler” to probe conformational changes in proteins to elucidate the mechanisms of their function (Ma *et al.*, 2014). In the manuscript in this chapter (M1), LD is used to assess donor/acceptor transition dipole moment alignment when dyes are conjugated to M13 bacteriophage. The effect on FRET efficiency of altering this alignment by changing the dye orientation is investigated. The reasons for this study are covered in section M1.2.

3.4. Project aims

It was the aim of this project to demonstrate the use of M13 bacteriophage as an alignment scaffold for the measurement of the LD of visible-region dyes. There were two reasons to investigate this: First to demonstrate the viability of this approach in extending the functionality of the assay format published by Pacheco-Gómez *et al.* (2012); and second to demonstrate how dye LD may be used to directly measure whether inefficient Förster resonance energy transfer is due to dye separation or misalignment. The motivation behind this second point is explained in the introduction section of the manuscript. To achieve these aims it was first necessary to determine the transition dipole polarisations of a selection of visible-region dyes using stretched-film LD spectroscopy.

3.5. Manuscript number 1 (M1)

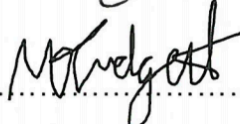
**Linear dichroism of visible region chromophores using
M13 bacteriophage as an alignment scaffold**

Matthew Tridgett, Charles Moore-Kelly, Jean-Louis H. A. Duprey, Lorea Orueta
Iturbe, Chi W. Tsang, Haydn A. Little, Sandeep K. Sandhu, Matthew R. Hicks,
Timothy R. Dafforn and Alison Rodger

RSC Advances, 2018, **8**, 29535

Author contribution statement: CMK assisted with the FRET experiment. JLHAD, LOI and MRH developed and performed the conjugation procedure for the Alexa Fluor dyes. CWT collected the mass spectrum. HAL provided technical advice. SKS conducted preliminary experiments that were not included in the manuscript. TRD edited the manuscript and was the supervisor. AR edited the manuscript and supervised linear dichroism data interpretation. MT contributed all other aspects.

Signed:.......... Timothy R. Dafforn

Signed:.......... Matthew Tridgett

M1.1. Abstract

It is a challenge within the field of biomimetics to recreate the properties of light-harvesting antennae found in plants and photosynthetic bacteria. Attempts to recreate these biological structures typically rely on the alignment of fluorescent moieties *via* attachment to an inert linear scaffold, e.g. DNA, RNA or amyloid fibrils, to enable Förster resonance energy transfer (FRET) between attached chromophores. While there has been some success in this approach, refinement of the alignment of the chromophores is often limited, which may limit the efficiency of energy transfer achieved. Here we demonstrate how linear dichroism spectroscopy may be used to ascertain the overall alignment of chromophores bound to M13 bacteriophage, a model linear scaffold, and demonstrate how this may be used to distinguish between lack of FRET efficiency due to chromophore separation, and chromophore misalignment. This approach will allow the refinement of artificial light-harvesting antennae in a directed fashion.

M1.2. Introduction

Natural light-harvesting complexes (LHCs) harvest energy from the sun leading to its transformation into a form that can be stored and used. They function as a result of highly ordered arrangements of biological chromophores called accessory pigments, which funnel light energy towards a reaction centre, which captures the energy in chemical form (Berg *et al.*, 2012). Pigment dipoles within photosynthetic organisms, including purple bacteria and green plants, are anisotropically organised within LHCs, which are approximately cylindrical transmembrane pigment-protein complexes (Cogdell *et al.*, 2006; Baker and Habershon, 2017; Külbrandt, 1994; McDermott *et*

al., 1995). The high degree of anisotropy of pigments within LHCs enables efficient energy transfer between chromophores and thus highly efficient light harvesting. LHC pigment organisation has been investigated using a variety of techniques, including X-ray crystallography (Cogdell *et al.*, 2006), circular dichroism (Georgakopoulou *et al.*, 2004; Georgakopoulou *et al.*, 2007), and linear dichroism (Garab and van Amerongen, 2009; Croce *et al.*, 1999). In turn, the supramolecular organisation of LHCs has been investigated using, for example, electron microscopy and atomic force microscopy (Boekema *et al.*, 1995; Bahatyrova *et al.*, 2004).

This concept is extremely attractive and researchers have often tried to mimic ordered arrangements of chromophores to achieve the same light harvesting effect *in vitro*. Approaches include the use of self-assembling nanoparticles to organise light-harvesting chromophores (Pu *et al.*, 2014), pigment micellisation (Peng *et al.*, 2012), self-assembly of chromophore-functionalised cellulose nanorods (Sakakibara *et al.*, 2013), macromolecular porphyrin self-assembly (Satake *et al.*, 2011), self-assembly of light-harvesting dendrimers (Arrigo *et al.*, 2017), and the construction of two-dimensional covalent organic frameworks of pigments (Feng *et al.*, 2016). What is common to all these approaches is the attempt to organise pigments anisotropically, thus mimicking natural LHCs.

An approach often taken to mimic natural LHCs involves the use of a high aspect ratio scaffold onto which a large number of chromophores are bound to allow unidirectional transfer of energy via resonance energy transfer, mimicking the light-capturing antennae that surround reaction centres in plants and photosynthetic

bacteria. High aspect ratio scaffolds used for the ordered arrangement of chromophores include: DNA (Dutta *et al.*, 2011); the coat proteins of the filamentous plant virus Tobacco Mosaic Virus (TMV; Miller *et al.*, 2007); M13 bacteriophage (Nam *et al.*, 2010); peptide nanotubes (Matsui *et al.*, 2001); and amyloid-like protein fibrils (Channon *et al.*, 2009).

While these techniques yielded functioning light-capturing antennae, there was often limited optimisation of the alignment of chromophores, or of the antennae, and surprisingly, a number of assumptions were made regarding the orientation of dyes associated with linear scaffolds: Dutta *et al.* (2011) relied on fluorescence anisotropy to demonstrate that dyes bound to DNA were not freely rotating and thus assumed that they were bound with strongly aligned transition dipoles. While it was mentioned that more detailed analysis would be required to determine the actual geometries of the dyes, no such analysis was provided. In contrast, Miller *et al.* (2007) assumed random orientation of chromophores on TMV coat proteins. They could have had greater insight and potential to optimise energy transfer by investigating the alignment of the dyes relative to the scaffold. Nam *et al.* (2010) did not optimise orientation of dyes bound to M13 bacteriophage; they relied on the flexibility of the N-terminus of the coat protein to enable energy transfer between dyes. This could have been optimised if information were available to determine the orientation of the dyes on the bacteriophage. Matsui and MacCuspie (2001) used infrared spectroscopy to infer the orientation of porphyrins bound to the surface of a peptide nanotube (Matsui and MacCuspie, 2001). While they were able to suggest an orientation, the model they proposed was only one of a number of possibilities. Finally, Channon *et*

al. (2009) relied on the assumption that the binding of fluorophores to a rod-like scaffold provides rigid orientation, a claim that could have been supported experimentally were information about the alignment of the dyes on the nanotubes available. It is clear from these examples that, were information regarding the alignment of the dyes relative to the scaffold available, rational optimisations of the dye scaffolds could be made to enable improved alignment of dye transition dipole moments, a requirement for optimal FRET efficiency and thus optimal light harvesting.

In this work we have used M13 bacteriophage as a well-defined biological scaffold to align light harvesting chromophores. We have used linear dichroism (LD) spectroscopy, a well-established technique (Thulstrup and Eggers, 1968; Thulstrup *et al.*, 1970; Michl *et al.*, 1970; Thulstrup and Michl, 1982; Matsuoka and Nordén, 1982; Bialek-Bylka *et al.*, 2000; Jonsson *et al.*, 1988; Nordén and Tjerneld, 1977), as a method to measure the alignment of visible-region chromophores bound to the biological scaffold. The method demonstrated here rapidly provides orientation information that can be used in directed optimisations of the dye arrays.

In order to show the versatility of our approach we illustrate how it can be used to assess the alignment of Cyanine3, Cyanine5 and Alexa Fluors 555 and 647, assembled on M13 bacteriophage as a scaffold. We used the stretched-film LD technique developed by Razmkhah *et al.* (2014a) to determine the transition dipole polarisations of the dyes, which are needed for the analysis.

M1.3. Experimental

M1.3.1. Materials

Cyanine3 NHS ester and Cyanine5 NHS ester were obtained from Lumiprobe GmbH (Germany). Alexa Fluors 555 C₂-maleimide and 647 C₂-maleimide were obtained from Invitrogen (USA). The film stretcher was built at the University of Warwick, UK. The film was cut from KitKare Ltd (UK) Clear Polythene Plastic Bags (120 gauge, 30 μm).

M1.3.2. Mass Spectrometry

Alexa Fluor 555 C₂-maleimide was dissolved in 50:50 water:acetonitrile with 0.5 % triethylamine. Negative electrospray ionisation time of flight mass spectrometry was performed at the Centre for Chemical and Material Analysis at the University of Birmingham.

M1.3.3. Stretched-film linear dichroism measurements

3 x 5 cm² polyethylene (PE) films were cut from KitKare Ltd Clear Polythene Plastic Bags (120 gauge, 30 μm). The films were then treated in a Harrick Plasma Cleaner PDC-32G-2 set to RF level HI for four minutes to produce oxidised PE (PE^{ox}). The PE^{ox} films were then clamped into a film stretcher built at the University of Warwick, with the clamps set at a separation of 2.5 cm and the film oriented with the manufacturing stretch direction aligned with the film stretcher stretching direction. In some experiments the film was stretched before adding the sample thus enabling the baseline to be collected on the same film. In others (where stretch was the variable being considered) the sample was added to the unstretched film and then stretched

and the baseline was a different film stretched to the same extent. The dye was then dried under vacuum for a further 15 minutes. The standard stretch amount was 1.8x its original length, 4.5 cm, unless the effect of stretching was being studied. All samples were measured using a Jasco J-1500 Circular Dichroism Spectrometer (parameters for each dye are provided in the Supporting information, Table M1.S1).

M1.3.4. Production of M13 bacteriophage

M13 bacteriophage stocks were grown using One Shot™ TOP10F' *Escherichia coli* (Thermo Fisher Scientific) as the host, and purified as previously published (Pacheco-Gómez *et al.*, 2012).

M1.3.5. Bacteriophage-dye conjugation

Cyanine3 NHS ester (Cy3) or Cyanine5 NHS ester (Cy5) was dissolved to 10 mg.mL⁻¹ in dimethyl sulfoxide (DMSO). To 980 µL of M13 bacteriophage at 2.5 mg.mL⁻¹ in 50 mM potassium phosphate buffer, pH 8.0 in a 1.5 mL microcentrifuge tube, 20 µL of a dye solution was added. Following overnight incubation in the dark at 20 °C with slow mixing, unbound dye was removed from the mixture using a PD midiTrap G-25 column (GE Healthcare), eluting into 1.5 mL of 50 mM potassium phosphate buffer, pH 8.0. When the bacteriophage was labelled with both Cy3 and Cy5, the same protocol was followed, simultaneously adding half the concentrations of each dye as above. When both dyes were bound to the mutant, each dye was diluted to 4 mg.mL⁻¹ before addition to the bacteriophage to account for the increased conjugation capacity of the mutant expressing an additional dye-binding site per pVIII subunit.

Alexa Fluor 555 C₂-maleimide or 647 C₂-maleimide was dissolved in DMSO to 1.19 mg.mL⁻¹. To 1 mL of a 2 mg.mL⁻¹ solution of M13 bacteriophage in 50 mM potassium phosphate buffer, pH 8.0, 74 µL of a 20 mg.mL⁻¹ solution of N-succinimidyl S-acetylthioacetate (SATA) in DMSO was added (20-fold molar excess of SATA to M13 major coat protein pVIII). Following incubation for one hour at room temperature, 100 µL of 2.5 M hydroxylamine and 50 mM ethylenediaminetetraacetic acid (EDTA) in 50 mM potassium phosphate buffer pH 8.0 was added to quench the remaining SATA. The thiolated M13 was then separated from unbound reagents using a PD-10 de-salting column (GE Healthcare), eluting into 3.5 mL of 50 mM potassium phosphate, 150 mM NaCl, 5 mM EDTA, pH 7.0 (conjugation buffer), following manufacturer's instructions. The eluate was then diluted with 7 mL of conjugation buffer and to this, 210 µL of dye solution was added. The mixture was incubated for one hour in the dark at room temperature. To block free thiol groups, after the incubation with the dye, 80 µL of a 10 mg.mL⁻¹ solution of N-ethylmaleimide in deionised water was added to the mixture and allowed to incubate for 15 minutes in the dark at room temperature. To remove unbound reagents, polyethylene glycol (PEG) precipitation was performed. To the reaction mix, 5.5 mL of 25 % PEG 6000 and 2.5 M NaCl in deionised water was added, before incubation at 4 °C in the dark for one hour to precipitate the M13-dye conjugate. The sample was then separated into 1.5 mL microcentrifuge tubes and centrifuged in a desktop centrifuge at full speed for 10 minutes. The supernatants were discarded and the pellets, containing the M13-dye conjugate, were suspended in a total volume of 2 mL of phosphate buffer.

M1.3.6. Bacteriophage-dye conjugate linear dichroism measurements

All bacteriophage-dye conjugate samples were diluted in 50 mM potassium phosphate buffer, pH 8.0. All LD measurements on the conjugates were made using a DIOP-0002 Ultra Low Volume Flow Linear Dichroism Accessory (non-thermostatted) (Dioptica Scientific, Rugby, UK), a 0.5 mm path length homemade quartz Couette cell rotating at 3000 rpm and a Jasco J-1500 Circular Dichroism Spectrometer with the parameters set to those detailed in the Supporting information (Table M1.S1). All samples were baselined against 50 mM potassium phosphate buffer, pH 8.0 rotating at 3000 rpm.

M1.3.7. Bacteriophage mutagenesis

Mutations were introduced to the bacteriophage following standard site-directed mutagenesis procedures using: pVIII_F (3' CTGTCTTTCGCTG**AGGAGAA**GACGATCCCG 5') and pVIII_R (3' CGGGATCGTCTT**TCTCCT**CAGCGAAAGACAG 5') mutagenic primers (altered nucleotides in bold; Tridgett *et al.*, 2018); M13KE vector (New England Biolabs) as template; and pfu polymerase (Promega).

M1.3.8. Bacteriophage-dye conjugate fluorescence measurements

Neat bacteriophage variants labelled with Cy3 and Cy5 in 50 mM potassium phosphate buffer, pH 8.0 were loaded into a DIOP-0002 Ultra Low Volume Flow Linear Dichroism Accessory (non-thermostatted) (Dioptica Scientific, Rugby, UK) in a 0.5 mm path length homemade quartz Couette cell either stationary or rotating at

3000 rpm. Samples were illuminated using a Jasco J-1500 Circular Dichroism Spectrometer set at 540 nm with a 9 nm bandwidth. Fluorescence in the range of 250-700 nm was collected using an Ocean Optics HR2000+ CCD detector with a 1000 μm fibre optic cable attachment. The fibre optic cable was positioned to collect light at 100° from the incident light at the front face of the Couette cell. Spectra were recorded using Ocean Optics SpectraSuite software with an integration time of 6 s and a total accumulation of 24 scans. Spinning and non-spinning samples were baseline subtracted and are presented with a 4 nm 0th order Savitzky-Golay smoothing window. Error bars correspond to the standard deviation of measurements made in triplicate.

M1.4. Results and Discussion

All of the dyes used in this work are based on the same chromophore: Cyanines 3 and 5 (Cy3 and Cy5, respectively), and Alexa Fluors 555 C₂-maleimide and 647 C₂-maleimide (AF555 and AF647, respectively) are all based on the cyanine chromophore as illustrated in Figure M1.1. AF555 is a proprietary dye whose structure is not in the literature. We therefore determined the mass of the dye (953.21 Da) and compared it to data on this dye family published in the patent database (Molecular Probes, 2001). This allowed us to assign the structure to the AF555 shown in Figure M1.1 e. Using the stretched-PE^{ox} film LD technique developed by Razmkhah *et al.* (2014a) we have characterised the transition dipole moment polarisations of the dyes in Figure M1.1 and used this information to infer their orientations when bound to M13 bacteriophage using the microvolume Couette cell LD technique developed by Marrington *et al.* (2004).

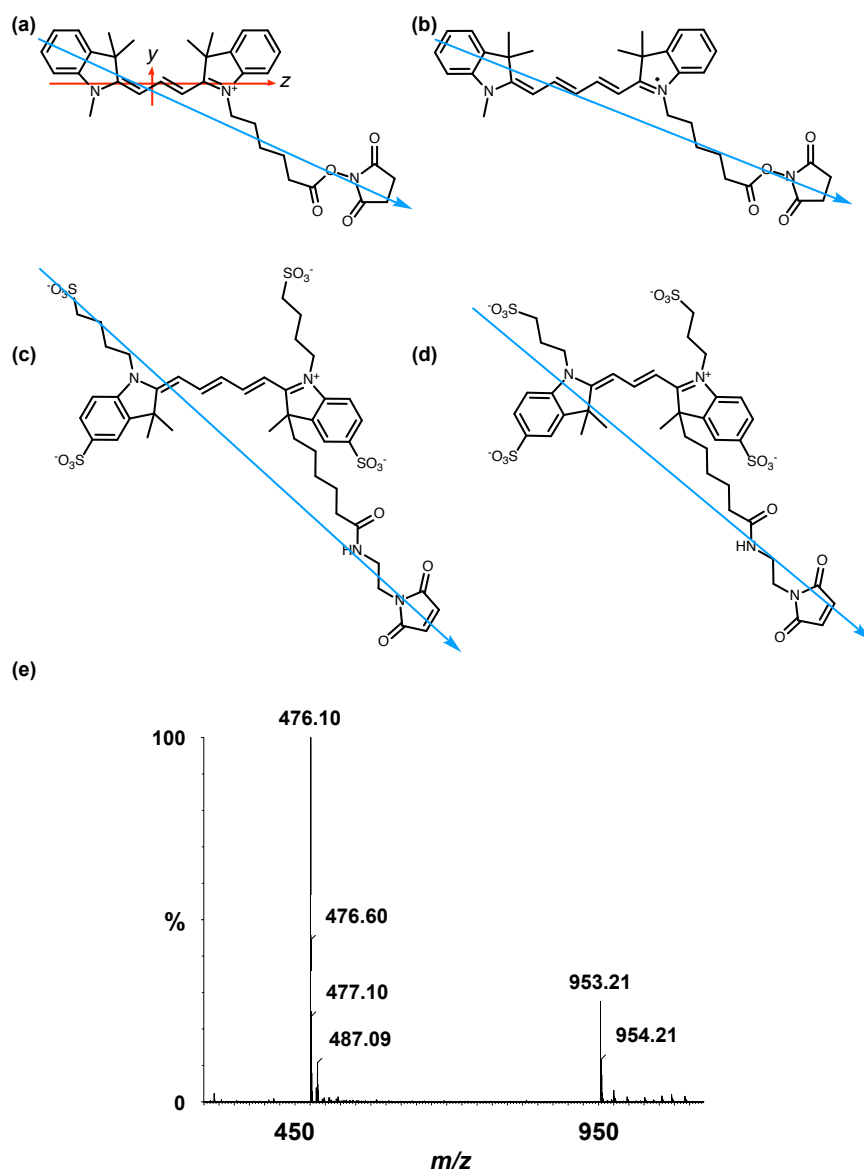


Figure M1.1. Dye structures. Molecular long axes denoted by blue arrow. (a) Cyanine3 NHS ester with long and short axes of the cyanine chromophore denoted with z and y , respectively. (b) Cyanine5 NHS ester. (c) Alexa Fluor 647 C₂-maleimide. (d) Alexa Fluor 555 C₂-maleimide. (e) Mass spectrum of Alexa Fluor 555 C₂-maleimide.

The dye orientation axis on the films is approximately the long axis illustrated in Figure M1.1. As we orient the film stretcher so the long axis is horizontal, a positive signal means the transition polarisation is less than 54.7° from this axis. Since

symmetry dictates that the dye chromophores have transitions approximately either along z or y (Figure M1.1 a). Bringing these two together, we can assign positive LD signals to z polarisation.

M1.4.1. Cyanine3 NHS ester

Figure M1.2 a shows an overlay of Cy3 absorbance in solution, on film with a mainly monomer population (0.025 mg.mL^{-1}) (see LD discussion below), on film with a mixture of monomers and oligomeric structures (0.2 mg.mL^{-1}), and Cy3 on the bacteriophage (M13Cy3). The wavelength of maximum absorption (λ_{max}) of Cy3 was bathochromically shifted relative to aqueous solution by 11 nm for M13Cy3, by 18 nm for the film monomer (deposited from 0.025 mg.mL^{-1}), and by 27 nm for the oligomeric structures on the film reflecting the increasing hydrophobicity of the Cy3 environments.

When Cy3 was deposited onto PE^{ox} after it had been stretched, the LD spectrum varied with stock solution concentration and contained bands that did not always correlate with the absorbance spectra: there were two negative bands at 505 nm and 547 nm and two positive bands at 445 nm and 585 nm in the LD spectra and just two bands at 527 nm and 570 nm in the absorbance spectra (data not shown) with different shaped spectra being observed for different amounts of sample deposited. The inconsistency of the wavelength and number of bands in the absorbance and LD spectra is consistent with the formation of higher order (at least dimeric) dye oligomers, albeit of unknown packing mode (Razmkhah *et al.*, 2014b). When $30 \mu\text{L}$ of 0.025 mg.mL^{-1} Cy3 was deposited onto un-stretched PE^{ox} and then stretched after

the dye had dried (Figure M1.2 b) stepwise from unstretched (though with manufacturer's stretching) to 1.8x, the LD spectrum changed to produce an LD spectrum that more closely represented the shape of the absorbance spectrum on film (Figure M1.2 b), with two positive transitions at 522 nm and 561 nm. This change in LD with stretch factor suggests the disruption of dye oligomers to produce a population of more monomeric dye close to the orienting environment of the film surface. The LD of Cy3 deposited from 0.025 mg.mL^{-1} at 1.8x stretch was closest to the absorbance in shape but still had a sloping LDr spectrum, which can be flattened by subtracting a small fraction (0.07) of the 0.1 mg.mL^{-1} spectrum. Thus we conclude that the Cy3 is still somewhat oligomeric near the film even at full stretch from 0.025 mg.mL^{-1} . As the monomers will align with the long axis of the dye with the stretch direction, and the cyanine chromophore long axis is about 30° (much less than the magic angle of 54.7°) from the stretch direction we can conclude that the Cy3 band between 450 and 600 nm is polarised along the cyanine long axis.

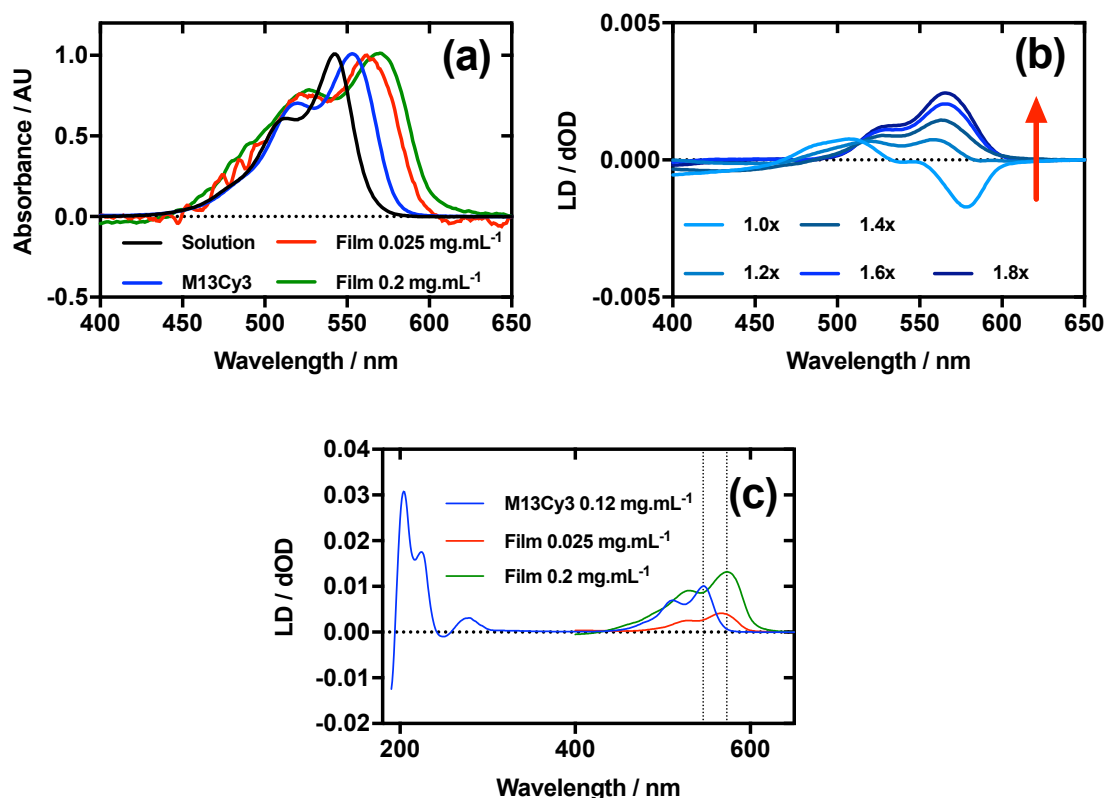


Figure M1.2. Linear dichroism spectra of Cyanine3 NHS ester and M13 bacteriophage Cy3 conjugate (M13Cy3). (a) Absorbance spectra of 2 $\mu\text{g.mL}^{-1}$ Cy3 in 50 mM potassium phosphate buffer, pH 8.0, dried onto PE^{ox} film from 0.2 mg.mL^{-1} and 0.025 mg.mL^{-1} solutions in 70:30 chloroform:methanol, and bound to M13 bacteriophage (M13Cy3) at 0.12 mg.mL^{-1} in 50 mM potassium phosphate buffer, pH 8.0. (b) Stretched-film LD spectra of Cy3 at 0.025 mg.mL^{-1} , with increasing stretch factor of the film as indicated in the figure. Stretching was performed after deposition and drying of the dye. (c) Couette LD spectrum of M13Cy3 conjugate at concentration indicated in the figure in 50 mM potassium phosphate buffer, pH 8.0, and film LD spectrum of Cy3 from 0.025 mg.mL^{-1} and 0.2 mg.mL^{-1} solutions in 70:30 chloroform:methanol, with the film being stretched after deposition and drying of the dye sample.

Following the conjugation of Cy3 to M13 bacteriophage, the LD spectrum of the conjugate was measured, revealing the UV-region bands previously shown to be attributable to the bacteriophage as well as bands that the stretched-film experiments demonstrated were attributable to the Cy3 cyanine chromophore long axis (Clack and Gray, 1992). As Cy3 is too small to flow align by itself, its LD signal in the

Couette setup (Figure M1.2 c) indicates successful conjugation. When the LD spectra of M13Cy3 at 0.015 mg.mL^{-1} and 0.12 mg.mL^{-1} are normalised at the wavelength of maximum LD ($\lambda_{LD_{max}}$) in the region attributable to Cy3 (561 nm), the spectra match almost exactly (data not shown), indicating no formation of oligomeric dye structures or dye driven M13 assembly, and indicating that standard interpretation of the LD spectra may be applied even at the highest concentration used, which was not the case for the film LD experiment. The bacteriophage is known to align with its long axis in the direction of the applied flow, which in our setup was the same orientation as the stretch direction of the film. As the Cy3 bands are again positive, we conclude that Cy3 was bound with the long axis of its cyanine chromophore polarised more parallel than perpendicular to the long axis of M13 bacteriophage (Figure M1.2 c).

M1.4.2. Cyanine5 NHS ester

Figure M1.3 a shows an overlay of Cy5 absorbance in solution, on film with a mainly monomer population (0.025 mg.mL^{-1}), on film with a mixture of monomers and oligomeric structures (0.2 mg.mL^{-1}), and Cy5 on the bacteriophage (M13Cy5). The $\lambda_{A_{max}}$ of Cy5 was bathochromically shifted relative to aqueous solution by 12 nm for M13Cy5, by 18 nm for the film monomer (deposited from 0.025 mg.mL^{-1}), and by 27 nm for the oligomeric structures on the film reflecting the increasing hydrophobicity of the Cy5 environments.

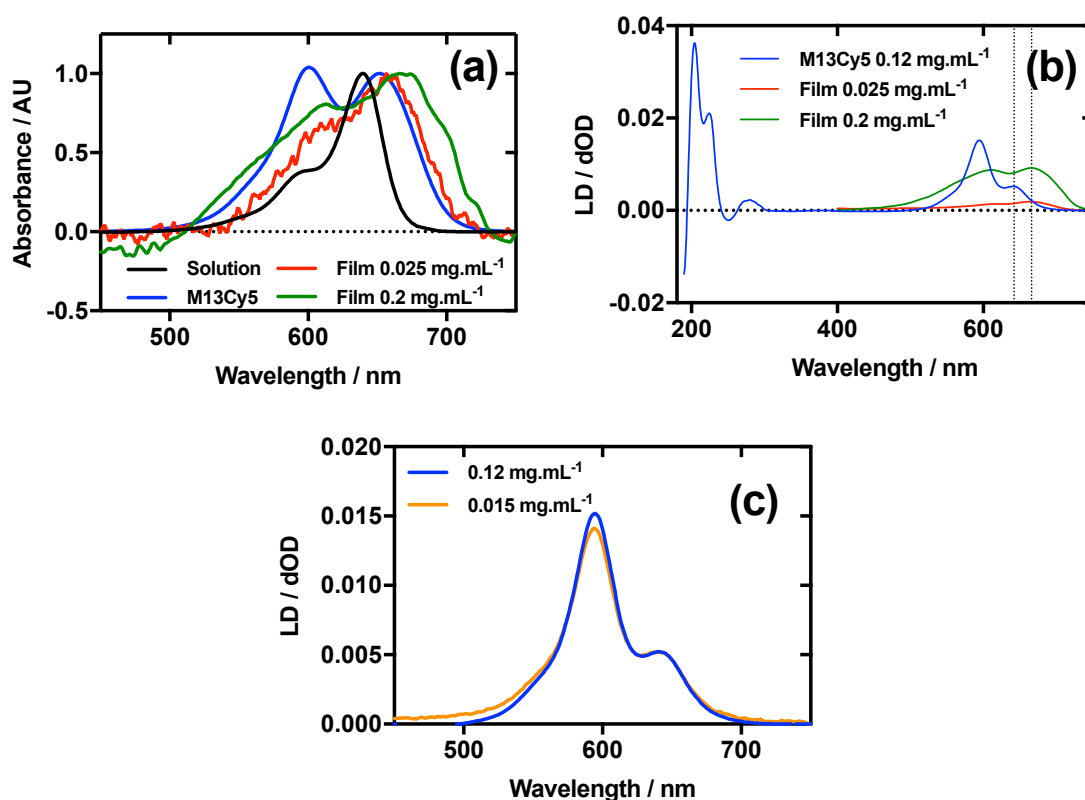


Figure M1.3. Linear dichroism spectra of Cyanine5 NHS ester and M13 bacteriophage Cy5 conjugate (M13Cy5). (a) Absorbance spectra of 2 $\mu\text{g.mL}^{-1}$ Cy5 in 50 mM potassium phosphate buffer, pH 8.0, dried onto PE^{ox} film from 0.2 mg.mL^{-1} and 0.025 mg.mL^{-1} solutions in 70:30 chloroform:methanol, and bound to M13 bacteriophage (M13Cy5) at 0.12 mg.mL^{-1} in 50 mM potassium phosphate buffer, pH 8.0. (b) Couette LD spectrum of M13Cy5 at concentration indicated in the figure in 50 mM potassium phosphate buffer, pH 8.0, and film LD spectra of Cy5 from 0.2 mg.mL^{-1} and 0.025 mg.mL^{-1} solutions in 70:30 chloroform:methanol, with the film being stretched after deposition and drying of the dye sample. (c) LD spectra of M13Cy5 normalised at 651 nm, at concentrations indicated in the figure.

The dye bound to the bacteriophage appears to be more H-aggregated than the other samples measured, as indicated by the large peak at 600 nm, which is only present as a shoulder in the other samples. The larger relative magnitude of this band in the 0.2 mg.mL^{-1} film spectrum relative to 0.025 mg.mL^{-1} supports this interpretation. As free dye was removed from the solution after conjugation, the H-aggregates are assumed to form either between adjacent covalently bound Cy5

groups on the same virion or between Cy5 groups each bound to different virions. The 0.025 mg.mL^{-1} stretched-film LD spectrum has two positive bands at 609 nm and 666 nm (Figure M1.3 b), approximately matching the film absorbance spectrum, which also has two bands at 609 nm and 657 nm (Figure M1.3 a and b). As monomeric Cy5 will align with the long axis of the dye with the stretch direction, and the cyanine chromophore long axis is about 30° (much less than the magic angle of 54.7°) from the stretch direction, we can conclude that the Cy5 band between 500 and 700 nm is polarised along the cyanine z-axis.

Following the conjugation of Cy5 to M13 bacteriophage, the LD spectrum of the conjugate was measured, as with Cy3, revealing the UV-region bands previously shown to be attributable to the bacteriophage as well as bands that the stretched-film experiments demonstrated were attributable to the Cy5 cyanine chromophore z-axis (Clack and Gray, 1992). As Cy5 is too small to flow align, its LD signal in the Couette setup indicates successful conjugation. In contrast to Cy3, when the LD spectra of M13Cy5 at 0.015 mg.mL^{-1} and 0.12 mg.mL^{-1} are normalised at the λA_{max} in the region attributable to Cy5 (651 nm), the spectra do not match perfectly, indicating the formation of oligomeric dye structures, and indicating that the standard interpretation of the LD spectra may not be applied at the highest concentration used, similar to the film LD experiment (Figure M1.3 c). The Cy5 bands are again positive, indicating that Cy5 was bound with the long axis of its cyanine chromophore polarised more parallel than perpendicular to the long axis of M13 bacteriophage (Figure M1.3 b) similar to the Cy3 case. However, its longer length linker has facilitated dye stacking. If the dye aggregates comprised dye groups bound to different virions, a loss of LD in the

bacteriophage region compared to the other M13-dye conjugates would be expected due to the formation of multi-virion assemblies. However, this is not seen here so it is concluded that the dye aggregates are formed between dye groups on the same virion.

M1.4.3. Alexa Fluor 555 C₂-maleimide

Figure M1.4 a shows an overlay of AF555 absorbance in solution, on film at low loading concentration (0.05 mg.mL^{-1}), on film at high loading concentration (0.2 mg.mL^{-1}), and AF555 on the bacteriophage (M13AF555). The $\lambda_{A_{\max}}$ of AF555 on M13 bacteriophage was not shifted relative to aqueous solution, whereas it was bathochromically shifted by 20 nm for the low concentration film and 20 nm for the high concentration film reflecting the increasing hydrophobicity of these AF555 environments.

When a 0.4 mg.mL^{-1} solution of AF555 was deposited onto un-stretched PE^{OX}, which was then stretched after drying, the resulting LD spectrum did not correlate closely to the absorbance spectrum: the LD spectrum had two negative bands at 524 nm and 561 nm, and one positive band at 590 nm, whereas the absorbance spectrum had two bands at 530 nm and 571 nm (data not shown). The inconsistency in number and wavelength of the bands suggested aggregation of the dye. However, upon dilution of AF555 to concentrations of 0.2 mg.mL^{-1} and lower, the resulting LD spectrum was similar in appearance to the film absorbance spectrum (Figure M1.4 b): The stretched-film LD spectrum had two positive bands at 531 nm and 572 nm, matching the film absorbance spectrum, which also had two bands at 531 nm and

572 nm (Figure M1.4 a and b). As monomeric AF555 will align the long axis of the dye with the stretch direction, and the cyanine chromophore long axis is about 30° (much less than the magic angle of 54.7°) from the stretch direction, we can conclude that the AF555 band between 450 and 600 nm is once again polarised along the cyanine long axis.

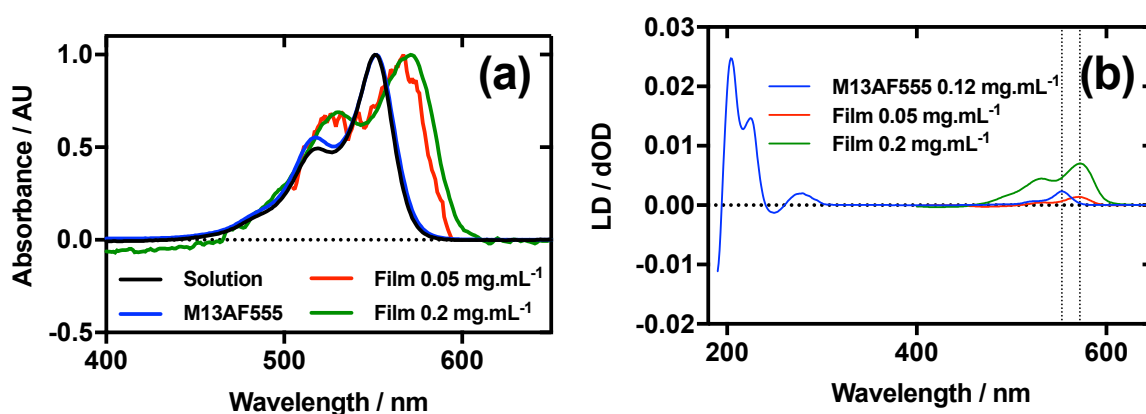


Figure M1.4. Linear dichroism spectra of Alexa Fluor 555 C₂-maleimide and M13 bacteriophage AF555 conjugate (M13AF555). (a) Absorbance spectra of $2 \mu\text{g.mL}^{-1}$ AF555 in 50 mM potassium phosphate buffer, pH 8.0, dried onto PE^{ox} film from 0.2 mg.mL^{-1} and 0.05 mg.mL^{-1} solutions in 70:30 chloroform:methanol, and bound to M13 bacteriophage (M13AF555) at 0.12 mg.mL^{-1} in 50 mM potassium phosphate buffer, pH 8.0. (b) Couette LD spectrum of M13AF555 at concentration indicated in the figure in 50 mM potassium phosphate buffer, pH 8.0, and film LD spectra of AF555 from 0.2 mg.mL^{-1} and 0.05 mg.mL^{-1} solutions in 70:30 chloroform:methanol, with the film being stretched after deposition and drying of the dye sample.

Following the conjugation of AF555 to M13 bacteriophage, the LD spectrum of the conjugate was measured, again revealing the UV-region bacteriophage-attributable bands as well as bands that the stretched-film experiments demonstrated were attributable to the AF555 cyanine chromophore long axis (Clack and Gray, 1992). As AF555 is too small to flow align, its LD signal in the Couette setup indicates successful conjugation. When the LD spectra of M13AF555 at 0.015 mg.mL^{-1} and

0.12 mg.mL⁻¹ are normalised at the $\lambda_{LD_{max}}$ in the region attributable to AF555 (553 nm), the spectra match almost exactly, indicating no formation of oligomeric dye structures, and indicating that standard interpretation of the LD spectra may be applied at the highest concentration used. The AF555 bands are again positive, indicating that AF555 was bound with the long axis of its cyanine chromophore polarised more parallel than perpendicular to the long axis of M13 bacteriophage (Figure M1.4 b).

M1.4.4. Alexa Fluor 647 C₂-maleimide

Figure M1.5 a shows an overlay of AF647 absorbance in solution, on film at low loading concentration (0.02 mg.mL⁻¹), on film at high loading concentration (0.2 mg.mL⁻¹), and AF647 on the bacteriophage (M13AF647). The $\lambda_{A_{max}}$ of AF647 on M13 bacteriophage was not shifted relative to aqueous solution, whereas it was bathochromically shifted by 11 nm for the low concentration film and 19 nm for the high concentration film, reflecting the increasing hydrophobicity of the environment in which AF647 is located. When AF647 was deposited onto PE^{ox} after it had been stretched, at concentrations ranging from 0.02 to 0.2 mg.mL⁻¹, the resulting LD spectra did not correlate with the corresponding absorbance spectra (Figure M1.5 c). While the LD spectra had two positive transitions at 532 nm and 700 nm, and two negative transitions at 607 nm and 651 nm (Figure M1.5 c), the absorbance spectrum of film-dried AF647 had only two transitions at 619 nm and 668 nm (Figure M1.5 a). The discrepancy in the number and wavelength of transitions in the spectra suggests the formation of AF647 assemblies and the consequent exciton interactions, resulting in positive/negative LD couplets about the absorbance

maxima. A similar effect was observed for Cy3 when deposited after the film was stretched, and for AF555 when deposited at 0.4 mg.mL^{-1} . For Cy3, this effect was removed by stretching the film after drying rather than before drying (Figure M1.2 b), and for AF555 this was removed by dilution, however these approaches were not effective for AF647 (Figure M1.5 b and c), thus it was not possible to determine the polarisation of the transition dipole moments of monomeric AF647 directly from the stretched-film LD data. However, as AF647, Cy3, Cy5 and AF555 share the cyanine chromophore, it can be inferred that the transition dipole moment of monomeric AF647 between 500 nm and 750 nm is polarised along the z-axis of the AF647 cyanine chromophore.

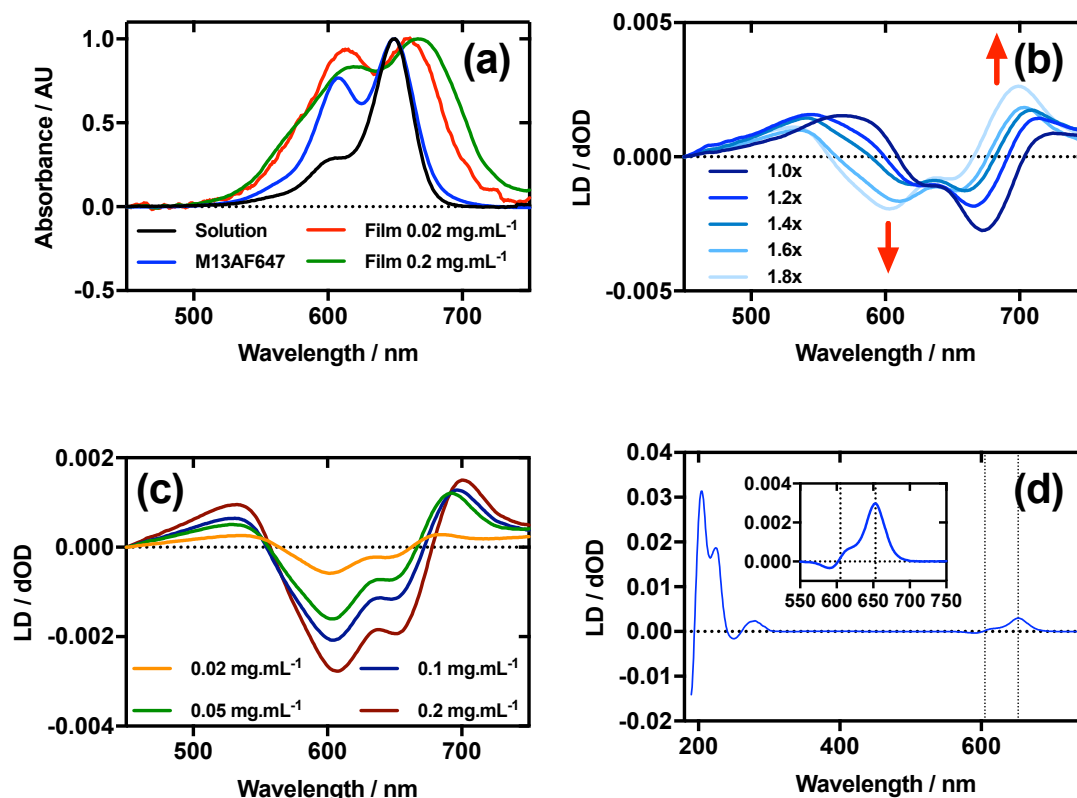


Figure M1.5. Linear dichroism spectra of Alexa Fluor 647 C₂-maleimide and M13 bacteriophage AF647 conjugate (M13AF647). (a) Absorbance spectra of 2 $\mu\text{g.mL}^{-1}$ AF647 in 50 mM potassium phosphate buffer, pH 8.0, dried onto PE^{ox} film from 0.2 mg.mL^{-1} and 0.02 mg.mL^{-1} solutions in 70:30 chloroform:methanol, and bound to M13 bacteriophage (M13AF647) at 0.12 mg.mL^{-1} in 50 mM potassium phosphate buffer, pH 8.0. (b) Stretched-film LD spectra of AF647 at 0.025 mg.mL^{-1} , with increasing stretch factor of the film as indicated in the figure. Stretching was performed after deposition and drying of the dye. (c) Stretched-film LD spectra of AF647 at concentrations indicated in the figure, stretching the film before dye deposition and drying. (d) Couette LD spectrum of M13AF647 at the concentration indicated in the figure in 50 mM potassium phosphate buffer, pH 8.0. Inset: bands attributable to AF647.

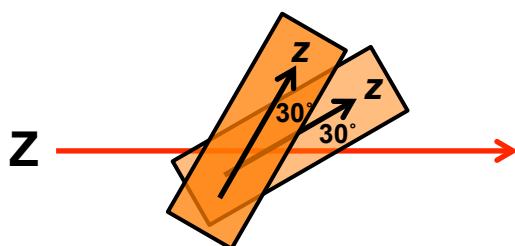


Figure M1.6. Proposed dimer geometry of Alexa Fluor 647. Z = orientation axis; z = cyanine chromophore long axis.

Following the conjugation of AF647 to M13 bacteriophage (M13AF647), the LD spectrum of the conjugate was measured, again revealing the UV-region bacteriophage-attributable bands as well as bands attributable to the AF647 cyanine chromophore z-axis (Clack and Gray, 1992). As AF647 is too small to flow align, its LD signal in the Couette setup indicates successful conjugation. When the LD spectra of M13AF647 at 0.015 mg.mL^{-1} and 0.12 mg.mL^{-1} are normalised at the $\lambda_{\text{LD}_{\text{max}}}$ in the region attributable to AF647 (652 nm), the spectra match almost exactly, indicating no change in dye oligomerisation over the range of concentrations tested. However, as the absorbance spectra indicate the presence of dye oligomers (at least dimers), the standard interpretation of LD is not applicable. The AF647 bands at 615 and 653 nm are positive, indicating that they are polarised more parallel than perpendicular to the long axis of M13 bacteriophage (Figure M1.5 d). However, the band at 590 nm is negative indicating that this transition is polarised more perpendicular than parallel to the bacteriophage long axis.

The wavelengths of the Couette LD signals suggest that at least some of the phage-bound dyes are managing to π - π stack. Given our inability to force AF647 on the films into monomeric form, it is clear that they have more affinity for each other than the dyes discussed above. So whether the π - π stacked dyes are all covalently bound or some covalent and some non-covalent we cannot determine. While the mode of packing of these dye assemblies is unknown, it is interesting to speculate about the geometry a dimer of AF647 might adopt to give rise to such patterns. One option is illustrated in Figure M1.6, where dimers contain one AF647 molecule with its cyanine

long axis (z) approximately 30° to the orientation axis (Z), and another AF647 molecule with its z-axis approximately 30° to the z-axis of the first.

Although only a small number of dyes were studied here, it is interesting to note any observed trends in the relationship between chemical structure and linear dichroism properties. We have noted in our laboratory in previous works that certain dyes either exhibit no LD or very weak LD when bound to M13 bacteriophage in the setup demonstrated here. These dyes include 4-chloro-7-nitrobenzofurazan (NBD-Cl), tetramethylrhodamine isothiocyanate (TRITC) and fluorescein isothiocyanate (FITC) (Sandhu, 2015). These three dyes all have structures that are less elongated than the cyanines studied here, which could explain their weaker tendency to align on the bacteriophage. Interestingly however, no trend was observed here between the length of the dye molecules and their LDr values at wavelength of maximal absorbance, indicating that there are other factors that affect alignment, which are not apparent from the small number of dyes studied here. It was observed, however, that all dyes tested (except AF647 as monomerisation could not be achieved) exhibited stronger LDr when aligned using film than bacteriophage, with values of the order of 0.15-0.23 and 0.03-0.09, respectively. This discrepancy could reflect the fact that the dyes bound to the bacteriophage are in solution and thus are less rigidly aligned than the dyes dried onto film.

M1.4.5. LD to inform FRET optimisation

It is well established that Förster resonance energy transfer (FRET) efficiency is dependent on the alignment of the TDMs of the donor and acceptor groups thus it

was reasoned that optimisation of dye arrays used to create biomimetic light-harvesting antennae would require alteration of the surface geometry of the scaffold used as well as alteration of the separation of the donors and acceptors (Lakowicz, 2010). To monitor the relative alignment of the donor/acceptor TDMs, LDr could be measured. Theoretically, if the two dyes' TDMs were polarised to the same axis, their LDr values would be equal so the ratio of the two would be 1, and their FRET efficiency would be maximised at the given distance. This would be advantageous to monitor during optimisations, as when only FRET is measured, effects on FRET efficiency due to donor-acceptor misalignment, rather than separation, cannot be measured directly.

To demonstrate this, we used an M13 mutant with Lysine at position 3 in pVIII coat protein, and therefore an additional alternative conjugation site for dyes to bind (Tridgett *et al.*, 2018). It was therefore expected that the mutant should bind dyes in two different orientations (and wild type only one, the amino-terminus of the bacteriophage major coat protein), and therefore should have lower correlation in LDr of the two dyes bound and therefore lower FRET efficiency than wild type even when the donor and acceptor groups are bound to the same extent to the two bacteriophage variants.

As LD is measured under shear flow to align the bacteriophage, FRET was also measured under shear flow to ensure that the alignment of the dyes relative to the bacteriophage and to each other was the same for both measurements. FRET was also measured in non-aligning conditions i.e. with no shear flow, to ascertain whether

there was an alteration in the dye alignment upon application of shear flow, which would be indicated by any alteration in FRET.

The results of this experiment indicate that even though the wild type and mutant bacteriophages bound Cy3 and Cy5 (donor and acceptor, respectively) to the same extent (Figure M1.7 a), the LD signals of the dyes were clearly different, resulting in different LDr in the regions attributable to Cy3 and Cy5 (Figure M1.7 b). When the ratio of LDr at 550 nm (Cy3) and 650 nm (Cy5) ($LDr^{550/650}$) is calculated, the result for wild type is 1.9 and the result for the mutant is 2.9 (Figure M1.7 d). The ideal situation, i.e. when the TDMs of the donor and acceptor are aligned about the same axis, would result in an $LDr^{550/650}$ of 1, thus in this case the dyes bound to the wild type are more similarly aligned than those on the mutant. It would thus be expected that the FRET efficiency of the dyes on the wild type would be greater than that of the dyes on the mutant. When the FRET was measured in aligning conditions (Figure M1.7 c, 3000 rpm) and the FRET efficiency was calculated, this was indeed the case. The fluorescence spectra of the two variant conjugates revealed greater fluorescence intensity due to the acceptor (Cy5; band at 660 nm) in the wild type than the mutant (Figure M1.7 c), indicating higher FRET efficiency. To quantify the difference, relative FRET efficiency ($E_{rel} = I_{650} / (I_{550} + I_{650})$, where I is the fluorescence intensity at the wavelength indicated by the subscript number) was calculated (Figure M1.7 e, 3000 rpm), revealing that the E_{rel} of the dyes bound to wild type was significantly higher ($p < 0.0001$) than that of those on the mutant, with values of 0.31 ± 0.02 and 0.25 ± 0.002 , respectively, a 24.9 % loss of FRET efficiency attributable, by measuring LD, to donor-acceptor misalignment.

When FRET was measured in non-aligning conditions (Figure M1.7 c and e, 0 rpm), the band attributable to the acceptor dye, Cy5 (660 nm), was less intense than under shear flow. This was the case for both mutant and wild type bacteriophages. The absolute difference in E_{rel} between the wild type and the mutant in non-orienting conditions was the same as under shear flow, with both losing 0.06, indicating that the perturbation in FRET caused by the mutation is preserved in both conditions. The fact that there was a change in FRET upon application of shear flow indicates that the dyes can rotate relative to the bacteriophage scaffold. The fact that the FRET efficiency increased upon application of shear flow indicates that the dyes became better aligned relative to each other under shear flow. Combining the fact that the FRET efficiency increased upon application of shear flow and the observation that the dyes align with their long axes more parallel than perpendicular to the bacteriophage long axis (LD experiments under shear flow) suggests that the dyes become more highly aligned to the bacteriophage long axis upon application of shear flow. The behaviour of the dyes on the bacteriophage is thus analogous to that of a flag on a moving vehicle.

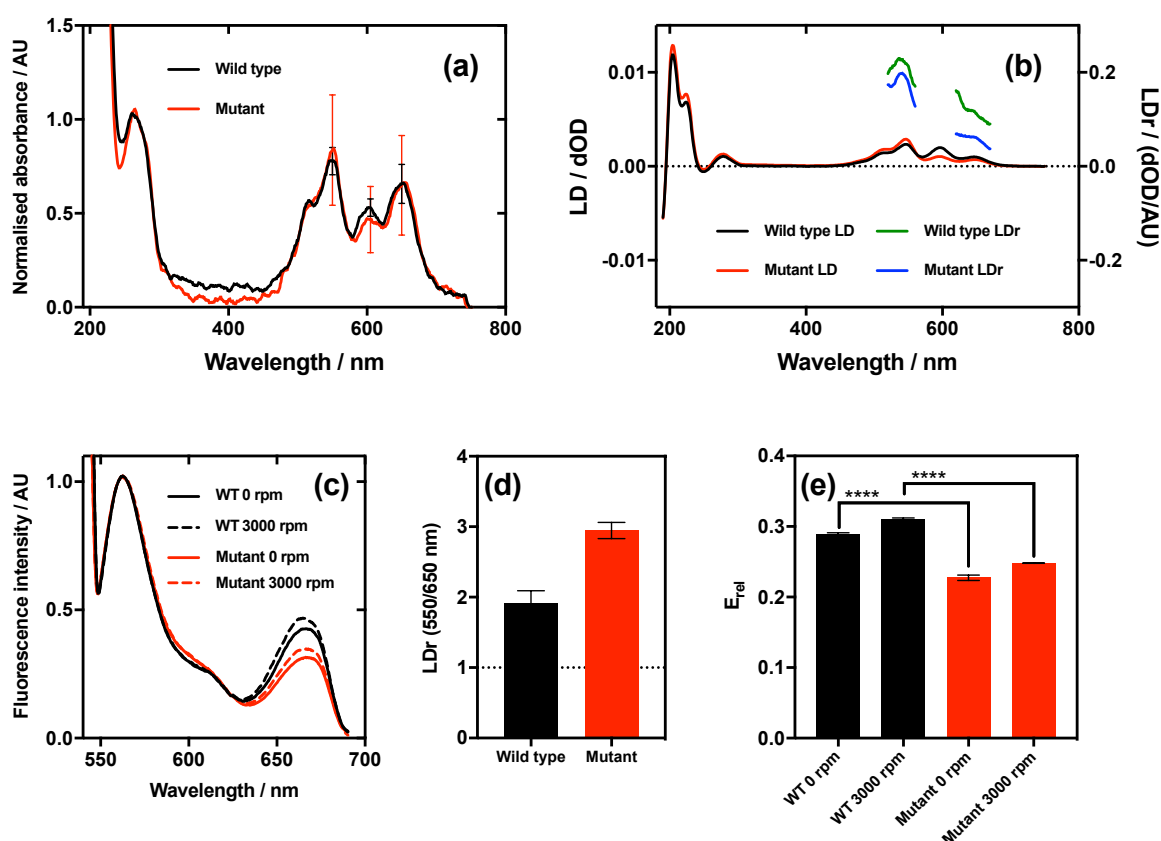


Figure M1.7. Relationship between dye relative alignment and FRET efficiency. (a) Absorbance spectra of wild type and mutant M13 bacteriophages labelled with Cy3 and Cy5. (b) LD and reduced LD (LDr) of wild type and mutant bacteriophage conjugates. (c) FRET emission spectra of wild type and mutant bacteriophage conjugates stationary (0 rpm) and under shear flow (3000 rpm). Band at 550 nm due to Cy3 (donor) emission, and band at 650 nm due to Cy5 (acceptor) emission. (d) Ratio of LDr at regions attributable to Cy3 and Cy5 (LDr 550/650 nm) of wild type and mutant bacteriophage conjugates. Line at ideal value of 1. (e) Ratiometric FRET efficiencies of dyes bound to wild type and mutant bacteriophages stationary and under shear flow.

M1.5. Conclusions

We have employed stretched-film LD spectroscopy on oxidised polyethylene to assign the TDM polarisations of a range of cyanine dyes. Following this we have been able to determine the alignment of the dyes when they are bound to M13 bacteriophage, a model linear scaffold for the generation of biomimetic light-harvesting antennae relying on FRET between donor and acceptor dyes. Furthermore, we have shown how LD spectroscopy may be used to distinguish between lack of FRET efficiency on the antennae due to dye separation and dye misalignment. This will enable rational design and optimisation of biomimetic light-harvesting antennae based upon linear scaffolds.

M1.6. Supporting information

Table M1.S1. Linear dichroism parameters

Parameter	Cy3	Cy5	Alexa Fluor 555	Alexa Fluor 647	M13Cy3	M13Cy5	M13AF555	M13AF647
Wavelength start / nm	650	750	650	750	650	750	650	750
Wavelength end / nm	190	190	190	190	190	190	190	190
Data interval / nm	1	1	1	1	1	1	1	1
Data pitch / nm	1	1	1	1	1	1	1	1
Digital integration time / s	1	1	1	1	1	1	1	1
Bandwidth / nm	2	2	2	2	2	2	2	2
Scanning speed / nm.min ⁻¹	200	200	200	200	200	200	200	200
Accumulations	2	2	2	2	2	2	2	2

3.6. Additional results

It was observed above that Cy5 and AF647 aggregated to a higher extent than the other dyes when bound to bacteriophage. Experiments were conducted to attempt to monomerise these bacteriophage-bound dyes and ascertain whether this affected their LD signal.

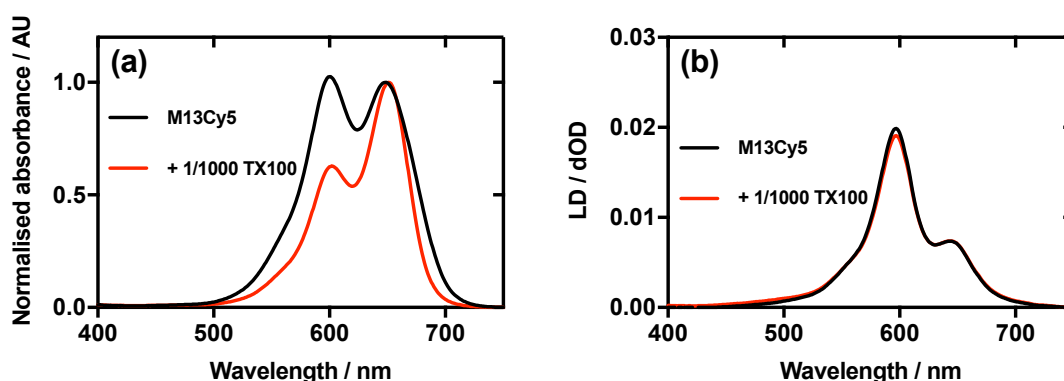


Figure 3.4. Disaggregation of Cy5 bound to M13 bacteriophage using Triton X-100. (a) Absorbance spectrum of $0.12 \text{ mg}\cdot\text{mL}^{-1}$ M13Cy5 before and after addition of Triton X-100 at a 1/1000 dilution. (b) LD spectrum of the same samples as in (a).

First, the absorbance and LD spectra of a $0.12 \text{ mg}\cdot\text{mL}^{-1}$ solution of M13Cy5 were measured, revealing in both cases a band at 651 nm and a more intense band at 600 nm. The presence and intensity of the H-band at 600 nm in the absorbance spectrum indicates dye aggregation (Figure 3.4). For comparison, an example spectrum of monomeric Cy5 can be found in Figure M1.3 a, in which the H-band is merely a shoulder on the main peak. Following the addition of Triton X-100 (TX100), the H-band at 600 nm in the absorbance spectrum was greatly reduced in intensity, indicating monomerisation of the dye (Figure 3.4 a). In contrast, there was very little change in the LD spectrum of the same sample (Figure 3.4 b). This indicates

negligible disruption to the orientation and mobility of the dyes bound to the bacteriophage during monomerisation.

The same experiment was conducted with M13AF647, which had proven to be the most difficult to monomerise throughout the experiments in Manuscript 1. The absorbance spectra during this experiment indicated very little change in the aggregation state of the dye bound to the bacteriophage even in the presence of twice the concentration of TX100 required to monomerise M13Cy5 (Figure 3.5). Likewise there was no change in the LD signal here.

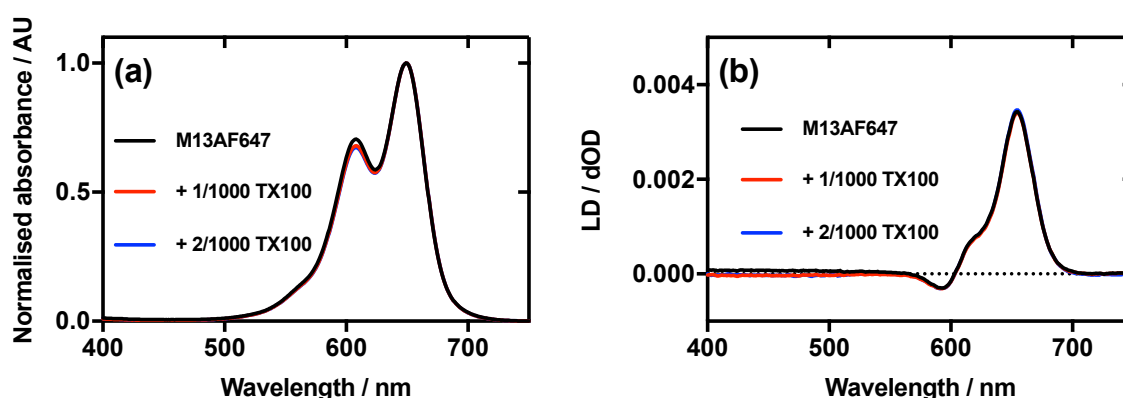


Figure 3.5. AF647 in the presence of Triton X-100. (a) Absorbance spectrum of 0.12 mg.mL^{-1} M13AF647 before and after addition of Triton X-100 at the concentrations indicated in the figure. (b) LD spectrum of the same samples as in (a).

3.7. Discussion

All the bacteriophage-bound dyes tested here exhibited strong LD in shear flow. This will enable further development of the Pacheco-Gómez assay. Specifically, it will enable development of multiplex assays and a reduction in equipment requirements.

It was observed previously, however, that some bacteriophage-bound dyes either exhibit very weak or no LD in shear flow (Sandhu, 2015). For example, 4-chloro-7-

nitrobenzofurazan (NBD-Cl), tetramethylrhodamine isothiocyanate (TRITC) and fluorescein isothiocyanate (FITC) do not exhibit strong LD on M13 bacteriophage. This is in contrast to the cyanines studied here. It is possible that because these molecules are less rod-like than the cyanine dyes they may have less rotational restriction on the bacteriophage. This would allow them to assume a larger number of orientations on the bacteriophage surface. As a consequence, these dyes would have a smaller S value (Equation 3.3) than the cyanines studied here, resulting in a smaller LD value.

The above explanation does not, however, account for the effects of shear flow. Figure M1.7, indicates that the orientations of the cyanine dyes in relation to the bacteriophage are affected by shear flow. It was concluded that the elongated cyanine dyes behave like flags on a moving vehicle. This model would explain why more-elongated dyes (i.e. the cyanines) would align with a higher S value on the bacteriophage than the lower aspect ratio dyes (NBD-Cl, TRITC and FITC). One would expect that the longer dyes would present a larger surface to generate drag than the shorter ones when in an unfavourable orientation (i.e. with their longest axis perpendicular to the long axis of the bacteriophage). This would cause the longer dyes to have a greater tendency to align than the shorter ones, and thus a stronger LD signal.

It has been established that the bacteriophage-bound cyanine dyes become better aligned relative to one another upon application of shear flow (Figure M1.7). It may thus be possible to further optimise FRET between donor/acceptor pairs. By

conjugating the dyes to a scaffold by groups on both ends of the cyanine moiety, one could rigidly align the dyes. This is in contrast to what was used here, where just one end was bound. This approach would restrict the rotation of the dyes when shear flow is not applied, as would be the case in normal use of these systems for light harvesting. This could enhance FRET efficiency but care would have to be taken to: (1) ensure that the dyes were bound in one defined orientation. This may be difficult to achieve due to the regular patterning of identical conjugation sites on the bacteriophage and on other linear scaffolds. For example, on the surface of M13 bacteriophage, six equivalent amine groups on adjacent pVIII subunits surround each N-terminal amine group of pVIII. These neighbouring groups are all between 27.0 Å and 33.5 Å from the central amine (PDB ID: 2MJZ; Morag *et al.*, 2015). It may therefore be challenging to design a bifunctionalised dye that bridges two amines in a preferential direction as all directions are highly similar; and (2) ensure that dually modified dyes do not bind two different scaffolds, as this would cause aggregation. This could be limited by performing conjugations at sufficient scaffold dilution.

During this study monomerisation of AF647 could not be achieved, either on film or on the bacteriophage. It was thought that this might indicate that it would not be a suitable candidate for use in the Pacheco-Gómez assay. It was reasoned that if the sample being analysed contained an agent that monomerised AF647, the LD signal would be altered, yielding an inaccurate reading. This was not the case, however. The results of the experiment in which TX100 was added to M13Cy5 indicate that the aggregation state of bacteriophage-bound dyes has little impact on the LD of said dyes. This indicates that samples containing compounds that disaggregate the dyes

would not cause erroneous results. This is advantageous for assay development as it means that dye choice is not limited to only dyes that have a low aggregation tendency.

In addition, the results of the experiment with M13Cy5 and TX100 provide information about the nature and orientation of the dye aggregates on the bacteriophage. Firstly, the data indicate that the Cy5 aggregates do not comprise a combination of M13-bound and free dyes. If this were the case one would expect that the dye LD would decrease significantly upon disaggregation as contributing dye molecules are released. This was not observed. In addition, the data indicate that the orientation of Cy5 on M13 is not significantly altered between its aggregated and disaggregated states. If it were altered, the concurrent change in α would result in a change in LD (Equation 3.3), which was not observed.

It is unclear why AF647 would dimerise more strongly than the other dyes tested here. There was a distinctly more pronounced dimerisation of AF647 and Cy5 compared to AF555 and Cy3 (Figures M1.2-4, absorbance spectra) when bound to the bacteriophage. The former two dyes each have a five-carbon polymethine bridge, whereas the latter two each have a three-carbon polymethine bridge. It is possible that this structural difference has an impact on the tendency of these molecules to aggregate. This is because molecules containing π orbitals are known to self-associate by π - π stacking: the polymethine bridge contains a number of π orbitals that is dependent on the length of the bridge. Thus a longer polymethine bridge could allow for more orbital overlap between two monomers and thus a higher tendency to

aggregate. However, Cy5 has a polymethine bridge of the same length as AF647 but could be monomerised on film. This indicates that polymethine chain length probably is not the sole determining factor in increased dimerisation tendency.

One could also envisage that the sulphonate groups, present on AF647 and AF555 but not Cy3 or Cy5, would prevent dimerisation by intermolecular like-charge repulsion. However in the case of AF647 this does not appear to be the case. AF647 dimerised more strongly than the other dyes, including those without sulphonate groups. It is possible that the sulphonate groups form an ionic bond with the positively charge nitrogen in the structure of AF647, resulting in a tight dimerisation. However, if this happened in AF647, one would also expect it to happen in AF555 based on the structure. As AF555 did not present the same issues as AF647 with respect to dimerisation, it seems unlikely that this is the cause of the tendency of AF647 to dimerise.

Overall, it is unclear why AF647 would have a greater tendency to aggregate than the other dyes studied here. In addition, the number of dyes examined is too low to observe any clear trends. The important observation from the TX100 experiments is that dye aggregation does not appear to affect LD, which is advantageous in development of the Pacheco-Gómez assay.

3.8. Conclusions

M13 bacteriophage has been demonstrated as a suitable scaffold for the alignment of small dyes in shear flow for the measurement of their linear dichroism. This will be important in the further development of the assay published by Pacheco-Gómez *et al.* (2012). This development will enable multiplex assay development, and miniaturisation, and therefore portability, of the assay. Furthermore, the use of LD spectroscopy in this way has been demonstrated as a possible tool for the optimisation of dye arrays on linear scaffolds. This could be useful in the development of *in vitro* biomimetic light-harvesting technologies.

**4. MUTATION OF M13 BACTERIOPHAGE MAJOR COAT
PROTEIN FOR INCREASED CONJUGATION TO
EXOGENOUS COMPOUNDS**

4.1. Introduction

It was demonstrated in the previous chapter that the use of visible-region dyes to extend the Pacheco-Gómez assay capability is viable. The next requirement was the optimisation of the signal from this approach.

The sensitivity and dynamic range of the Pacheco-Gómez assay is dependent on the LD signal strength. This in turn is dependent on the extent of bacteriophage labelling with dye. Maximisation of conjugation efficiency by bacteriophage mutation was thus investigated in this chapter.

In addition, limited conjugation efficiency has hindered development of a number of technologies reliant on M13 bacteriophage bioconjugation. Thus this project has scope beyond our laboratory, as is discussed in the introduction of Manuscript 2, below.

4.2. Project aims

It was the aim of this project to develop a strain of M13 bacteriophage that expresses a greater number of conjugation sites than the wild type. Such a variant would therefore have a greater conjugation capacity than the wild type. This would enable improvement of the dynamic range and sensitivity of the Pacheco-Gómez assay. In addition it would enable the improvement of other M13-based bioconjugates, as discussed in the manuscript introduction.

4.3. Manuscript number 2 (M2)

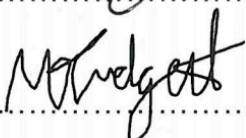
Mutation of M13 bacteriophage major coat protein for increased conjugation to exogenous compounds

Matthew Tridgett, James R. Lloyd, Jack Kennefick, Charles Moore-Kelly and Timothy R. Dafforn

Bioconjugate Chemistry, 2018, **29**, 1872-1875

Author contribution statement: JRL conducted mutant (G3K_{A1E}) bacteriophage preparation and dye conjugations to the same mutant strain. JK conducted experiments that ascertained that some mutants were non-viable. CMK assembled the autosampler used in the buffer optimisation. TRD was the lead supervisor. MT contributed all other aspects.

Signed:.......... Timothy R. Dafforn

Signed:.......... Matthew Tridgett

M2.1. Abstract

Over the past ten years there has been an increasing interest in the conjugation of exogenous compounds to the surface of M13 bacteriophage. M13 offers a convenient scaffold for the development of nano-assemblies with useful functions, such as highly specific drug delivery and pathogen detection. However, the progress of these technologies has been hindered by the limited efficiency of conjugation to the bacteriophage. Here we generate a mutant version of M13 with an additional lysine residue expressed on the outer surface of the M13 major coat protein, pVIII. We show that this mutation is accommodated by the bacteriophage and that up to a further 520 exogenous groups can be attached to the bacteriophage surface via amine-directed conjugation. These results could aid the development of high payload drug delivery nano-assemblies and pathogen detection systems with increased sensitivity.

M2.2. Introduction

M13 bacteriophage (M13) is a filamentous, nonlytic coliphage that was first isolated around fifty years ago (Hofschneider, 1963). M13 has a simple and highly efficient genome with only eleven genes, two of which overlap entirely with neighbouring genes whilst producing discrete gene products (Kokoska and Steege, 1998; Haigh and Webster, 1999; Rapoza and Webster, 1995; van Wezenbeek *et al.*, 1980). The coat of M13 comprises ~2700 copies of the major coat protein, pVIII and five copies each of the minor coat proteins pIII, pVI, pVII and pIX. The pVIII coat is arranged as stacked pentameric rings, giving M13 a cylindrical shape with a high aspect ratio of ~6 nm by ~1000 nm (Lee *et al.*, 2013; Marvin, 1998; Morag *et al.*, 2015). The 50

amino acid major coat protein, pVIII, is almost entirely alpha-helical and is arranged with its carboxyl-terminus associated with the single-stranded circular DNA at the core of the virion, and its amino-terminus surface-exposed (Armstrong *et al.*, 1983).

Functional groups within the pVIII coat of M13 can be targeted for the chemical conjugation of exogenous molecules to the bacteriophage to create nano-assemblies with non-biological functions (Bernard and Francis, 2014). For amine-directed conjugation, it is the amine group of the amino-terminus of pVIII, and to a lesser extent the ϵ -amine group of the lysine residue at position eight that are targeted for conjugation of exogenous compounds (Li *et al.*, 2010). Conjugated species include antibiotics (Yacoby *et al.*, 2006), anti-cancer drugs (Suthiwangcharoen *et al.*, 2011), chromophores (Li *et al.*, 2010; Carrico *et al.*, 2012; Hilderbrand *et al.*, 2008), NMR contrast agents (Palaniappan *et al.*, 2013), antibodies and aptamers. However each of these studies have identified a common issue with using M13. In all cases the level of conjugation to the virion surface limited the performance of the product. This limitation was starkly demonstrated in the use of M13 to target folate receptors on the surface of cancer cells by conjugating folate to the surface of M13. In this case multivalency was said to play a role in strengthening the bond between the conjugated molecules and their target (Li *et al.*, 2011), meaning that increasing conjugation of folate to the surface of the M13 would have increased the effectiveness of the reagent. We have observed the same limitation in our laboratory where we aim to use dye-labelled M13 as the basis of a diagnostics test (Pacheco-Gómez *et al.*, 2012). Our experience is that the number of dye molecules on the bacteriophage surface is directly related to the eventual sensitivity of the assay. We

have studied the conjugation of wild type M13 using the model dye 4-chloro-7-nitrobenzofurazan (NBD-Cl). NBD-Cl is a relatively small dye meaning that steric effects on conjugation should be kept to a minimum. Our studies have shown that conjugation efficiencies of approximately 1200 dye molecules per virion are the maximum that can be achieved. This result agrees with previous studies on this subject (Li *et al.*, 2011; Hilderbrand *et al.*, 2008). We suspect that this upper limit indicates that despite its small size NBD-Cl conjugation is still limited by steric hindrance from other side chains that surround the conjugation site.

As smaller dyes are not readily available one solution to this problem would be to introduce additional conjugation sites onto the surface. Presented here is a systematic study of the effect of substituting additional lysine residues into a variety of positions on the solvent-exposed face of pVIII. For each mutant the effect on viral viability is assessed and if the mutation is non-lethal then the conjugation efficiency is also quantified. Using this approach we were able to introduce an additional lysine residue – and thereby an additional ~2700 amine groups to the overall surface of M13 – to the amino-terminal region of bacteriophage M13 major coat protein pVIII (Figure M2.1), imparting an increased capacity for amine-directed conjugation of exogenous compounds. To prove the utility of this new mutant form of M13, conjugation of a range of dyes (including NBD-Cl, Cyanine3 (Cy3), Tetramethylrhodamine isothiocyanate (TRITC) and Cyanine5 (Cy5)) were tested for their conjugation efficiency to bacteriophage. These data showed that in all cases dye conjugation efficiency was improved in the mutant bacteriophage expressing an

mutations attempted during the production of mutant M13, we observed that all those that caused a net positive change in the charge of pVIII were nonviable (Table M2.1). This is a significant issue as the conjugation systems often used rely on the presence of the positively charged amine on the side chain of lysine. The observation of this abolition of viability is consistent with the findings of Schuenemann *et al.* (1999), who showed that prior to the assembly of M13 inside its host, the proton motive force across the inner membrane of *E. coli* inhibits the translocation of positively charged residues from the cytoplasm to the periplasm, thus preventing completion of the M13 replicative cycle when additional positive charge is added to the amino terminal region of pVIII.

Table M2.1. Effect of mutation on major coat protein charge and bacteriophage viability

Mutation	Δ charge ^a	Viable? Y/N ^b
A1K	+1	N
E2K	+2	N
G3K	+1	N
D4K	+2	N
D5K	+2	N
A1K _{N12D}	0	Y
A1K _{G3E}	0	N
G3K _{N12D}	0	Y
G3K _{A1E}	0	Y

^a Per pVIII monomer; ^b As determined by DNA sequencing

Applying the findings of Schuenemann *et al.* (1999), the mutations that resulted in a change in charge of +1 per pVIII monomer (A1K and G3K) were repeated alongside a secondary mutation that would cancel out the addition of a positive charge by the addition of a negatively charged residue (asparagine at position 12 to aspartic acid,

N12D). The two mutants resulting from this approach, A1K_{N12D} and G3K_{N12D}, were viable (Table M2.1). Conjugation experiments using NBD-Cl were carried out to examine whether the new mutant forms of M13 could be labelled with a higher number of exogenous groups than wild type. Unfortunately UV-vis spectroscopy showed that neither A1K_{N12D} nor G3K_{N12D} increased the level of conjugation despite the addition of an additional lysine residue. Examination of the structure of the M13 coat suggests strongly that introduction of a negatively charged aspartate group at position 12 (D12) could lead to the formation of a salt bridge between D12 and the Lys residue at position eight (K8), altering the orientation of K8 (Morag *et al.*, 2011). K8 contains one of the two solvent accessible amine groups in wild type M13 that are derivatised during conjugation reactions. It seems likely that if the introduction of an aspartate at position 12 is leading to an ion bridge then this will inhibit conjugation of K8, meaning that one conjugation site was added at positions one or three whilst another was effectively removed from position eight (Figure M2.S1) leading to no improvement in conjugation efficiency.

To overcome this issue two alternative mutations (at positions 1 or 3) were made in an attempt at balancing the charge of an introduced lysine while not forming a salt bridge with the wild type K8. Analysis of these mutants found that A1K_{G3E} was nonviable however G3K_{A1E} was found to be viable by plaque assay with sequencing showing that viability was not the result of genetic reversion (Table M2.1).

To test the conjugation efficiency of G3K_{A1E} compared to wild type M13, the two bacteriophage variants were separately combined with NBD-Cl before removing

unreacted dye by size exclusion chromatography. UV-vis analysis was used to quantify the number of dye molecules bound to the surface of M13 as the two entities have clear and distinct absorbance spectra. M13 has a band at 269 nm with an extinction coefficient of $3.84 \text{ mg}^{-1} \cdot \text{cm}^{-2}$ (Berkowitz and Day, 1976), while NBD-Cl when bound to an amine group absorbs at 475 nm with an extinction coefficient of $18293 \text{ M}^{-1} \cdot \text{cm}^{-1}$ (Figure M2.S2). When the two reaction products were compared by UV-vis analysis, the peaks attributable to dye were more prominent in the sample that contained G3K_{A1E} than wild type M13 (Figure M2.2 a), indicating that there was more dye bound to the mutant than the wild type. Quantification of the number of NBD groups bound to each type of bacteriophage indicated that there were 1201 ± 12 NBD groups per wild type virion (consistent with our findings that this was the upper limit of NBD-Cl conjugation to the wild type bacteriophage, Figure M2.S3) and 1491 ± 20 NBD groups per G3K_{A1E} virion, a significant increase ($p < 0.0001$) of 290 dye molecules per virion (Figure M2.2 a and e).

When the experiment was repeated with Cy3 in place of NBD-Cl, the absorbance spectra of the dye when bound to the different bacteriophage variants did not match closely, indicating dye aggregation (Figure M2.2 b, solid lines), which in the case of H-aggregation causes hypochromicity, thus suggesting that the absorbance values did not represent the true concentration of the dye bound to the bacteriophage variants, making proper comparison of the conjugation efficiencies unreliable. To overcome this, the samples were measured again in the presence of Triton X-100 at a 1/1000 (v/v) concentration to prevent dye aggregation. Analysis of the resulting spectra (Figure M2.2 b, dashed lines) revealed 1417 ± 28 Cy3 groups per wild type

virion compared to 1937 ± 320 Cy3 groups per G3K_{A1E} virion, a significant increase ($p < 0.05$) of 520 dye molecules per virion (Figure M2.2 e).

When the conjugation was repeated with TRITC, UV-vis analysis revealed 359 ± 8 TRITC groups per wild type virion compared to 672 ± 65 TRITC groups per G3K_{A1E} virion, a significant increase ($p = 0.001$) of 313 TRITC groups per virion (Figure M2.2 c and e).

Finally, when the conjugation experiment was repeated with Cy5, as with Cy3, the spectra of the dye bound to the different bacteriophage samples did not match closely (Figure M2.2 d, solid lines), indicating dye aggregation, thus Triton X-100 was added and the UV-vis measurements were repeated. Analysis of the resulting spectra (Figure M2.2 d, dashed lines) revealed 614 ± 160 Cy5 groups per wild type virion compared to 1067 ± 24 Cy5 groups per G3K_{A1E} virion, a significant increase ($p = 0.008$) of 453 Cy5 groups per virion (Figure M2.2 d and e). Furthermore, gel electrophoresis in denaturing conditions confirmed dye conjugation to bacteriophage (Figure M2.S4).

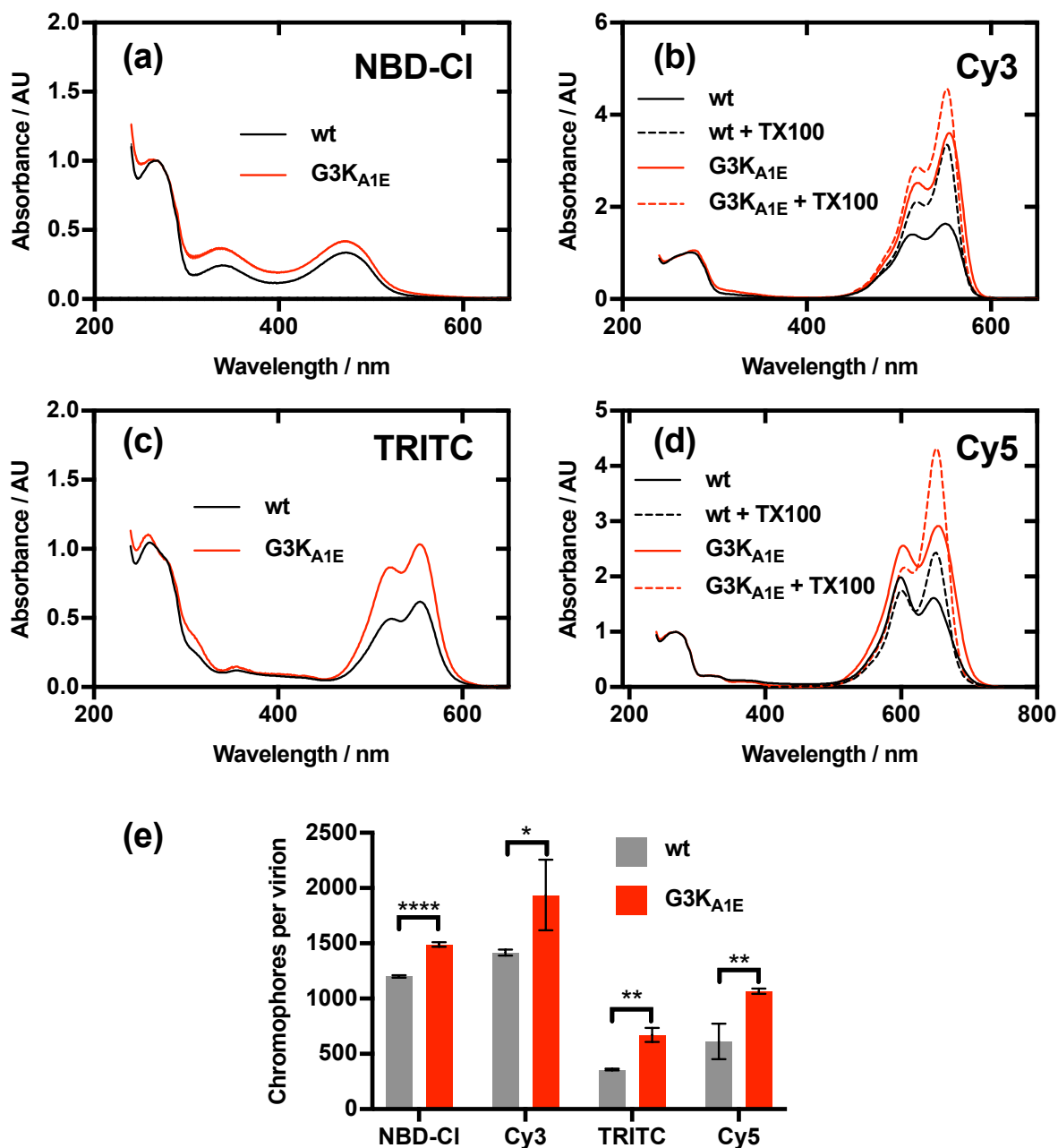


Figure M2.2. Conjugation of exogenous chromophores to M13 variants ($n=3$, error bars represent one standard deviation). (a) Absorbance spectra of wild type (wt) and G3K_{A1E} M13 bacteriophage following conjugation to (a) NBD-CI, (b) Cy3, (c) TRITC and (d) Cy5. (e) Conjugation efficiencies of wt and G3K_{A1E} M13 bacteriophage to dyes indicated in the figure. Where Triton X-100 was used, the values used to calculate conjugation efficiency were those from the spectra measured in the presence of Triton X-100.

M2.4. Discussion

We have shown that the introduction of additional lysine residues into the coat of M13 adversely affects viral propagation. This results from an increase in positive charge on pVIII that interferes with the viral assembly process. This observation is consistent with results obtained by: 1) Merzlyak and Lee (2009), who – when attempting to introduce up to six Lys residues to the amino-terminal region of pVIII in a partial library approach - found that they were able to introduce only one additional Lys residue and that the attempted introduction of 2-6 Lys residues only yielded plaques due to deletions or wild type DNA; 2) Schuenemann *et al.* (1999), who observed that the proton motive force across the inner membrane of *E. coli* prevents the translocation of M13 immature pVIII when positively charged residues are added via mutagenesis, thus halting M13 replication; and 3) Kuzmicheva *et al.* (2008), who observed an under-representation of positively charged residues in pVIII phage display, suggesting that there is a disadvantage to the expression of such residues. Applying these observations, we designed rescue mutations in an effort to allow the expression of an additional Lys residue in pVIII. While the introduction of a second, charge-neutralising mutation alongside A1K (N12D) and G3K (N12D or A1E) allowed the propagation of these mutations (albeit with a reduced titer compared to wild type, Figure M2.S5), which were nonviable when introduced to a wild type background, not all rescue mutations allowed propagation (A1K_{G3E}), demonstrating that this approach is not always effective, suggesting that there are determinants of M13 viability that are as yet not understood. Following the generation of the mutants, their conjugation efficiencies were determined by binding to NBD-Cl, Cy3, TRITC and Cy5. Of the

three mutants generated, only G3K_{A1E} showed an increase in conjugation efficiency compared to wild type M13.

M2.5. Conclusion

We have shown that the addition of lysine residues to the coat of M13 is not a trivial process and that certain rules need to be followed to ensure that the virus is viable and that conjugation sites are available. By following these rules we have developed a mutant strain of M13 that is viable and has increased conjugation efficiency above wild type. As a number of studies have cited that their progress was limited by conjugation efficiency, we propose that this mutant form of M13 could find use in the development of new – or the improvement of existing – technologies that rely on the conjugation of exogenous compounds to the outer surface of M13 bacteriophage.

M2.6. Supporting information

M2.6.1. Experimental procedures

M2.6.1.i. Mutagenesis

Polymerase chain reaction was performed using the mutagenic primers in Table M2.S1 (Sigma), Ph.D.TM Peptide Display Cloning System (NEB) as template DNA and pfu polymerase (Promega). Following digestion with FastDigest DpnI (ThermoFisher), PCR product was purified using a QIAquick PCR Purification Kit (Qiagen). Heat shock was used to introduce mutant M13 DNA to One Shot® TOP10F' Chemically Competent *E. coli* cells (ThermoScientific), followed by a 30-minute recovery period, to minimise the selective advantage of fast-replicating bacteriophage variants (Noren and Noren, 2001). Plaque assays were conducted as

detailed in the New England Biolabs instruction manual for Ph.D.TM Phage Displays Libraries with bottom agar supplemented with 5 $\mu\text{g}\cdot\text{mL}^{-1}$ tetracycline, and 2xYT 1% agar used as top agar. DNA content was assessed by NanodropTM analysis.

M2.6.1.ii. DNA sequencing

Sanger sequencing was performed at the University of Birmingham Functional Genomics Facility, using primer pVIII_seq (Table M2.S1). Single-stranded DNA for sequencing was prepared as detailed in the New England Biolabs instruction manual for Ph.D.TM Phage Displays Libraries.

Table M2.S1. Mutagenic and sequencing primers

Primer ID	Sequence 5' to 3'
A1K_F	CTGTCTTTCGCTAAAGAGGGTGACGATC
A1K_R	GATCGTCACCCTCTTTAGCGAAAGACAG
E2K_F	CTGTCTTTCGCTGCTAAAGGTGACGATC
E2K_R	GATCGTCACCTTTAGCAGCGAAAGACAG
G3K_F	CTTTCGCTGCTGAGAAAGACGATCCCGC
G3K_R	GCGGGATCGTCAGCCTCAGCAGCGAAAG
D4K_F	CTGCTGAGGGTAAAGATCCCGCAAAGC
D4K_R	GCTTTTGCGGGATCAAACCCTCAGCAG
D5K_F	GCTGAGGGTGACAAACCCGCAAAGCG
D5K_R	CGCTTTTGCGGGTTTGTACCCTCAGC
N12D_F	GCAAAGCGGCCTTTGACTCCCTGCAAG
N12D_R	CTTGCAGGGAGTCAAAGGCCGCTTTTGC
A1K_G3E_F	CTGTCTTTCGCTAAAGAGGAGGACGATCCCG
A1K_G3E_R	CGGGATCGTCCTCCTCTTTAGCGAAAGACAG
G3K_A1E_F	CTGTCTTTCGCTGAGGAGAAAGACGATCCCG
G3K_A1E_R	CGGGATCGTCTTTCTCCTCAGCGAAAGACAG
wtM13_F	CTGTCTTTCGCTGCTGAGGGTGACGATC
wtM13_R	GATCGTCACCCTCAGCAGCGAAAGACAG
pVIII_seq	CAGACAACCCTCATAGTTAGCG

M2.6.1.iii. Conjugation of exogenous chromophores to M13

M13 was grown to milligram quantities using *E. coli* TOP10F' cells as the propagation strain (Pacheco-Gómez *et al.*, 2012). In a 1.5 mL microcentrifuge tube M13 was combined with NBD-Cl at final concentrations of 0.156 mg.mL⁻¹ and 2 mg.mL⁻¹, respectively. The buffer used was potassium phosphate buffer, pH 8.0 and DMSO, at a ratio of 80:20. For Cy3, TRITC, or Cy5, 980 µL of 2 mg.mL⁻¹ M13 in 50 mM potassium phosphate buffer, pH 8.0 was combined with 20 µL of dye at 10 mg.mL⁻¹ in DMSO. Following overnight incubation in the dark at 20 °C with constant rotation, the conjugation mixture was de-salted through a PD G-25 MiniTrap buffer exchange column, which had been pre-equilibrated with 15 mL of potassium phosphate buffer. Each 1 mL sample was eluted with 1.5 mL of potassium phosphate buffer.

M2.6.1.iv. Quantification of exogenous chromophores bound to M13

A_{475} and ϵ_{475} (18293 M⁻¹.cm⁻¹, Figure M2.S2) were used to quantify NBD-Cl using the Beer-Lambert law. A_{555} and ϵ_{555} (150000 M⁻¹.cm⁻¹, Manufacturer's instructions) were used to quantify Cy3 using the Beer-Lambert law. A_{544} and ϵ_{544} (100,000 M⁻¹.cm⁻¹, Manufacturer's instructions) were used to quantify TRITC using the Beer-Lambert law. A_{646} and ϵ_{646} (250000 M⁻¹.cm⁻¹, Manufacturer's instructions) were used to quantify Cy5 using the Beer-Lambert law. A_{269} and ϵ_{269} of 3.84 mg⁻¹.cm⁻² were used to quantify M13 in the conjugates (Berkowitz and Day, 1976). Absorbance spectra of M13 bound to Cy3 and Cy5 were also measured in the presence of 1/1000 (v/v) Triton X-100 to disaggregate hypochromic dye aggregates and allow proper quantification.

M2.6.2. Effect of N12D mutation on conjugation efficiency

Prior to the production of the successful G3K_{A1E} mutant, two other mutants expressing additional Lys residues were generated: A1K_{N12D} and G3K_{N12D}. Unexpectedly, these mutations had no significant effect on the conjugation efficiency to 4-chloro-7-nitrobenzofurazan (NBD-Cl) compared to the wild type. Presented in this section are the experiments undertaken to ascertain what effect the N12D rescue mutation had on the ability of M13 to bind to NBD-Cl.

While the addition of the rescue mutation N12D allowed the propagation of M13 with A1K and G3K mutations, there was no significant effect on the conjugation efficiency compared to the wild type (-4.74 ± 2.94 % for A1K_{N12D} and $+5.45 \pm 4.09$ % for G3K_{N12D}, see Figure M2.S1). When an M13 variant containing only the N12D was tested, there was a -16.62 ± 2.33 % change in conjugation efficiency compared to wild type. A recent study comparing the structures of fd and M13 bacteriophage, which differ in their structures only by the N12D mutation, found that the orientation of lysine at position 8 (K8) is altered in fd by the formation of a salt bridge with D12 (Morag *et al.*, 2011). We inferred from this that the N12D mutation might inhibit dye access to K8, causing loss of conjugation efficiency at the same time as a concurrent gain in conjugation caused by the additional Lys residues in A1K_{N12D} and G3K_{N12D}, thus no net change in conjugation efficiency. To determine what portion of conjugation is attributable to K8, this residue was replaced with arginine (K8R) and the conjugation efficiency was tested. This mutation resulted in a -17.06 ± 2.22 % change in conjugation efficiency compared to the wild type, a change that is highly similar to that induced by the N12D mutation, which strongly suggests that the loss of

conjugation caused by N12D was due to an inhibitory interaction with K8. Furthermore, the sum of the change in conjugation efficiency due to G3K_{A1E} and N12D was $+7.55 \pm 3.03$ % (Figure M2.S1, 'calculated G3K_{N12D}'), very similar to the measured change in conjugation efficiency caused by G3K_{N12D}. This strongly suggests that the lack of change in conjugation efficiency caused by G3K_{N12D} was due to the combined positive and negative effects of the G3K and N12D mutations, respectively.

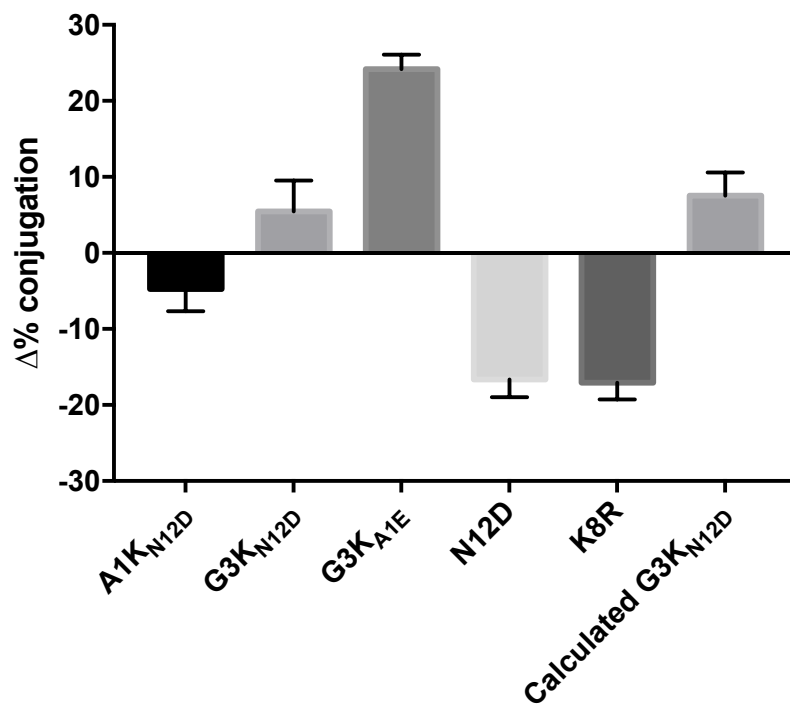


Figure M2.S1. Effect of various bacteriophage mutations on conjugation efficiency.

M2.6.3. Determination of ϵ_{475} of 4-chloro-7-nitrobenzofurazan following reaction with amine group

M2.6.3.i. Method

In a 1.5 mL microcentrifuge tube, a 1 mL reaction mixture was made containing 0.22 M alanine and 0.55 mM NBD-Cl (400x excess of alanine) in 50 mM potassium phosphate buffer, pH 8.0. As a control, in a separate tube, the same concentration of NBD-Cl was prepared without alanine. The solutions were heated to 60 °C for one minute then left rotating at 20 °C in the dark for 24 hours. The process of heating and incubating in the dark was repeated at the same time each day for nine days. Each day at the same time, an aliquot was taken from each tube and diluted so that the concentration of NBD-Cl was 0.041 mM. The absorbance spectra from 220-540 nm were taken using a 1 cm path length cuvette in a Jasco V-550 UV-vis spectrophotometer. As NBD-Cl was reacted with a 400-fold molar excess of Ala, the concentration of Ala could only decrease by 0.25% even if the reaction proceeded to completion, so the rate of reaction was assumed to be solely dependent on the concentration of NBD-Cl, thus first order kinetics were assumed. Nonlinear regression was performed against the negative of the equation for single-phase exponential decay using Graphpad Prism 7 on a plot of absorbance at 475 nm (A_{475}) against time; from this the plateau value for A_{475} was determined. As the concentration of NBD-Cl was known (using A_{475} and $\epsilon_{336} = 9800 \text{ M}^{-1} \cdot \text{cm}^{-1}$ at time = 0) it was possible to determine, using the Beer-Lambert law, the value for ϵ_{475} of NBD-Cl when conjugated to an amine group.

M2.6.3.ii. Results

In order to accurately quantify the amount of 4-chloro-7-nitrobenzofurazan (NBD-Cl) bound to the surface of M13, it was necessary to determine its molar extinction coefficient at 475 nm (ϵ_{475}) when bound to an amine group. To quantify this value, NBD-Cl was allowed to react with L-Alanine (Ala) as a substitute for the N-terminal amino acid of pVIII. Monitoring the absorbance spectrum of the reaction as it progressed showed the emergence of a peak at 475 nm, a phenomenon that did not occur in the no-Ala control (Figure M2.S2). A_{475} was plotted against time, allowing the plateau value of A_{475} to be determined by nonlinear regression. From this value ϵ_{475} was calculated at $18293 \text{ M}^{-1} \cdot \text{cm}^{-1}$. The no-Ala control experiment shows that NBD-Cl in these conditions reacted to a very small extent with the buffer used. This is in contrast to the findings in earlier references, which found the reaction of NBD-Cl with water to be problematic (Warrener *et al.*, 1983; Stoilovic *et al.*, 1984).

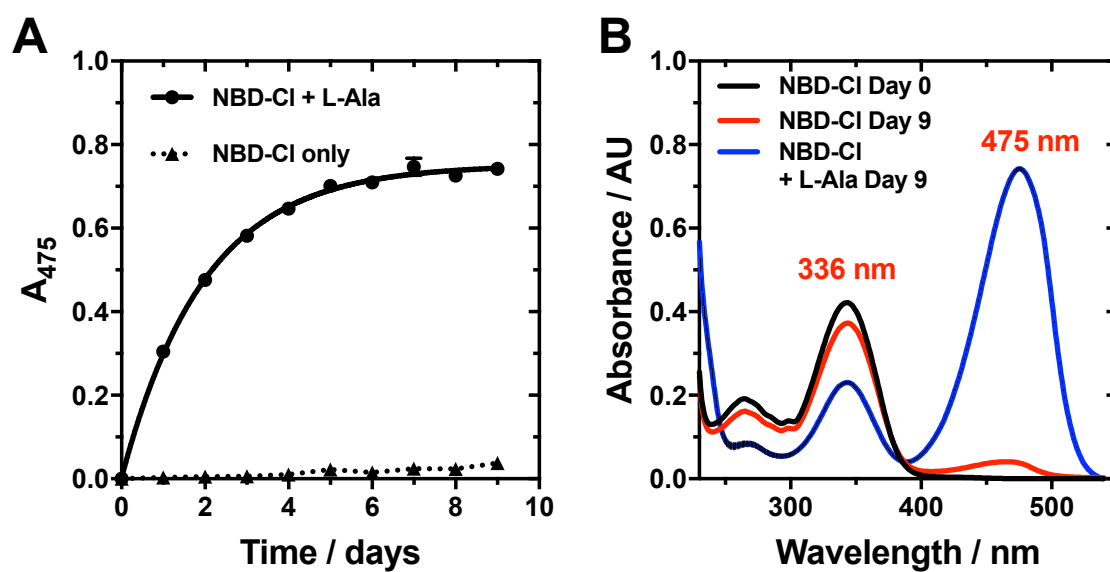


Figure M2.S2. Determination of the molar extinction coefficient at 475 nm of NBD-Cl when conjugated to an amine moiety. (A) Reaction trace of NBD-Cl with L-Alanine and a no-alanine control. (B) Absorbance spectrum of NBD-Cl before and after reaction with L-Alanine, and no-Ala control after same time period ($n=3$, error bars indicate one standard deviation).

M2.6.4. Optimisation of conjugation to wild type M13 bacteriophage

M2.6.4.i. Method

Bacteriophage/dye samples were prepared in 96-well plates in 50 mM Bicine buffers with pH values 8.0-9.0 and 50 mM potassium phosphate buffer, pH 8.0, and sodium chloride at a range of concentrations between 0.0 M and 0.5 M. The first screen had NBD-Cl at a 15 X molar excess over pVIII. The second screen used 50 mM potassium phosphate with no sodium chloride as the buffer and had NBD-Cl at a range of molar excesses between 15 X and 500 X. Conjugation was allowed to proceed for 16 hours in the dark with gently mixing, was indicated by absorbance at 475 nm and was measured using a Jasco J1500 CD spectrophotometer and a Jasco AS-2055 plus autosampler, with a 1.2 mm path length flow cell.

M2.6.4.ii. Results

Prior to taking a mutational approach to optimisation of dye conjugation to M13, buffer conditions (pH, salt concentration and dye-to-bacteriophage concentration ratio) were screened to find the upper limit of the wild type using NBD-Cl as a model conjugation agent. An initial screen of pH and sodium chloride concentration indicated that the optimal buffer condition was 50 mM potassium phosphate buffer, pH 8.0 (Figure M2.S3 a). A second screen of dye-to-bacteriophage ratio in 50 mM potassium phosphate buffer, pH 8.0 indicated that there was no increase in conjugation above a 400-fold molar excess of NBD-Cl over pVIII subunits (Figure M2.S3 b). When this reaction condition was scaled up to a 1 mL reaction, the conjugation efficiency was found to be approximately 1200 molecules per bacteriophage.

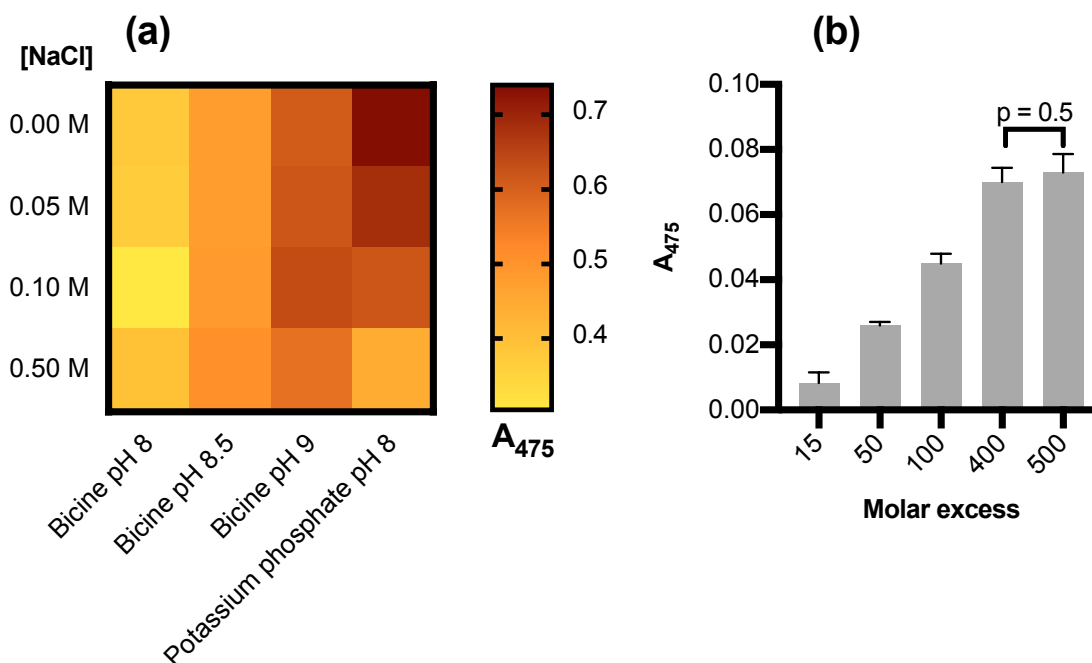


Figure M2.S3. Screen for optimised conjugation reaction conditions. (a) Screen for optimal buffer pH and salt concentration. (b) Screen for optimal molar excess of 4-chloro-7-nitrobenzofurazan (NBD-Cl) over bacteriophage major coat protein pVIII. A_{475} indicates coupling of NBD-Cl to amine groups.

M2.6.5. Gel analysis of dye conjugation

M2.6.5.i. Method

Bacteriophage samples (5 μ L) were combined with 15 μ L of loading buffer (0.125 M Tris pH 6.8, 20 % (v/v) glycerol, 0.1 % sodium dodecyl sulphate) and incubated at 50 °C for 15 minutes. Samples and Broad Range Blue Protein Standard (New England Biolabs) were electrophoresed at 140 V in a Criterion XT Precast Gel in 1 x BIORAD XT MES Running buffer. Electrophoresed gels were stain with InstantBlue Coomassie protein stain.

M2.6.5.ii. Results

To confirm conjugation of dyes to the bacteriophage, unlabelled bacteriophage and labelled bacteriophage samples were electrophoresed in denaturing conditions. Fluorescent imaging and colour imaging prior to staining of the resulting gel indicated the locations of the dyes (Figure M2.S4 a,b). Unlabelled bacteriophage protein was not visible by this method (Figure M2.S4 a and b, lane 1), indicating that the fluorescence was not due to protein. Samples conjugated with NBD-Cl, Cy3 and TRITC all produced bands on that could be visualised when excited using UV light (Figure M2.S4 a, lanes 2-7). Protein conjugated with Cy5 was only detectable by its absorbance (Figure M2.S4, b and c, lanes 8 and 9) as its excitation spectrum fell outside the emission envelope of the UV lamp used. It is also worth noting that for all dyes apart from Cy presence of dyes conjugated to the pVIII protein induces a change in the migration of the protein, this is likely to be the result of the modification of the amine groups and further highlights the successful conjugation of M13.

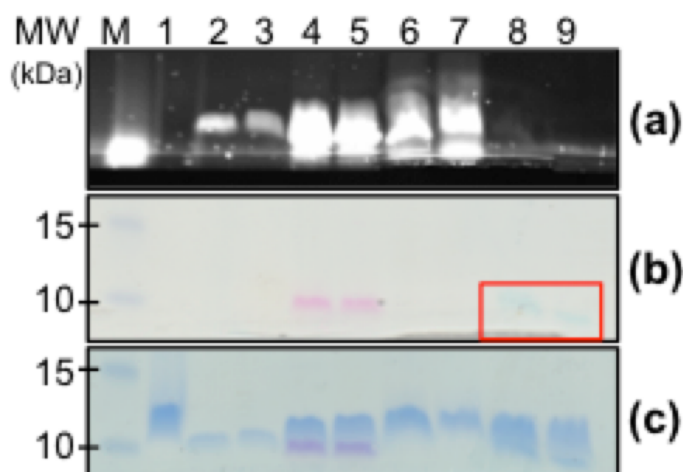


Figure M2.S4. Analysis of dye conjugation by gel electrophoresis in denaturing conditions. (a) Fluorescent image of gel. (b) Colour photograph of gel prior to staining. (c) Colour photograph of gel after staining. Lanes: M, Molecular weight marker; 1, Unlabelled M13 bacteriophage; 2, Wild type M13 bacteriophage labelled with NBD-Cl; 3, Mutant (G3K_{A1E}) M13 bacteriophage labelled with NBD-Cl; 4, Wild type M13 bacteriophage labelled with Cy3; 5, Mutant (G3K_{A1E}) M13 bacteriophage labelled with Cy3; 6, Wild type M13 bacteriophage labelled with TRITC; 7, Mutant (G3K_{A1E}) M13 bacteriophage labelled with TRITC; 8, Wild type M13 bacteriophage labelled with Cy5; 9, Mutant (G3K_{A1E}) M13 bacteriophage labelled with Cy5.

M2.6.6. Plaque-forming ability of bacteriophage mutants

Once it had been established by DNA sequencing which mutants were viable i.e. capable of completing the bacteriophage life cycle, it was necessary to ascertain whether the mutations had had an effect on the viral fitness. To assess this, the mutagenesis procedure above was performed and the amount of DNA used in the heat shock step was quantified by Nanodrop analysis. Wild type DNA was generated using the same procedure as for the mutants, using primers “wtM13_F” and “wtM13_R” (Table M2.S1). Following this procedure, plaques were counted, allowing the expression of viral fitness in terms of plaque-forming units per unit mass of DNA used in the heat-shock step (pfu.ng⁻¹). Results of this experiment indicate that all of the viable mutants had reduced fitness compared to the wild type (Figure M2.S5),

indicating that during large-scale propagation of mutant bacteriophage, care should be taken to avoid outgrowth by the wild type.

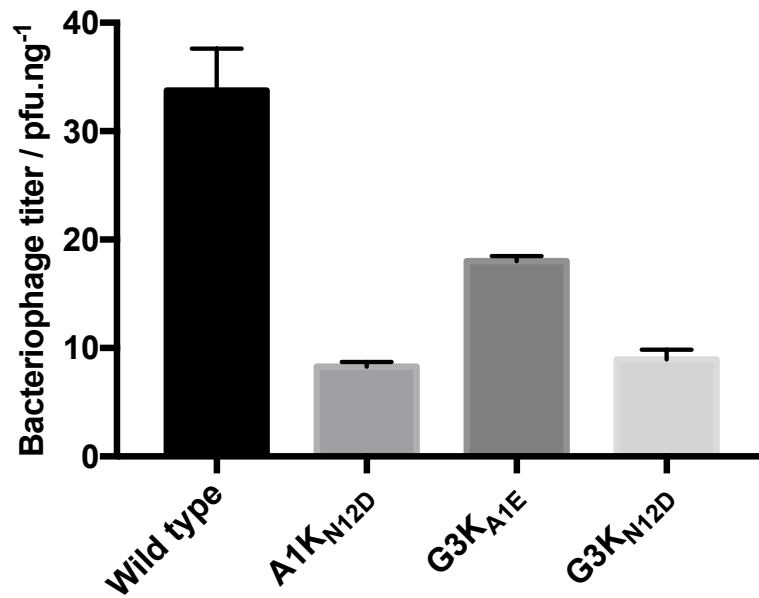


Figure M2.S5. Titre of M13 bacteriophage mutants and wild type. Fitness is quantified as the number of plaque-forming units (pfu) arising per unit mass of DNA introduced to the host during heat-shock.

4.4. Additional results

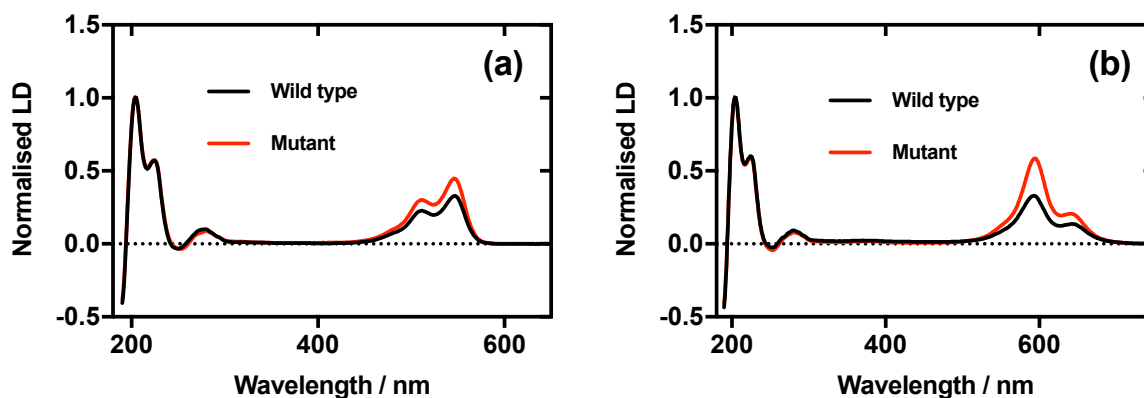


Figure 4.1. Linear dichroism of bacteriophage-dye conjugates. (a) M13Cy3, both wild type and G3K_{A1E}. (b) M13Cy5, both wild type and G3K_{A1E}.

The increased labelling of G3K_{A1E} compared to wild type was established using absorbance spectroscopy (Figure M2.2). It was next necessary to establish whether the additional dyes bound also gave rise to an increased LD signal. This was to demonstrate whether the mutant could be applicable in the Pacheco-Gómez assay. As discussed in Chapter 3, Cy3 and Cy5 align on M13 bacteriophage, producing an LD signal in the visible region, whereas NBD-Cl and TRITC do not. Consequently, the LD spectra of the Cy3- and Cy5-labelled wild type and G3K_{A1E} bacteriophages were recorded. Examination of the data from this experiment reveals that for both dyes, there was a more intense LD in the regions attributable to the dyes in the mutant sample compared to wild type (Figure 4.1). A 36 ± 4.0 % increase in LD due to Cy3 (LD₅₄₆; Figure 4.1 a) and a 77 ± 2.4 % increase in LD due to Cy5 (LD₅₉₃; Figure 4.1 b) was observed.

4.5. Discussion

During this project it was observed that A1K_{G3E} is a nonviable mutant. This is in contrast to the others with charge-neutralising rescue mutations, which indicates that there are other unknown determinants of M13 viability. Possibilities include: protein misfolding caused by the A1K_{G3E} mutation; lack of pVIII maturation due to altered recognition by signal peptidase; inhibition of interaction with the pI/IV/XI complex. Whatever the cause of nonviability, it is unusual that the G3E mutation is viable in other mutants (Park *et al.*, 2014; Khalil *et al.*, 2007; Lee *et al.*, 2012; Merzlyak and Lee, 2009), and that A1K is viable in the A1K_{N12D} mutant. The fact that both mutations are viable in isolation rules out that either one causes any bacteriophage-lethal effect. The lethal effect must be due to their co-presence in the protein. Clearly, further experiments would be required to elucidate additional determinants of M13 viability.

All mutants tested showed reduced fitness compared to the wild type (Figure M2.S5). As stated in the manuscript, this means that care has to be taken to avoid contamination by wild type bacteriophage during propagation. This may have to be a caveat that is accepted when taking this approach. This would be expected when using any M13 mutant that had not specifically been selected for enhanced replication rate above the wild type (Nguyen *et al.*, 2014; Kehoe and Kay, 2005; Derda *et al.*, 2010). Outgrowth was not a problem during this project and standard aseptic technique yielded consistently clonal mutant stocks. However, were this persistently problematic, one could select a fast growing strain that also displays an additional Lys residue using the partial library approach (Merzlyak and Lee, 2009).

The G3K_{A1E} mutant labelled with higher levels of Cy3 and Cy5 than the wild type produced higher dye LD compared to wild type conjugates (36 ± 4.0 % and 77 ± 2.4 % increase for Cy3 and Cy5, respectively). This correlates well with the observed increase in conjugation level. As determined by UV-Vis absorbance spectroscopy, Cy3 conjugation increased by 37 ± 1.7 % and Cy5 74 ± 2.6 %. The raised dye LD afforded by the increased dye conjugation to M13 bacteriophage will enable an improvement to the dynamic range of the Pacheco-Gómez assay. Furthermore, the mutation imparted an increased binding capacity to a range of dyes. This may indicate that a greater number of antibodies could be bound to the surface of the mutant than the wild type. This would allow an improvement in the sensitivity of the assay.

Finally, although the G3K_{A1E} mutant showed an advantage in bioconjugation, the Pacheco-Gómez assay requires the structural integrity of the bacteriophage in unrefrigerated environments. It was thus necessary to ascertain what, if any, effect the mutations had on the thermal stability of the bacteriophage. This was investigated and is covered in the next chapter.

4.6. Conclusions

In summary, a mutant strain of M13 bacteriophage was generated, which showed a greater capacity for bioconjugation than the wild type. As stated in the final section of the manuscript, it is anticipated that this strain could be used to improve technologies based on M13 bacteriophage bioconjugates that are currently hindered by limited conjugation efficiency.

5. BACTERIOPHAGE THERMAL STABILITY

5.1. Introduction

In the previous chapter, M13 bacteriophage mutants were generated. Their intended use was in an assay that relies on the structural integrity of the bacteriophage for a proper readout (Pacheco-Gómez *et al.*, 2012; Carr-Smith *et al.*, 2015). As such, it is important that any bacteriophage used retains its structural integrity at temperatures that may be reached during transport and use. The experiments described in the following chapter were thus carried out to compare the thermal stability of the G3K_{A1E} mutant to wild type bacteriophage. This was to investigate whether or not the mutations introduced had had any effect on the thermal stability of the bacteriophage.

It is well established that mutations introduced into the sequence of proteins can disrupt their folding and alter their stability (Creighton, 1997; Berg *et al.*, 2012). In M13 bacteriophage it is known that while the pVIII protein can tolerate small sequence alterations (Smith and Petrenko, 1997), it is the least tolerant of the M13 bacteriophage coat proteins to mutation (Kuhn and Wickner, 1985). As such, it was reasoned that it would be prudent to compare the mutant to the wild type. Even if the mutant had greater conjugation efficiency, if it was structurally destabilised it would have been of little use in the assay as it would be unable to align in Couette flow.

To compare the thermal stability of G3K_{A1E} to wild type bacteriophage, their circular dichroism signals were monitored during thermal denaturation. Insights into the structural composition of bacteriophage when denatured were also validated by thioflavin T assay. Circular dichroism and how it may be used to derive protein structural information and melting temperature are introduced below. Finally, uses

and limitations of the thioflavin T assay for insights into protein structure are also introduced in the following sections.

5.1.1. Circular dichroism spectroscopy

To understand circular dichroism (CD), it is first necessary to understand light polarisation. Light comprises an electric field and a magnetic field. These oscillate at right angles to each other, propagating along a common axis. There is no preferential direction of oscillation of the electric or magnetic fields in isotropic light (Figure 5.1 a). Linearly polarised light, however, has a preferential oscillation direction, and the waves of pure linearly polarised light oscillate in only one direction. The direction of oscillation of the electric field is used to describe the polarisation of the light (Figure 5.1 b). Circularly polarised light is formed by the sum of two orthogonally polarised light waves out of phase by 90° . With this phase shift the point of maximum amplitude of one wave coincides with the point of zero amplitude of the other on the propagation axis. When looking towards the light source along the propagation axis, if the circularly polarised light traces out a clockwise spiral it is said to be left-handed circularly polarised (LHCP) (Figure 5.1 c). Right-handed circularly polarised (RHCP) light traces an anti-clockwise spiral (Figure 5.1 d).

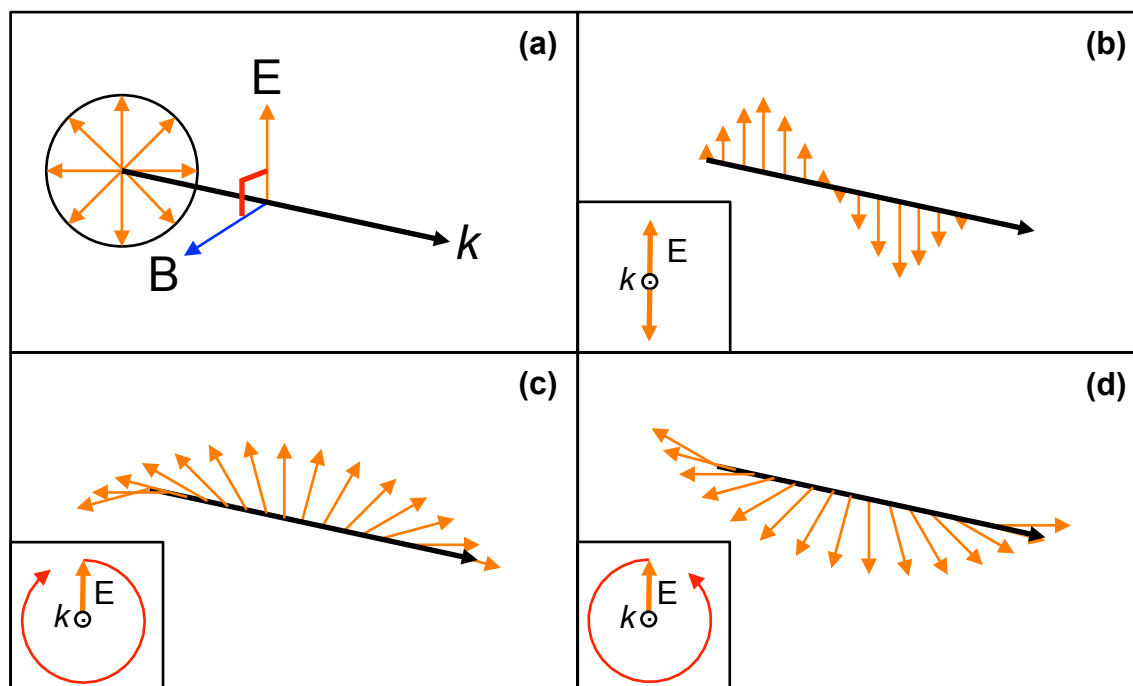


Figure 5.1. Light polarisation. (a) Isotropic light. E = electric field vector; B = magnetic field vector; k = light propagation axis. (b) Linearly polarised light. Inset: view along k towards light source. (c) Left-handed circularly polarised light. Inset: view along k towards light source. (d) Right-handed circularly polarised light. Inset: view along k towards light source.

Chiral samples absorb L/RHCP light differently, i.e. they exhibit circular dichroism. Non-chiral compounds, however, do not. Thus, a sample of a chiral compound may be characterised by measuring its relative absorption of L/RHCP light. This provides the CD spectrum of the compound when measured as a function of wavelength. As enantiomer pairs interact in an equal and opposite way to each other with L/RHCP light, their CD spectra are equal and opposite. Thus, a racemic mixture has no net CD, meaning that CD spectroscopy may be used to assess the enantiopurity of a sample of a chiral compound (Okuom *et al.*, 2015).

As many biological molecules contain chiral elements, they exhibit CD, making it a useful technique to study biological structures and processes. Specifically, CD

spectra can be deconvoluted to yield information about the secondary structure composition of a proteinaceous sample. Thus it is a useful technique for monitoring the structural integrity of M13 when heated. Moreover, it is ideal for comparing the thermal stabilities of M13 variants.

5.1.2. Derivation of protein structural information from circular dichroism spectroscopy

Proteins can absorb light in two distinct wavelength regions, near UV (250-300 nm) and far UV (~190-250 nm). Near UV absorption is attributable to aromatic amino acid side chains. Far UV absorption is attributable to the amide bonds of the protein backbone (Rodger, 2003).

The far-UV CD signal of a protein is the result of the coupling of backbone amide excitons, which in turn is dependent on backbone geometry. Interaction of the backbone with circularly polarised light is thus also dependent on backbone geometry. Accordingly, different secondary structural elements (which contain different backbone geometries) have characteristic CD spectra in the far UV region (Figure 5.2). This allows information about the secondary structure of a protein to be gathered from CD data (Nordén *et al.*, 2010; Greenfield, 2006).

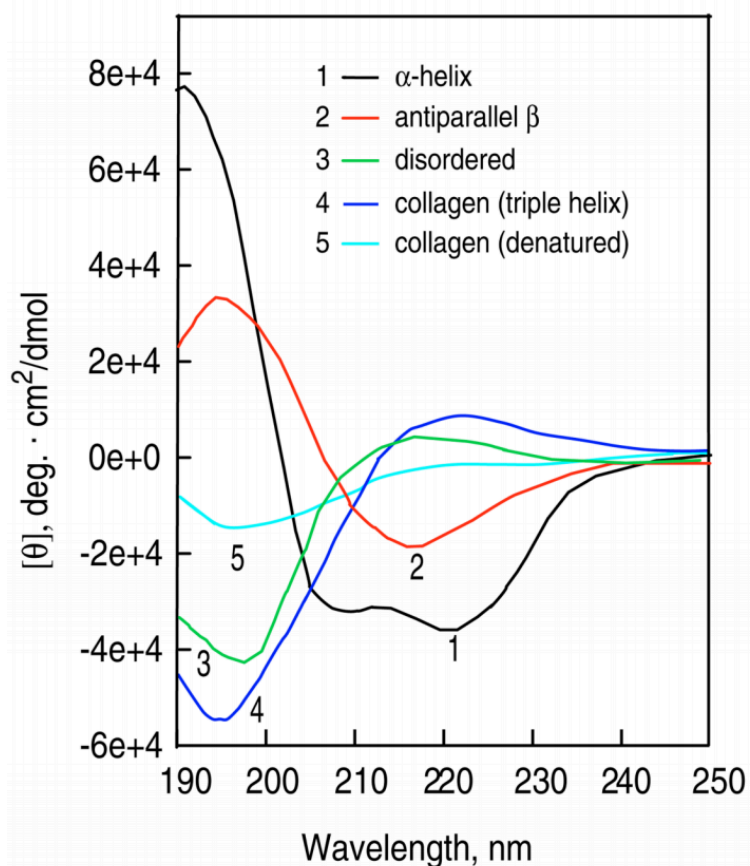


Figure 5.2. Typical circular dichroism spectra of protein secondary structure elements ($[\theta]$ = mean residue ellipticity; reproduced from Greenfield (2006)).

Quantification of the structural content of a protein requires deconvolution of CD spectra. This yields a statement of what percentage of the constituent amino acid residues are in a given secondary structural element. CD deconvolution programs compare spectra of proteins of known structural composition to the input spectrum. By finding the sum of standard spectra that reproduces the input spectrum, they calculate the percentage structural composition of the input spectrum (Nordén *et al.*, 2010).

5.1.3. Thioflavin T

Structural insights into the unfolding of bacteriophage were gained from CD spectroscopy data in the following results section. To corroborate the findings, assays were also performed using the fluorophore thioflavin T. It should be noted that the dye Congo red could have been used here in place of thioflavin T (Fernandez-Flores, 2011). However, thioflavin T is more sensitive than Congo red and is widely regarded to be the gold standard fluorimetric method for amyloid detection (Cooper, 1969; Biancalana and Koide, 2010; Malmos *et al.*, 2017). Thus, Thioflavin T was used here.

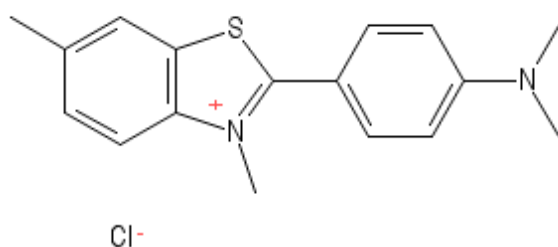


Figure 5.3. Chemical structure of thioflavin T. Drawn using ChemDraw Professional software.

Thioflavin T (3,6-dimethyl-2-(4-dimethylaminophenyl)-benzothiazolium cation) (ThT) (Figure 5.3) is a fluorescent dye. In isolation, it has a wavelength of maximal excitation (λ_{ex}) of 385 nm and a wavelength of maximal emission (λ_{em}) of 445 nm. When ThT is combined with protein rich in beta-sheet, especially beta amyloid, it rapidly associates with the protein. The association triggers a bathochromic (red) shift in the ThT absorbance and emission spectra ($\lambda_{\text{ex}} = 440$ nm, $\lambda_{\text{em}} = 482$ nm) along with an increase in fluorescence quantum yield (Naiki *et al.*, 1989). Because of this property, ThT is often used to monitor the formation of protein aggregates, especially

beta amyloid. In particular it is used to study diseases where protein aggregation is involved or believed to be involved in the mechanism of the disease. This includes Alzheimer's disease (Wu *et al.*, 2008), Parkinson's disease (Jethva *et al.*, 2011), and transmissible spongiform encephalopathy (Gray *et al.*, 2016). ThT was used here to compare the structural composition of bacteriophage variants before and after heat denaturation to validate CD spectroscopy data.

5.1.4. Thioflavin T assay limitations

While ThT is widely used to monitor the formation of beta sheet-rich structures, it has a number of limitations. Firstly, ThT does not exclusively bind to proteins rich in beta-sheet. Examples include the mainly α -helical peripheral site of acetylcholinesterase (Harel *et al.*, 2008), and hydrophobic pockets in a range of serum albumins in their native conformations (Sen *et al.*, 2009). False positive results, i.e. indicating aggregation when there is none, are thus possible. Accordingly, the native protein should be assayed alongside the denatured protein.

In addition, lysine residues within the primary sequence of a protein can decrease the affinity of ThT for beta sheet-rich structures comprising said protein (Wu *et al.*, 2009). Such an amino acid composition dependence means that comparisons between the aggregation states of proteins with different primary sequences are not as meaningful as comparing the native and denatured states of one protein only. This limitation also gives rise to the possibility of false negative results. This is because ThT might not bind well to either native or denatured conformations of a protein due to its primary

sequence. In this case a suitable control would be to use an orthogonal technique to monitor the secondary structure of the protein e.g. circular dichroism.

Furthermore, it has been shown that quantification of the formation of beta sheet/amyloid by ThT assay can be distorted by the presence of some polyphenolic compounds (Hudson *et al.*, 2009). A number of such compounds have been investigated as potential anti-amyloid drugs. However, such compounds were not used here so this was not a factor during this work.

Finally, ThT has been shown to bind to double-stranded DNA (Ilanchelian and Ramaraj, 2004). It might be anticipated that, during bacteriophage thermal denaturation, the DNA core could be released, binding to ThT, and causing a false positive result. However, this should not present an issue with M13 bacteriophage as it contains only single-stranded DNA.

5.2. Project aims

The aim of this chapter was to compare the thermal stability of the G3K_{A1E} mutant bacteriophage generated in the previous chapter to the wild type. In addition, to ascertain whether any effect observed was mutation-specific, three other bacteriophage mutants were analysed. The G3K_{A1E} mutant was intended for use in an in-field assay that required that the bacteriophage retained structural integrity. Accordingly, it was necessary to test that it was as robust as the wild type under heat stress.

5.3. Results

5.3.1. Bacteriophage melting temperature

To elucidate the melting profile of the M13 variants, thermal denaturations were conducted, measuring CD₂₂₂ only (wavelength of maximum CD intensity), in steps of 0.5 °C (Figure 5.10). Melting temperatures were derived by calculating the first derivative of the melting curve with respect to temperature.

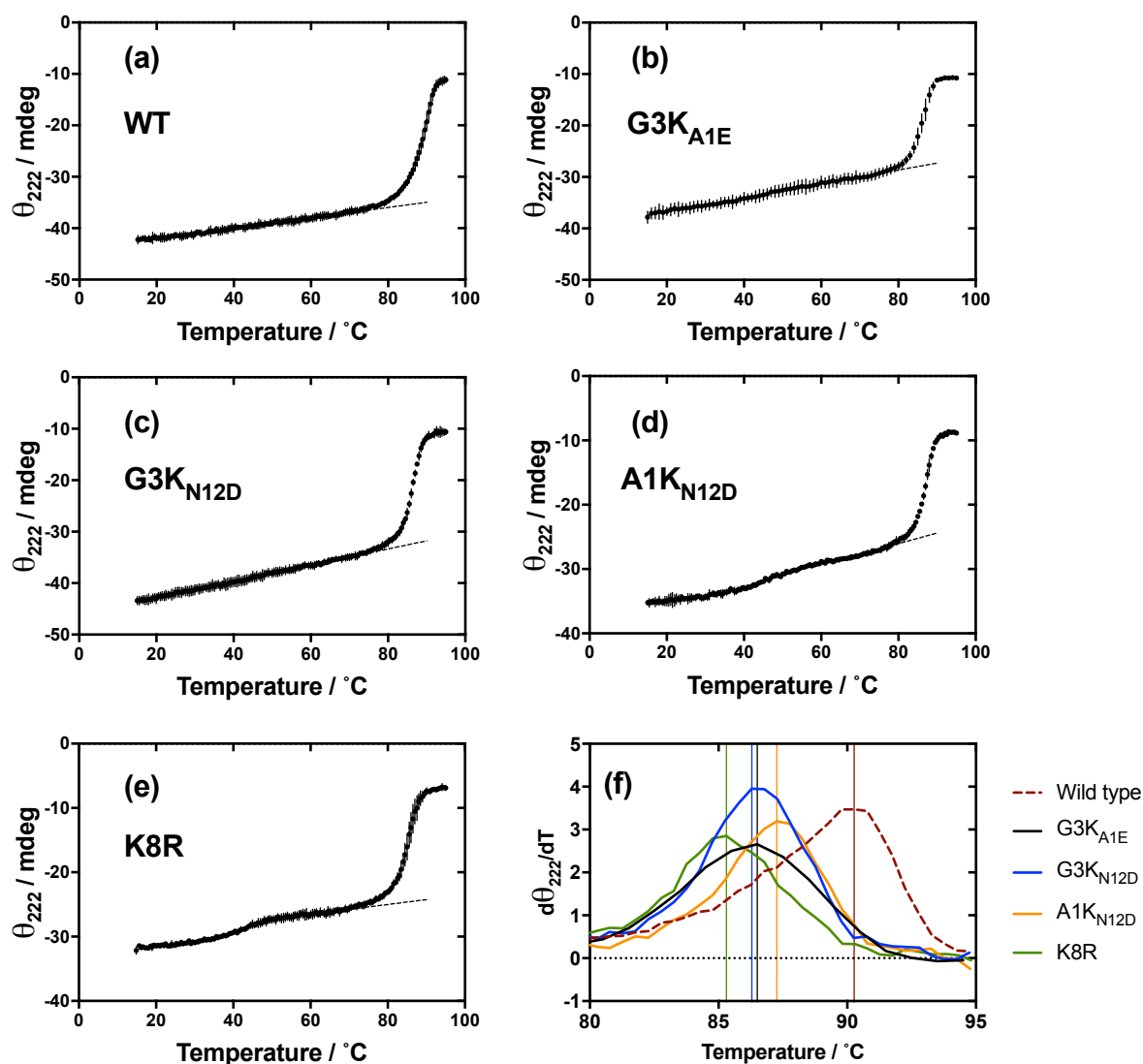


Figure 5.4. Denaturation curves of bacteriophage variants (a-e) as determined by measurement of circular dichroism at 222 nm (ellipticity; θ_{222}). WT = wild type. (f) First derivative of bacteriophage denaturation curves. Vertical lines indicate melting temperatures of bacteriophage variants. ($n = 3$). Error bars indicate one standard deviation.

The melting profiles in Figure 5.4 all show the same overall trend: high CD_{222} up to approximately 80 °C, followed by a rapid loss of CD_{222} , indicative of a large denaturation event. The CD_{222} of all bacteriophage variants was linearly dependent on temperature at temperatures below the large denaturation event. Thus the

structure of the bacteriophage variants was influenced by temperature in their folded state (Figure 5.4 a-e).

To determine the melting temperatures of the bacteriophage variants, the first derivative with respect to temperature of the raw CD₂₂₂ data was plotted to yield peaks with maximal y-axis values at the melting temperature. This analysis revealed that G3K_{A1E} has a lower melting temperature than wild type bacteriophage, with a value of 86.5 °C compared to 90.3 °C (Figure 5.4 f). This indicates a destabilisation of the pVIII coat of G3K_{A1E} compared to wild type. Analysis of G3K_{N12D}, A1K_{N12D} and K8R revealed a similar decrease in melting temperature, with values of 86.3 °C, 87.3 °C and 85.3 °C, respectively, indicating that this destabilisation was not specific to the G3K_{A1E} mutation.

5.3.2. Bacteriophage secondary structure during thermal denaturation

The experiment above yielded data that demonstrated a loss of CD₂₂₂ with temperature. To ascertain the secondary structure dependence on temperature, the M13 mutants and wild type were heated from 15 °C to 95 °C, with a CD spectrum being taken from 200-270 nm in 5 °C intervals. Figure 5.5 shows the CD spectra before and after heating and reveals a typical alpha helical trace at 15 °C and a typical beta sheet-like trace at 95 °C. Each spectrum was deconvoluted and the alpha helix and beta sheet content was plotted against temperature (Figure 5.6). The results for all variants show an initially high alpha helix content, as expected from the M13 bacteriophage structure (Morag *et al.*, 2015). This was lost as temperature increased. In contrast, the initially low beta sheet content increased with temperature.

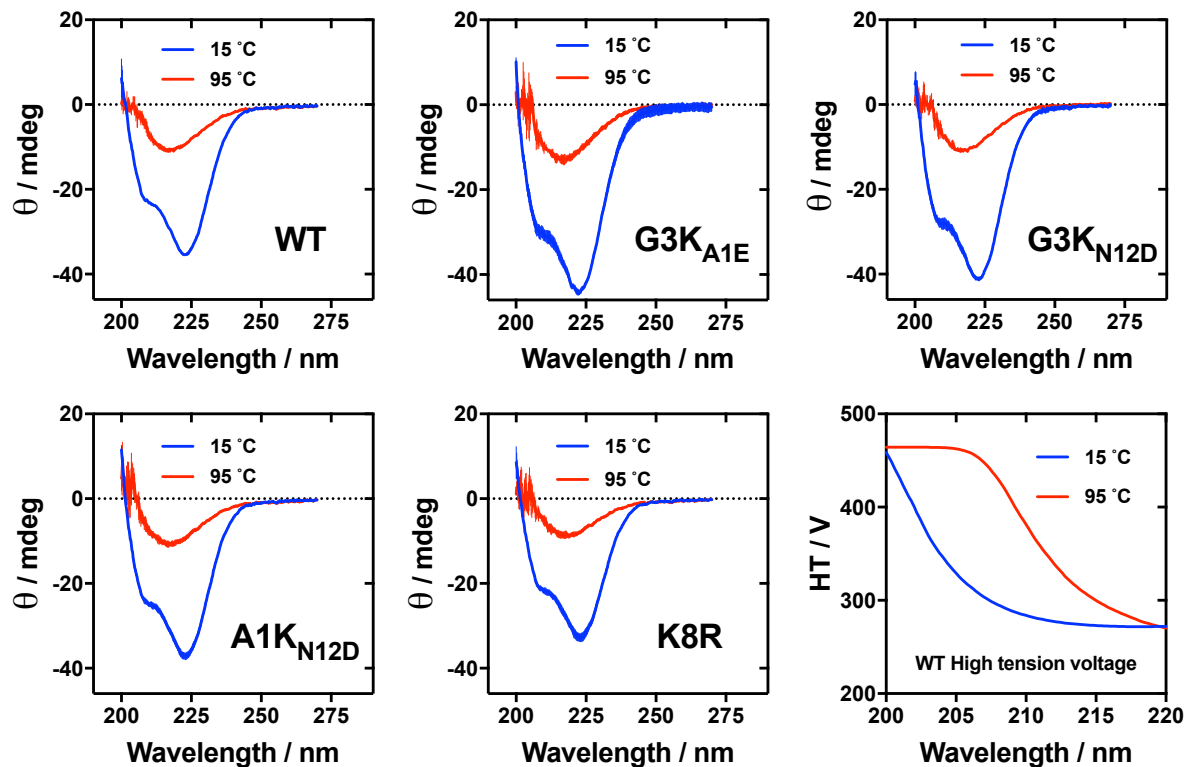


Figure 5.5. Circular dichroism (ellipticity; θ) of bacteriophage variants, and high tension (HT) voltage of wild type bacteriophage before and after thermal denaturation. WT = wild type. ($n = 3$). Error bars indicate one standard deviation.

Interestingly, both variants containing the G3K mutation appeared to have a much higher alpha helix content prior to denaturation (~80 %) than wild type and the other mutants (~60 %). As all samples were freshly prepared and were in identical buffer conditions, this result suggests a change to the native structure of pVIII following introduction of the G3K mutation.

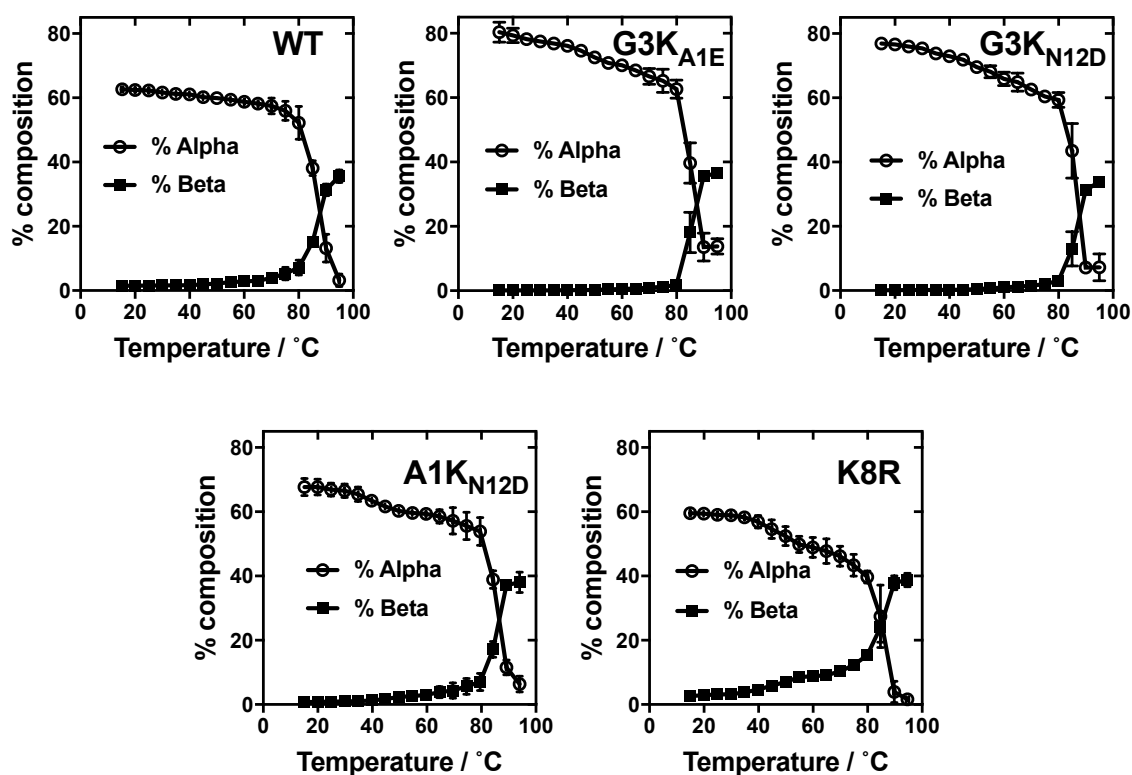


Figure 5.6. Protein secondary structure composition of bacteriophage variants during thermal denaturation. WT= wild type. (n = 3). Error bars indicate one standard deviation. CD data deconvolution performed using K2D3 software (Louis-Jeune *et al.*, 2011).

Although deconvolution of the spectra at 95 °C revealed that all bacteriophage variants had become mainly beta sheet in their structural composition in their denatured state, the high temperature spectra had large amounts of noise in the region between 200 nm and 210 nm. This was possibly due to light scattering by small bubbles forming in localised areas of boiling, or light scattering from aggregated protein (Hecht, 2002). Light scattering by the samples at high temperatures is evident in the high tension (HT) voltage spectrum, and is exemplified here by that of the wild type at 15 °C and 95 °C (Figure 5.5). The absence of negative CD signal below 200 nm (Figure 5.5) indicates strongly that there is little random coil in the sample (Figure 5.2), thus strengthening the evidence that the samples were

mainly beta sheet. However, as large levels of noise can interfere with deconvolution, it seemed prudent to use an orthogonal technique to examine the reliability of this finding. Thus, native and heat-denatured bacteriophage samples were subjected to ThT assay (Figure 5.7). The results from this assay show that when native bacteriophage was added to ThT, there was a small positive change in fluorescence intensity at 482 nm (ΔI_{482}) (<+10 %), suggesting that ThT bound to bacteriophage in its native conformation. Little difference in ΔI_{482} was observed between native variants. When heat-denatured bacteriophage (at ambient temperature) was added to ThT, a much larger positive ΔI_{482} was observed (+37-49 %), again with little difference between variants. This result indicates that ThT binds more strongly to heat-denatured bacteriophage than native bacteriophage. This is indicative of the formation of a more beta-rich structure upon heat denaturation. Thus, the results of this experiment corroborate the CD spectroscopy data.

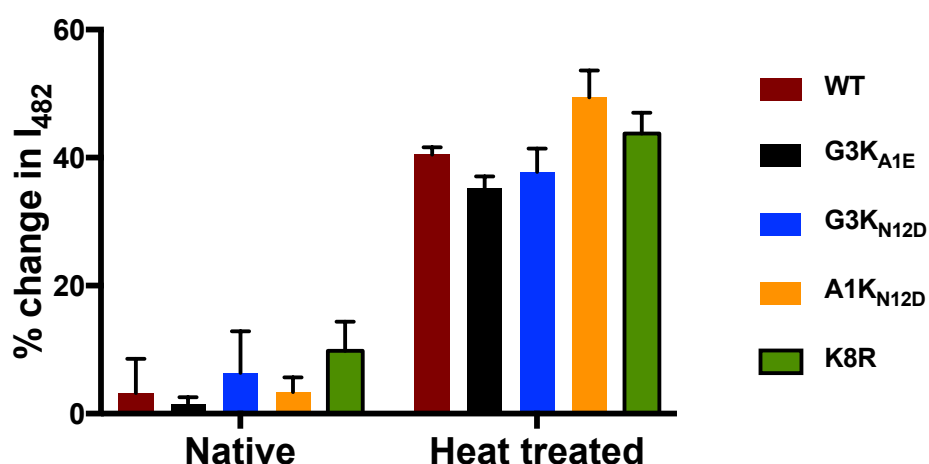


Figure 5.7. Thioflavin T assay on heat-denatured bacteriophage variants. Per-cent change was calculated against fluorescence intensity at 482 nm (I_{482}) of thioflavin T before bacteriophage sample was added. (Accumulations = 6, N=3, n=3). Error bars indicate one standard deviation.

Close inspection of Figure 5.4 and 5.6 reveals a subtle difference in the way A1K_{N12D} and K8R degraded compared to wild type M13, G3K_{A1E} and G3K_{N12D}. A1K_{N12D} and K8R appeared to lose alpha helix configuration in two stages; a small loss around 48 °C followed by a large loss around 80 °C. In contrast, the other variants only appeared to lose alpha helix in one step around 80 °C. A one-step denaturation is consistent with previously published data on wild type M13 bacteriophage, which was generated using linear dichroism spectroscopy (Carr-Smith *et al.*, 2015). This suggests that the introduction of the mutations A1K_{N12D} and K8R affected the folding of the pVIII coat, destabilising it in temperatures around 48 °C.

To investigate the structural stability of G3K_{A1E} compared to wild type at temperatures below the denaturation temperature, a further experiment was conducted, investigating the reversibility of unfolding up to 60 °C.

5.3.3. Bacteriophage unfolding and re-folding

To yield further information about the relative stabilities of G3K_{A1E} and wild type bacteriophages, the reversibility of unfolding was investigated. This was deemed necessary to investigate as the results would give an indication of the robustness of the bacteriophage variants when exposed to heat-cool cycles, which would be expected if used in an environment where refrigeration were not available. The CD spectrum of bacteriophage variants was monitored while heating from 15 °C to 60 °C then cooling back down to 15 °C. CD spectra were taken at 5 °C intervals and the results are displayed as the CD at 222 nm (θ_{222} ; Figure 5.8), per-cent alpha helix content as derived by deconvolution of the spectra gathered (Figure 5.9), and the initial spectrum at 15 °C (Figure 5.10, 15 °C i), the spectrum at 60 °C (Figure 5.10, 60 °C), and the final spectrum at 15 °C after the heat-cool process (Figure 5.10, 15 °C f).

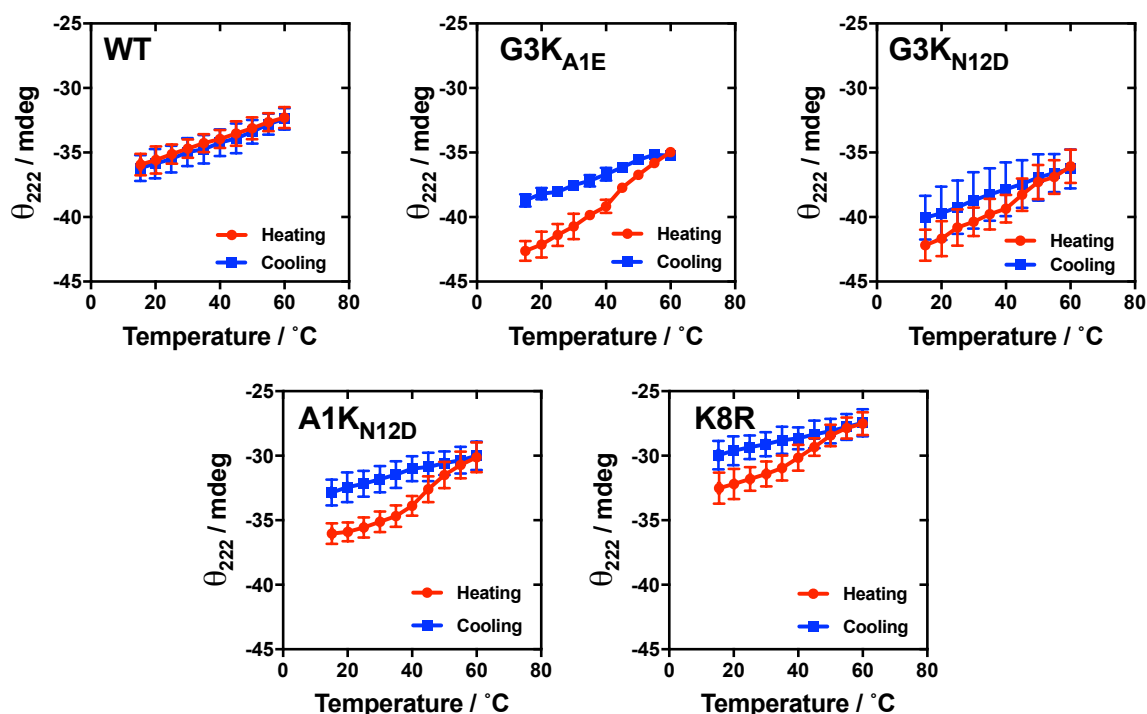


Figure 5.8. Circular dichroism at 222 nm (ellipticity; θ_{222}) of bacteriophage variants during heating and cooling. WT = wild type. (n = 3). Error bars indicate one standard deviation.

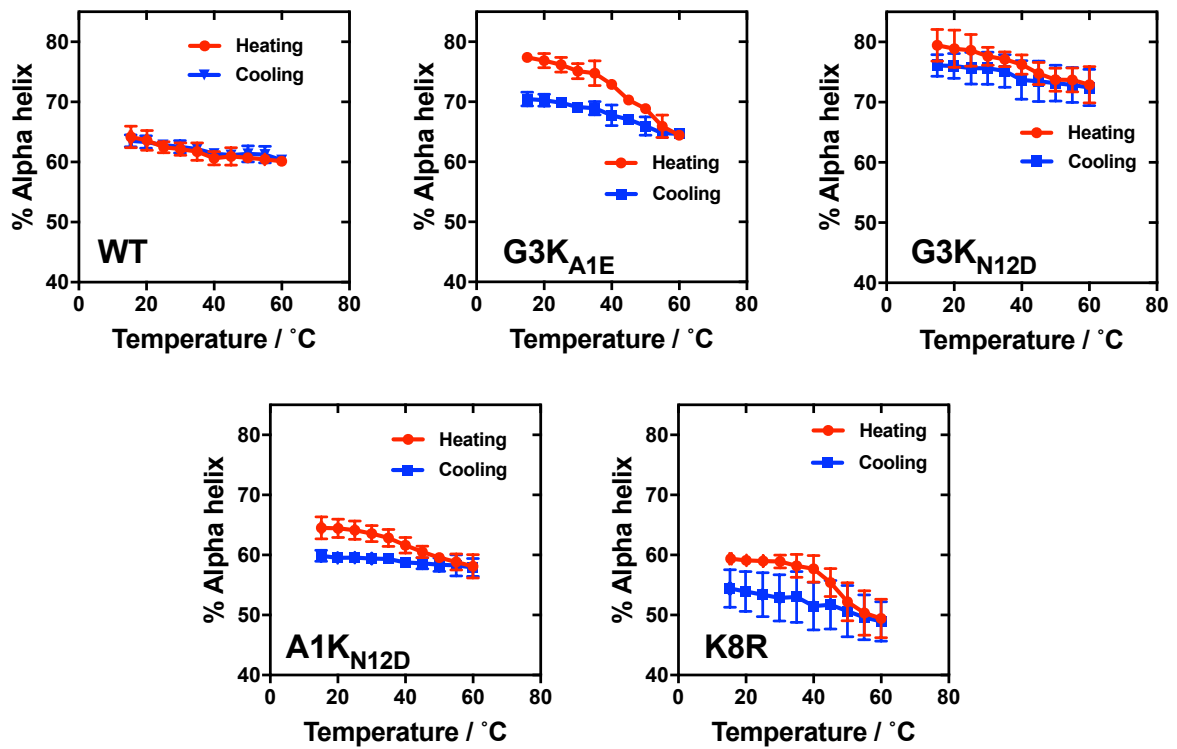


Figure 5.9. Alpha helical content of bacteriophage variants during heating and cooling. WT = wild type. (n = 3). Error bars indicate one standard deviation. CD data deconvolution performed using K2D3 software (Louis-Jeune *et al.*, 2011).

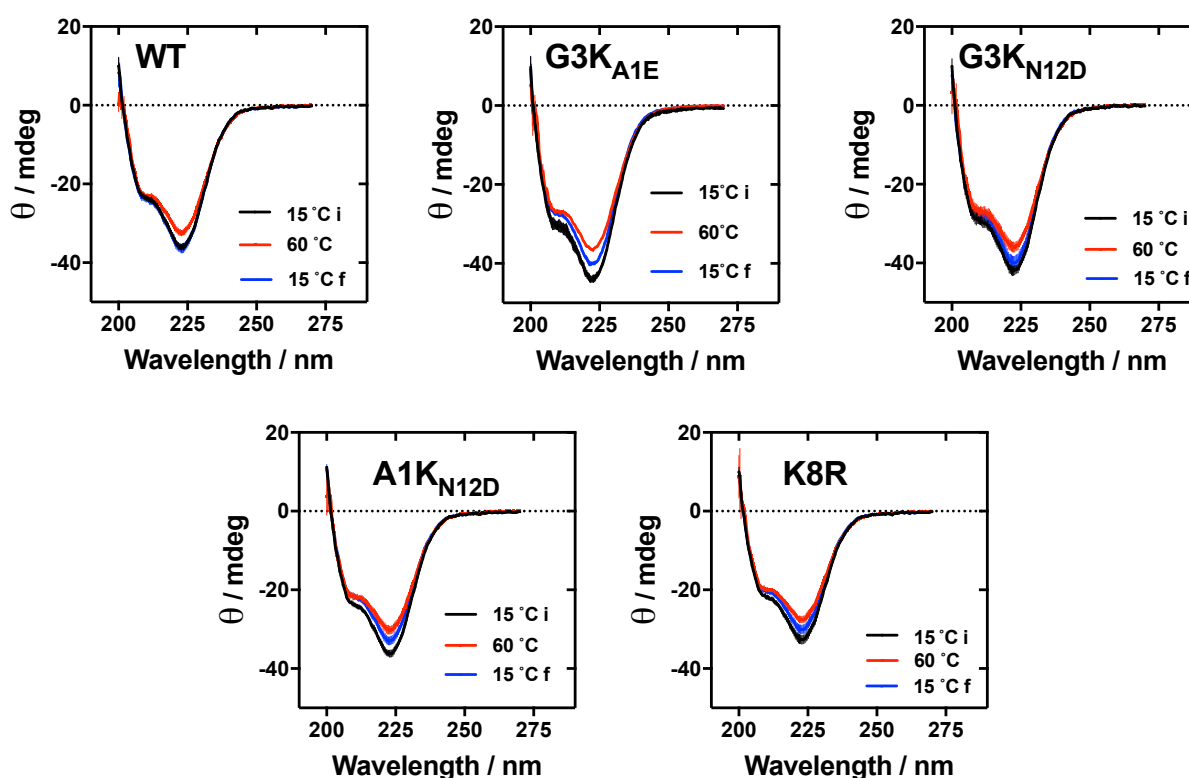


Figure 5.10. Circular dichroism spectra (ellipticity; θ) of bacteriophage variants before (15 °C i), during (60 °C) and after (15 °C f) heating. WT = wild type. ($n = 3$). Error bars indicate one standard deviation.

Examination of Figure 5.8 reveals that the CD_{222} of all bacteriophage variants decreased in magnitude upon heating to 60 °C. This is indicative of a loss of alpha helix content. This was confirmed by deconvolution of the spectra, yielding the data in Figure 5.9. The CD_{222} and alpha helix content traces gathered for heating and cooling wild type bacteriophage overlapped, showing that the process is reversible. By contrast, the traces for heating and cooling G3K_{A1E} did not overlap. In addition, examination of the CD spectra gathered before, during and after heating reveals that the wild type spectrum returned to its original state following the heat-cool process (Figure 5.10, 15 °C i overlaps with 15 °C f in the WT box). The CD spectrum of G3K_{A1E}, however, did not return to its original state following the heat-cool process.

The results of this experiment indicate a destabilisation of the pVIII coat in the presence of the G3K_{A1E} mutation. This could indicate either: that the pVIII proteins of the mutant had undergone an irreversible transition upon heating; that the kinetics of re-folding had been slowed by the mutation; or that the kinetics of unfolding had been increased in rate by the mutation. To determine whether this effect was specific to the G3K_{A1E} mutation, bacteriophage mutants G3K_{N12D}, A1K_{N12D} and K8R were subjected to the same thermal treatment. As can be seen in Figures 5.8, 5.9 and 5.10, similar to G3K_{A1E} none of the other mutants fully regained their secondary structure following heating to 60 °C and re-cooling to 15 °C. This indicates that all mutants were destabilised in a similar way to the G3K_{A1E} mutant when compared to wild type. It is thus concluded that this effect is not specific to the G3K_{A1E} mutation.

In summary, comparing the results for each variant, it is clear that wild type pVIII refolded more effectively than the mutants. This is evident as the alpha helix content of wild type M13 returned to its initial value upon re-cooling, whereas that of the mutants did not. The same trend is apparent in the CD₂₂₂ and spectral data. These show that the mutant raw signal values did not return to their initial states upon re-cooling but the wild type signal did.

5.4. Discussion

It was the aim of this chapter to investigate whether or not the G3K_{A1E} mutation had altered the thermal stability of the protein coat of M13 bacteriophage compared to the wild type. It was necessary to investigate this as if the bacteriophage had been

significantly thermally destabilised by the mutation it would not have been useful in an assay that required its structural integrity for the read-out (Pacheco-Gómez *et al.*, 2012).

In the experiments where spectral CD data were collected and deconvoluted (Figures 5.6 and 5.9), G3K_{A1E} bacteriophage appeared to have a higher alpha helix content than the wild type in its native state (~75-80 % compared to ~60-65 %), suggesting that the introduction of this mutation altered the folding of the pVIII coat protein. G3K_{N12D} also had a similar increase in alpha helix content whereas A1K_{N12D} and K8R did not. This suggests that this alteration in structure may be due specifically to the G3K mutation. According to Arnold *et al.* (1992), fd bacteriophage (closely related to M13) has an unusual CD spectrum in that the ratio of the peaks at 222 nm and 208 nm ($CD_{222/208}$) is around 1.5. In normal alpha helices, this value is typically between 0.85 and 1.15 and can vary depending on the hydrophobicity of the environment (Nordén *et al.*, 2010). M13 bacteriophage also has this unusual feature in its CD spectrum, as was observed here. Arnold *et al.* concluded that this alteration in relative peak intensity is due to the stacking of aromatic residues between neighbouring pVIII subunits. The authors state that this has implications for deconvolution of bacteriophage CD data and has led to erroneous estimates of alpha helical content in references cited within, as deconvolution algorithms compare input data to standard databases, which would be expected to contain spectra with $CD_{222/208}$ values within the typical range. Given this information, it seems more likely that the discrepancy in the apparent alpha helix content of G3K_{A1E} and G3K_{N12D} and the other bacteriophage variants was due to some small change in the aromatic side-

chain conformation of the pVIII coat than a large alteration in the number of alpha-helical residues. It may seem unusual to suggest that a mutation to an unstructured (Stopar *et al.*, 2003) region in the pVIII protein (residues 1-5) could affect the conformation of the alpha-helical aromatic residues (residues Y21, Y24 and W26). However, Morag *et al.* (2015) observed intersubunit contact, as indicated by homonuclear correlation in nuclear magnetic resonance (NMR) spectroscopy experiments, between the E2 and D5 residues of one pVIII subunit and the E20 and W26 residues of adjacent pVIII subunits (Figure 5.11). The N-terminal region is flexible, however this observation highlights that the residues of the N-terminal region can come into close proximity of the region of pVIII where aromatic residues are most abundant. It is thus conceivable that a mutated residue within the N-terminal region could make contact with, and potentially alter the conformation of, the aromatic residues within the pVIII protein. Validation of this would of course require further study, as the nature of the suggested conformational change cannot be determined from the type of data in this chapter.

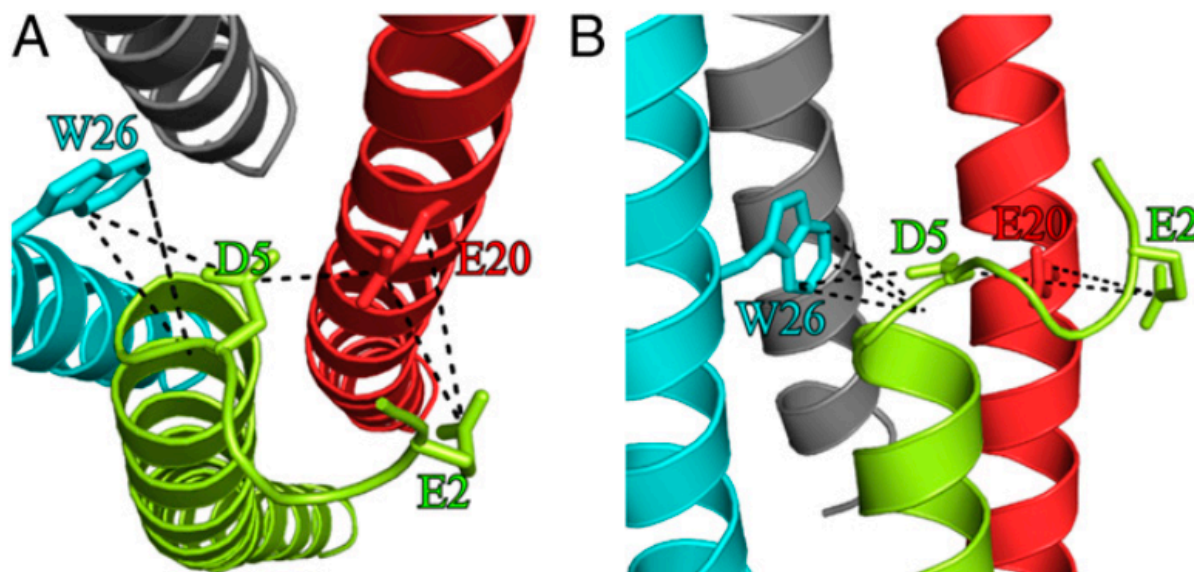


Figure 5.11. Intersubunit contact between pVIII N-terminal residues and region where aromatic residues are most abundant (determined by nuclear magnetic resonance spectroscopy). (A) View from top. (B) View from side. (Reproduced from Morag *et al.*, 2015).

One might reason that increased apparent alpha helix content of a protein may indicate increased stability compared to the equivalent protein with lower apparent alpha helix content. This is because it would suggest that the protein was more highly folded. One might then reason that this indicates that the G3K-containing variants are therefore more stable than the others tested here. However, no other results in any other experiments conducted indicated this. In fact, all experiments indicated that the G3K-containing variants were less stable than the wild type. Therefore, when combining this observation with all other results in this chapter, it can be concluded that the apparent increase in alpha helix content of variants expressing the G3K mutation has no positive impact on the thermal stability of the bacteriophage.

G3K_{A1E} had a slightly reduced melting temperature compared to the wild type. This indicates a loss of coat protein stability induced by the mutation. In addition, all other

mutants tested had a similar loss of stability, indicating that this effect is not specific to the G3K_{A1E} mutation. The melting temperature of G3K_{A1E} remains above 80 °C, however. It thus seems unlikely that this would be a cause for concern in the practical deployment of G3K_{A1E} in the assay format published by Pacheco-Gómez *et al.* (2012).

What might be perceived to be problematic, however, is that the G3K_{A1E} mutant did not fully refold in conditions that permitted the wild type bacteriophage to fully refold (Figures 5.8, 5.9 and 5.10). Again, all other mutants showed a similar loss of stability, indicating that this effect is not specific to the G3K_{A1E} mutation. This indicates that the mutations affected the folding/unfolding thermodynamics, kinetics or both. It is feasible that if the cooling process were slowed down sufficiently, the mutants could fully refold. However, while this may be possible in a laboratory, in a practical setting the heating and cooling rate of the bacteriophage would not be controllable. Thus it might be an important finding that G3K_{A1E} (and the other mutants) do not refold as effectively as the wild type. However, it could be interpreted that the heat-cool cycle used here is at the very extremes of what the assay might be exposed to. Thus, from this perspective, the loss of ~9 % CD signal (Figure 5.8 G3K_{A1E}) might not give cause for concern. Thus the G3K_{A1E} mutant could be used in place of the wild type in the Pacheco-Gómez assay without any practically significant loss of thermal stability.

Figures 5.8-5.10 indicate the changes in bacteriophage coat protein secondary structure during the heat-cool cycle. While this was sufficient to detect changes in thermal stability, there are other determinants of bacteriophage stability that are not

detectable by this data: these are quaternary structure and the interaction between pVIII and the DNA core. It is likely that the temperatures at which the secondary structure was affected similarly affect these structural elements. Thus to gain more insight into the mechanism of the bacteriophage refolding upon cooling, it might be interesting to repeat the experiment, monitoring the LD signal of the bacteriophage against temperature. This would indicate the structural integrity of the bacteriophage particle as a whole, rather than focussing on the secondary structure of the mutated coat protein. This would also be more relevant than Figures 5.8-5.10 to the desired application of the bacteriophage in the Pacheco-Gómez assay.

It may be important to optimise mutants for their thermal stability and refolding efficiency to generate a mutant that is as stable as, if not more stable than, the wild type. This could be achieved using bacteriophage partial library approaches where randomised residues flank a lysine residue and the library of bacteriophages is subjected to repeated rounds of heat exposure and amplification. This would select for those most resilient to heat, whilst retaining expression of the additional lysine residue for dye conjugation (Merzlyak and Lee, 2009; Pershad and Kay, 2013).

5.5. Conclusions

In conclusion, M13 bacteriophage with the G3K_{A1E} mutation is marginally less thermally stable than the wild type. The fact that a range of different mutations caused a similar effect indicates that this effect is not specific to the G3K_{A1E} mutation. However, the effect on thermal stability was not large enough to indicate a barrier to the use of the G3K_{A1E} M13 bacteriophage in an assay that is intended to be used in the field without refrigeration (Pacheco-Gómez *et al.*, 2012). It is thus concluded that the G3K_{A1E} mutant is fit for purpose.

6. ASSEMBLY OF MULTI-VIRION STRUCTURES VIA DYE H- AGGREGATION

6.1. Introduction

There are two points to keep in mind while reading this chapter. The first is that it is distinct from the others in that it is better categorised as incremental nanotechnology than evolutionary. The second point is that this chapter contains two lines of investigation. The first is the ordered assembly of organic dyes on the surface of M13 bacteriophage. The second is the use of said dyes to drive the assembly of multi-bacteriophage structures.

It is the aim of this introductory section to provide the reader with an understanding of the ordered assembly of organic dyes and the motivation behind the deliberate induction of assembly. Furthermore, the fluorescent dye tetramethylrhodamine isothiocyanate (TRITC) is introduced as this was used in the manuscript in this chapter. The motivation behind the generation of multi-virion assemblies of M13 bacteriophage is covered in the introduction chapter (section 1.3.4) and in the introduction section in the manuscript in this chapter.

6.2. Ordered assembly of organic dyes

A frequently encountered phenomenon in the use of organic dye molecules is their tendency to form ordered self-assemblies. These can be H-aggregates (so named for their characteristic hypsochromically (blue-) shifted absorbance spectrum) or J-aggregates (named after their discoverer; Jelley, 1936). Dye molecules can self-associate by π -electron stacking, van der Waals forces, hydrogen bonding and ionic interactions (Zhang and Cole, 2017). They can be induced into H- or J-aggregation by a number of methods, reviewed in the following sections.

H- and J-aggregates are defined by their 'slip angle' (Figure 6.1). This is the angle between the lines drawn through the centres of dye molecules in a stack, and the transition dipole moment of one of the dye molecules. Aggregates with slip angles greater than 54.7° are H-aggregates, and those with slip angles less than 54.7° are J-aggregates (Zhang and Cole, 2017).



Figure 6.1. Schematic of H- and J-aggregates. Thick black line = long axis of dye molecules; Blue dashed line = line through centres of dye molecules; Angle = slip angle.

H- and J-aggregates may be distinguished experimentally by their characteristic absorbance spectra. H-aggregated dyes have a hypsochromically-shifted absorbance spectrum compared to the monomer. In contrast, the absorbance spectrum of J-aggregated dyes is bathochromically (red-) shifted relative to the monomer. These effects are due to excitonic coupling: the intermolecular interaction of dye transition dipoles when they are induced by light.

When the separation of two transition dipoles is small, i.e. within an aggregate, their lowest unoccupied molecular orbitals (LUMO), of energy E , will split into two states with energies E' and E'' (Figure 6.2, Jablonski diagram), lower and greater than E ,

respectively. Transition to either of these states is favoured depending on the relative orientation of the transition dipoles. In the case of H-aggregates, a parallel (Figure 6.2, arrowheads adjacent) arrangement of transition dipoles has energy E'' , and an antiparallel arrangement (Figure 6.2, arrowheads opposite) has energy of E' . This is due to destabilisation and stabilisation from partial charge repulsion and attraction, respectively. As an antiparallel arrangement of two side-by-side (H-aggregated) dipoles yields no net dipole, whereas a parallel arrangement does, the lower energy transition is forbidden, giving rise to the characteristic hypsochromic shift in the absorbance spectrum of H-aggregated dyes compared to the monomeric form (Figure 6.2).

In the case of J-aggregates, a parallel arrangement of transition dipoles has energy of E' , whereas an antiparallel arrangement has energy of E'' , again due to partial charge attraction and repulsion, respectively. In contrast to H-aggregates, in a J-aggregate an antiparallel arrangement of dipoles gives rise to no net dipole and therefore a forbidden transition. However, a parallel arrangement has a net dipole and is therefore permitted. This gives rise to the characteristic bathochromic shift in the absorbance spectrum of a J-aggregated dye (Bardeen, 2014).

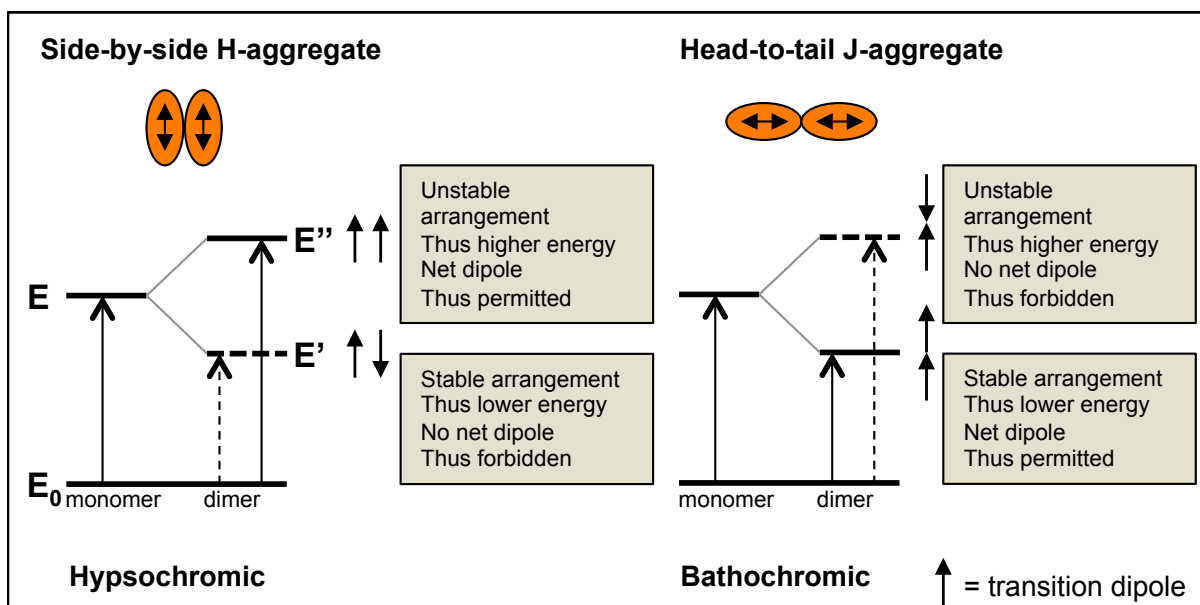


Figure 6.2. H- and J-aggregation of dyes. Transition dipole pairs with like ends adjacent give rise to a higher-energy transition than the monomer. Where transition dipole pairs have no net dipole, the transition is forbidden, as indicated by dashed arrows (permitted transitions indicated by solid arrows). The increased band gap in H-aggregates gives rise to the hypsochromic shift, and the decreased band gap in J-aggregates gives rise to the bathochromic shift.

6.3. Why are J-aggregates sought-after?

The involvement of dyes in the assemblies explained above gives rise to a number of interesting optical properties not displayed by the monomeric dye. For example, both H- and J-aggregates have been shown to exhibit superradiance, a phenomenon in which a large number of assembled dye molecules simultaneously fluoresce, giving rise to coherent emitted light (Ratner, 2003; Meinardi *et al.*, 2003). Superradiance of rubidium-87 has been harnessed to produce a new type of laser with improved coherence over traditional lasers but as of yet the superradiance of H- and J-aggregated dyes have not been used in this way (Bohnet *et al.*, 2012).

Of particular interest to researchers in biomimetics is the use of J-aggregates to harness solar energy. The reasoning behind this is that in biological photosystems

chromophores are precisely arranged to maximise electron transport, and thus light harvesting efficiency (Scholes *et al.*, 2011). Researchers aim to mimic this and harness the additional properties that J-aggregation affords, as explained below.

J-aggregates exhibit highly efficient exciton transport along the length of the aggregate (Valleau *et al.*, 2012). Consequently, there have been attempts to use them to capture light energy - mimicking bacterial light-harvesting antennae (chlorosomes) - and to inject electrons into circuits within dye-sensitised solar cells (DSSCs) (Marek *et al.*, 2011; Zhang and Cole, 2017). Conversely, H-aggregates do not possess high exciton transport efficiency. H-aggregates have been trialled in DSSCs, however, and in some cases have been shown to improve light-capturing efficiency from spectral broadening (Mann *et al.*, 2008; Mulhern *et al.*, 2011; Zhang and Cole, 2017).

Furthermore, J-aggregates show ultrafast electron injection compared to their monomeric counterparts. This reduces back-transfer of electrons from the DSSC circuit to the sensitising dye. This in turn improves the light conversion efficiency of the device compared to when monomeric dyes are used (Verma and Ghosh, 2012).

There have been attempts to harness the precise arrangement of biological light-harvesting chromophores without directly controlling the assembly of dyes. Modesto-Lopez *et al.* (2010) incorporated whole bacterial chlorosomes into a functioning DSSC. The resulting device harnesses the precise arrangement of bacteriochlorophyll molecules within. They aim to use this approach to incorporate

synthetic chromophores into chlorosomes. This would allow for the expansion of spectral coverage by incorporating broadly absorbing dyes. This approach takes advantage of the chromophore order displayed in chlorosomes, thus circumventing the challenges associated with controlling chromophore assembly.

Overall, J-aggregates have a number of interesting potential applications due to their properties not displayed by their monomeric counterparts. Thus their production is highly sought-after.

6.4. Production of dye aggregates

Dye aggregate formation can be promoted by either altering the solvent conditions, altering the dye structure, by providing a scaffold onto which a small subset of the dye population adsorbs and promotes the growth of dye aggregates, or by forcing the association of dye molecules by covalent attachment to a molecular scaffold. This final approach relies on the regular spacing of binding sites rather than the growth of dye aggregates upon a nucleation site.

Solvent conditions shown to affect the growth of dye aggregates include: solvent polarity (Choi, 2008); dye concentration (von Berlepsch *et al.*, 2000); salt concentration (Slavnova *et al.*, 2005); temperature (Chakraborty *et al.*, 2015); and solvent pH (Egawa *et al.*, 2007). In addition, the tendency of a dye to form aggregates may be tuned by the alteration of substituent groups surrounding the dye chromophore (Biver *et al.*, 2007).

Scaffolds used to promote nucleation and growth of dye aggregates include AgBr crystals (Saijo and Shiojiri, 1996) and dendrimers (branched polymers) (Steiger *et al.*, 2009). An advantage of using polymers is that, within the limits of chemical synthesis, they may be tuned and optimised to promote nucleation and growth of aggregates of the chosen dye, meaning that this approach is not limited by the affinity of any particular dye to any particular scaffold.

DNA has been used to generate both H- and J-aggregates of Cyanine3 (Cy3) and Cyanine5 (Cy5) dyes (Markova *et al.*, 2013; Nicoli *et al.*, 2016). By the specific labelling of DNA bases within a short nucleotide sequence, the distance between and orientation of the attached dyes may be tuned. This allows the generation of specific dye aggregates. While the previously cited studies investigated the effect of dye separation and relative orientation on the exciton coupling, they did not investigate the effect of the surrounding DNA sequence. Cunningham *et al.* (2018) investigated this approach, and found that sequences containing guanine and cytosine base pairs flanking the Cy3-modified base pair promoted the formation of J-like aggregates. This indicated that, like chemical polymers, biological scaffolds may also be tuned to promote the chosen dye aggregate. Furthermore, Cy3 aggregate conformation on DNA scaffolds has been shown to be temperature-dependent, again highlighting the tunability of this approach (Kringle *et al.*, 2018). This approach to generating dye aggregates has subsequently been employed to generate nanomaterials capable of photonic energy transfer along DNA strands, mimicking the light-harvesting antennae of phototrophic bacteria (Nicoli *et al.*, 2017; Boulais *et al.*, 2018).

It was hypothesised for this project that the protein coat of M13 bacteriophage might be used to template the growth of dye aggregates. Because the outer coat of M13 displays a regularly patterned array of functional groups, it can be chemically targeted for dye conjugation. Dyes could be induced into aggregation either by proximity-induced aggregation, or by providing a nucleation site for subsequent aggregate growth.

Were this approach successful in the generation of J-aggregates, it would be advantageous over the existing J-aggregate production techniques as it would be possible to use phage display to generate a phage variant that could deliver the dye assembly to a molecular location. This could be advantageous in a dye-sensitised solar cell, where efficiency of charge injection into the circuit depends on the proximity of the dye and the titanium dioxide electrode within the circuit.

6.5. Tetramethylrhodamine isothiocyanate (TRITC)

TRITC (Figure 6.3) is a fluorescent dye that is used to label proteins for cell imaging studies (Kutyrev *et al.*, 2017). As depicted in Figure 6.3, the isothiocyanate group (-NCS) of TRITC reacts to form a covalent linkage with amine groups (Aslam and Dent, 1998). These are present on the amino-terminus and lysine residues of proteins. TRITC has been reported to H-aggregate upon binding to proteins (Panchuk-Voloshina *et al.*, 1999; Ravdin and Axelrod, 1977). It was thus used in the manuscript in this chapter (M3) in an attempt to induce the assembly of multi-virion structures of M13 bacteriophage by forming H-aggregates between virions.

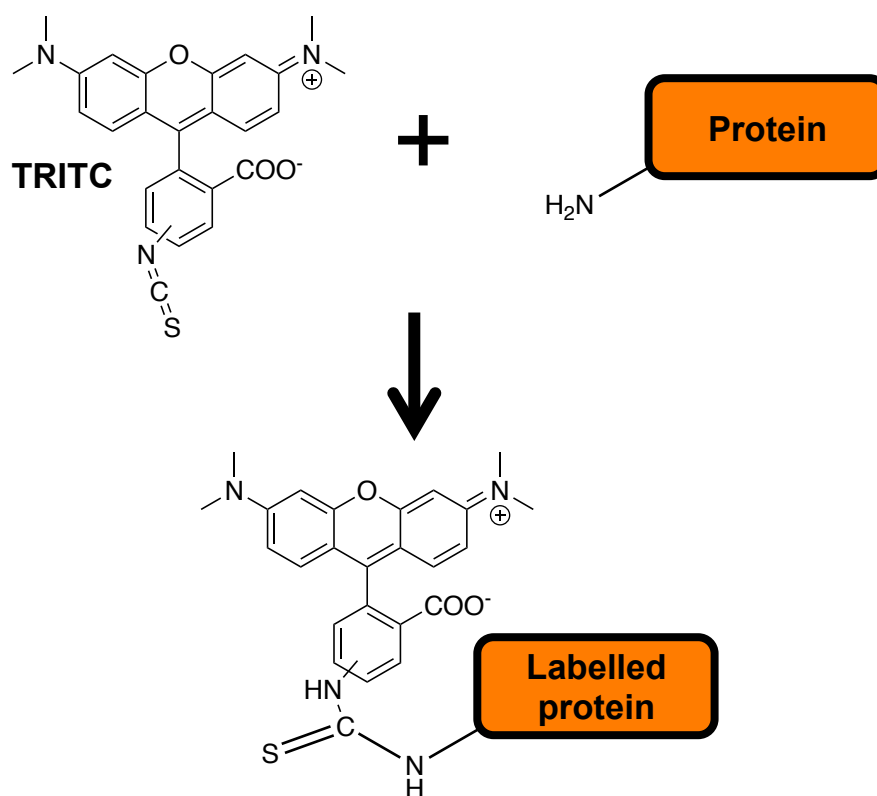


Figure 6.3. Protein labelling with tetramethylrhodamine isothiocyanate. Structures drawn using ChemDraw Professional 16.0.

6.6. Project aims

This project had two aims: first, to investigate the suitability of the surface of M13 bacteriophage as a template for the growth of ordered dye assemblies; and second to develop novel nano-architectures of M13 bacteriophage following modification with organic dyes and to investigate whether said architectures exhibited properties that the individual bacteriophage did not.

6.7. Manuscript number 3 (M3)

**Dye aggregate-mediated self-assembly of bacteriophage
bioconjugates**

Matthew Tridgett, Lucía Lozano, Paolo Passaretti, Nimai R. Desai, Toby J. Proctor,
Haydn A. Little, Richard T. Logan, Kenton P. Arkill, Pola Goldberg Oppenheimer, and
Timothy R. Dafforn

Bioconjugate Chemistry, 2018, **29**, 3705-3714

Author contribution statement: LL contributed to the UV-Vis data collection. PP conducted the atomic force microscopy experiments. NRD, TJP and KPA conducted preliminary experiments that were not included in this manuscript. HAL and RTL provided technical advice. PGO provided technical advice and assistance with the SERS experiment, and gathered STEM images. TRD was the supervisor and edited the manuscript. MT contributed all other aspects.

Signed:.......... Timothy R. Dafforn

Signed:.......... Matthew Tridgett

M3.1. Abstract

One of the central themes of biomolecular engineering is the challenge of exploiting the properties of biological materials. Part of this challenge has been uncovering and harnessing properties of biological components that only emerge following their ordered self-assembly. One biomolecular building block that has received significant interest in the past decade is M13 bacteriophage. There have been a number of recent attempts to trigger the ordered assembly of M13 bacteriophage into multi-virion structures, relying on the innate tendency of M13 to form liquid crystals at high concentrations. These, in general, yield planar two-dimensional materials. Presented here is the production of multi-virion assemblies of M13 bacteriophage via the chemical modification of its surface by the covalent attachment of the xanthene-based dye tetramethylrhodamine (TMR) isothiocyanate (TRITC). We show that TMR induces the formation of three-dimensional aster-like assemblies of M13 by providing “adhesive” action between bacteriophage particles through the formation of H-aggregates (face-to-face stacking of dye molecules). We also show that the H-aggregation of TMR is greatly enhanced by covalent attachment to M13 and is enhanced further still upon the ordered self-assembly of M13, leading to the suggestion that M13 could be used to promote the self-assembly of dyes that form J-aggregates, a desirable arrangement of fluorescent dye, which has interesting optical properties and potential applications in the fields of medicine and light harvesting technology.

M3.2. Introduction

There are a number of examples in nature where the ordered self-assembly of discrete structural components or “parts” into larger structures leads to the emergence of properties that the individual parts do not possess. Examples include: the ordered self-assembly of colourless “parts” giving rise to the emergence of structural colour (Vignolini *et al.*, 2012; Michielsen and Stavenga, 2008; Srinivasarao, 1999; Vignolini *et al.*, 2015; Barrows and Bartl, 2014); the formation of multienzyme complexes, which are more efficient catalysts than the mixture of their individual components (Agapakis *et al.*, 2012); and the formation of structurally dynamic microtubules, which can be responsible for chromosome separation during cell division, or cell motility, depending on the self-organisation of the “part” that comprises its structure, the protein tubulin (Berg *et al.*, 2012; Dumont and Prakash, 2014). A challenge within the field of bioengineering is understanding and replicating these phenomena and ultimately, exploiting the properties that emerge when self-assembly processes are created *in-vitro*. As extensively reviewed (Sun *et al.*, 2017), the “parts” used in such artificial self-assembly processes are usually enzymes, natural or artificial, in single- or multi-species mixtures; viral coat proteins, such as Tobacco Mosaic Virus coat protein, used to generate nano-scale rings and rods, which are then used to template the assembly of multi-enzyme complexes; or proteins of other sources, in single- or multi-species mixtures, used in the production of protein hydrogels, which are anticipated to have applications in tissue engineering and regenerative medicine.

One such biological entity that has often been used as a “part” in the development of materials is M13 bacteriophage, a filamentous virus with dimensions of 6 x ~1000 nm that replicates via infection of *Escherichia coli* (*E. coli*) cells expressing the F-pilus. M13 bacteriophage has a very simple structure, comprising 2700 repeats of major coat protein, pVIII, and five repeats of each of the minor coat proteins pIII and pVI on one end, and pVII and pIX on the other end (Marvin, 1998; Morag *et al.*, 2015). Because of the structural and genetic simplicity of M13 bacteriophage, its physical and chemical characteristics can easily be manipulated via chemical and genetic modifications. This physico-chemical flexibility has been exploited by a number of groups to develop advanced materials for a range of applications from cancer cell labelling to antibiotic drug delivery (Li *et al.*, 2010; Yacoby *et al.*, 2006; Suthiwangcharoen *et al.*, 2011; Carrico *et al.*, 2012; Palaniappan *et al.*, 2013; Hilderbrand *et al.*, 2008; Kelly *et al.*, 2006; Pacheco-Gómez *et al.*, 2012; Dang *et al.*, 2011). Of particular recent interest is the use of M13 bacteriophage as a building block in the production of multi-bacteriophage assemblies to generate bacteriophage films. In combination with genetic or chemical modifications, the tendency of M13 to form multi-bacteriophage assemblies has been employed by researchers in the development of materials based on biological parts (Lee *et al.*, 2003; Merzlyak *et al.*, 2009). In some cases the self-assembly of M13 has generated emergent properties that have been used in materials development. For example, it has been shown that when a sample of M13 bacteriophage is drawn up from solution onto a gold-coated silicon substrate, it forms ordered liquid crystalline structures without any modification made to the surface of the bacteriophage. This material made from M13 bacteriophage has the property of chiral reflectivity, a property that, prior to ordered

self-assembly, individual M13 virions do not possess (Chung *et al.*, 2011). However despite these clear successes there still remains a significant gap in our ability to control the higher order assemblies of bacteriophage M13.

Presented here is a method that allows production of multi-virion assemblies of M13 bacteriophage via chemical modification of its outer coat with the xanthene-based dye, tetramethylrhodamine (TMR) through the use of its amine specific derivative tetramethylrhodamine isothiocyanate (TRITC). The process harnesses the interactions between TMR moieties to provide an inter-virion “adhesive”. We show that the TMR groups drive the formation of multi-phage assemblies that resemble asters. These asters are also able to link to form a “beads on a string” morphology. The combination of these new morphologies with the presence of visible chromophores offers exciting new routes for the future development of bio-photonics devices.

M3.3. Experimental section

M3.3.1. Growth of M13 bacteriophage

Bacteriophage stocks were grown and purified as previously described (Pacheco-Gómez *et al.*, 2012).

M3.3.2. Conjugation of tetramethylrhodamine isothiocyanate to M13 bacteriophage

Tetramethylrhodamine-5-(and-6)-Isothiocyanate (mixed isomers) (TRITC) (Thermo Fisher Scientific) was dissolved in dimethyl sulfoxide (DMSO) to a concentration of

22.5 mM (10 mg.mL^{-1}) and a 150 nM (2.5 mg.mL^{-1}) solution of M13 was made in 50 mM potassium phosphate buffer, pH 8.0. In a 1.5 mL microcentrifuge tube, 20 μL of the TRITC solution was added to 980 μL of the M13 solution. The reaction mix was left rotating overnight in the dark at 20 °C. To remove unbound dye the reaction mix was buffer exchanged, using a PD midiTrap G-25 column (GE Healthcare), into 1.5 mL of fresh 50 mM potassium phosphate buffer pH 8.0, following manufacturer's instructions.

M3.3.3. Mass spectrometry

Equal volumes of chloroform and M13 or M13TRITC at 96 nM (1.6 mg.mL^{-1}) were combined in a 1.5 mL microcentrifuge tube and vortexed. Following centrifugation at 11000 x g for 15 minutes, the upper fraction was discarded, the pellet was removed from the interface and resuspended in 500 μL of Milli-Q water, and the lower fraction was also discarded. To the pellet resuspension 500 μL of chloroform was added. After the above process was repeated twice, the pellet was removed from the interface and resuspended in 400 μL of isopropanol + 0.1% (v/v) glacial acetic acid. The solution was then vortexed and centrifuged as before for 20 minutes and the pellet was retained for analysis. Mass spectrometry analysis was conducted at the Centre for Chemical and Materials Analysis at the University of Birmingham.

M3.3.4. Conjugation of TRITC to L-Alanine

In a 1.5 mL microcentrifuge tube, in 50 mM potassium phosphate buffer pH 8.0, L-Alanine (Sigma) and TRITC were combined at 50 mM and 0.2 mM, respectively, to a

total volume of 1 mL. The mixture was left to conjugate overnight in the dark at 20 °C with constant slow mixing before any experiments were conducted with the material.

M3.3.5. Conjugation of M13 to N-succinimidyl S-acetylthioacetate

In a 1.5 mL microcentrifuge tube, M13 (120 nM; 2 mg.mL⁻¹) and N-succinimidyl S-acetylthioacetate (3 mM) (Calbiochem) were combined in 50 mM potassium phosphate buffer pH 8.0, to a total volume of 1 mL. The mixture was incubated overnight in the dark at 20 °C with constant slow mixing. The M13 conjugate was extracted from the reaction mix using a PD midiTrap G-25 column (GE Healthcare) to produce 1.5 mL of M13 conjugate in 50 mM potassium phosphate buffer pH 8.0.

M3.3.6. Ammonium sulphate precipitation

When UV-visible (UV-Vis) absorbance or fluorescence anisotropy was measured, M13 and TRITC were combined at concentrations of 11 nM (0.18 mg.mL⁻¹) and 1.2 μM, respectively, whether alone or in the various conjugates. When LD was measured, the bacteriophage concentration was 2.7 nM (0.045 mg.mL⁻¹) and the TRITC concentration was 0.3 μM. All experiments were carried out in 50 mM potassium phosphate buffer pH 8.0 with varying concentrations of ammonium sulphate (0.00 – 2.25 M).

M3.3.7. Absorbance measurements

All absorbance spectra were measured using an unthermostatted Jasco V-550 UV-Vis Spectrophotometer. Either 0.1 cm or 1 cm path length cuvettes were used for measurements depending upon the absorbance of the sample. The following

parameters were used: bandwidth, 1.0 nm; data pitch 1.0 nm; scanning speed 200 nm.min⁻¹; 1 accumulation. Samples were blanked against appropriate buffers and zeroed at 650 nm using Spectra Manager software. TRITC concentrations stated above were calculated using the absorbance value at 544 nm and a molar extinction coefficient of 100000 M⁻¹.cm⁻¹, as per manufacturer's instructions. M13 concentrations were calculated using the absorbance value at 269 nm and an extinction coefficient of 3.84 mg⁻¹.cm⁻² (Berkowitz and Day, 1976).

M3.3.8. Linear dichroism measurements

All linear dichroism spectra were collected using an unthermostatted Jasco J-1500 CD Spectrometer, a Dioptica DIOP-0002 Ultra Low Volume Linear Dichroism Couette Flow Cell and a 0.5 mm path length Couette cell. The following parameters were used: bandwidth, 2.0 nm; data pitch, 1.0 nm; scanning speed, 100 nm.min⁻¹; digital integration time, 1 s; data interval, 1 nm; 3 accumulations. Readings taken with no rotation were subtracted from readings taken at 3000 revolutions per minute using Spectra Manager 2 software to produce the final corrected spectra.

M3.3.9. Fluorescence anisotropy measurements

All fluorescence anisotropy measurements were made using an unthermostatted Perkin Elmer LS50B Luminescence Spectrometer with the following settings: λ_{ex} 555 nm, λ_{em} 577 nm, excitation slit width of 5 nm, emission slit width of 5 nm, integration time 5 s. The cuvette used was 1 cm path length in the excitation direction and 5 mm in the emission direction.

M3.3.10. Transmission electron microscopy

On a glow discharge-treated copper TEM support grid, 4 μL of the 0.00 M, 1.00 M and 2.00 M ammonium sulphate-containing bacteriophage samples used in the LD experiments were deposited. After one minute, uranyl acetate was added before the grids were air-dried. All TEM images were gathered using a JEOL JEM2200-FS transmission electron microscope with 4000-10000X magnification at the School of Life Sciences Microscopy Suite at the University of Warwick, UK.

M3.3.11. Scanning transmission electron microscopy

STEM images were obtained using a Hitachi s5500 scanning transmission electron microscope with a cold field emission source and lens detector with 4 \AA resolution, allowing adjustable acceptance angle STEM imaging, at acceleration voltages of 1.0 and 30.0 kV.

M3.3.12. Atomic force microscopy

M13 and M13TRITC (bacteriophage concentration 3 nM ($0.05 \text{ mg}\cdot\text{mL}^{-1}$)) in 50 mM potassium phosphate pH 8.0 ± 1.00 M ammonium sulphate were dried on P-type silicon wafer and characterised with AFM (BRUKER – Innova®). Images were acquired in tapping mode (scan rate: 0.5 Hz and 1.0 Hz for $5 \mu\text{m}^2$ and $10\text{-}20 \mu\text{m}^2$ areas, respectively) with BRUKER RTESPA-300 probe (T: $3.4 \mu\text{m}$; L: $125 \mu\text{m}$; W: $40 \mu\text{m}$; f_0 : 300 kHz; k: 40 N/m). Images and cross sections were processed and exported with Gwyddion®.

M3.3.13. Dynamic light scattering

DLS measurements were taken using a Malvern Zetasizer Nano S DLS system with a 633 nm laser. M13 and TRITC were combined at concentrations of 10.8 nM (0.18 mg.mL⁻¹) and 1.2 μM, respectively, whether alone or in the various conjugates. The bacteriophage samples were in 50 mM potassium phosphate buffer, pH 8.0, with either 0.00 M or 1.00 M ammonium sulphate.

M3.4. Results and discussion

The aim of this study was to produce a self-assembling nanostructure using M13 bacteriophage as a building block. One of the challenges in this sort of study is having an easily available signal to identify when assembly has taken place. To address this we have chosen to use TRITC as an inter-phage assembly agent. The TMR group on TRITC is known to self-associate in an H-aggregate formation, which is the non-covalent, face-to-face stacking of dye molecules. This is in contrast to the brickwork-like stacking of dye molecules in J-aggregates. Formation of the H-aggregate is detectable as a hypsochromic (blue) shift in its absorbance spectrum. This provides an elegant method to assess whether intermolecular interactions between TMR moieties (and anything to which they are conjugated) are occurring.

M3.4.1. Conjugation of TRITC to M13 bacteriophage

Before assessing the use of TRITC as an inter-phage assembly agent in a multi-phage nano-assembly, it was first necessary to confirm the attachment of the dye to the bacteriophage to form the conjugate, M13TRITC. In these experiments, a reactive isothiocyanate group on the TRITC was used to conjugate the dye to the

M13 virion via free amine groups. The majority of free amine groups occur on the pVIII protein of the virion coat. There are close to 2700 pVIII proteins per virion particle and each pVIII has two solvent accessible amine groups, one at the N-terminus of the protein and the other within the lysine residue at position eight. After the reaction between TRITC and M13 the unreacted dye was removed using gel permeation chromatography. The resulting product was analysed using absorbance spectroscopy taking advantage of the specific absorbance signals from M13 bacteriophage and TRITC. These data show that the species eluted from the column loaded with the conjugate had absorbance peaks attributable to both M13 (269 nm) and TRITC (552 nm) confirming that the conjugation had been successful (Figure M3.1 a). This indicates that approximately 13% of pVIII protein subunits (~350 per virion) were labelled with TRITC. Control experiments where dye alone was added to the column showed no detectable TRITC eluted from the column (*Control eluate*, Figure M3.1 a). This demonstrates that the elution of TRITC in the experiment containing the conjugate was not due to overloading of the column, thereby confirming that elution of dye in the conjugate was due to association of the dye with M13 bacteriophage. The conjugation was further analysed by positive electrospray ionisation time of flight mass spectrometry (TOF MS ES+). These data show that for unlabelled M13 a peak at m/z 1309.8 ($z = 4$, thus $m = 5235$) was observed that correlated with the calculated monoisotopic mass of M13 major coat protein pVIII (Figure M3.1 b). The same analysis of the product of the conjugation procedure, M13TRITC, yielded peaks both at m/z 1309.8 ($z = 4$, thus $m = 5235$) and at m/z 947.4 ($z = 6$, thus $m = 5678.52$). This latter peak is equal to the monoisotopic mass of pVIII protein conjugated to a single TRITC molecule. The results of mass

spectrometry analysis thus confirmed the covalent attachment of TRITC to M13 major coat protein, pVIII following the conjugation procedure.

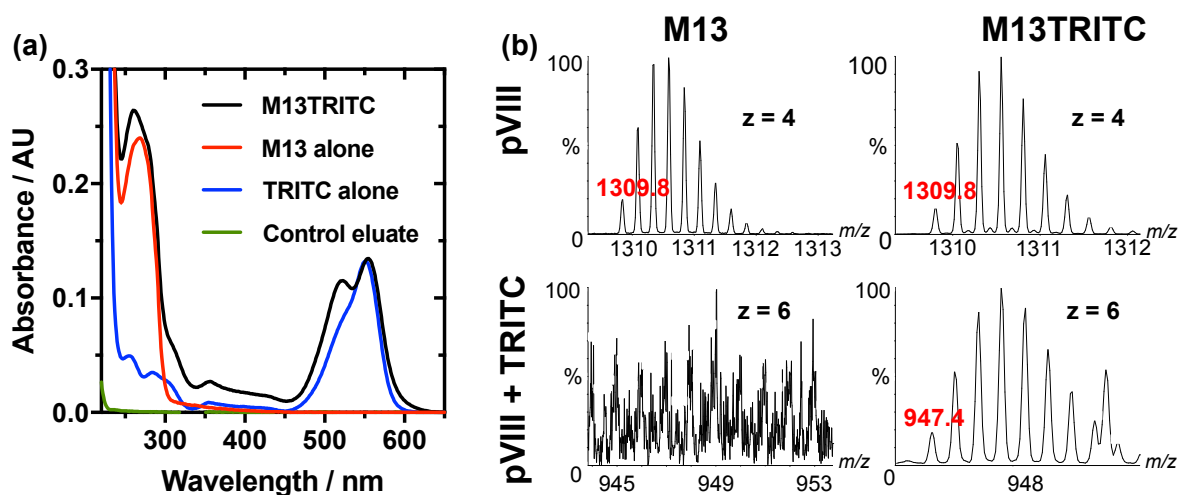


Figure M3.1. (a) UV-Vis spectrum of M13 bacteriophage before and after conjugation to tetramethylrhodamine isothiocyanate (TRITC). (b) Mass spectrum of M13 before and after conjugation to TRITC. Where m = mass and z = charge. $pVIII$ = M13 major coat protein pVIII, $m/z = 1309.8$, $z = 4$, therefore $m = 5235$. $pVIII + TRITC$ = M13 major coat protein labelled with TRITC ($M_r = 443.52$), $m/z = 947.42$, $z = 6$, therefore $m = 5678.52 = 5235 + 443.52 = m$ of pVIII + m of TRITC.

M3.4.2. Formation of TRITC H-aggregates

Before experiments were conducted with M13TRITC, the behaviour of the dye alone was investigated to establish the conditions under which the dye would assemble into H-aggregates. Previous studies have shown that the extent of dye assembly can be assessed by monitoring the ratio of absorbance values at spectral regions attributable to different states of dye assembly (Shakiba *et al.*, 2016; Somasundaran, 2006). To monitor TRITC assembly the ratio of peaks at 525 nm (H-band; attributable to H-aggregate species of TRITC) and 552 nm (Monomeric TRITC band) (H:mono ratio) is used (Figure M3.2 a). Note the absorbance values of the peaks are not used to determine the molar ratio of aggregated and monomeric dye species, only to compare the relative extent of assembly of samples.

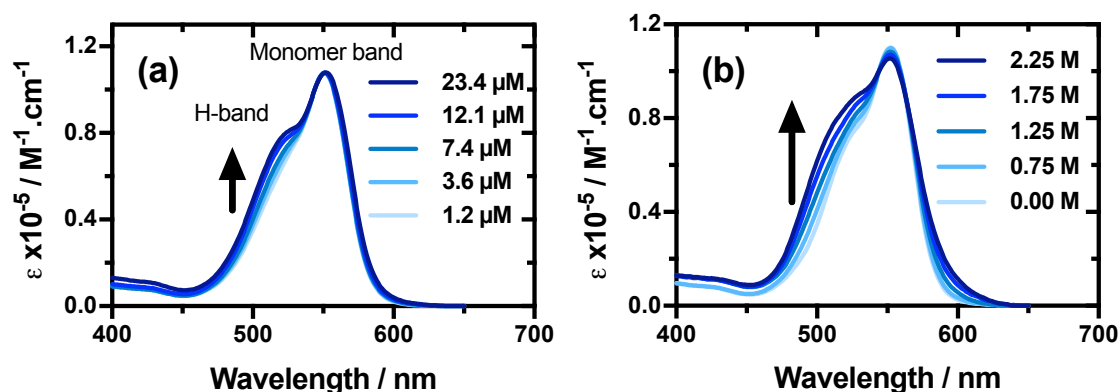


Figure M3.2. (a) Changes in the absorbance spectrum of TRITC with respect to TRITC concentration in 50 mM potassium phosphate buffer at pH 8.0. H-band at 525 nm and monomer band at 552 nm ($n=3$). (b) Effect of ammonium sulphate concentrations on the absorbance spectrum of TRITC in 50 mM potassium phosphate buffer at pH 8.0 with ammonium sulphate ranging from 0.00-2.25 M ($n=3$).

The first experiment shows the concentration dependence of the TRITC absorbance spectra. These show that as the concentration of TRITC increases the H-aggregate form of the dye appears (as indicated by the presence of the peak at 525 nm). These data were then used to calculate the H:mono ratio. To normalise these data the concentration of TRITC was calculated using the A_{544} value and the extinction coefficient for TRITC of $100000 \text{ M}^{-1}.\text{cm}^{-1}$ (Manufacturer's instructions). As expected increasing the concentration of TRITC increased the H:mono ratio from 0.65 at 1.2 μM to 0.74 at 23.4 μM (Figure M3.2 b), indicating that the formation of TRITC H-aggregates is concentration-dependent.

M3.4.3. Induction of H-aggregate formation using ammonium sulphate

One of the aims of this study was to not only induce assembly of M13 bacteriophage, but to also introduce a chemical trigger for association. It is a routine procedure in protein purification to add ammonium sulphate to decrease the solubility of a protein

whilst retaining its native conformation (Wingfield, 2001). It was reasoned here that as the outer surface of M13 bacteriophage is proteinaceous, ammonium sulphate could be used to induce it to precipitate whilst bound to TRITC, thus bringing TRITC into closer self-association and possibly potentiating the formation of H-aggregates without the need to increase M13 concentration. To examine the effectiveness of ammonium sulphate in inducing H-aggregates, a low concentration of TRITC (1.2 μM) (which was not in the H-aggregate form) was incubated with a range of ammonium sulphate concentrations ranging from 0.00-2.25 M. The degree of H-aggregate formation was assessed using absorbance spectroscopy and showed that addition of 2.25 M ammonium sulphate increased the H:mono ratio from 0.67 to 0.83 (Figure M3.2 b). This indicates that to some extent ammonium sulphate was effective at increasing the local concentration of TRITC and forcing it into self-association to a greater extent than when the concentration was increased to 23.4 μM in the previous experiment, which resulted in an H:mono ratio of 0.74. The result of this experiment provided a rationale for the suggestion that TMR moiety when bound to M13 bacteriophage might be used to join bacteriophage particles in a multi-virion structure in a manner that is concentration dependent and inducible by ammonium sulphate.

M3.4.4. Assembly of M13 bacteriophage using TRITC

With the behaviour of the dye alone elucidated, the above experiment was repeated with M13TRITC to determine whether TRITC conjugation could induce assembly of M13 bacteriophage. M13TRITC was diluted to a range of concentrations and the region of the absorbance spectrum corresponding to the dye was measured. It should be noted that M13 bacteriophage does not have any spectroscopic signals in

this region meaning that there is no interference from M13 bacteriophage signals. As with the equivalent experiment with free dye the concentration of TRITC in the M13TRITC conjugate was calculated using the A_{544} value. A first examination of the spectral data shows that at low concentrations there is a predominance of the monomeric form of the dye. As the concentration of M13TRITC increases the 525 nm peak increases in relative intensity indicating an increase in H-aggregate formation (Figure M3.3 a).

When these data are processed to provide the H:mono ratio (Figure M3.3 b) it can be seen that the amount of H-aggregate increases before eventually plateauing at TRITC concentrations above 10 mM. When this is compared to TRITC alone it is clear that there is a significant difference between the behaviour of the dye alone and the dye when conjugated to M13. Firstly the dye alone does not reach a plateau but continues to rise beyond the maximum concentration used in the experiment. Additionally, the H:mono ratio, indicating the overall amount of H-aggregate present in the sample, at 20 μ M TRITC was significantly lower in the sample containing the dye alone (0.74) than the sample containing the conjugate (1.11).

It might be suggested that the increased H-aggregation of TRITC when bound to M13 may be due to some effect of the presence of M13 in the solution, for example, increased viscosity or an alteration in ionic strength. To rule out these explanations and confirm that the covalent attachment of M13 to TRITC is necessary to increase dye H-aggregation, TRITC was combined with M13 with its TRITC-reactive amine groups blocked by N-succinimidyl S-acetylthioacetate (SATA; conjugate = M13SATA)

at concentrations ranging from 0.40-17.00 μM (Figure M3.3 b). There was no effect on the H-aggregation of TRITC in this control experiment, ruling out that the mere presence of M13 caused the increased H-aggregation of TRITC and confirming that covalent attachment of TRITC to M13 is essential to induce this change.

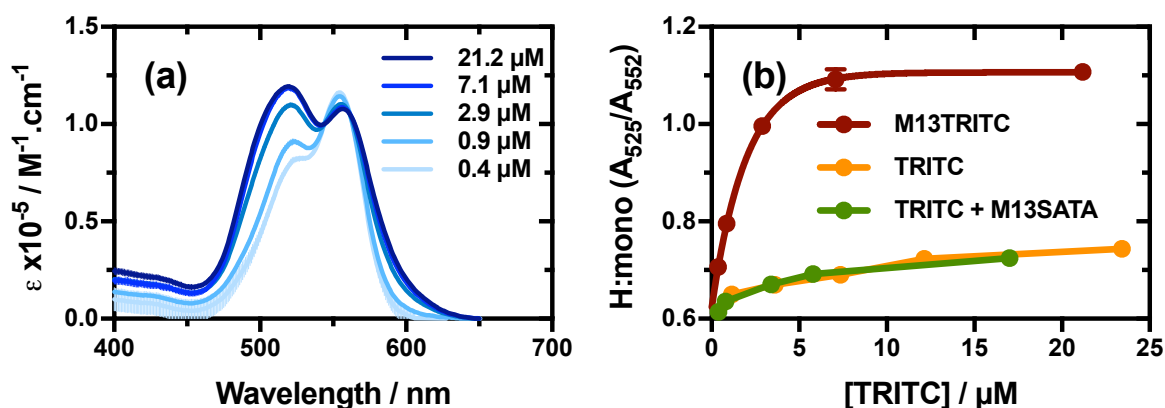


Figure M3.3. (a) Molar absorptance spectrum of M13TRITC at varying dilutions in 50 mM potassium phosphate buffer at pH 8.0 ($n=3$). (b) Extent of H-aggregation of TRITC at varying concentrations, free, when bound to M13 bacteriophage, and free but in the presence of M13 bacteriophage (M13SATA), in 50 mM potassium phosphate buffer at pH 8.0 ($n=3$; error bars represent one standard deviation).

Together these data show that TRITC is able to form H-aggregates even when conjugated to M13. This means that despite being attached to the complex surface structure of the virus the structure does not obstruct the formation of the H-aggregate form. Perhaps surprisingly the attachment to the M13 actually enhanced H-aggregate formation. Why this is the case is unclear, but it could be the result of a number of aspects of the assembly. First it could be an effect of an increase in local concentration of the dye brought about by the regular arrangement of the conjugation groups on the viral surface. One could envisage that an initial productive collision between two bacteriophage particles where an H-aggregate forms between two TRITC moieties on two separate particles then brings other TRITCs on the two

particles into close contact. This could induce a “zipping up” of the TRITCs effectively enhancing the affinity of the TRITC moieties for one another. A second possibility is that the chemical environment around the conjugation site in some way enhances the formation of individual H-aggregates, perhaps by providing an alteration in hydrophobicity that enhances effective affinity. Finally a third option could be that the TRITC moieties are constrained within the M13 structure in the correct orientation for H-aggregate formation. This would reduce the entropic cost of complex formation effectively enhancing affinity. Whatever mechanism explains the increased affinity the effect is helpful for further studies.

M3.4.5. Induction of H-aggregate formation using ammonium sulphate

Our data has shown that ammonium sulphate is able to increase the formation of H-aggregates in samples of free dye. Given that we have also shown that H-aggregate formation is also possible when the dye is conjugated to M13 it is interesting to examine whether ammonium sulphate retains its ability to enhance H-aggregate formation. To assess this, the experiment carried out with free dye was repeated with the M13TRITC conjugate (Figure M3.4). To ensure consistency between experiments the concentration of TRITC in the conjugate was matched to that used in the free dye experiments.

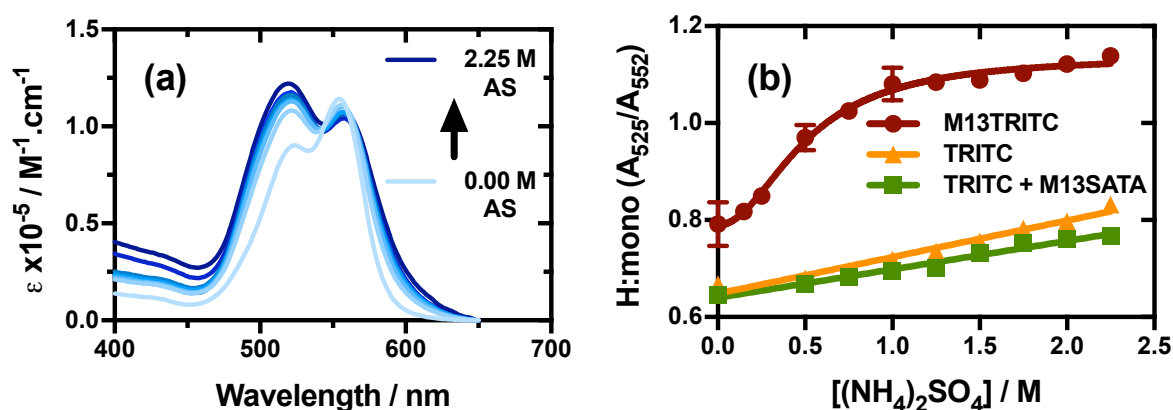


Figure M3.4. (a) Molar absorption of 1.2 μM TRITC covalently bound to M13 in varying concentrations of ammonium sulphate in 50 mM potassium phosphate buffer at pH 8.0. AS = ammonium sulphate. ($n=3$). (b) H-aggregation of TRITC and M13-TRITC conjugate at 1.2 μM dye concentration in varying concentrations of ammonium sulphate in 50 mM potassium phosphate buffer at pH 8.0 ($n=3$; error bars represent one standard deviation).

These data show a significant difference between the behaviour of the free dye and the conjugate (Figure M3.4 b). As might have been expected from the previous experiments the conjugated dye assembles more readily into the H-aggregate form than the free dye when ammonium sulphate is added. This again suggests that the conjugation of the dye to the M13 in some way enhances the ability of the dye to form H-aggregates. Again, to rule out that there was an effect on H-aggregation induced by the mere presence of M13 in the solution, the experiment was repeated with TRITC and M13SATA (Figure M3.4 b). The results of this control match the experiment with TRITC alone, confirming that the inclusion of M13 in the buffer is insufficient to alter the assembly state of TRITC, and therefore that the increase in assembly of TRITC when in the conjugate was caused by the covalent association of TRITC with M13.

M3.4.6. Linear dichroism studies of M13TRITC association

To investigate the formation of multi-bacteriophage structures and how this process is dependent on the concentration of ammonium sulphate, linear dichroism was used to monitor bacteriophage precipitation in solution.

Ourselves and others have previously shown that when a shear flow is applied to a solution containing M13, the bacteriophage particles align in an ordered fashion (Pacheco-Gómez *et al.*, 2012; Clack and Gray, 1992). In this form of flow the hydrodynamic properties of the M13 bacteriophage mean that the long axis of the particle aligns parallel to the direction of flow. When M13 is aligned in such a way, its LD spectrum, as defined by the difference in absorbance of two beams of plane polarised light where the plane of polarisation of one beam is parallel to the alignment axis and the second is perpendicular (Nordén *et al.*, 2010), can be measured. The intensity of the LD signal is then related to the alignment of the overall system in shear flow and the orientation of individual chromophores in the system. The signal would also be proportional to the degree of alignment of the M13 sample, which in turn is an indicator of the behaviour of the particle in shear flow (Nordén *et al.*, 2010). We have previously shown that LD not only has utility in studying the alignment of chromophores in fiber systems but also that the relatively minor alterations in the shape of these systems, e.g. two base pair mismatches in a length of DNA of over 1000 base pairs, can lead to a large change in LD signal (Halsall *et al.*, 2001).

The LD spectrum of M13 comprises a number of peaks between 190 and 350 nm, which are attributable to different aspects of its structure, as explained in detail by Clack and Gray (1992). The intensity of LD at 205 nm (LD_{205}), which corresponds to the low energy $\pi - \pi^*$ transition of α -helical peptides, is used here as a measure of the degree of alignment of M13 in solution because the LD spectrum of M13 is most intense at this wavelength, giving the largest possible dynamic range.

In this set of experiments we used LD_{205} as a measure of the alignment of M13 bacteriophage in shear flow. If the formation of the H-aggregates perturbs this, as it would be expected to do if it induces association of multiple virions, then the intensity of the LD signal would be altered. Conceptually the intensity could increase (if the ordered bacteriophage assemblies are longer and/or more ordered than monomeric phage) or decrease (if the assemblies are less ordered or have a lower aspect ratio). The first experiment involved the measurement of an LD spectrum for the conjugate in the non/low H-aggregate form. This provides important information on whether the mere presence of dye molecules (without any intermolecular interactions) altered the structure of the bacteriophage. Examination of the spectrum of this unassociated conjugate showed no perturbation of the features of the spectrum that correspond to the backbone (190 nm and 205 nm), aromatic side chains (225 nm and 280 nm) and DNA (240-260 nm) in the M13 structure. This shows that addition of TRITC to the structure does not alter the arrangement of the elements that make up the bacteriophage.

We then used the LD signal intensity of M13 and M13TRITC to monitor any changes in alignment that occur with increasing concentrations of ammonium sulphate, which would indicate the formation of multi-bacteriophage assemblies (Figure M3.5).

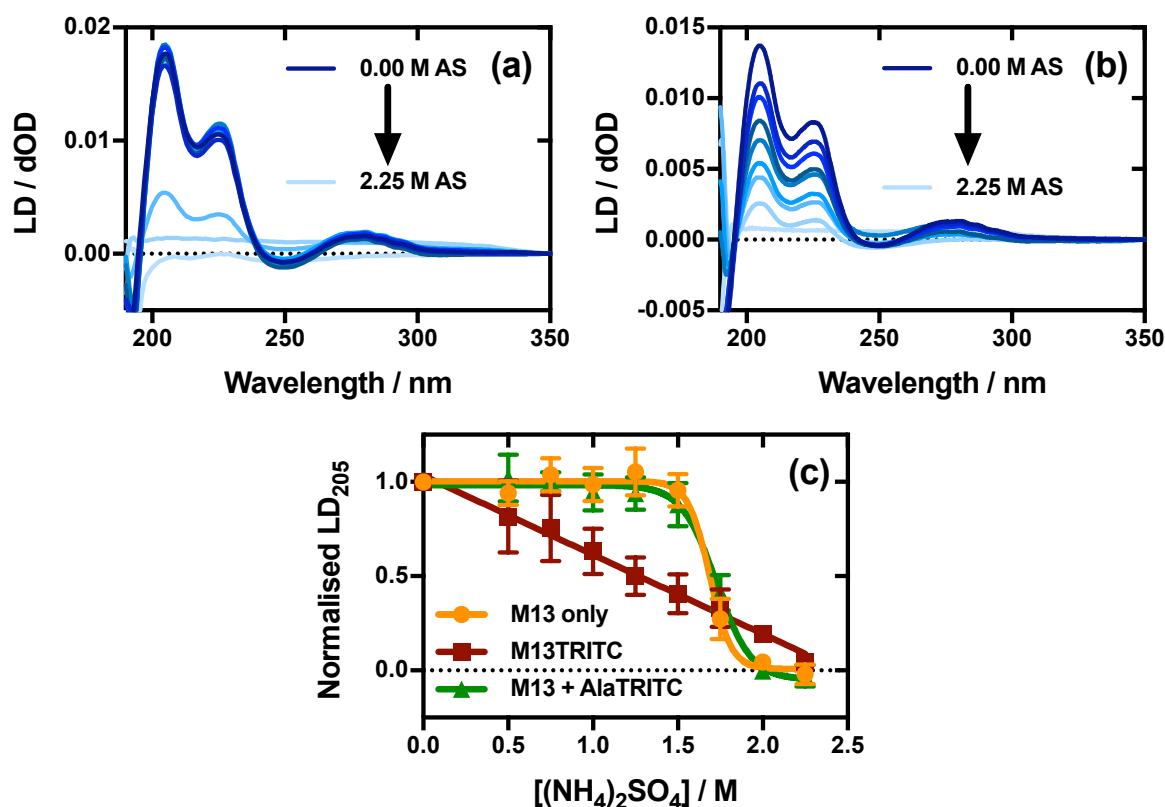


Figure M3.5. Relationship between linear dichroism signal of M13 alone (a) and in M13TRITC conjugate (b), and concentration of ammonium sulphate up to 2.25 M in 50 mM potassium phosphate buffer at pH 8.0. Bacteriophage at 2.7 nM (0.045 mg.mL⁻¹) (n=3). (c) Comparison between linear dichroism at 205 nm of M13 alone, M13TRITC and M13 in the presence of AlaTRITC, in the presence of ammonium sulphate up to 2.25 M (n=3; error bars represent one standard deviation).

Analysis of these experiments shows that the LD signal of unlabelled M13 remained unchanged at concentrations of ammonium sulphate below 1.25 M (Figure M3.5 a and c). This indicates no change in the hydrodynamic behaviour of the M13 particle and thus no formation of multi-bacteriophage assemblies. Above 1.25 M there was a rapid decrease in LD signal at all wavelengths until no LD was observed at 2.00 M.

This indicates a catastrophic loss of alignment of the M13 particle. The known aggregation effect of ammonium sulphate could explain this sudden drop in LD signal, as precipitation of the bacteriophage would result in a loss of signal (Wingfield, 2001). Furthermore, evidence for a sudden precipitation can be seen in the last LD spectrum, which has a significant upward trend in the LD signal towards low wavelength. This is known to be evidence of an increase in light scattering that would be consistent with an increase in particle size associated with precipitation (Demeester *et al.*, 2005; Marrington *et al.*, 2005).

Examination of these data for the equivalent experiment but with M13TRITC shows a very different behaviour to that observed for the unlabelled M13 (Figure M3.5 b and c). Instead of a sudden loss of LD signal the LD signal for the conjugate declined in a linear fashion over the entire range of ammonium sulphate concentrations used in the experiment. This indicates that a very different process is occurring here mediated at least in part by the presence of the TRITC moieties. The decrease in LD signal over a range of ammonium sulphate concentrations for which unlabelled M13 shows no change but that we know H-aggregate formation is occurring strongly suggests that H-aggregate formation is driving associations between individual M13 particles. Comparison of the LD signal change with the previous experiment directly measuring H-aggregate formation indicates the presence of an extra process of association separate from a solely H-aggregate driven association. The measurements of H-aggregate formation show that the vast majority of associations between chromophores have occurred at 1.40 M ammonium sulphate. If H-aggregate formation were the sole driver for M13 assembly then it would be expected that

changes in LD should track this with no change being observed above 1.40 M. Instead the decrease in LD signal continued past 1.40 M until, like the unlabelled M13, no LD signal was detectable at 2.25 M ammonium sulphate. One explanation of this behaviour is that until 1.40 M, association is driven by H-aggregate assembly until all possible H-aggregates have been formed. After 1.40 M increasing ammonium sulphate concentration drives assembly via a mechanism common to that for unlabelled M13. The lack of a sudden loss of LD signal could be the result of the later stages of ammonium sulphate mediated assembly being dominated by the annealing of complexes between relatively few H-aggregate driven superstructures.

To rule out that the early perturbation in LD signal was due to non-covalent interaction between M13 and TRITC a control experiment using a mixture of M13 and TRITC with its isothiocyanate (ITC, amine-reactive group) moiety blocked with L-alanine, forming what is called AlaTRITC was carried out. M13 in this experiment behaved in the same way as M13 alone indicating that covalent interaction between M13 and TRITC is essential for the alteration of the assembly of M13 in these conditions.

M3.4.7. Fluorescence anisotropy studies of M13TRITC assembly

While the LD experiments show that the precipitation of M13TRITC is altered compared to unlabelled M13, the involvement of TRITC in this process cannot be monitored using LD as TRITC does not align in shear flow thus it has no LD signal. To address this the experiment was repeated monitoring the fluorescence anisotropy signal of TRITC alone and in the M13TRITC conjugate. One would expect that if

TRITC were involved in the process of M13TRITC assembly, its fluorescence anisotropy would be much higher than if it were not bound to M13. In this experiment, the anisotropy of TRITC was greatly increased when covalently attached to M13 compared to free TRITC at 0.00 M ammonium sulphate, as would be expected upon binding to a particle much larger than itself (Figure M3.6). One would expect that if TRITC were involved in the assembly of multi-virion particles via H-aggregation, its fluorescence anisotropy would increase by a greater extent upon the addition of a precipitant than when alone, as the large particle the dye is already bound to would become larger still by association with other virions. In addition, the increased H-aggregation of the dye would restrict dye rotation on the bacteriophage surface thus increasing its anisotropy further still. Upon addition of ammonium sulphate up to 2.25 M the fluorescence anisotropy of TRITC increased from 0.003 to 0.02. Over the same range of ammonium sulphate concentrations the fluorescence anisotropy of M13TRITC increased from 0.03 to 0.10, a much larger change in anisotropy than TRITC in the same conditions. This reflects the increase in H-aggregation observed in previous experiments and the linear increase in M13TRITC anisotropy correlates well with the linear decrease in bacteriophage LD, which strongly suggests that the increased H-aggregation of TRITC in the conjugate was the cause of the altered precipitation of M13TRITC compared to M13.

As with previous experiments, it was necessary to rule out that any change in the behaviour of the dye was simply due to the presence of the bacteriophage without a covalent interaction having taking place. To address this, the fluorescence anisotropy of TRITC was monitored in ammonium sulphate concentrations ranging from 0.00-

2.25 M in the presence of M13 with its free amine moieties blocked SATA (M13SATA) (Figure M3.6). In this case, there was again an increase in the anisotropy but to a lesser extent than when covalently bound, demonstrating that the increase in anisotropy in the experiment with M13TRITC was due mainly to the covalent association with the bacteriophage. Together, these experiments demonstrate that TRITC may be used as an inter-bacteriophage “adhesive” in the production of multi-bacteriophage structures.

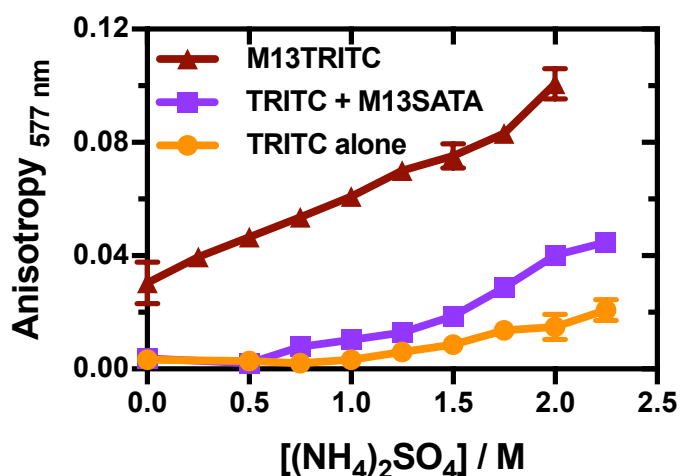


Figure M3.6. Fluorescence anisotropy of TRITC and M13TRITC during ammonium sulphate precipitation ($n=3$; error bars represent one standard deviation).

M3.4.8. Mechanism of H-aggregation

While the data from the experiments above demonstrate that TRITC H-aggregates may be used to mediate the formation of multi-bacteriophage structures, they do not make it clear whether the H-aggregates formed were solely between M13TRITC particles or involved free TRITC. To address this question, the M13TRITC conjugate was repeatedly passed through a size exclusion column (Sephadex G-25, size exclusion limit 5000 M_r) to remove any unbound dye that might remain in the

solution. Initial spectroscopic analysis of the M13TRITC conjugate suggested that approximately 13% of the 2700 pVIII subunits of M13 (~350 per virion) were labelled with TRITC following the conjugation procedure. However, upon repeat passage through buffer exchange column with two-fold dilution each time, the concentration of TRITC decreased relative to M13, indicating that not all TRITC in the sample was covalently associated with M13. After the second passage the apparent extent of labelling was 10% (~270 TRITC per M13) and after the third passage this number was 5% (~135 TRITC per M13). The second filtration had no effect on the behaviour of the conjugate in ammonium sulphate (as determined by UV-Vis and LD analysis; Figure M3.S1), however, after the third filtration, the conjugate behaved like unlabelled M13 in the LD experiment (Figure M3.5) and had a far less significant impact on the H-aggregation of TRITC compared to when it had been filtered only once. These results strongly suggests that the potentiated TRITC H-aggregation shown above occurs not by the formation of H-aggregates solely between TRITC molecules covalently bound to the surface of M13 but rather by the growth of H-aggregates comprising TRITC molecules bound covalently to M13 and free TRITC molecules in solution.

M3.4.9. Structure of the M13TRITC assembly

To gain insight into the arrangement of bacteriophage particles within the M13TRITC conjugate, the assembled structure was imaged using transmission electron microscopy (TEM). As can be seen below in Figure M3.7 a i and a iv, M13TRITC in the absence of ammonium sulphate has the same structural morphology as unlabelled M13. In both samples the bacteriophage particles are largely

unassembled with some random crossing of virions probably due to the deposition and drying process involved in sample preparation for TEM. However, while unlabelled M13 aggregated in an apparently random way in the presence of ammonium sulphate (Figure M3.7 a ii and iii), M13TRITC formed aster-like structures in the same conditions (Figure M3.7 a v and vi). The extent of the structuring of M13TRITC appears to correlate with the concentration of ammonium sulphate as in the presence of 1.00 M ammonium sulphate the asters were single and discrete (Figures M3.7 a v and M3.S2), whereas in 2.00 M ammonium sulphate the outer projections of the asters appeared entwined, forming multi-aster structures (Figure M3.7 a vi). The fact that the bacteriophage asters are approximately 2 μm in diameter indicates that they are formed by the nucleation of the ends of M13 virions (M13 is ~ 1 μm in length).

As TEM images are two-dimensional they cannot be used to ascertain whether the multi-virion structures of M13TRITC extend into the third dimension. To determine which form the structures took M13TRITC in 1.00 M ammonium sulphate was imaged under scanning transmission electron microscope (STEM) (Figure M3.7 b). The multi-virion structures appeared raised with virions pointing upwards from the grid as well as lying flat against it, taking the form of diffuse domes rather than diffuse discs.

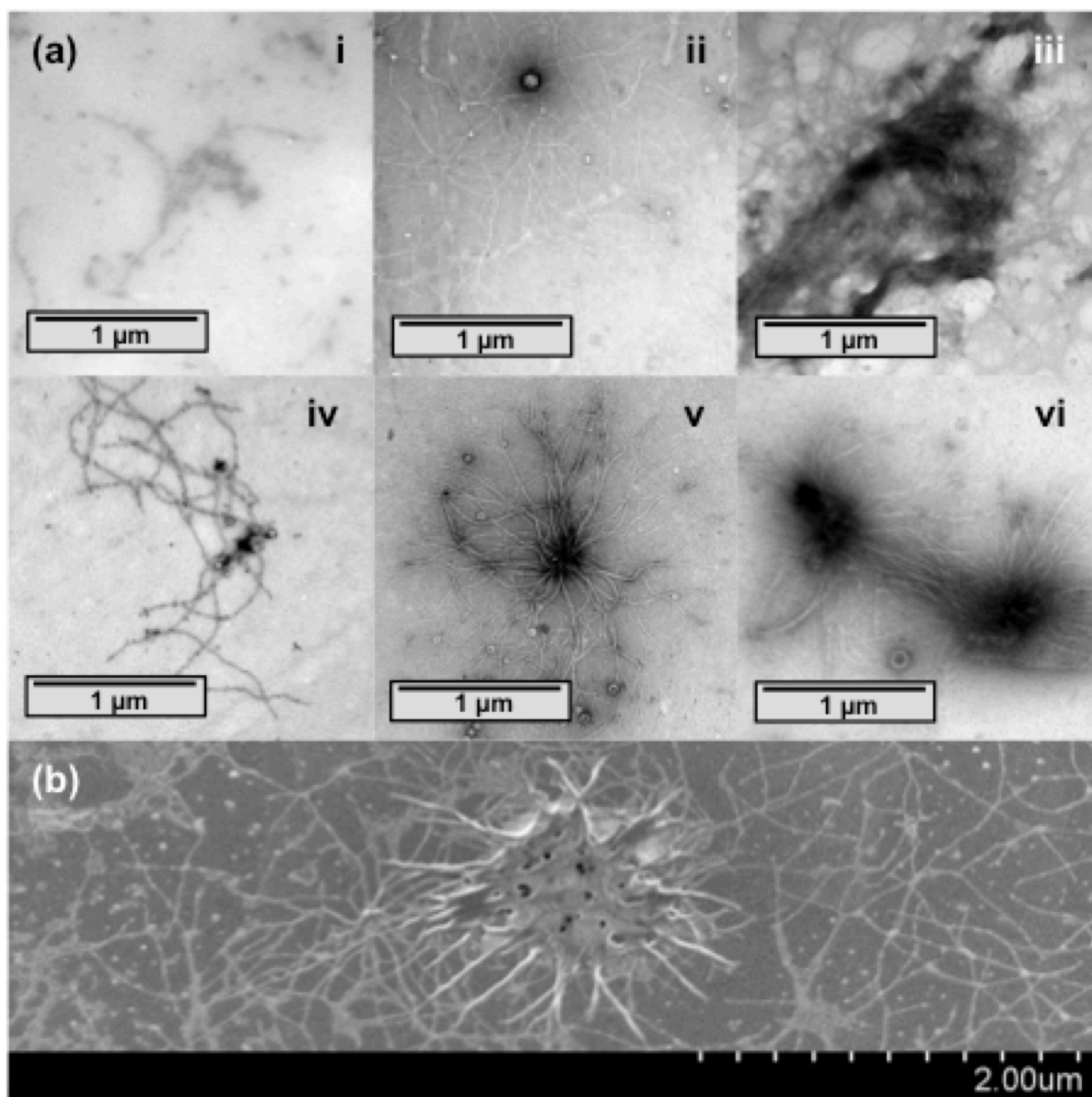


Figure M3.7. Electron micrographs of M13 and M13TRITC conjugate in 50 mM potassium phosphate buffer at pH 8.0, in varying concentrations of ammonium sulphate (AS) up to 2.00 M. (a) Transmission electron micrographs of M13 in (i) 0.00 M, (ii) 1.00 M, and (iii) 2.00 M ammonium sulphate; and M13TRITC in (iv) 0.00 M, (v) 1.00 M, and (vi) 2.00 M ammonium sulphate. (b) Scanning transmission electron micrograph of M13TRITC in 1.00 M ammonium sulphate with 28° tilt.

As TEM requires the immobilisation of the sample on a copper grid and staining with uranyl acetate, control experiments were carried out to rule these out as having caused the formation of the M13TRITC structures. To rule out copper and uranyl acetate, the experiment was repeated on a silicon wafer with no stain and imaged using atomic

force microscopy (AFM) (Figure M3.8 a-d). The resulting images correlate with what was observed under TEM (Figure M3.7 a i-v). As with the previous experiment, no multi-virion structures were observed for unlabelled M13 in 0.00 M or 1.00 M ammonium sulphate (Figure M3.8 a and b), or for M13TRITC in 0.00 M ammonium sulphate (Figure M3.8 a c). In contrast, bundles of virions were observed on the slide onto which M13TRITC in 1.00 M ammonium sulphate had been deposited (Figure M3.8 d), as was also observed under TEM (Figure M3.7), thus ruling out that the formation of the multi-virion structures was due to the copper grid or the uranyl acetate used to prepare the samples for TEM analysis.

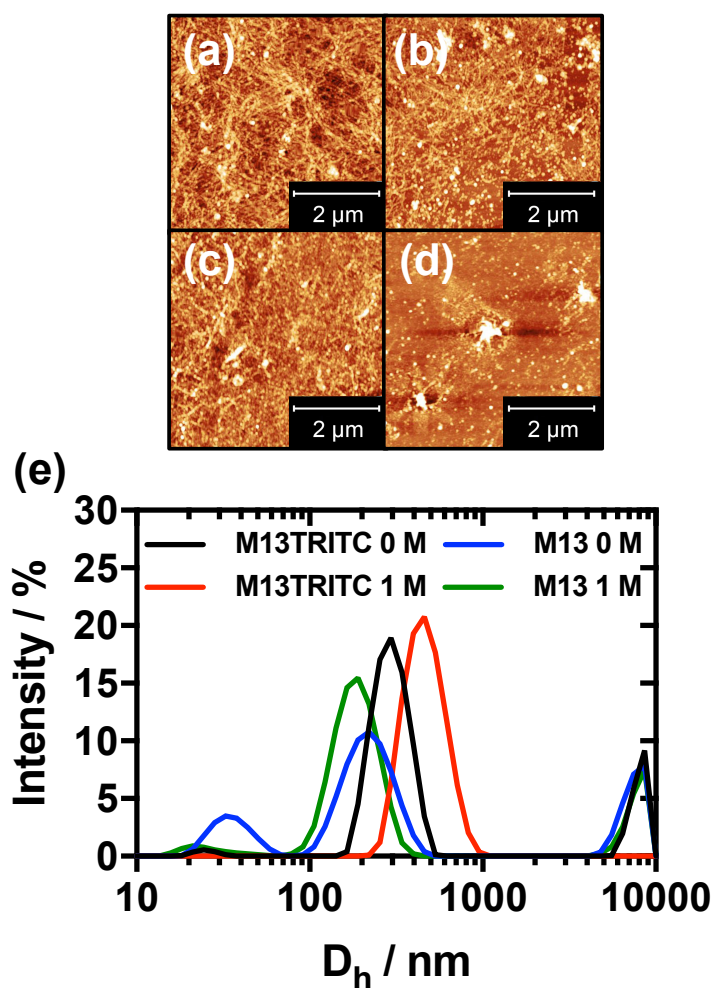


Figure M3.8. Characterisation of M13TRITC structure in varying contexts. Atomic force microscope images of unlabelled M13 in (a) 0.00 M ammonium sulphate and (b) 1.00 M ammonium sulphate, and M13TRITC in (c) 0.00 M ammonium sulphate and (d) 1.00 M ammonium sulphate. (e) Intensity distributions of a-d derived from dynamic light scattering analysis.

M3.4.10. Dynamic light scattering analysis of M13TRITC assembly

To rule out that the formation of the structures was due to drying and to corroborate that the loss of LD signal seen in Figure M3.5 was due to the formation of multi-virion structures in solution, dynamic light scattering (DLS) analysis was performed on the bacteriophage samples (Figure M3.8 e). The samples containing M13 in 0.00 M or 1.00 M ammonium sulphate or M13TRITC in 0.00 M ammonium sulphate each had three apparent hydrodynamic radii (D_h), reflecting the multiple modes of diffusion

expected of rod-like particles: translational diffusion along the long/short axes; and rotational diffusion about the centre of the long axis. In contrast, the sample containing M13TRITC in 1.00 M ammonium sulphate had only one apparent D_h , as would be expected for a spherical particle with one detectable mode of diffusion: translational. These data suggest that only M13TRITC in 1.00 M ammonium sulphate formed multi-bacteriophage structures, and thus corroborate the LD results, which suggested the same. The formation of the aster-like structures imaged with TEM and AFM was therefore not due to drying, thus these structures must have formed in solution prior to this step.

M3.5. Conclusion

One of the aims of the field of directed assembly is to use nano-scale building blocks to generate larger structures on the micron scale and above. Biology elegantly shows how this process can yield multi-component structures with some displaying properties that the individual components do not express. It is this inspiration that has led scientists to try and use biomolecules as building blocks. In this work we have shown how directed assembly can be used to take a biological building block, bacteriophage M13, and turn it into two structures that are not observed in nature. The structures were assembled by exploiting TMR H-aggregation. This route for driving self-assembly has two clear strengths: Firstly the structure of the H-aggregate is well defined enabling the formation of ordered assemblies of bacteriophage; Secondly the assembly state of the structure is controllable by the alteration of the concentration of M13TRITC and by the addition of ammonium sulphate. The aster-like structure assembled using TMR H-aggregate formation is a three-dimensional

assembly, in contrast to typical bacteriophage structures, which in general are closer to two-dimensional. While H-aggregation was shown to be required for the assembly process, which of the bacteriophage coat proteins is involved in the assembly is currently unclear. However, given the end-to-end arrangement of the virions in the aster-like structures, it seems likely that at least one of the minor coat proteins is involved. Elucidating the mechanism would require mutation or selective chemical blocking of amine groups within the virion structure. This will be a challenging experiment and will form the basis of future work. How this aster-like morphology might be used to produce advanced materials will be the focus of further studies, but one might consider that the new structure could offer exciting potential as a photonics device. For example, one could envisage a chromophore assembly on the bacteriophage absorbing light energy and then transferring it to a reaction centre in the middle of the aster. Going one stage further, our observations that asters can link together could extend this effect to scales beyond the micron scale. Overall we have demonstrated a method for directing the self-assembly of a bacteriophage M13 bioconjugate and used it to produce two assemblies with morphologies which may have the potential to generate materials with advanced functionalities.

M3.6. Supporting information

M3.6.1. Mechanism of H-aggregation

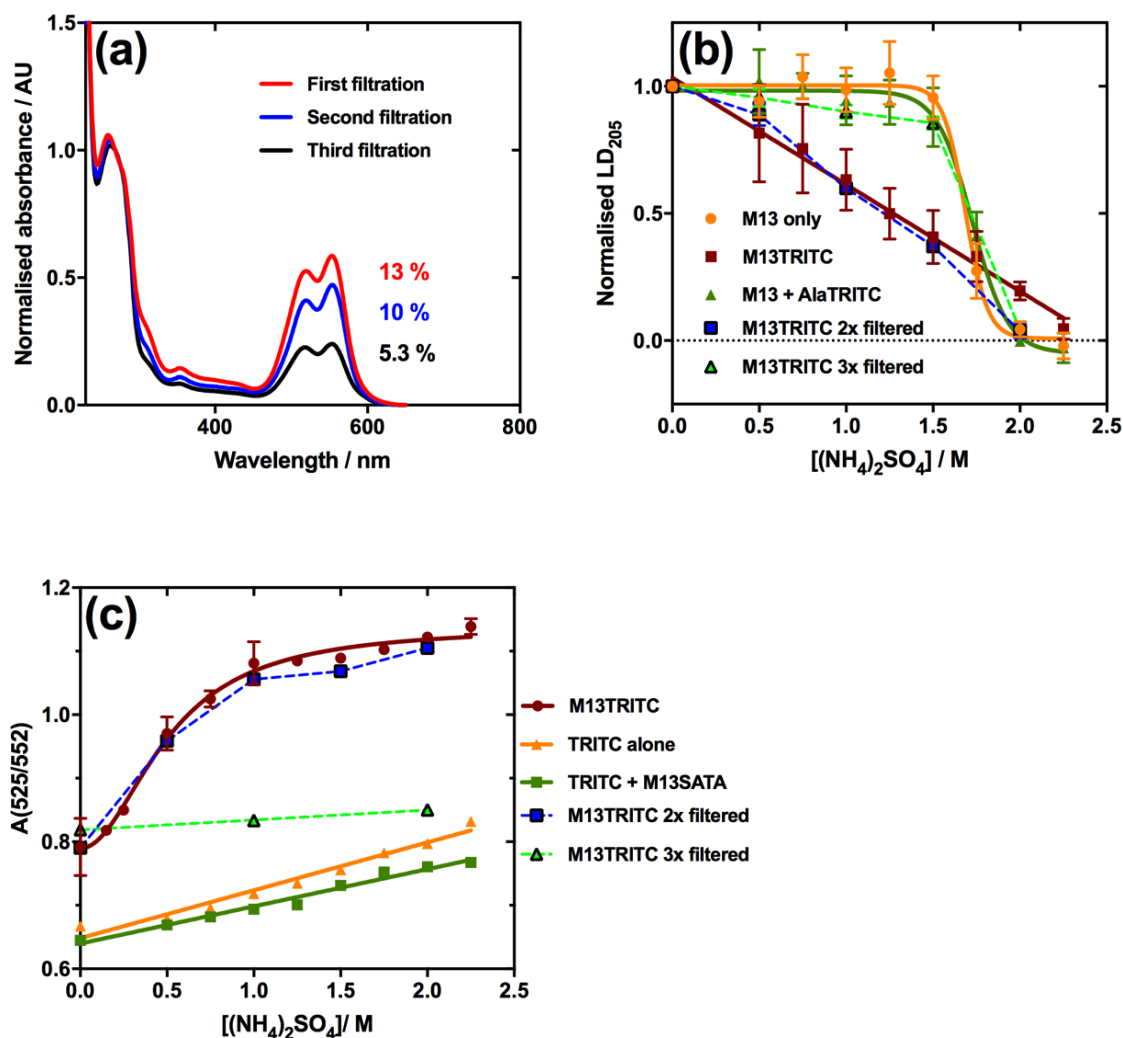


Figure M3.S1. Removal of free dye by filtration. (a) UV-Vis spectra of M13TRITC conjugate following repeated filtration. (b) Linear dichroism of M13TRITC conjugate following repeated filtration, in varying concentrations of ammonium sulphate compared to unlabelled bacteriophage in the same conditions. (c) Extent of H-aggregation of TRITC within the M13TRITC conjugate, expressed as the ratio of absorbance values at 525 nm and 552 nm, following repeated filtration, in varying concentrations of ammonium sulphate compared to unlabelled bacteriophage in the same conditions.

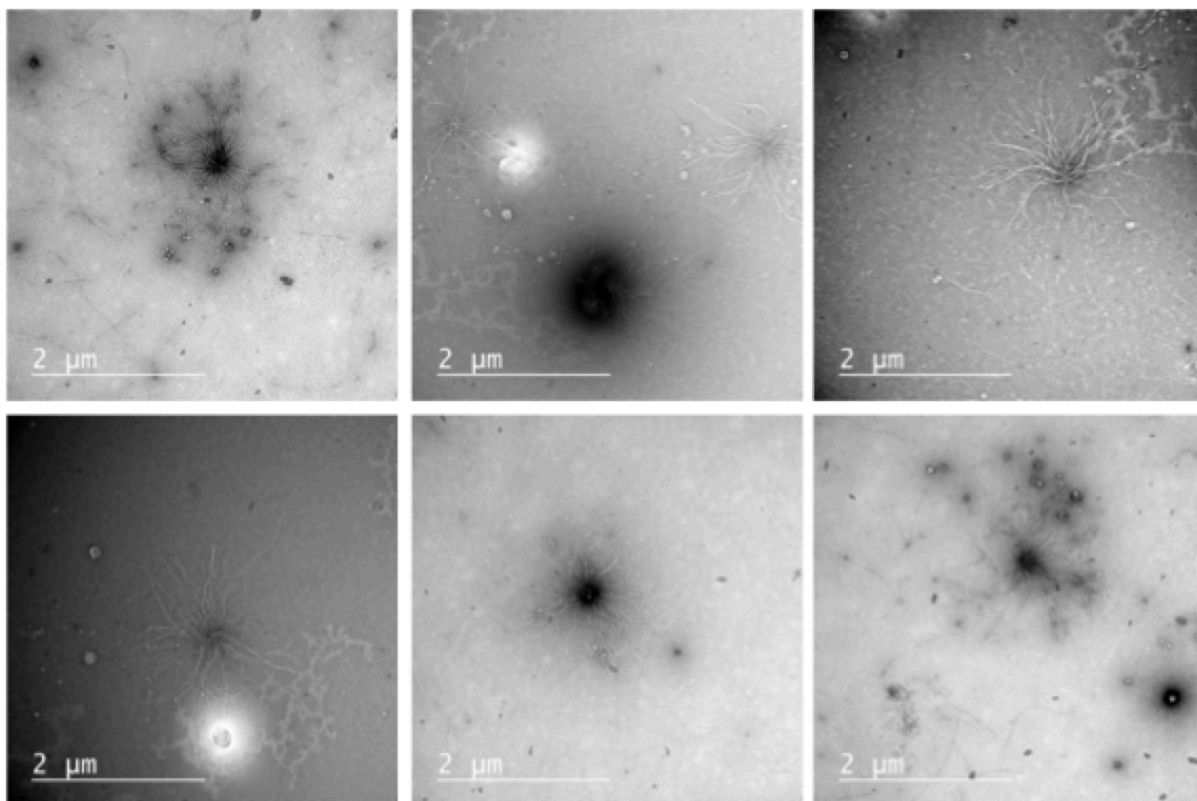
M3.6.2. Transmission electron micrographs of bacteriophage structures

Figure M3.S2. Transmission Electron Micrographs of M13TRITC conjugate in 1.00 M ammonium sulphate.

6.8. Additional results

The manuscript concluded by suggesting the idea of using M13 bacteriophage to induce J-aggregation of organic dyes, which could have applications in solar energy harvesting. To investigate this, a cyanine, a type of dye with a previously observed propensity towards J-aggregation (Chowdhury *et al.*, 2001; Hada *et al.*, 1985; Gadde *et al.*, 2009; Saito *et al.*, 1994), was trialled in place of TRITC. Furthermore, to investigate whether the effect induced by ammonium sulphate was ion-specific a range of salts were screened for their ability to induce H-aggregation of TRITC both free and bound to M13.

6.8.1. Cyanine3 NHS ester

Cyanine dyes are known to form J-aggregates (Chowdhury *et al.*, 2001; Hada *et al.*, 1985; Gadde *et al.*, 2009; Saito *et al.*, 1994). In addition, Cyanine 3 NHS ester (Cy3) (Figure 6.4) can be bound to amine groups in a one-step reaction. For these reasons Cy3 was chosen as a candidate for the enhanced or induced formation of J-aggregates by covalent conjugation of dye to M13 bacteriophage.

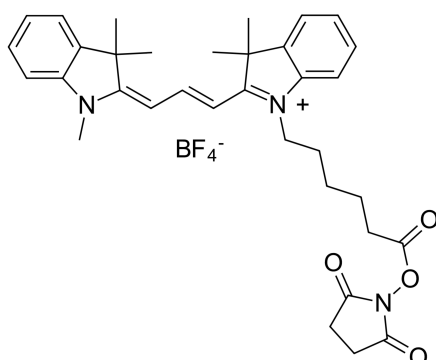


Figure 6.4. Chemical structure of Cyanine 3 NHS ester. Drawn using ChemDraw Professional software.

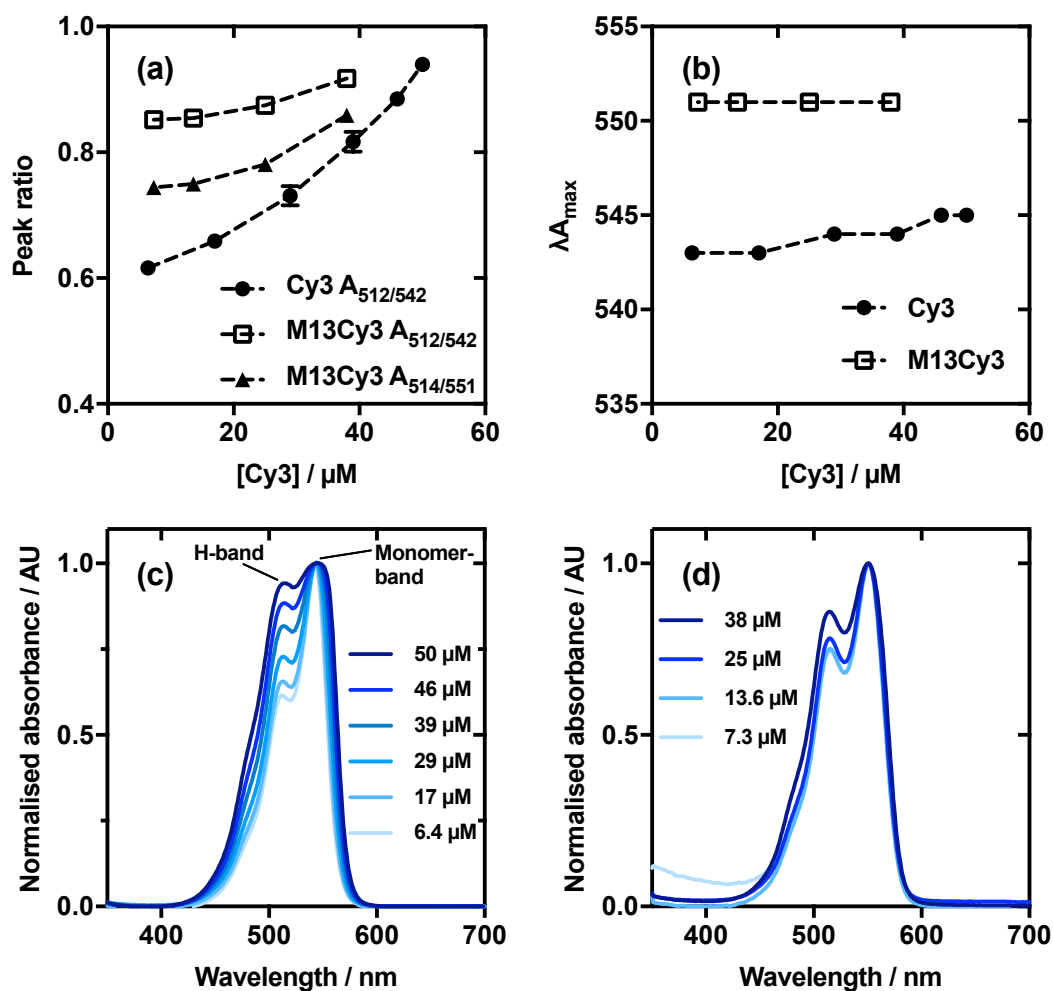


Figure 6.5. Spectral properties of Cy3 alone and when bound to M13 bacteriophage. (a) Ratio of H-band intensity (A_{512}) to monomer band intensity (A_{542}) of Cy3 alone and Cy3 bound to M13 bacteriophage (M13Cy3), as a function of Cy3 concentration. (b) Wavelength at absorbance maximum of Cy3 alone and M13Cy3 as a function of Cy3 concentration. (c) Absorbance spectra of Cy3 at 6.4–50 μM in 50 mM potassium phosphate buffer, pH 8.0. (d) Absorbance spectra of M13Cy3 at 7.3–38 μM in 50 mM potassium phosphate buffer, pH 8.0.

Firstly, the effect of concentration on the spectral properties of Cy3 and M13Cy3 was investigated (Figure 6.5). Absorbance spectra were measured upon serial dilution of the conjugate and the free dye. The H-band and monomer band of the Cy3 spectrum were identified at 512 nm and 542 nm. The relative extent of H-aggregation was thus taken as A_{512}/A_{542} . J-aggregation was monitored by the wavelength at maximum absorbance ($\lambda_{A_{\text{max}}}$; Cunningham *et al.*, 2018).

Figure 6.5 a reveals that upon binding Cy3 to M13 bacteriophage there was an increase in the H-band/monomer band ratio (A_{512}/A_{542}). This suggests increased H-aggregation of the dye. The graphs also show concentration dependence of A_{512}/A_{542} , both on-and-off the bacteriophage. While there was an enhanced H-aggregation of Cy3 when bound to M13 at the lower concentrations shown here, it appears that Cy3 has a strong tendency towards H-aggregation as a function of its own concentration. This was indicated by the steep upward trend beyond the tested concentrations of M13Cy3. As a result of this trend, the difference in Cy3 H-aggregation on-and-off bacteriophage is less distinct with increasing concentration.

The fact that the concentration dependence was weaker on-bacteriophage than off, suggests disruption of the ability of Cy3 to form H-aggregates following binding to the bacteriophage. This may also suggest that the overall increased H:mono ratio simply reflects the increased hydrophobicity of the dye environment compared to aqueous solution, rather than any potentiated dye stacking. The overall increase in A_{512}/A_{542} is certainly enhanced by the red shift in the monomer peak following bacteriophage conjugation. However, if this effect is corrected for, by taking the ratio at the M13Cy3 peak maxima (A_{514}/A_{551} ; Figure 6.5 a), the trend is the same, only the line is systematically shifted downwards by 0.1 on average. Thus the conclusions drawn do not change.

Figure 6.5 b reveals that there was a bathochromic shift upon binding to bacteriophage. The change in wavelength at A_{\max} indicates this. A bathochromically shifted A_{\max} may be taken to indicate J-aggregation (Cunningham *et al.*, 2018). However, the λA_{\max} of

M13Cy3 did not change upon dilution. This suggests that this effect may be due to some change in the chemical surroundings of the dye when bound to M13. One would expect if J-aggregates had formed, they would be disrupted by dilution.

As with the experiments on M13TRITC, it was investigated whether ammonium sulphate could be used to induce H or J aggregation of dye or conjugate at a concentration shown to have a low level of aggregation in the above experiment.

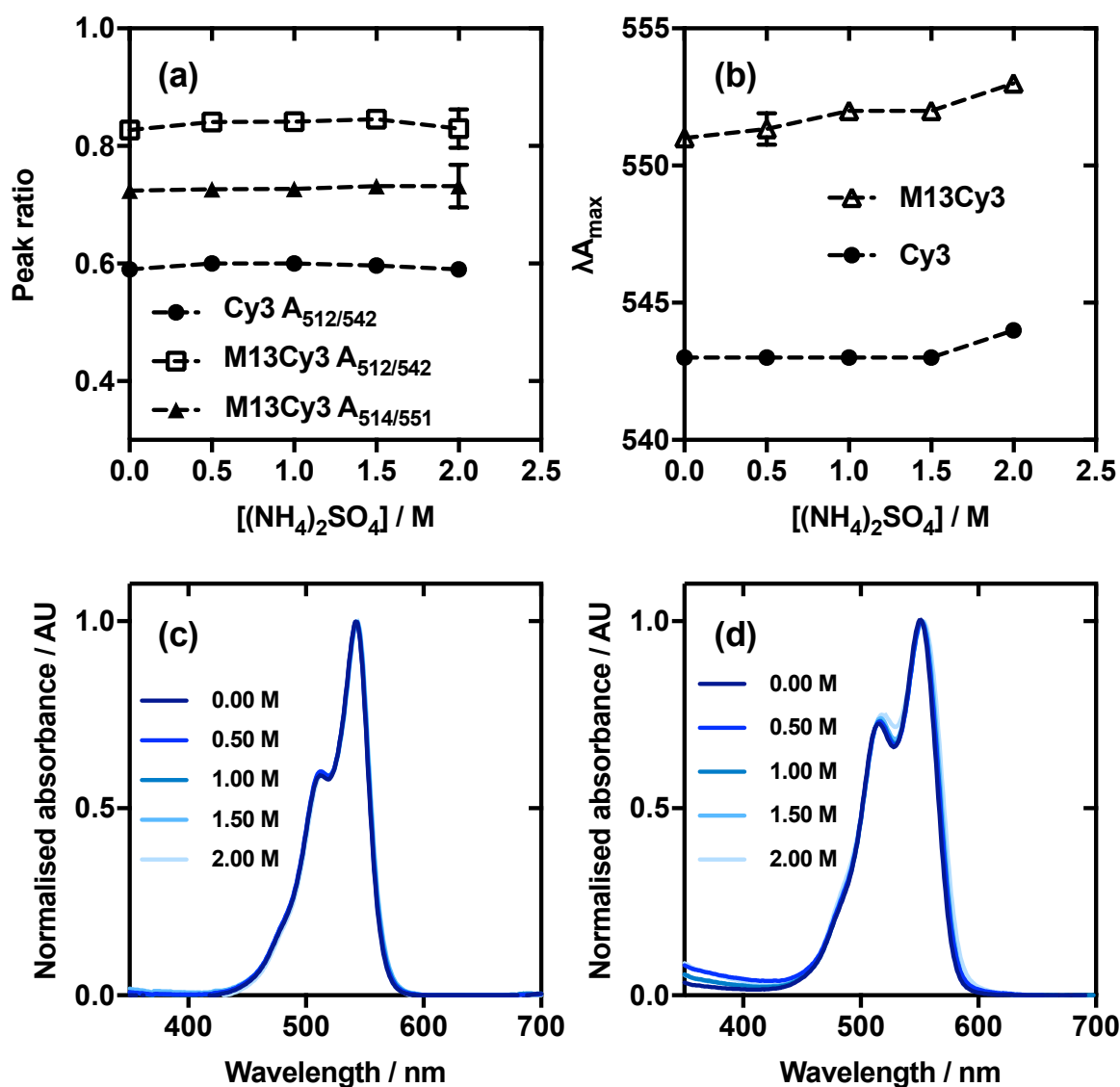


Figure 6.6. Addition of ammonium sulphate to Cy3 and M13Cy3. (a) H-band/monomer band ratio (A_{512}/A_{542}) of Cy3 and M13Cy3 upon addition of ammonium sulphate up to 2.0 M. (b) Wavelength at maximum absorbance of Cy3 and M13Cy3 upon addition of ammonium sulphate up to 2.0 M. (c) Absorbance spectrum of Cy3 upon addition of ammonium sulphate up to 2.0 M. (d) Absorbance spectrum of M13Cy3 upon addition of ammonium sulphate up to 2.0 M.

Figure 6.6 a reveals that the A_{512}/A_{542} , and therefore the H-aggregation, of M13Cy3 was higher than the dye alone. This is consistent with the previous experiment. Figure 6.6 a also reveals no clear effect on A_{512}/A_{542} by the addition of ammonium sulphate to either free dye or M13-bound dye. This indicates that there was no change in the H-

aggregation in this experiment. Again, when the wavelengths used to calculate the ratio are adjusted to reflect the bathochromic shift of M13Cy3 (Figure 6.6 a), there is a systematic decrease in the ratio value but no change in the trend.

This result is in contrast to the equivalent experiment with M13TRITC, which showed a strong effect on the H-aggregation of M13-bound dye upon addition of ammonium sulphate. Figure 6.6 b-d shows a very minor bathochromic shift in the spectra upon addition of ammonium sulphate, which was more pronounced in the conjugate than Cy3 alone. However, the shift is not very large compared to what would be expected upon J-aggregation so it is concluded that this effect is likely due to altered surroundings when bound to bacteriophage.

As with the experiments on M13TRITC, the effect on the LD signal of M13Cy3 upon the addition of ammonium sulphate was investigated to identify any change in the precipitation of bacteriophage induced by conjugation to dye.

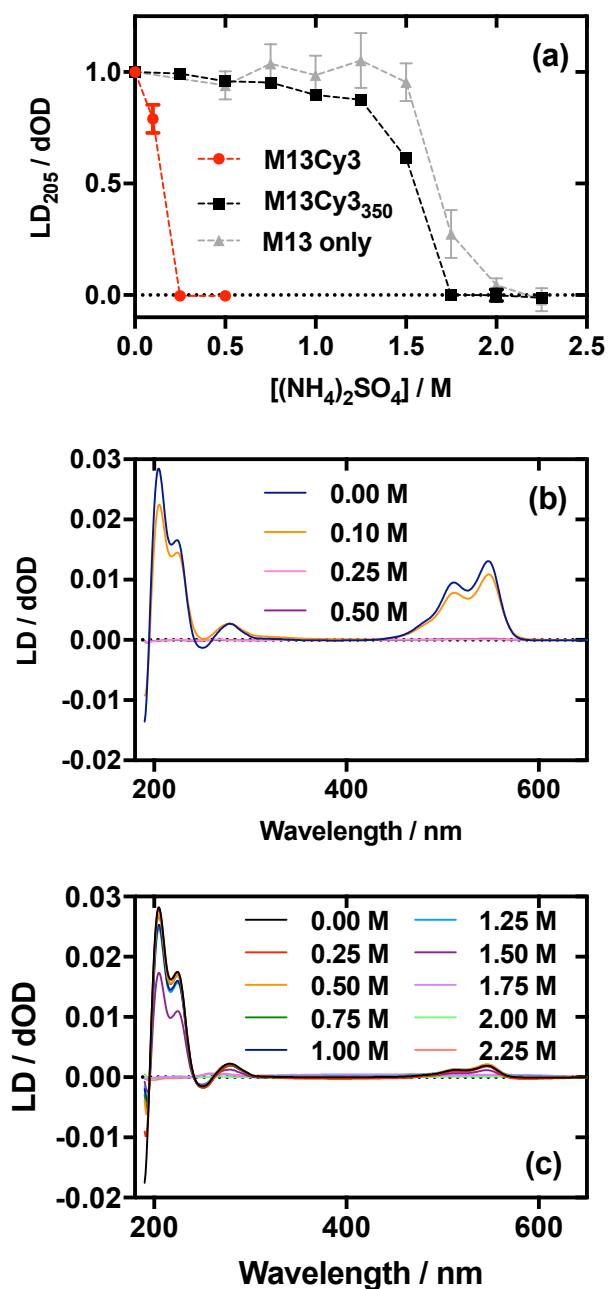


Figure 6.7. Linear dichroism of M13 bacteriophage-Cy3 conjugate in the presence of precipitant. (a) Linear dichroism at 205 nm of M13, M13Cy3 and M13Cy3₃₅₀ (M13 with ~350 Cy3 groups per virion) at concentrations of ammonium sulphate indicated in the figure. Linear dichroism spectra of (b) M13Cy3 and (c) M13Cy3₃₅₀ at concentrations of ammonium sulphate indicated in the figure.

M13Cy3 and unlabelled M13 were exposed to increasing concentrations of ammonium sulphate (Figure 6.7). M13Cy3 precipitated in a lower concentration of

ammonium sulphate than unlabelled M13, losing all LD₂₀₅ signal in 0.25 M ammonium sulphate (Figure 6.7 a). There was, however, no spectrally detectable change in the interaction between Cy3 groups attached to the bacteriophage (Figure 6.6). Thus, the early precipitation of M13Cy3 could not be attributed to the formation of dye H-aggregates between bacteriophage particles. The change in bacteriophage precipitation here could be due to increased hydrophobicity of the bacteriophage particles. This could be attributable to the attachment of hydrophobic Cy3 groups, and the concurrent blockage of hydrophilic amine groups. Either would decrease the solubility of the bacteriophage in aqueous conditions, thus increasing its tendency to precipitate. This result also suggests that the altered precipitation of M13TRITC was not wholly due to the inter-bacteriophage H-aggregation of TRITC groups. However, when the experiment was repeated with a preparation of M13Cy3 with approximately the same level of labelling as a typical M13TRITC preparation (~350 dye groups per virion) (M13Cy3₃₅₀), the dependence of LD₂₀₅ approximately matched that of unlabelled M13 (Figure 6.7 a and c). This indicates that H-aggregation was necessary to alter the precipitation of M13TRITC in ammonium sulphate.

6.8.2. Screen for alternative salts to induce dye H-aggregation

To determine whether the effects induced upon the addition of ammonium sulphate to TRITC and M13TRITC were ion-specific, low concentrations of TRITC or M13TRITC were added to a screen of 1.00 M salts. The salt screen was chosen to include ions from the kosmotropic and chaotropic ends of the Hofmeister series. UV-Vis absorbance spectroscopy was used to determine the extent of H-aggregation of

each of these samples compared to an equivalent sample in 50 mM potassium phosphate buffer, pH 8.0.

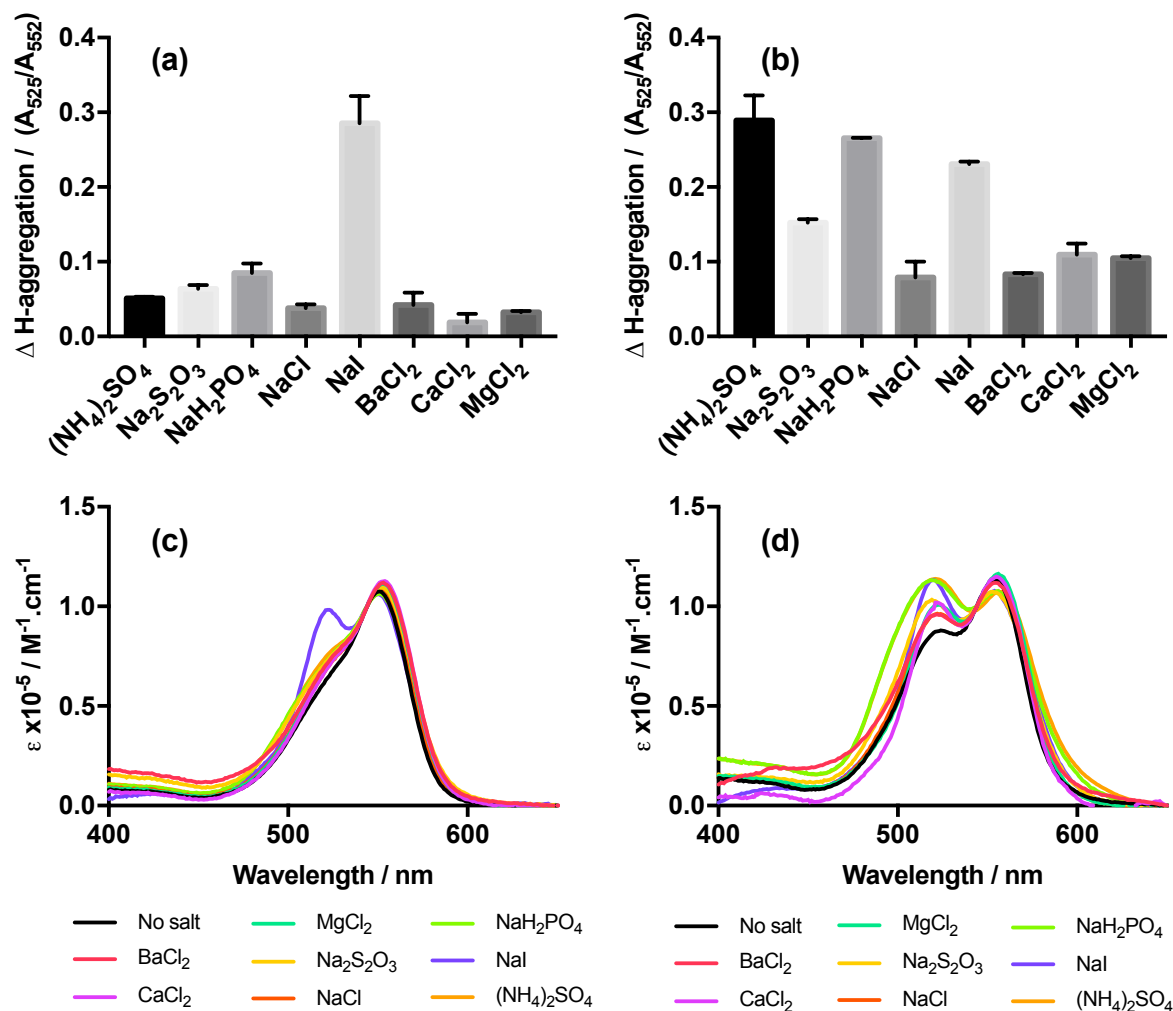


Figure 6.8. Screen for salts to induce H-aggregation of TRITC alone and bound to M13 bacteriophage. (a) Change in $A_{525/552}$ (H:mono ratio) of (a) TRITC and (b) M13TRITC, in 1.00 M salts indicated in the figure, compared to equivalent concentration of TRITC or M13TRITC in 50 mM potassium phosphate buffer, pH 8.0. Molar absorptivity spectra of (c) TRITC and (d) M13TRITC samples in 1.00 M solutions of the salts indicated in the figure.

To compare the extent to which the salts changed the H-aggregation state of TRITC and M13TRITC, the H:mono ratios of the samples were compared to that of the equivalent sample in 50 mM potassium phosphate buffer pH 8.0, giving ΔH -

aggregation (= H:mono ratio in 1.00 M salt – H:mono ratio in 50 mM potassium phosphate buffer, pH 8.0). The results of this experiment reveal that all of the salts tested induced a positive change to the H-aggregation of TRITC (Figure 6.8 a). All the salts tested induced a ΔH -aggregation of less than 0.10, with the exception of NaI, which induced a ΔH -aggregation of 0.29. This suggested that NaI might be a promising candidate to induce multi-virion structures when applied to M13TRITC. However, when the ΔH -aggregation of TRITC and M13TRITC are compared, giving $\Delta\Delta H$ -aggregation (= ΔH -aggregation M13TRITC - ΔH -aggregation TRITC), NaI appears to be the least effective at inducing H-aggregation of TRITC on the bacteriophage. In fact, NaI was the only salt with a negative $\Delta\Delta H$ -aggregation (-0.05). Most other salts induced a $\Delta\Delta H$ -aggregation of less than 0.1, with the exception of $(\text{NH}_4)_2\text{SO}_4$ and NaH_2PO_4 , which induced a $\Delta\Delta H$ -aggregation of 0.24 and 0.18, respectively (Figure 6.9).

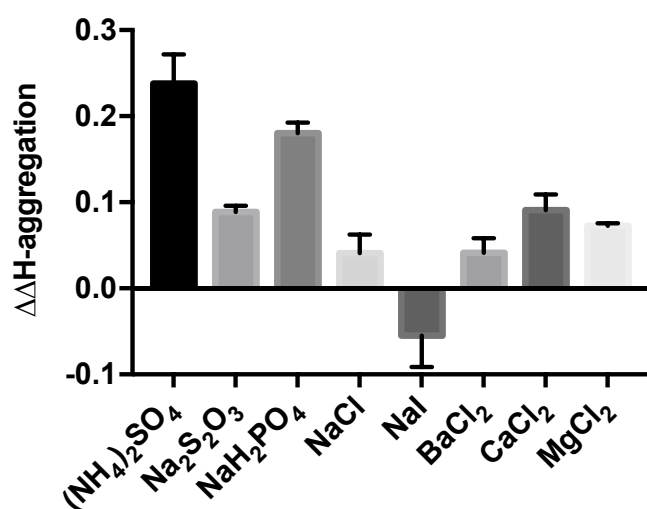


Figure 6.9. Comparison of H-aggregation of TRITC and M13TRITC in various 1.00 M salt solutions. $\Delta\Delta H$ -aggregation is calculated as the difference in ΔH -aggregation of M13TRITC and TRITC induced by the addition of the various salts.

As NaH_2PO_4 had the highest $\Delta\Delta\text{H}$ -aggregation except for $(\text{NH}_4)_2\text{SO}_4$, which had already been investigated, its ability to induce the formation of multi-virion structures was investigated. To do so, the LD spectrum of M13TRITC was measured in concentrations of NaH_2PO_4 ranging from 0.00-2.25 M. Similar to the experiments conducted with $(\text{NH}_4)_2\text{SO}_4$ (Figure M3.5), the LD_{205} of M13TRITC decreased in an approximately linear fashion. In total, it lost around 70 % of its LD_{205} over the entire concentration range. This is in contrast to unlabelled M13 in the same conditions, which lost around 30 % of its LD_{205} in an approximately linear fashion between 0.00 M and 1.75 M. This preceded a rapid loss of LD_{205} between 1.75 M and 2.00M to approximately 50 % of its original signal. LD_{205} then remained constant between 2.00 M and 2.25 M (Figure 6.10 a). This result is similar to that seen for $(\text{NH}_4)_2\text{SO}_4$. However the extent of signal loss over the concentration range was not as large in this experiment compared to the experiment with $(\text{NH}_4)_2\text{SO}_4$. All LD_{205} signal was lost over the range of $(\text{NH}_4)_2\text{SO}_4$ concentrations tested.

Measurement of the CD_{222} of M13 in solutions of the two salts from 0.00-2.00 M revealed little difference in the structural integrity of the bacteriophage up to 1.50 M. Above 1.50 M a large loss of CD_{222} was observed in the sample containing $(\text{NH}_4)_2\text{SO}_4$. This indicates loss of alpha helix content. The CD signal was constant across the entire concentration range for NaH_2PO_4 , however (Figure 6.10 b). The denaturing effect of $(\text{NH}_4)_2\text{SO}_4$ may account for the greater loss of LD signal compared to the equivalent concentration of NaH_2PO_4 . The main focus of the manuscript, however, is on the phage structures at 1.00 M, so denaturation would not

be an issue when using $(\text{NH}_4)_2\text{SO}_4$. Therefore, there may be little advantage to using NaH_2PO_4 over $(\text{NH}_4)_2\text{SO}_4$.

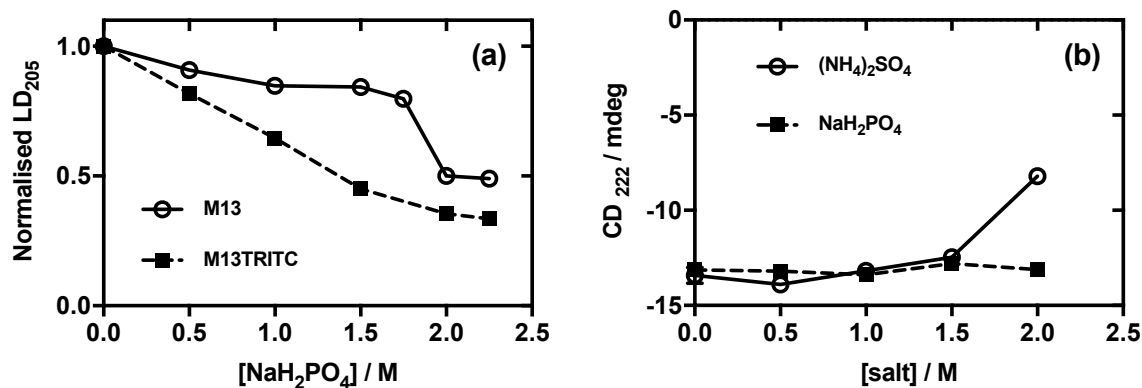


Figure 6.10. (a) Linear dichroism of M13 and M13TRITC in 0.00-2.25 M NaH_2PO_4 . (b) Circular dichroism at 222 nm of M13 bacteriophage in 0.00-2.00 M $(\text{NH}_4)_2\text{SO}_4$ and NaH_2PO_4 .

6.9. Discussion

The purpose of this discussion is to cover the additional experiments, and how they relate to the findings of Manuscript 3.

6.9.1. Dye assembly

TRITC H-aggregation is potentiated by binding to M13 bacteriophage, and potentiated further still by the addition of ammonium sulphate. This effect could not be reproduced using Cy3 in place of TRITC. This indicates that this approach is not universally applicable to induce the ordered assembly of dyes. It also suggests that chemical structure and inherent propensity towards aggregation may be factors determining dye assembly on the bacteriophage.

The TRITC H-aggregates were determined to comprise TRITC molecules both on and off M13. In addition, increased TRITC H-aggregation has been observed on other proteins (Panchuk-Voloshina *et al.*, 1999; Ravdin and Axelrod, 1977). It therefore seems unlikely that the high order in the arrangement of the pVIII coat is the driving factor behind the increased H-aggregation of TRITC. The effect may be more like what drives the formation of dye aggregates on crystals and branched polymers. This is a nucleation effect (Saijo and Shiojiri, 1996; Steiger *et al.*, 2009). Equally, it could be due to the altered chemical environment associated with being bound to the bacteriophage protein coat. Nevertheless, this does not rule out that the outer surface of M13 may be used to direct the assembly of a J-aggregating dye or other H-aggregating dyes. This would, however, depend on the structure of the dyes and their tendencies to form the given types of aggregate.

6.9.2. Bacteriophage assembly

The effect of ammonium sulphate on TRITC H-aggregation on and off M13 was partially reproduced using sodium dihydrogen phosphate. It is thus concluded that the effect of ammonium sulphate is not ion-specific. However, perturbation of M13TRITC LD, suggestive of multi-virion structure formation, was more prominent in the samples containing ammonium sulphate than sodium dihydrogen phosphate. This could be due to a number of factors: (1) Different ionic strengths of the two salts. The ions that comprise the two salts are differently charged. Thus, a 1 M solution of $(\text{NH}_4)_2\text{SO}_4$ has an ionic strength of 3 M^{-1} . A 1 M solution of NaH_2PO_4 , however, has an ionic strength of 1 M^{-1} ; (2) Different salt kosmotropivities. $(\text{NH}_4)_2\text{SO}_4$ is more highly kosmotropic than NaH_2PO_4 , meaning that their effects on protein precipitation

will differ; (3) Different solution pH. A 1 M solution of $(\text{NH}_4)_2\text{SO}_4$ is ~pH 7, whereas a 1 M solution of NaH_2PO_4 is ~pH 5. When the pH of NaH_2PO_4 was adjusted using NaOH, the salt crystallised. This was likely due to the loss of a proton to form the much less soluble Na_2HPO_4 (NaH_2PO_4 solubility in water at 20 °C is 85 g/100 mL, whereas Na_2HPO_4 solubility in water at 20 °C is 7.7 g/100 mL). As a result, the experiment could not be performed at the same pH as the $(\text{NH}_4)_2\text{SO}_4$ experiments, making mechanistic comparisons hard to draw; (4) Different salt effects on bacteriophage protein secondary structure (Figure 6.10 b). Due to the number of confounding possibilities that could explain the difference in effect of the two salts on bacteriophage LD, it is not possible to draw a strong conclusion on the reason for the difference. However, the CD spectroscopy data (Figure 6.10 b) indicates that ammonium sulphate has a denaturing effect on M13. Sodium dihydrogen phosphate, however, does not at the concentrations tested. This could explain the greater total loss of M13 LD caused by ammonium sulphate, albeit non-mechanistically.

Experiments where M13TRITC was exposed to ammonium sulphate indicated that H-aggregation of TRITC was necessary to induce assembly of bacteriophage. This was indicated by perturbed LD at concentrations of ammonium sulphate lower than what is required to perturb the LD of unlabelled M13. Unexpectedly, LD perturbation could be recreated with M13Cy3 even though there was no detectable dye aggregation induced by ammonium sulphate. However, when the number of dye molecules involved in each conjugate was normalised, only M13TRITC had altered LD perturbation compared to unlabelled M13. This indicates that H-aggregation was necessary to induce this effect. In addition, when TRITC was incrementally removed

from M13TRITC, H-aggregation was lost and so was LD perturbation. This further supports the notion that H-aggregation is required to induce bacteriophage assembly in this system.

6.10. Conclusions

As stated in the manuscript, binding TRITC to M13 potentiates the formation of TRITC H-aggregates. This was taken as proof-of-concept that by binding dyes to the surface of M13 bacteriophage, they could be induced into higher order structures, meaning that it may be possible to trigger or enhance the formation of J-aggregates of fluorescent dyes with this method. Use of Cy3 in this way did not show any J-aggregation, however. This indicates that this approach cannot be applied to all dyes. It does not, however, rule out that it may be effective with other dyes. Thus the conclusions regarding dye aggregation are not changed from those in Manuscript 3 by the findings of the additional results section.

In a recent publication by Thomas Gibaud, various routes towards assembly of multi-virion structures were reviewed. In the article, bioconjugation was discussed as a method to alter the bacteriophage, and thereby the structures yielded. However, this was covered only with the view towards altering the innate tendency of the bacteriophage to form liquid crystals. All bioconjugation approaches reviewed in Gibaud (2017) share a common set of steps. First, some chemical alteration to the bacteriophage structure is made. Next the bioconjugate is concentrated. Finally, the resulting liquid crystal is characterised and compared to one comprising unaltered bacteriophage. In contrast, Manuscript 3 and the additional results section here

demonstrate that bioconjugation with the addition of a precipitant is also a viable method for the induction of multi-virion structure self-assembly. As this approach does not rely on the innate tendency of the bacteriophage to form liquid crystals, it is distinct from those covered in Gibaud (2017). The results presented here also suggest that further experimentation with different dyes and precipitants could yield structures that cannot be produced by previously published methods.

7. DISCUSSION AND FUTURE WORK

7.1. Discussion

The first three results chapters of this thesis aimed to make developments that would improve the capabilities of the assay developed by Pacheco-Gómez *et al.* (2012) whilst being of interest to the broader research community within bionanomaterials development. The final results chapter also aimed to make developments within bionanotechnology, specifically the subcategory of incremental bionanotechnology.

7.1.1. Linear dichroism of organic dyes using M13 bacteriophage as an alignment scaffold

It was demonstrated in the first results chapter that labelling M13 bacteriophage with cyanine dyes introduces an additional signal to its LD spectrum under shear flow (Figures M.1.2-5). This finding will enable the further development of the Pacheco-Gómez assay by enabling multiplex assay development and by reducing of equipment requirements. It may also be of use to those who aim to create and optimise biomimetic light-harvesting antennae by the covalent attachment of chromophores to linear scaffolds. The characterisation of the transition dipole moments of the dyes and the observation that their alignment relative to the linear scaffold can be altered by shear flow (Figure M.1.7) may enable rational optimisations of linear scaffolds. Thus, this could potentially enable the development of more efficient biomimetic light harvesting antennae than previously achieved.

Future experiments towards this line of investigation could include the use/development of dyes that cannot rotate on the bacteriophage by binding via two points (Hirayama *et al.*, 2007; Wang *et al.*, 2010). This would potentially increase the

LD signal of said dyes by increasing the S value (orientation parameter) in the LD equation. This would be useful in the Pacheco-Gómez assay, as it would increase the dynamic range of the assay. This approach could also be useful in the applications surrounding the *in vitro* recreation of light-harvesting complexes as dyes with more rigidly aligned transition dipoles would theoretically have higher FRET efficiency. This would of course require that the dipoles be aligned when rigidly bound, which might be challenging to achieve.

7.1.2. Mutation of M13 bacteriophage major coat protein for increased conjugation to exogenous compounds

The demonstration that the mutagenic introduction of an additional lysine residue to pVIII enables increased conjugation efficiency to a range of dyes (Figure M2.2), and thereby an increased LD signal in the region attributable to the dye (Figure 4.1), indicates that this approach may be used to optimise the Pacheco-Gómez assay. Specifically, by improving the dynamic range of the readout. Furthermore, the fact that conjugation to all the dyes tested was improved using this approach suggests that it might also be more broadly applicable to technologies where other small molecules are bound to the bacteriophage e.g. anticancer drugs (Suthiwangcharoen *et al.*, 2011) and antimicrobial drugs (Yacoby *et al.*, 2006).

One of the drawbacks of this approach is that the mutants generated all had reduced titre compared to the wild type (Figure M2.S5), meaning that contamination with wild type would lead to outgrowth and loss of the mutant. This could be countered by the isolation of a mutant that displays an additional Lys and is also fast replicating, using

the partial library method (Merzlyak and Lee, 2009). In this approach, the codon for the mutated residue is flanked by randomised codons for 1-3 amino acids. This DNA library is transformed into host cells and bacteriophage variants expressing the desired residue are selected based on their replication speed.

7.1.3. Thermal stability of bacteriophage mutants

The mutant with improved conjugation efficiency compared to wild type (G3K_{A1E}) showed reduced melting temperature compared to wild type (Figure 5.4 f). As did all other mutants tested. As only a small number of mutants were examined, broad conclusions about the effect of pVIII mutation on the bacteriophage structure cannot be drawn. However, as it has been demonstrated in a number of studies that thermal stability of various viral coats can be enhanced by certain mutations (Rincón *et al.*, 2014; Adeyemi *et al.*, 2017), the notion that all mutations cause a loss of thermal stability can be ruled out. The aims of the third results chapter were very closely focused on the needs of the development of the Pacheco-Gómez assay. However, if the study were extended to include a systematic review of the effect on thermal stability of mutation of all residues of pVIII, one-by-one, the elements of the structure that determine coat stability could be ascertained. Furthermore, the partial library method could be used to screen for a thermally stable mutant that also contains a rationally designed mutation, by using heat treatment as a selection method (Merzlyak and Lee, 2009). The results of this proposed study could in turn be used to inform the rational design of mutations to the bacteriophage coat whilst preserving thermal stability.

7.1.4. Assembly of multi-virion structures via dye H-aggregation

The formation of J-aggregates on the surface of M13 bacteriophage was not achieved during this work but it is still plausible to be achievable.

However, the observation that the bacteriophage may be induced into assembling multi-virion structures by controlling the H-aggregation of the dyes bound to its surface will be of interest to the research community that aims to develop nanomaterials based upon the assembly of biologically derived starting materials.

A notable finding within the final results chapter is that the self-assembly of M13 bacteriophage can be induced by the chemical modification of its surface and the addition of a precipitant. All previous studies investigating the self-assembly of multi-virion structures relied on the innate tendency of the bacteriophage to form liquid crystals at high concentrations (Gibaud, 2017 and references within). This observation therefore suggests that the library of materials that can be generated by the self-assembly of an altered base biomaterial can be expanded further by the alteration of solvent conditions without highly concentrating the bacteriophage.

In a recent review (Gibaud, 2017), a number of studies were covered that used site-directed mutagenesis to generate a range of bacteriophages with varying material properties, e.g. altered surface charge and stiffness, and investigated their altered self-assembly into multi-virion structures. With these studies in mind it might be interesting to investigate whether the G3K_{A1E} mutant, with its altered binding to dyes compared to the wild type, gives rise to different M13TRITC structures in ammonium

sulphate compared to wild type bacteriophage. Finally, it follows logically that any advanced property endowed upon the bacteriophage by its ordered self-assembly into the observed star-like clusters would be enhanced by the isolation and purification of the clusters. The TEM and STEM images showed that surrounding the bacteriophage assemblies were unassembled virions (Figure M3.7). If the virions are in equilibrium between being assembled and disassembled, however, the removal of disassembled virions may cause the disassembly of the remaining clusters. In this case, the assemblies may benefit from being covalently cross-linked prior to isolation.

7.1.5. General discussion

The results chapters are not entirely independent as there are some results that have implications for the findings of others. When observing the chapters in combination, some noteworthy observations become apparent.

The altered precipitation of M13TRITC in ammonium sulphate observed in Chapter 6 proved useful in the construction of multi-virion structures. However, in the context of Chapters 3 and 4, where dye-labelled bacteriophage was investigated for its use in the Pacheco-Gómez assay, this result and other observations made in Chapter 6 could indicate a number of obstacles to the use of this approach. Firstly, M13Cy3 also precipitated in lower concentrations of ammonium sulphate than unlabelled bacteriophage. This may also cause issues when the bacteriophage is highly labelled or labelled with a dye that has a high propensity to aggregate. The issue would be the occurrence of false positive results produced by the assay brought about by the aggregation and loss of LD of the labelled bacteriophage. This could be mitigated by

the inclusion of a reference probe i.e. one without antibodies that would respond only to non-specific causes of LD signal loss. This would thus indicate false positive results.

In addition, the evidence gathered that indicates that the ammonium sulphate-driven precipitation of dye-labelled M13 is not ion-specific (Figure 6.10) suggests that there could be a large number of disruptive agents encountered during the use of the assay with real samples.

Furthermore, the results in Figure 6.7 indicated that the altered precipitation of the dye-labelled bacteriophage is dependent on the number of dyes bound. Binding more dyes makes the bacteriophage more sensitive to precipitants. This indicates that the approaches taken to maximise the number of dyes bound to the bacteriophage in Chapter 4 would further enhance the problem of non-specific aggregation of dye-labelled bacteriophage. This could therefore create issues during the deployment of the assay, as it would become more prone to producing false positive results.

An approach to counter the above issue may be to incorporate unnatural amino acids (UAAs) that absorb visible light into a region of the pVIII sequence that is not solvent exposed. This would be achieved by growth of M13 in a host strain that uses a UAA in place of a natural amino acid that is coded within the sequence of pVIII. UAA options include 4-cyanotryptophan (Hilaire *et al.*, 2017), Aladan (an alanine derivative of 6-dimethylamino-2-acylnaphthalene; Cohen *et al.*, 2002), 6-cyanotryptophan, 7-cyanotryptophan, and *N*-methyl 7-cyanotryptophan (Talukder *et al.*, 2015), among

others. This could simultaneously solve the problem of achieving 100 % labelling efficiency and the problem of reduced bacteriophage solubility upon high labelling.

The above approach would, however, present a number of challenges. First would be the development of *E. coli* strains that are capable of expressing both UAAs and the F-pilus. This could be achieved by either transformation of a UAA-expressing strain with the F plasmid, or transformation of commercially available F' or F⁺ cells with a UAA expression system. The second challenge would be achieving good bacteriophage yield, as expression of UAAs by bacteria often causes a reduction in fitness (Tack *et al.*, 2018). Slow host cell growth would in turn cause a reduction in bacteriophage yield, even without considering the effect that incorporation of the UAA would have on the fitness of the bacteriophage itself. Introduction of a UAA to the bacteriophage coat should theoretically be no riskier than introduction of a mutant natural amino acid as in either case the bacteriophage coat is not optimised to accommodate the introduced residue. Irrespective of its presence in nature, neither residue is native to the bacteriophage coat. However, the buried residues in the pVIII protein have been found to be highly sensitive to mutation (Spruijt *et al.*, 1996). The third challenge may be the effect of the UAA introduction on the thermal stability of the bacteriophage.

The effects on bacteriophage fitness and thermal stability could both be ameliorated by the use of the partial library approach (Merzlyak and Lee, 2009). This could be followed by multiple rounds of heat treatment and propagation to select for a variant that expresses the UAA and is also fast replicating and thermally robust. Overall,

while this approach may be more challenging than those taken in this thesis, it has the potential to overcome the limitations of the developments made in this work.

7.2. Conclusions

The notable findings of this thesis are: 1) that M13 bacteriophage can be endowed with a visible-region LD signal by labelling it with dyes that absorb in that range; 2) that amine-directed bioconjugation to M13 bacteriophage can be increased by the mutagenic addition of a lysine residue to its major coat protein; 3) that the aforementioned mutation causes no practically important disruption to the thermal stability of M13 bacteriophage; and 4) that the self-assembly of M13 bacteriophage into multi-virion structures can be induced by labelling it with the fluorescent dye TRITC, and adding ammonium sulphate. Findings one-three will facilitate the further development of the M13 bacteriophage-based immunoassay first developed by Pacheco-Gómez *et al.* (2012). Specifically, the extension of the bacteriophage LD signal into the visible region will enable both reduction of equipment size (and thus increased portability of the assay) and will enable the development of a multiplex version of the assay. In addition, the improvement in the number of dyes that can be conjugated to the surface of the bacteriophage will enable an increase in assay sensitivity. The impact of finding four will become apparent following further investigations into the properties of the assemblies. Until then, however, it adds to the body of information on how the self-assembly of nano-scale rod-like particles is affected by the alteration of their surface chemistry.

References

- Abramov, G., Shaharabani, R., Morag, O., Avinery, R., Haimovich, A., Oz, I., Beck, R. and Goldbourt, A. (2017). Structural effects of single mutations in a filamentous viral capsid across multiple length scales. *Biomacromolecules*, 18(8), 2258-2266.
- Accardo, A., Tesauro, D. and Morelli, G. (2013). Peptide-based targeting strategies for simultaneous imaging and therapy with nanovectors. *Polymer Journal*, 45, 481-493.
- Adeyemi, O. O., Nicol, C., Stonehouse, N. J. and Rowlands, D. J. (2017). Increasing type I poliovirus capsid stability by thermal selection. *Journal of Virology*, 91(4), e01586-16.
- Agapakis, C. M., Boyle, P. M. and Silver, P. A. (2012). Natural strategies for the spatial optimization of metabolism in synthetic biology. *Nature Chemical Biology*. 8(6), 527-535.
- Andrienko, D. (2018). Introduction to liquid crystals. *Journal of Molecular Liquids*, 267, 520-541.
- Armstrong, J., Hewitt, J. A. and Perham, R. N. (1983). Chemical modification of the coat protein in bacteriophage fd and orientation of the virion during assembly and disassembly. *The European Molecular Biology Organization Journal*, 2(10), 1641-1646.
- Arnold, G. E., Day, L. A. and Dunker, A. K. (1992). Tryptophan contributes to the unusual circular dichroism of fd bacteriophage. *Biochemistry*, 31, 7948-7956.
- Arrigo, A., La Ganga, G., Nastasi, F., Serroni, S., Santoro, A., Santoni, M. P., Galletta, M., Campagna S. and Puntoriero, F. (2017). Artificial, molecular-based light-harvesting antenna systems made of metal dendrimers and multibodipy species. *Comptes Rendus Chimie*, 20, 209-220.
- Aslam, M. and Dent, A. (1998). *Bioconjugation: Protein coupling techniques for the biomedical sciences*. London: Macmillan. p.400.
- Bahatyrova, S., Frese, R. N., Siebert, C. A., Olsen, J. D., van der Werf, K. O., van Grondelle, R., Niederman, R. A., Bullough, P. A., Otto, C. and Hunter, C. N. (2004). The native architecture of a photosynthetic membrane. *Nature*, 430, 1058-1062.
- Baker, L. A. and Habershon, S. (2017). Photosynthetic pigment-protein complexes as highly connected networks: implications for robust energy transport. *Proceedings of the Royal Society A*, 473, 20170112.
- Bardeen, C. J. (2014). The structure and dynamics of molecular excitons. *Annual Review of Physical Chemistry*, 65, 127-148.
- Barrows, F. P. and Bartl, M. H. (2014). Photonics structures in biology: A possible blueprint for nanotechnology. *Nanomaterials and Nanotechnology*. 4(1) 1-12.
- Barry, E., Beller, D. and Dogic, Z. (2009). A model liquid crystalline system based on rodlike viruses with variable chirality and persistence length. *Soft Matter*, 5, 2563-2570.

- Beck, K. and Duenki, R. M. (1990). Flexibility of bacteriophage M13: Comparison of hydrodynamic measurements with electron microscopy. *Journal of Structural Biology*, 105, 22-27.
- Bera, D., Qian, L., Tseng, T. K. and Holloway, P. H. (2010). Quantum dots and their multimodal applications: A review. *Materials (Basel)*, 3, 2260-2345.
- Berg, J. M., Tymoczko, J. L. and Stryer, L. (2012). *Biochemistry*. 7th ed. New York: W. H. Freeman and Company. pp.136, 601 and 1061.
- Berkowitz, S. A. and Day, L. A. (1976). Mass, length, composition and structure of the filamentous bacterial virus fd. *Journal of Molecular Biology*. 102, 531-547.
- Bernard, J. M. L. and Francis, M. B. (2014). Covalent strategies for the covalent modification of filamentous phage. *Frontiers in Microbiology*. 5(734), 1-7.
- Berngruber, T. W., Weissing, F. J. and Gandon, S. (2010). Inhibition of superinfection and the evolution of viral latency. *Journal of Virology*, 84(19), 10200-10208.
- Białek-Bylka, G. E., Sofrova, D., Szurkowski, J., Skwarek, R., Sopko, B. and Manikowski, H. (2000). Linear dichroism, fluorescence polarisation, and path of the thermal deactivation of excited cyanobacterial (*Syechococcus elongatus*) photosystem I immobilised and oriented in polymer films. *Photosynthetica*, 38, 143-148.
- Biancalana, M. and Koide, S. (2010). Molecular mechanism of thioflavin-T binding to amyloid fibrils. *Biochimica Physica Acta*, 1804(7), 1405-1412.
- Binns, C. (2010). *Introduction to nanoscience and nanotechnology*. Oxford: John Wiley and Sons, Inc.
- Bird, G. R., Parrish Jr., M. and Blout, E. R. (1958). Apparatus for the observation of infrared streaming dichroism of polymer solutions. *The Review of Scientific Instruments*, 29(4), 305-309.
- Biver, T., Boggioni, A., Secco, F., Turriani, E., Venturini, M. and Yarmoluk, S. (2007). Influence of cyanine dye structure on self-aggregation and interaction with nucleic acids: A kinetic approach to TO and BO binding. *Archives of Biochemistry and Biophysics*, 465, 90-100.
- Boekema, E. J., Hankamer, B., Bald, D., Kruij, J., Nield, J., Boonstra, A. F., Barber, J. and Rögner, M. (1995). Supramolecular structure of the photosystem II complex from green plants and cyanobacteria. *Proceedings of the National Academy of Sciences of the United States of America*, 92, 175-179.
- Bohnet, J. G., Chen, Z., Weiner, J. M., Meiser, D., Holland, M. J. and Thompson, J. K. (2012). A steady-state superradiant laser with less than one intracavity photon. *Nature*, 484, 78-81.
- Borejdo, J. (1989). Orientation of DNA in agarose gels. *Biophysical Journal*, 55, 1183-1190.
- Borejdo, J. and Ortega, H. (1989). Electrophoresis and orientation of F-actin in agarose gels. *Biophysical Journal*, 56, 285-293.
- Borucki, B., Otto, H. and Heyn, M. P. (1998). Linear dichroism measurements on oriented purple membranes between parallel polarizers: contribution of linear

birefringence and applications to chromophore isomerization. *Journal of Physical Chemistry B*, 102, 3821-3829.

Boulais, É., Sawaya, N. P. D., Veneziano, R., Andreoni, A., Banal, J. L., Kondo, T., Mandal, S., Lin, S., Schlau-Cohen, G. S., Woodbury, N. W., Yan, H., Aspuru-Guzik, A. and Bathe, M. (2018). Programmed coherent coupling in a synthetic DNA-based excitonic circuit. *Nature Materials*, 17, 159-166.

Branston, S. D., Stanley, E. C., Ward, J. M. and Keshavarz-Moore, E. (2013). Determination of the survival of bacteriophage M13 from chemical and physical challenges to assist in its sustainable bioprocessing. *Biotechnology and Bioprocess Engineering*, 18, 560-566.

British Standards Institution (2007). *Terminology for Nanomaterials*. London: British Standards Institution, p.2.

Bruce, D. and Biggins, J. (1985). Mechanism of the light state transition in photosynthesis. V. 77 K linear dichroism of *Anacystis nidulans* in state 1 and state 2. *Biochimica et Biophysica Acta*, 810, 295-301.

Brutlag, D., Schekman, R. and Kornberg, A. (1971). A possible role for RNA polymerase in the initiation of M13 DNA synthesis. *Proceedings of the National Academy of Sciences of the United States of America*, 68(11), 2826-2829.

Cao, Q., Han, S.-J., Tulevski, G. S., Zhu, Y., Lu, D. D. and Haensch, W. (2013). Arrays of single-walled carbon nanotubes with full surface coverage for high-performance electronics. *Nature*, 8, 180-186.

Carr-Smith, J., Pacheco-Gómez, R., Little, H. A., Hicks, M. R., Sandhu, S., Steinke, N., Smith, D. J., Rodger, A., Goodchild, S. A., Lukaszewski, R. A., Tucker, J. H. R. and Dafforn, T. R. (2015). Polymerase chain reaction on a viral nanoparticle. *ACS Synthetic Biology*, 4, 1316-1325.

Carrico, Z. M., Farkas, M. E., Zhou, Y., Hsiao, S. C., Marks, J. D., Chokhawala, H., Clark, D. S., and Francis, M. B. (2012). N-terminal labelling of filamentous phage to create cancer marker imaging agents. *ACS Nano*. 6(8), 6675-6680.

Carter, P., Presta, L., Gorman, C. M., Ridgway, J. B. B., Henner, D., Wong, W. L. T., Rowland, A. M., Kotts, C., Carver, M. E. and Shepard, H. M. (1992). Humanisation of an anti-p185^{HER2} antibody for human cancer therapy. *Proceedings of the National Academy of Sciences of the United States of America*, 89, 4285-4289.

Cavaliere, L. F., Rosenberg, B. H. and Rosoff, M. (1956). Flow dichroism and its application to the study of deoxyribonucleic acid structure. *Journal of the American Chemical Society*, 78, 5235-5238.

Chakraborty, S., Bhattacharjee, D., Soda, H., Tominaga, M., Suzuki, Y., Kawamata, J. and Hussain, S. A. (2015). Temperature and concentration dependence of J-aggregate of a cyanine dye in a laponite film fabricated by Langmuir-Blodgett technique. *Applied Clay Science*, 104, 245-251.

Channon, K. J., Devlin, G. L. and MacPhee, C. E. (2009). Energy efficient transfer within self-assembling peptide fibers: a route to light-harvesting nanomaterials. *Journal of the American Chemical Society*, 131, 12520-12521.

- Chen, P. Y., Dang, X., Klug, M. T., Qi, J., Courchesne, M. N. D., Burpo, F. J., Fang, N., Hammond, P. T. and Belcher, A. M. (2013). A versatile three-dimensional virus-based template for dye-sensitized solar cells with improved electron transport and light harvesting. *American Chemical Society Nano*, 7(8), 6563-6574.
- Choi, M. S. (2008). One-dimensional porphyrin H-aggregates induced by solvent polarity. *Tetrahedron Letters*, 49, 7050-7053.
- Chowdhury, A., Wachsmann-Hogiu, S., Bangal, P. R., Raheem, I. and Peteanu, L. A. (2001). Characterization of chiral H and J aggregates of cyanine dyes formed by DNA templating using Stark and fluorescence spectroscopies. *Journal of Physical Chemistry*, 105, 12196-12201.
- Chung, W. J., Oh, J. W., Kwak, K., Lee, B. Y., Meyer, J., Wang, E., Hexemer, A. and Lee, S. W. (2011). Biomimetic self-templating supramolecular structures. *Nature*, 478, 364-368.
- Clack, B. A. and Gray, D. M. (1992). Flow linear dichroism spectra of four filamentous bacteriophages: DNA and coat protein contributions. *Biopolymers*, 32, 795-810.
- Cogdell, R. J., Gall, A. and Köhler, J. (2006). The architecture and function of the light-harvesting apparatus of purple bacteria: from single molecules to in vivo membranes. *Quarterly Reviews of Biophysics*, 39, 227-324.
- Cohen, B. E., McAnaney, T. B., Park, E. S., Jan, Y. N., Boxer, S. G. and Jan, L. Y. (2002). Probing protein electrostatics with a synthetic fluorescent amino acid. *Science*, 296, 1700-1703.
- Cooper, J. H. (1969). An evaluation of current methods for diagnostic histochemistry of amyloid. *Journal of Clinical Pathology*, 22, 410-413.
- Courchesne, N. M. D., Klug, M. T., Chen, P. Y., Kooi, S. E., Yun, D. S., Hong, N., Fang, N. X., Belcher, A. M. and Hammond, P. T. (2014). Assembly of a bacteriophage-based template for the organization of materials into nanoporous networks. *Advanced Materials*, 26(21), 3398-3404.
- Creative Biolabs. (2019). Phage display library construction. [ONLINE] Available at: <https://www.creative-biolabs.com/phage-display-library-construction.html>. [Accessed 6 February 2019].
- Creighton, T. E. ed., (1997). *Protein structure: a practical approach*. 2nd ed. Oxford: Oxford University Press, pp.310-316.
- Croce, R., Remelli, R., Varotto, C., Breton, J. and Bassi, R. (1999). The neoxanthin binding site of the major light-harvesting complex (LHCII) from higher plants. *FEBS Letters*, 456, 1-6.
- Cui, Y., Kim, S. N., Jones, S. E., Wissler, L. L., Naik, R. R. and McAlpine, M. C. (2010). Chemical functionalization of graphene enabled by phage displayed peptides. *Nano Letters*, 10(11), 4559-4565.
- Cunningham, P. D., Kim, Y. C., Díaz, S. A., Buckhout-White, S., Mathur, D., Medintz, I. L. and Melinger, J. S. (2018). Optical properties of vibronically coupled Cy3 dimers on DNA scaffolds. *The Journal of Physical Chemistry B*, 122, 5020-5029.

- Dafforn, T. R., Rajendra, J., Halsall, D. J., Serpell, L. C. and Rodger, A. (2004). Protein fiber linear dichroism for structure determination and kinetics in a low-volume, low-wavelength Couette flow cell. *Biophysical Journal*, 86, 404-410.
- Dang, X., Yi, H., Ham, M. H., Qi, J., Yun, D. S., Ladewski, R., Strano, M. S., Hammod, P. T. and Belcher, A. M. (2011). Virus-templated self-assembled single-walled carbon nanotubes for highly efficient electron collection in photovoltaic devices. *Nature Nanotechnology*, 6, 377-384.
- Demeester, J., De Smedt, S., Sanders, N. N., Haestraede, J., Jiskoot, W. and Crommelin, D. J. A. (2005). *Methods for structural analysis of protein pharmaceuticals*. Arlington: AAPS Press, p.245.
- Derda, R., Tang, S. K. Y. and Whitesides, G. M. (2010). Uniform amplification of phage with different growth characteristics in individual compartments consisting of monodisperse droplets. *Angewandte Chemie International Edition in English*, 49(31), 5301-5304.
- DichroWeb User Guide. [online] Available at: <http://dichroweb.cryst.bbk.ac.uk/html/userguide.shtml> [Date accessed 18/06/2018]
- Diekmann, S., Hillen, W., Jung, M., Wells, R. D. and Pörshcke, D. (1982). Electric properties and structure of DNA restriction fragments from measurements of the electric dichroism. *Biophysical Chemistry*, 15, 157-167.
- Dogic, Z. and Fraden, S. (1997). Smectic phase in a colloidal suspension of semiflexible virus particles. *Physical Review Letters*, 78(12), 2417-2420.
- Dogic, Z. and Fraden, S. (2000). Cholesteric phase in viral suspensions. *Langmuir*, 16, 7820-7824.
- Dohan, J. M. and Masschelein, W. J. (1987). The photochemical generation of ozone: Present state-of-the-art. *Ozone: Science and Engineering*, 9(4), 315-334.
- Dumont, S. and Prakash, M. (2014). Emergent mechanics of biological structures. *Molecular Biology of the Cell*. 25(22), 3461-3465.
- Dutta, P. K., Varghese, R., Nangreave, J., Lin, S., Yan, H. and Liu, Y. (2011). DNA-directed artificial light-harvesting antennae. *Journal of the American Chemical Society*, 133, 11985-11993.
- Egawa, Y., Hayashida, R. and Anzai, J. I. (2007). pH-induced interconversion between J-aggregates and H-aggregates of 5,10,15,20-tetrakis(4-sulfonatophenyl)porphyrin in polyelectrolyte multilayer films. *Langmuir*, 23, 13146-13150.
- Feng, J. N., Model, P. and Russel, M. (1999). A trans-envelope protein complex needed for filamentous phage assembly and export. *Molecular Microbiology*, 34(4), 745-755.
- Feng, X., Ding, X., Chen, L., Wu, Y., Liu, L., Addicoat, M., Irle, S., Dong, Y. and Jiang, D. (2016). Two-dimensional artificial light-harvesting antennae with predesigned high-order structure and robust photosensitising activity. *Scientific Reports*, 6, 32944.

- Fernandez-Flores, A. (2011). A review of amyloid staining: methods and artifacts. *Biotechnic and Histochemistry*, 86, 293-301.
- Ferrari, M. (2005). Nanovector therapeutics. *Current Opinion in Chemical Biology*, 9, 343-346.
- Fisher Bioreagents. (2018). *Preparation of 0.1 M potassium phosphate buffer at 25 °C.* [online] Available at <https://www.fishersci.co.uk/webfiles/uk/web-docs/PAGE728.PDF> [Date accessed 07/09/2018]
- Food and Drug Administration (FDA), (1998). *Letter of approval: Trastuzumab*, Rockville Pike: FDA.
- Fornasiero, D. and Grieser, F. (1987). A linear dichroism study of colloidal silver in stretched polymer films. *Chemical Physics Letters*, 139(1), 103-108.
- Gadde, S., Batchelor, E. K. and Kaifer, A., E. (2009). Controlling the formation of cyanine dye H- and J-aggregates with cucurbituril hosts in the presence of anionic polyelectrolytes. *Chemistry: A European Journal*. 15(24), 6025-6031.
- Ganago, I. B., Klimov, V. V., Ganago, A. O., Shuvalov, V. A. and Erokhin, Y. E. (1982). Linear dichroism and orientation of pheophytin, the intermediary electron acceptor in photosystem II reaction centers. *FEBS Letters*, 140(1), 127-130.
- Garab, G. and van Amerongen, H. (2009). Linear dichroism and circular dichroism in photosynthesis research. *Photosynthesis Research*, 101, 135-146.
- Garnock-Jones, K. P., Keating, G. M. and Scott, L. J. (2010). Trastuzumab: a review of its use as adjuvant treatment in human epidermal growth factor 2 (HER2) positive early breast cancer. *Drugs*, 70, 215-239.
- Georgakopoulou, S., van der Zwan, G., Bassi, R., van Grondelle, R., van Amerongen, H. and Croce, R. (2007). Understanding the changes in circular dichroism of light-harvesting complex II upon varying its pigment composition and organisation. *Biochemistry*, 46, 4745-4754.
- Georgakopoulou, S., van Grondelle, R. and van der Zwan, G. (2004). Circular dichroism of carotenoids in bacterial light-harvesting complexes: experiments and modelling. *Biophysical Journal*, 87, 3010-3022.
- Ghosh, D., Kohli, A. G., Moser, F., Endy, D. and Belcher, A. M. (2012). Refactored M13 bacteriophage as a platform for tumor cell imaging and drug delivery. *American Chemical Society Synthetic Biology*, 1(12), 576-582.
- Gibaud, T. (2017). Filamentous phages as building blocks for reconfigurable and hierarchical self-assembly. *Journal of Physics: Condensed Matter*, 29, 493003.
- Gray, J. G., Graham, C., Dudas, S., Paxman, E., Vuong, B. and Czub, S. (2016). Defining and assessing analytical performance criteria for transmissible spongiform encephalopathy-detecting amyloid seeding assays. *Journal of Molecular Diagnostics*. 18(3), 454-467.
- Greenfield, N. J. (2006). Using circular dichroism spectra to estimate protein secondary structure. *Nature Protocols*. 1(6), 2876-2890.

- Grieco, S. H. H., Lee, S., Dunbar, W. S., MacGillivray, R. T. A. and Curtis S. B. (2009). Maximizing filamentous phage yield during computer-controlled fermentation. *Bioprocess and Biosystems Engineering*, 32(6), 773-779.
- Grieco, S. H. H., Wong, A. Y. K., Dunbar, W. S., MacGillivray, R. T. A. and Curtis, S. B. (2012). Optimization of fermentation parameters in phage production using response surface methodology. *Journal of Industrial Microbiology and Biotechnology*, 39, 1515-1522.
- Griffith, J., Manning, M. and Dunn, K. (1981). Filamentous bacteriophage contract into hollow spheroid particles upon exposure to a chloroform-water interface. *Cell*, 23, 747-753.
- Gryczknski, Z., Paolesse, R., Smith, K. M. and Bucci, E. (1997). Effect of central metal substitution on linear dichroism of porphyrins: evidence of out-of-plane transition moments. *Biophysical Chemistry*, 69, 71-84.
- Hada, H., Hanawa, R., Haraguci, A. and Yonezawa, Y. (1985). Preparation of the J aggregate of cyanine dyes by the means of the Langmuir-Blodgett technique. *American Chemical Society*. 89(4), 560-562.
- Haight, N. G. and Webster, R. E. (1999). The pI and pXI assembly proteins serve separate and essential roles in filamentous phage assembly. *Journal of Molecular Biology*, 293, 1017-1027.
- Halsall, D. J., Rodger, A. and Dafforn, T. R. (2001). Linear dichroism for the detection of single base pair mutations. *Chemical Communications*. 23, 2410-2411.
- Harel, M., Sonoda, L. K., Silman, I., Sussman, J. L. and Rosenberry, T. L. (2008). Crystal structure of thioflavin T bound to the peripheral site of *Torpedo californica* acetylcholinesterase reveals how thioflavin T acts as a sensitive fluorescent reporter of ligand binding to the acylation site. *Journal of the American Chemical Society*. 130(25), 7856-7861.
- Hasanzadeh, M. and Mottaghitalab, V. (2014). The role of shear-thickening fluids (STFs) in ballistic and stab-resistance improvement of flexible armour. *Journal of Materials Engineering and Performance*, 23, 1182-1196.
- Hecht, E. (2002). *Optics*. 4th ed. San Francisco: Addison Wesley.
- Henry, K. A., Arbabi-Ghahruji, M. and Scott, J. K. (2015). Beyond phage display: non-traditional applications of the filamentous bacteriophage as a vaccine carrier, therapeutic biologic, and bioconjugation scaffold. *Frontiers in Microbiology*, 6, 755.
- Hilaire, M. R., Ahmed, I. A., Lin C. W., Jo, H., DeGrado, W. F. and Gai, F. (2017). Blue fluorescent amino acid for biological spectroscopy and microscopy. *Proceedings of the National Academy of Sciences of the United States of America*, 114(23), 6005-6009.
- Hilderbrand, S. A., Kelly, K. A., Niedre, M., and Weissleder, R. (2008). Near infrared fluorescence-based bacteriophage particles for ratiometric pH imaging. *Bioconjugate Chemistry*. 19(8), 1635-1639.
- Hirayama, T., Iyoshi, S., Taki, M., Maeda, Y. and Yamamoto, Y. (2007). Synthesis of a new bifunctionalised fluorescent label and physical properties of the bound form on model peptide Troponin C. *Organic and Biomolecular Chemistry*, 5, 2040-2045.

- Hofschneider, P. (1963). [Discovery of Bacteriophage M13]. *Naturforschung B Chemistry Biochemistry Biophysics and Biology*, 18b, 203-205.
- Hogan, M., Dattagupta, N. and Crothers, D. M. (1978). Transient electric dichroism of rod-like DNA molecules. *Proceedings of the National Academy of Sciences of the United States of America*, 75(1), 195-199.
- Honek, J. (2013). Bionanotechnology and bionanomaterials: John Honek explains the good things that can come in very small packages. *BMC Biochemistry*, 14, 29.
- Hou, P-X., Liu, C. and Cheng, H-M. (2008). Purification of carbon nanotubes. *Carbon*, 46, 2003-2025.
- Houssier, C. and Fredericq, E. (1966). Electro-optical properties of nucleic acids and nucleoproteins I. Study of the gel-forming deoxyribonucleohistone. *Biochimica et Biophysica Acta*, 120, 113-130.
- Huang, J. H., Bishop-Hurley, S. L. and Cooper, M. A. (2012). Development of anti-infectives using phage display: biological agents against bacteria, viruses and parasites. *Antimicrobial Agents and Chemotherapy*, 56(9), 4569-4582.
- Huang, Y., Chiang, C. Y., Lee, S. K., Gao, Y., Hu, E. L., De Yoreo, J. and Belcher, A. M. (2005). Programmable assembly of nanoarchitectures using genetically engineered viruses. *Nano Letters*, 5(7), 1429-1434.
- Hudson, S. A., Ecroyd, H., Kee, T. W. and Carver, J. A. (2009). The thioflavin T fluorescence assay for amyloid fibril detection can be biased by the presence of exogenous compounds. *FEBS Journal*. 276(20), 5960-5972.
- Hunter, G. J., Rowitch, D. H. and Perham, R. N. (1987). Interactions between DNA and coat protein in the structure and assembly of filamentous bacteriophage fd. *Nature*, 327(21), 252-254.
- Ilanchelian, M. and Ramaraj, R. (2004). Emission of thioflavin T and its control in the presence of DNA. *Journal of Photochemistry and Photobiology*. 162(1), 129-137.
- Ivask, A., Kurvet, I., Kasemets, K., Blinova, I., Aruoja, V., Suppi, S., Vija, H., Käkinen, A., Titma, T., Heinlaan, M., Visnapuu, M., Koller, D., Kisand, V. and Kahru, A. (2014). Size-dependent toxicity of silver nanoparticles to bacteria, yeast, algae, crustaceans and mammalian cells in vitro. *Public Library of Science One*, 9(7), e102108.
- Jacob, E. and Hofschneider, P. H. (1969). Replication of the single-stranded DNA bacteriophage M13: messenger RNA synthesis directed by M13 replicative form RNA. *Journal of Molecular Biology*, 46, 359-363.
- Jakobi, H., Novak, A. and Kuhn, H. (1962). IR dichroism of elongated molecules in stretched polyethylene and polyvinyl alcohol films. *Journal of Electrochemistry*, 66(10), 863-870.
- Jelley, E. E. (1936). Spectral absorption and fluorescence of dyes in the molecular state. *Nature*, 1009.
- Jeon, J-Y. and Ha, T-J. (2016). High-performance single-walled carbon nanotube-based thin-film transistors by reducing charge transfer. *Institute of Electrical and Electronics Engineers Transactions on Electron Devices*, 63(2), 827-831.

- Jethva, P. N., Kardani, J. R. and Roy, I. (2011). Modulation of α -synuclein aggregation by dopamine in the presence of MPTP and its metabolite. *FEBS Journal*, 278, 1688-1698.
- Jin, S., Hu, Y., Gu, Z., Liu, L. and Wu, H-C. (2011). Application of quantum dots in biological imaging. *Journal of Nanomaterials*, 2011, 834139.
- Jones, R. A. L. (2004). *Soft machines nanotechnology and life*. Oxford: Oxford University Press.
- Jonsson, M., Åkerman, B. and Nordén, B. (1988). Orientation of DNA during gel electrophoresis studied with linear dichroism spectroscopy. *Biopolymers*, 27, 381-414.
- Kappert, R. J. H., Vogel, J., Sacchi, M. and Fuggle, J. C. (1993). Linear-dichroism studies of thin Dy overlayers on Ni(110) and Cu(110) substrates. *Physical Review B*, 48(4), 2711-2720.
- Kehoe, J. W. and Kay, B. K. (2005). Filamentous phage display in the new millennium. *Chemical Reviews*, 105, 4056-4072.
- Kelly, K. A., Waterman, P., and Weissleder, R. (2006). *In vivo* imaging of molecularly targeted phage. *Neoplasia*, 8(12), 1011-1018.
- Kersharwani, P. and Iyer, A. K. (2015). Recent advances in dendrimer-based nanovectors for tumour-targeted drug and gene delivery. *Drug Discovery Today*, 20(5), 536-547.
- Khalil, A. S., Ferrer, J. M., Brau, R. R., Kottmann, S. T., Noren, C. J., Lang, M. J. and Belcher, A. M. (2007). Single M13 bacteriophage tethering and stretching. *Proceedings of the National Academy of Sciences of the United States of America*, 104(12), 4892-4897.
- Khurana, C., Vala, A. K., Andharya, N., Pandey, O. P. and Chudasama, B. (2013). Antibacterial activity of silver: The role of hydrodynamic particle size at nanoscale. *Journal of Biomedical Materials Research Part A*, 102(10), 3361-3368.
- Kim, A., Lee, E. H., Choi, S-H. and Kim, C-K. (2004). In vitro and in vivo transfection efficiency of a novel ultradeformable cationic liposome. *Biomaterials*, 25, 305-313.
- Klumpp, C., Kostarelos, K., Prato, M. and Bianco, A. (2006). Functionalized carbon nanotubes as emerging nanovectors for the delivery of therapeutics. *Biochimica et Biophysica Acta*, 1758, 404-412.
- Kokoska, R. J. and Steege, D. A. (1998). Appropriate expression of filamentous phage f1 DNA replication genes II and X requires RNase E-dependent processing and separate mRNAs. *Journal of Bacteriology*, 180(12), 3245-3249.
- Kringle, L., Sawaya, N. P. D., Widom, J., Adams, C., Raymer, M. G., Aspuru-Guzik, A. and Marcus, A. H. (2018). Temperature-dependent conformations of exciton-coupled Cy3 dimers in double-stranded DNA. *The Journal of Chemical Physics*, 148, 085101.
- Kuhn, A. and Wickner, W. (1985). Isolation of mutants in M13 coat protein that affect its synthesis, processing and assembly into phage. *The Journal of Biological Chemistry*, 260(29), 15907-15913.

- Külbrandt, W. (1994). Structure and function of the plant light-harvesting complex, LHC-II. *Current Opinion in Structural Biology*, 4, 519-528.
- Kutyrev, I. A., Biserova, N. M., Olennikov, D. N., Korneva, J. V. and Mazur, O. E. (2017). Prostaglandins E₂ and D₂-regulators of host immunity in the model parasite *Diphyllobothrium dendriticum*: An immunocytochemical and biochemical study. *Molecular and Biochemical Parasitology*, 212, 33-45.
- Kuzmicheva, G., Jayanna, P., Sorokulova, I. and Petrenko, V. (2008). Diversity and censoring of landscape phage libraries. *Protein Engineering, Design and Selection*, 22(1), 9-18.
- Lakowicz, J. R. (2010). *Principles of fluorescence spectroscopy*. New York: Springer Science+Business Media, LLC., p.443.
- Laocharoensuk, R., Burdick, J. and Wang, J. (2008). Carbon-nanotube-induced acceleration of catalytic nanomotors. *American Chemical Society Nano*, 2(5), 1069-1075.
- Lee, B. Y., Zhang, J., Zueger, C., Chung, W. J., Yoo, S. Y., Wang, E., Meyer, J., Ramesh, R. and Lee, S. W. (2012). Virus-based piezoelectric energy generation. *Nature Nanotechnology*, 7, 351-356.
- Lee, J. H., Fan, B., Samdin, T. D., Monteiro, D. A., Desai, M. S., Scheideler, O., Jin, H. E., Kim, S. and Lee, S. W. (2017). Phage-based structural color sensors and their pattern recognition sensing system. *American Chemical Society Nano*, 11, 3632-3641.
- Lee, J., Song, J., Hwang, M., and Lee, K. (2013). Nanoscale bacteriophage biosensors beyond phage display. *International Journal of Nanomedicine*, 8, 3917-3925.
- Lee, S. W., Mao, C., Flynn, C. E. and Belcher, A. M. (2002). Ordering of quantum dots using genetically engineered viruses. *Science*, 296, 892-895.
- Lee, S. W., Wood, B. M. and Belcher, A. M. (2003). Chiral smectic C structures of virus-based films. *Langmuir*, 19, 1592-1598.
- Lee, Y. M., Jung, B., Kim, Y. H., Park, A. R., Han, S., Choe, W. S. and Yoo, P. J. (2014). Nanomesh-structured ultrathin membranes harnessing the unidirectional alignment of viruses on a graphene-oxide film. *Advanced Materials*, 26, 3899-3904.
- Legut, D., Tesch, M. F., Mertins, H. Ch., Gilbert, M. C., Jansing, C., Bürgler, D. E., Schneider, C. M., Gaupp, A., Hamrle, J. and Oppeneer, P. M. (2014). Influence of the crystal structure of thin Co films on X-ray magnetic linear dichroism – Comparison of ab initio theory and reflectometry experiments. *Journal of Applied Physics*, 115, 17E132.
- Li, J., Papadopoulos, C., Xu, J. (1999). Growing Y-junction carbon nanotubes. *Nature*, 402, 253-254.
- Li, K., Chen, Y., Li, S., Nguyen, H. G., Niu, Z., You, S., Mello, C. M., Lu, X. and Wang, Q. (2010). Chemical modification of M13 bacteriophage and its application in cancer cell imaging. *Bioconjugate Chemistry*, 21, 1369-1377.

- Liechty, W. B., Kryscio, D. R., Slaughter, B. V. and Peppas, N. A. (2010). Polymers for drug delivery systems. *Annual Review of Chemical and Biomolecular Engineering*, 1, 149-173.
- Lin, N. S. C. and Pratt, D. (1972). Role of bacteriophage M13 gene 2 in viral DNA replication. *Journal of Molecular Biology*, 72, 37-49.
- Louis-Jeune, C. Andrade-Navarro, M. A. and Perez-Iratxeta, C. (2011). Prediction of protein secondary structure from circular dichroism using theoretically derived spectra. *Proteins: Structure, function and bioinformatics*, 80, 374-381.
- Lu, Z., Rong, K., Li, J., Yang, H. and Chen, R. (2013). Size-dependent antibacterial activities of silver nanoparticles against oral anaerobic pathogenic bacteria. *Journal of Materials Science: Materials in Medicine*, 24, 1465-1471.
- Lubkowski, J., Hannecke, F., Plückthun, A. and Wlodawer, A. (1999). Filamentous phage infection: crystal structure of g3p in complex with its coreceptor, the C-terminal domain of TolA. *Structure*, 7(6), 711-722.
- Ma, L., Yang, F. and Zheng, J. (2014). Application of fluorescence resonance energy transfer in protein studies. *Journal of Molecular Structure*, 1077, 87-100.
- Malmos, K. G., Blancas-Mejia, L. M., Weber, B., Buchner, J., Ramirez-Alvarado, M., Naiki, H. and Otzen, D. (2017). ThT 101: a primer on the use of thioflavin T to investigate amyloid formation. *Amyloid*, 24(1), 1-16.
- Mann, J. R., Gannon, M. K., Fitzgibbons, T. C., Detty, M. R. and Watson D. F. (2008). Optimising the photocurrent efficiency of dye-sensitised solar cells through the controlled aggregation of chalcogenoxanthylum dyes on nanocrystalline titania films. *Journal of Physical Chemistry C Letters*, 112, 13057-13061.
- Marek, P. L., Hahn, H. and Balaban, T. S. (2011). On the way to biomimetic dye aggregate solar cells. *Energy and Environmental Science*, 4, 2366-2378.
- Markova, L. I., Malinovskii, V. L., Patsenker, L. D. and Häner, R. (2013). J- vs. H-type assembly: pentamethine cyanine (Cy5) as a near-IR chiroptical reporter. *Chemical Communications*, 49, 5298-5300.
- Marrington, R., Dafforn, T. R., Halsall, D. J. and Rodger, A. (2004). Micro-volume Couette flow sample orientation for absorbance and fluorescence linear dichroism. *Biophysical Journal*, 87, 2002-2012.
- Marrington, R., Dafforn, T. R., Halsall, D. J., MacDonald, J. I., Hicks, M. and Rodger, A. (2005). Validation of new micro-volume Couette flow linear dichroism cells. *Analyst*. 130, 1608-1616.
- Marvin, D. A. (1998). Filamentous phage structure, infection and assembly. *Current Opinions in Structural Biology*. 8(2), 150-158.
- Matsui, H. and MacCuspie, R. (2001). Metalloporphyrin nanotube fabrication using peptide nanotubes as templates. *Nano Letters*, 1, 672-675.
- Matsuoka, Y. and Nordén, B. (1982). Linear dichroism studies of nucleic acid bases in stretched poly(vinyl alcohol) film. Molecular orientation and electronic transition moment directions. *The Journal of Physical Chemistry*, 86, 1378-1386.

- McDermott, G., Prince, S. M., Freer, A. A., Hawthornthwaite-Lawless, A. M., Papiz, M. Z., Cogdell, R. J. and Isaacs, N. W. (1995). Crystal structure of an integral membrane light-harvesting complex from photosynthetic bacteria. *Nature*, 374, 517-521.
- Meinardi, F., Cerminara, M., Sassella, A., Bonifacio, R. and Tubino, R. (2003). Superradiance in molecular H-aggregates. *Physical Review Letters*, 91(24), 247401.
- Melkozernov, A. N., Olson, J. M., Li, Y. F., Allen, J. P. and Blankenship, R. E. (1998). Orientation and excitonic interactions of the Fenn-Matthews-Olson bacteriochlorophyll α -protein in membranes of the green sulphur bacterium *Chlorobium tepidum*. *Photosynthesis Research*, 56, 315-328.
- Mena, M. A. and Daugherty, P. S. (2005). Automated design of degenerate codon libraries. *Protein Engineering, Design and Selection*, 18, 559-561.
- Merzlyak, A. and Lee, S. W. (2009). Engineered phage materials with desired peptide display: rational design sustained through natural selection. *Bioconjugate Chemistry*, 20, 2300-2310.
- Merzlyak, A., Indrakanti, S. and Lee, S. W. (2009). Genetically engineered nanofiber-like viruses for tissue regenerating materials. *Nano Letters*, 9(2), 846-852.
- Michielsen, K. and Stavenga, D. G. (2008). Gyroid cuticular structures in butterfly wing scales: biological photonic crystals. *Journal of the Royal Society Interface*. 5(18), 85-94.
- Michl, J., Thulstrup, E. W. and Eggers, J. H. (1970). Polarization spectra in stretched polymer sheets. III. Physical significance of the orientation factors and determination of π - π^* transition moment directions in molecules of low symmetry. *The Journal of Physical Chemistry*, 74(22), 3878-3884.
- Miller, R. A., Presley, A. D. and Francis, M. B. (2007). Self-assembling light-harvesting systems from synthetically modified tobacco mosaic virus coat proteins. *Journal of the American Chemical Society*, 129, 3104-3109.
- Modesto-Lopez, L. B., Thimsen, E. J., Collins, A. M., Blankenship, R. E. and Biswas, P. (2010). Electro spray-assisted characterisation and deposition of chlorosomes to fabricate a biomimetic light-harvesting device. *Energy and Environmental Science*, 3, 216-222.
- Moghimian, P., Srot, V., Pichon, B. P., Facey, S. J. and van Aken, P. A. (2016). Stability of M13 phage in organic solvents. *Journal of Biomaterials and Nanobiotechnology*, 7, 72-77.
- Molecular Probes, Inc., (2001). Modified carbocyanine dyes and their conjugates. EP1322710 B9.
- Molek, P., Strukelj, B. and Bratkovic, T. (2011). Peptide phage display as a tool for drug discovery: targeting membrane receptors. *Molecules*, 16, 857-887.
- Morag, O., Abramov, G. and Goldbourt, A. (2011). Similarities and differences within members of the Ff family of filamentous bacteriophage viruses. *The Journal of Physical Chemistry*. 115, 15370-15379.

- Morag, O., Sgourakis, N. G., Baker, D. and Goldbourt, A. (2015). The NMR Rosetta capsid model of M13 bacteriophage reveals a quadrupled hydrophobic packing epitope. *Proceedings of the National Academy of Sciences of the United States of America*, 112(4), 971-976.
- Morita, Y., Ohsugi, T., Iwasa, Y. and Tamiya, E. (2004). A screening of phage displayed peptides for the recognition of fullerene (C60). *Journal of Molecular Catalysis: B Enzymatic*, 28, 185-190.
- Mulhern, K. R., Detty, M. R. and Watson, D. F. (2011). Aggregation-induced increase of the quantum yield of electron injection from chalcogenorhodamine dyes to TiO₂. *The Journal of Physical Chemistry C*, 115, 6010-6018.
- Naiki, H., Higuchi, K., Hosokawa, M. and Takeda, T. (1989). Fluorometric determination of amyloid fibrils *in vitro* using the fluorescent dye, thioflavine T¹. *Analytical Biochemistry*, 177, 244-249.
- Nam, Y. S., Shin, T., Park, H., Magyar, A. P., Choi, K., Fantner, G., Nelson, K. A. and Belcher, A. M. (2010). Virus-templated assembly of porphyrins into light-harvesting nanoantennae. *Journal of the American Chemical Society*, 132, 1462-1463.
- Natarajan, L. V., Robinson, M. and Blankenship, R. E. (1983). Linear dichroism of cyanine dyes in stretched polyvinyl alcohol films. *Journal of Chemical Education*, 60(3), 241-243.
- Nguyen, K. T. H., Adamkiewicz, M. A., Hebert, L. E., Zygiel, E. M., Boyle, H. R., Martone, C. M., Meléndez-Ríos, C. B., Noren, K. A., Noren, C. J. and Fitzsimons Hall, M. (2014). Identification and characterization of mutant clones with enhanced propagation rates from phage-displayed peptide libraries. *Analytical Biochemistry*, 462, 35-43.
- Nicoli, F., Barth, A., Bae, W., Neukirchinger, F., Crevenna, A. H., Lamb, D. C. and Liedl, T. (2017). Directional photonic wire mediated by homo-Förster resonance energy transfer on a DNA origami platform. *ACS Nano*, 11, 11264-11272.
- Nicoli, F., Roos, M. K., Hemmig, E. A., Di Antonio, M., de Vivie-Riedle, R. and Liedl, T. (2016). Proximity-induced H-aggregation of cyanine dyes on DNA-duplexes. *The Journal of Physical Chemistry A*, 120, 9941-9947.
- Niu, Z., Bruckman, M. A., Harp, B., Mello, C. M. and Wang, Q. (2008). Bacteriophage M13 as a scaffold for preparing conductive polymeric composite fibers. *Nano Research*, 1, 235-241.
- Nordén, B. and Tjerneld, F. (1977). Optical studies on complexes between DNA and pseudoisocyanine. *Biophysical Chemistry*, 6, 31-45.
- Nordén, B., Lindblom, G. and Jonáš, I. (1977). Linear dichroism spectroscopy as a tool for studying molecular orientation in model membrane systems. *The Journal of Physical Chemistry*, 81(22), 2086-2093.
- Nordén, B., Rodger, A. and Dafforn, T. R. (2010). *Linear dichroism and circular dichroism: A textbook on polarized-light spectroscopy*. Cambridge: RSC Publishing.
- Noren, K. A. and Noren, C. J. (2001). Construction of high-complexity combinatorial phage display peptide libraries. *Methods*, 23, 169-178.

- Oey, J. L. and Knippers, R. (1972). Properties of the isolated gene 5 protein of bacteriophage fd. *Journal of Molecular Biology*, 68, 125-138.
- Okuom, M. O., Burks, R., Naylor, C. and Holmes, A. E. (2015). Applied circular dichroism: a facile spectroscopic tool for configurational assignment and determination of enantiopurity. *Journal of Analytical Methods in Chemistry*, 2015, 865605.
- Overman, S. A., Tsuboi, M. and Thomas, G. J. Jr. (1996). Subunit orientation in the filamentous virus Ff (fd, f1, M13). *Journal of Molecular Biology*, 259, 331-336.
- Pacheco-Gómez, R., Kraemer, J., Stokoe, S., England, H. J., Penn, C. W., Stanley, E., Rodger, A., Ward, J., Hicks, M. R. and Dafforn, T. R. (2012). Detection of pathogenic bacteria using a homogeneous immunoassay based on shear alignment of virus particles and linear dichroism. *Analytical Chemistry*, 84, 91-97.
- Palaniappan, K. K., Ramirez, R. M., Bajaj, V. S., Wemmer, D. E., Pines, A., and Francis, M. B. (2013). Molecular imaging of cancer cells using a bacteriophage-based ¹²⁹Xe NMR biosensor. *Angewandte Chemie International Edition in English*. 52, 4849-4853.
- Panchuk-Voloshina, N., Haugland, Rosaria, P., Bishop-Stewart, J., Bhalgat, M. K., Millard, P. J., Mao, F., Leung, W. Y. and Haugland, R. P. (1999). Alex dyes, a series of new fluorescent dyes that yield exceptionally bright, photostable conjugates. *The Journal of Histochemistry & Cytochemistry*, 47(9), 1179-1188.
- Park, J. P., Do, M., Jin, H. E., Lee, S. W. and Lee, H. (2014). M13 bacteriophage displaying DOPA on surfaces: fabrication of various nanostructured inorganic materials without time-consuming screening processes. *ACS Applied Materials and Interfaces*, 6, 18653-18660.
- Peng, H. Q., Chen, Y. Z., Zhao, Y., Yang, Q. Z., Wu, L. Z., Tung, C. H., Zhang, L. P. and Tong, Q. X. (2012). Artificial light-harvesting system based on multifunctional surface-cross-linked micelles. *Angewandte Chemie International Edition*, 51, 2088-2092.
- Peng, L-M., Zhang, Z. and Wang, S. (2014). Carbon nanotube electronics: recent advances. *Materials Today*, 17(9), 433-442.
- Pershad, K. and Kay, B. K. (2013). Generating thermal stable variants of protein domains through phage display. *Methods*, 60, 38-45.
- Ploss, M., Facey, F. J., Bruhn, C., Zemel, L., Hofmann, K., Stark, R. W., Albert, B. and Hauer, B. (2014). Selection of peptides binding to metallic borides by screening M13 phage display libraries. *Biomed Central Biotechnology*, 14, 12.
- Pu, F., Wu, L., Ju, E., Ran, X., Ren, J. and Qu, X. (2014). Artificial light-harvesting material based on self-assembly of coordination polymer nanoparticles. *Advanced Functional Materials*, 24, 4549-4555.
- Qiao, J., Kong, X., Hu, Z., Yang, F. and Ji, W. (2014). High-mobility transport anisotropy and linear dichroism in few-layer black phosphorus. *Nature Communications*, 5, 4475.

- Rapoza, M. P. and Webster, R. E. (1995). The products of gene I and the overlapping in-frame gene XI are required for filamentous phage assembly. *Journal of Molecular Biology*, 248, 627-638.
- Rasmussen, U. B., Schreiber, V., Schultz, H., Mischler, F. and Schughart, K. (2002). Tumor cell-targeting by phage-displayed peptides. *Cancer Gene Therapy*, 9, 606-612.
- Ratner, M. A. (2003). Superradance of J-aggregates: correspondence between an infinite disordered chain and a regular finite chain. *Low Temperature Physics*, 29(7), 602-605.
- Ravdin, P. and Axelrod, D. (1977). Fluorescent tetramethyl rhodamine derivatives of α -bungarotoxin: preparation, separation and characterisation. *Analytical Biochemistry*, 80, 585-592.
- Ray, D. S. (1970). Replication of bacteriophage M13: Synthesis of M13-specific DNA in the presence of chloramphenicol. *Journal of Molecular Biology*, 53, 239-250.
- Razmkhah, K., Chmel, N. P., Gibson, M. I. and Rodger, A. (2014a). Oxidized polyethylene films for orienting polar molecules for linear dichroism spectroscopy. *Analyst*, 139, 1372-1382.
- Razmkhah, K., Little, H., Sandhu, S., Dafforn, T. R. and Rodger, A. (2014b). Optical properties of xanthene based fluorescent dyes studied by stretched-film linear dichroism. *RSC Advances*, 4, 37510-37515.
- Reetz, M. T. (2016). What are the limitations of enzymes in synthetic organic chemistry? *The Chemical Record*, 16, 2449-2459.
- Riechmann, L. and Holliger, P. (1997). The C-terminal domain of TolA is the coreceptor for filamentous phage infection of *E. coli*. *Cell*, 90, 351-360.
- Riggin, C. H., Beltz, G. A., Hung, C. H., Thorn, R. M. and Marciani, D. J. (1987). Detection of antibodies to human immunodeficiency virus by latex agglutination with recombinant antigen. *Journal of Clinical Microbiology*, 25, 1772-1773.
- Rincón, V., Rodríguez-Huete, A., López-Argüello, S., Ibarra-Molero, B., Sanchez-Ruiz, J. M., Harmsen, M. M. and Mateu, M. G. (2014). Identification of the structural basis of thermal lability of a virus provides a rationale for improved vaccines. *Structure*, 22, 1560-1570.
- Robertson, J. D., Rizzello, L., Avila-Olias, M., Gaitzch, J., Contini, C., Magoñ, M. S., Renshaw, S. A. and Battaglia, G. (2016). Purification of nanoparticles by size and shape. *Scientific Reports*, 6, 27494.
- Roco, M. C. (2011). The long view of nanotechnology development: the national nanotechnology initiative at 10 years. *Journal of Nanoparticle Research*, 13, 427-445.
- Rodger, A. (2003). Near UV protein CD. Berlin Heidelberg: *Springer*, p. 1694.
- Royal Society and Royal Academy of Engineering (2004). *Nanoscience and nanotechnologies: opportunities and uncertainties*. Plymouth, UK: Latimer Trend Ltd., p.5.

- Russel, M. and Model, P. (1989). Genetic analysis of the filamentous bacteriophage packaging signal and of the proteins that interact with it. *Journal of Virology*, 63(8), 3284-3295.
- Saijo, H. and Shiojiri, M. (1996). J-aggregates of cyanine dye molecules adsorbed on AgBr emulsion crystal surfaces. *Journal of Crystal Growth*, 166, 930-934.
- Saito, K., Honda, S., Watanabe, M. and Yokoyama, H. (1994). Optical anisotropic behaviour in cyanine dye J-aggregate Langmuir-Blodgett films. *Japanese Journal of Applied Physics*. 33, part 1 (11), 6218-6219.
- Sakakibara, K., Granström, M., Kilpeläinen, I., Helaja, J., Heinilehto, S., Inoue, R., Kanaya, T., Hill, J. P., Nakatsubo, F., Tsujii Y. and Ariga, K. (2013). Light-harvesting nanorods based on pheophorbide-appending cellulose. *Biomacromolecules*, 14, 3223-3230.
- Salstrom, J. S. and Pratt, D. (1971). Role of coliphage M13 gene 5 in single-stranded DNA production. *Journal of Molecular Biology*, 61, 489-501.
- Samuelson, J. C., Chen, M., Jiang, F., Möller, I., Wiedmann, M., Kuhn, A., Phillips, G. J. and Dalbey, R. E. (2000). YidC mediates membrane protein insertion in bacteria. *Nature*, 406, 637-641.
- Sandhu, S. (2015). Development of a biosensor based on linear dichroism spectroscopy. Ph.D. thesis, University of Birmingham, Birmingham, UK.
- Satake, A., Azuma, S., Kuramochi, Y., Hirota, S. and Kobuke, Y. (2011). Supramolecular organisation of light-harvesting porphyrin macrorings. *Chemistry: A European Journal*, 17, 855-865.
- Scholes, G. D., Fleming, G. R., Olaya-Castro, A. and van Grondelle, R. (2011). Lessons from nature about solar light harvesting. *Nature Chemistry*, 3, 763-774.
- Schuenemann, T. A., Delgado-Nixon, V. M., and Dalbey, R. E. (1999). Direct evidence that the proton motive force inhibits membrane translocation of positively charged residues within membrane proteins. *Journal of Biological Chemistry*. 274(11), 6855-6864.
- Scientific Committee on Emerging and Newly Identified Health Risks (2006). *The appropriateness of existing methodologies to assess the potential risks with engineered and adventitious products of nanotechnologies*. Brussels: European Commission, p.9.
- Sen, P., Fatima, S., Ahmad, B. and Khan, R. H. (2009). Interactions of thioflavin T with serum albumins: spectroscopic analyses. *Spectrochimica Acta Part A: Molecular and Bioanalytical Spectroscopy*. 74(1), 94-99.
- Sercombe, L., Veerati, T., Moheimani, F., Wu, S. Y., Sood, A. K. and Hua, S. (2015). Advances and challenges of liposome assisted drug delivery. *Frontiers in Pharmacology*, 6, 286.
- Shakiba, M., Ng, K. K., Huynh, E., Chan, H., Charron, D. M., Chen, J., Muhanna, N., Foster, F. S., Wilson, B. C. and Zheng, G. (2016). Stable J-aggregation enabled dual photoacoustic and fluorescence nanoparticles for intraoperative cancer imaging. *Nanoscale*. 8, 12618-12625.

- Shukla, A. A. and Thömmes, J. (2010). Recent advances in large-scale production of monoclonal antibodies and related proteins. *Trends in Biotechnology*, 28(5), 253-261.
- Shulaker, M. M., Hills, G., Patil, N., Wei, H., Chen, H-U., Wong, H. S. P. and Mitra, S. (2013). Carbon nanotube computer. *Nature*, 501, 526-530.
- Slavnova, T. D., Chibisov, A. K. and Görner, H. (2005). Kinetics of salt-induced J-aggregation of cyanine dyes. *Journal of Physical Chemistry A*, 109, 4758-4765.
- Smith, G. P. (1985). Filamentous fusion phage: novel expression vectors that display cloned antigens on the virion surface. *Science*, 228, 1315-1317.
- Smith, G. P. and Petrenko, V. A. (1997). Phage display. *Chemical Reviews*, 97, 391-410.
- Somasundaran, P. Encyclopaedia of surface and colloid science; vol. 3; CRC Press: Boca Raton, 2006; p.2329.
- Spruijt, R. B., Wolfs, C. J. A. M., Verver, J. W. G. and Hemminga M. A. (1996). Accessibility and environment probing using cysteine residues introduced along the putative transmembrane domain of the major coat protein of bacteriophage M13. *Biochemistry*, 35, 10383-10391.
- Sreeram, K. J., Narayan, S., Gopal, A., Hayhurst, A. and Mao, C. (2010). Architectonics of phage-liposome nanowebs as optimized photosensitizer vehicles for photodynamic cancer therapy. *Molecular Cancer Therapeutics*, 9(9), 2524-2535.
- Srinivasarao, M. (1999). Nano-optics in the biological world: Beetles, butterflies, birds and moths. *Chemical Reviews*. 99, 1935-1961.
- Staudenbauer, W. L. and Hofschneider, P. H. (1973). Positive role of gene-5 protein in single-stranded DNA synthesis. *European Journal of Biochemistry*, 34, 569-576.
- Steiger, R., Pugin, R. and Heier, J. (2009). J-aggregation of cyanine dyes by self-assembly. *Colloids and Surfaces B: Biointerfaces*, 74, 484-491.
- Stoilovic, M., Warrenner, R. N., and Kobus, H. J. (1984). An evaluation of the reagent NBD chloride for the production of luminescent fingerprints on paper: II. A comparison with ninhydrin. *Forensic Science International*. 24, 279-284.
- Stopar, D., Spruijt, R. B., Wolfs, C. J. A. M. and Hemminga, M. A. (2003). Protein-lipid interactions of bacteriophage M13 major coat protein. *Biochimica et Biophysica Acta*, 1611, 5-15.
- Sun, H., Luo, Q., Hou, C. and Liu, J. (2017). Nano-structures based on protein self-assembly: From hierarchical construction to bioinspired materials. *Nano Today*. 14, 16-41.
- Suthiwangcharoen, N., Li, T., Li, K., Thompson, P., You, S. and Wang, Q. (2011). M13 bacteriophage-polymer nanoassemblies as drug delivery vehicles. *Nano Research*, 4(5), 483-493.
- Tack, D. S., Cole, A. C., Shroff, R., Morrow, B. R. and Ellington, A. D. (2018). Evolving bacterial fitness with an expanded genetic code. *Scientific Reports*, 8, 3288.
- Talley, K. and Alexov, E. (2010). On the pH-optimum of activity and stability of proteins. *Proteins*, 78, 2699-2706.

- Talukder, P., Chen, S., Roy, B., Yakovchuk, P., Spiering, M. M., Alam, M. P., Madathil, M. M., Bhattacharya, C., Benkovic, S. J. and Hecht, S. M. (2015). Cyanotryptophans as novel fluorescent probes for studying protein conformational changes and DNA-protein interaction. *Biochemistry*, 54, 7457-7469.
- Thulstrup, E. W. and Eggers, J. H. (1968). Moment directions of the electronic transitions of fluoranthene. *Chemical Physics Letters*, 1, 690-692.
- Thulstrup, E. W. and Michl, J. (1982). Orientation and linear dichroism of symmetrical aromatic molecules imbedded in stretched polyethylene. *Journal of the American Chemical Society*, 104(21), 5594-5604.
- Thulstrup, E. W., Michl, J. and Eggers, J. H. (1970). Polarization spectra in stretched polymer sheets. II. Separation of π - π^* absorption of symmetrical molecules into components. *The Journal of Physical Chemistry*, 74(22), 3868-3878.
- Tørring, T. and Gothelf, K. V. (2013). DNA nanotechnology: a curiosity or a promising technology? *F1000 Prime Reports*, 5, 14.
- Tridgett, M., Lloyd, J. R., Kennefick, J., Moore-Kelly, C. and Dafforn, T. R. (2018). Mutation of M13 bacteriophage major coat protein for increased conjugation to exogenous compounds. *Bioconjugate Chemistry*, 29, 1872-1875.
- Tseng, B. Y. and Marvin, D. A. (1972). Role of fd gene 2 in deoxyribonucleic acid replication. *Journal of Virology*, 10(3), 384-391.
- Tumpane, J., Karousis, N., Tagmatarchis, N. and Nordén, B. (2008). Alignment of carbon nanotubes in weak magnetic fields. *Angewandte Chemie International Edition in English*, 47, 5148-5152.
- Umemura, J., Takenaka, T., Hayashi, S. and Gotoh, R. (1968). Infrared dichroism and orientation parameters of plasticizers in stretched polyvinylchloride films. *Bulletin of the Institute for Chemical Research, Kyoto University*, 46(5), 228-238.
- Valleau, S., Saikin, S. K., Yung, M. H. and Guzik, A. A. (2012). Exciton transport in thin-film cyanine dye J-aggregates. *The Journal of Chemical Physics*, 137, 034109.
- Van Wezenbeek, P. M. G. F., Hulsebos, T. J. M., and Schoenmakers, J. G. G. (1980). Nucleotide sequence of the filamentous bacteriophage M13 DNA genome: comparison with phage fd. *Gene*. 11, 129-148.
- Verma, S. and Ghosh, H. N. (2012). Exciton energy and exciton transfer in porphyrin aggregate/semiconductor (TiO₂) composites. *The Journal of Physical Chemistry Letters*, 3, 1877-1884.
- Vignolini, S., Moyroud, E., Hingant, T., Banks, H., Rudall, P. J., Steiner, U. and Glover, B. J. (2015). The flower of Hibiscus trionium is both visibly and measurably iridescent. *New Phytologist*. 205(1), 97-101.
- Vignolini, S., Rudall, P. J., Rowland, A. V., Reed, A., Moyroud, E., Faden, R. B., Baumberg, J. J., Glover, B. J. and Steiner, U. (2012). Pointillist structural color in Pollia fruit. *Proceedings of the National Academy of Sciences*. 109(39), 15712-15715.

- Von Berlepsch, H., Böttcher, C. and Dähne, L. (2000). Structure of J-aggregates of pseudoisocyanine dye in aqueous solution. *Journal of Physical Chemistry*, 104, 8792-8799.
- Wada, A. (1964). Chain regularity and flow dichroism of deoxyribonucleic acids in solution. *Biopolymers*, 2, 361-380.
- Wada, A. and Kozawa, S. (1964). Instrument for the studies of differential flow dichroism of polymer solutions. *Journal of Polymer Science: Part A*, 2, 853-864.
- Wang, L., Fan, J., Qiao, X., Peng, X., Dai, B., Wang, B., Sun, S., Zhang, L. and Zhang, Y. (2010). Novel asymmetric Cy5 dyes: Synthesis, photostabilities and high sensitivity in protein fluorescence labelling. *Journal of Photochemistry and Photobiology A: Chemistry*, 210, 168-172.
- Wang, Y. A., Yu, X., Overman, S., Tsuboi, M., Thomas, G. J. Jr. and Egelman, E. (2006). The structure of a filamentous bacteriophage. *Journal of Molecular Biology*, 361, 209-215.
- Wang, Y., Chen, M., Zhou, F. and Ma, E. (2002). High tensile ductility in a nanostructured metal. *Nature*, 419, 912-915.
- Warner, C. M., Barker, N., Lee, S. W. and Perkins E. J. (2014). M13 bacteriophage production for large-scale applications. *Bioprocess and Biosystems Engineering*, 37, 2067-2072.
- Warrener, R. N., Kobus, H. J., and Stoilovic, M. (1983). An evaluation of the reagent NBD chloride for the production of luminescent fingerprints on paper: I. Support for a xenon arc lamp being a cheaper and valuable alternative to an argon ion laser as an excitation source. *Forensic Science International*. 23, 179-188.
- Weertman, J. R., Farkas, D., Hemker, K., Kung, H., Mayo, M., Mitra, R. and Van Swygenhoven, H. (1999). Structure and mechanical behavior of bulk nanocrystalline materials. *Materials Research Society Bulletin*, 24(2), 44-53.
- Whitten, W. B., Pearlstein, R. M., Phares, E. F. and Geacintov, N. E. (1977). Linear dichroism of electric field oriented bacteriochlorophyll α -protein from green photosynthetic bacteria. *Biochimica et Biophysica Acta*, 503, 491-498.
- Wickner, W., Moore, K., Dibb, N., Geissert, D. and Rice, M. (1987). Inhibition of purified *Escherichia coli* leader peptidase by the leader (signal) peptide of bacteriophage M13 procoat. *Journal of Bacteriology*, 169(8), 3821-3822.
- Wingfield, P. T. (2001). Protein precipitation using ammonium sulfate. *Current Protocols in Protein Science*. Appendix-3F.
- World Health Organisation (WHO). (2015). *19th WHO model list of essential medicines*. Geneva: WHO.
- Wu, C., Biancalana, M., Koide, S. and Shea, J-E. (2009). Binding modes of thioflavin T to the single-layer β -sheet of the peptide self-assembly mimics. *Journal of Molecular Biology*. 294(4), 627-633.
- Wu, C., Wang, Z., Lei, H., Duan, Y., Bowers, M. T. and Shea, J-E. (2008). The binding of thioflavin T and its neutral analogue BTA-1 to protofibrils of the Alzheimer's

disease Abeta(16-22) peptide probed by molecular dynamics simulations. *Journal of Molecular Biology*, 384(3), 718-729.

Yacoby, I., Chamis, M., Bar, H., Shabat, D., and Benhar, I. (2006). Targeting antibacterial agents by using drug-carrying filamentous bacteriophages. *Antimicrobial Agents and Chemotherapy*, 50(6), 2087-2097.

Yu, H., Lu, C., Tieu, A. K., Liu, X., Sun, Y., Yu, Q. and Kong, C. (2012). Asymmetric cryorolling for fabrication of nanostructural aluminium sheets. *Scientific Reports*, 2, 772.

Yu, H., Yan, M., Lu, C., Tieu, A. K., Li, H., Zhu, Q., Godbole, A., Li, J., Su, L. and Kong, C. (2016). Superstrength of nanograined steel with nanoscale intermetallic precipitates transformed from shock-compressed martensitic steel. *Scientific Reports*, 6, 36810.

Zhang, L. and Cole, J. M. (2017). Dye aggregation in dye-sensitized solar cells. *Journal of Materials Chemistry A*, 5, 19451.

Zhou, Q. and Shao, W. L. (2010). Molecular genetic characterisation of the thermostable L-lactate dehydrogenase gene (*ldhL*) of *Thermoanaerobacter ethanolicus* JW200 and biochemical characterisation of the enzyme. *Biochemistry (Moscow)*, 75, 526-530.

Zhu, G., Cansiz, S., You, M., Qiu, L., Han, D., Zhang, L., Mei, L., Fu, T., Chen, Z. and Tan, W. (2015). Nuclease-resistant drug-DNA adducts: programmable drug-DNA conjugation for targeted anticancer drug delivery. *NPG Asia Materials*, 7, e169.

Zirpel, N. K., Arslan, T. and Lee, H. (2015). Engineering filamentous bacteriophages for enhanced gold binding and metallization properties. *Journal of Colloid and Interface Science*, 454, 80-88.